SYNERGISTIC EXPERIMENTATION AND NUMERICAL SIMULATION APPROACH TO CONJUGATE PHENOMENA OCCURRING IN CRYOSURGICAL DEVICES

A DISSERTATION
SUBMITTED TO THE FACULTY OF THE GRADUATE SCHOOL
OF THE UNIVERSITY OF MINNESOTA
BY

AMEETA RAUT GOYAL

IN PARTIAL FULFILLMENT OF THE REQUIREMENTS
FOR THE DEGREE OF
DOCTOR OF PHILOSOPHY

Dr. EPHRAIM SPARROW

April 2014

Acknowledgements

I express my sincere gratitude and heartfelt appreciation towards Professor Ephraim Sparrow for his invaluable guidance, treasured knowledge, brilliant suggestions, support, patience and help during my graduate studies.

I thank Dr. Chris Hogan, Dr. Xiaojia Wang and Dr. Shakar Zahra for their willingness to serve on my advisory committee and for their generous support. I thank Dr. Hogan also for serving as Chair of the committee. I am deeply touched by Professor Zahra's commitment as he went beyond the call of duty to give me his valuable time.

I thank current and past members of our research team especially- John Gorman, Jung Ahn, Dr. Reza Ramadani-Rend, Dr. Ryan Lovik, Dave Bennett, and Dan Bettenhausen for their help and discussions during my doctoral studies. Brainstorming with John helped me at some critical times during the research. I am grateful to Dr. Satish Ramadhyani for his support and valuable advice, Dr. Issac Fox and Patricia Williamson for their support, help and kindness. I am grateful to my friends Namita, Prajakta, Shilpa, Radhika, Meghana, Madhurima, Gayatri, Teja, Wei and Peihui for their wonderful friendship and support.

I thank my parents-in-law for all their love, blessings and support. I express my gratitude to my grandparents, family and Ruth May Sparrow for their blessings and best wishes.

I am deeply grateful to my husband, Deepak, for his love, support, encouragement and patience. *अशीच साथ लाभो!*

I am indebted to my parents for their love, support, and encouragement.
तुमच्या कुशीत मिळालेल्या ऊब, ऊर्जा, बळ, आशीर्वाद आणी प्रोत्साहनास समर्पित!

Dedication

वक्र तुण्ड महाकाय, सूर्य कोटि सम प्रभः।
निर्विघ्नं कुरू मे देव, शुभ कार्येषु सर्वदा।

To Parents, Deepak and Eph

Abstract

Cryosurgery has served as an alternative to scalpel-based surgery for over fifty years. A significant amount of research has been performed to improve the procedure. The goal of this research is to quantify the fluid mechanic, thermodynamic, and heat transfer processes which take place within two cryosurgical devices: a cryoprobe and a cryoballoon. A cryoprobe is a long, thin, cylindrical concentric tube which is inserted directly onto the cancerous tissue to be necrosed. A cryoballoon is a device that is deployed in a deflated state and is later inflated using a cryofluid that changes phase to cause low temperatures on the outer wall of the balloon to cause necrosis. Of the two aforementioned modalities, a heavy research focus has been seen on the study of the cryoprobes. However, it appears that the literature is void of any reported investigation that encompasses the entirety of all the participating physical processes. With respect to the cryoballoon, the literature appears to be without significant research publications.

An extensive and in-depth analysis of cryoprobe fundamental mechanisms like the Joule-Thomson (J-T) effect, compressibility driven high-speed flow, shocks, expansion waves, 180-degree turns, and heat transfer between the spent and virgin cryofluid. A rigorous, assumption-free in-probe and ex-probe phenomenological model was created here and implemented by synergistic use of numerical simulation and experimentation. The experiments were designed to verify the fidelity of the simulation model, and comparisons between the outcomes of the simulation and the experimentation were highly favorable. The capacity of a cryoprobe to extract heat from surrounding tissue has, for the first time, been demonstrated to be predictable from first principles alone, thereby, enabling logic-based design of cryoprobes.

A similarly first-principles model, devoid of empiricism and simplifying assumptions, was created for the study of cryoballoon-based necrosis. This investigation involved change of phase of liquid nitrous oxide to vapor. The available incremental experimental

data was used for comparison and provided excellent verification. It is believed that the models created and implemented here are sufficiently well supported to be regarded as universal approaches to be used when other cryosurgical devices are to be evaluated and quantified.

Table of Contents

List of Tables

List of Figures

Nomenclature

μ_{JT}	J-T coefficient
T	Temperature
P	Pressure
H	Enthalpy
$\dot{Q}$	Rate of heat transfer to the flowing fluid
$\dot{W}$	Rate at which the fluid does work on the surroundings
$\dot{m}$	Mass flowrate
V	Velocity
g	Gravitational acceleration
z	Elevation
M	Molecular weight
R	Universal gas constant
A	Model constant
$E_{\gamma 1}$, $E_{\gamma 2}$	Intermittency destruction terms
F_1, F_2	Blending functions in the SST model
P_k	Production term for the turbulent kinetic energy
$P_{\gamma 1}$, $P_{\gamma 2}$	Intermittency production terms
$P_{\Pi,t}$	Production term for the transition onset Reynolds number
S	Absolute value of the shear strain rate
u	Local velocity
x_i	Tensor coordinate direction
α	SST model constant
β_1, β_2	SST model constants
ω	Turbulent eddy frequency
μ	Molecular viscosity
μ_{turb}	Turbulent viscosity

v	Kinematic viscosity
σ	Prandtl-number-like diffusion coefficient
γ	Damping factor
ρ	Fluid density
Π	Turbulent adjunct function
Pr_{turb}	Turbulent Prandtl number
h_{tot}	Total enthalpy
k	Thermal conductivity
k_{turb}	Turbulent conductivity
φ	Dissipation function
$\hat{h}$	Overall heat transfer coefficient
β	Thermal expansion coefficient
Ra	Rayleigh number at position
Pr	Prandtl number

Chapter 1 Introduction

1.1 Background

1.1.1 Cryosurgery in Early Era

Cryosurgery, also referred to as cryotherapy or cryoablation, employs very low temperatures to destroy diseased tissues, and has gone through a long term process of development. As early as 2500 B.C. the Egyptians used ice as local anesthetic in the treatment of wounds and other ailments [1] [2]. Even during the fifth century B.C. cold treatments were clinically used to cure diseases in bones and joints [2]. During the Middle Ages and later into the 16^{th} and the 17^{th} century, cold baths as seen in Figure 1.1 and cold wet sheets were used to reduce fever and ameliorate inflammation [3].

Napoleaon's legendary surgeon, Dominique-Jean Larrey, used cold treatments to facilitate amputations during the historic retreat from Moscow [4]. Dr. James Arnott of Brighton, in England during 1845 and 1851 described the benefits of cold application in the treatment of numerous conditions like headaches and neuralgia. He used salt solutions containing crushed ice at a temperature of -18 to -24C to freeze breast, cervica and skin cancers. He observed the shrinking the tumors causes significant decrease in pain [5] He also designed an apparatus for the application of cold. This apparatus was displayed at the Great Exhibition in London in 1851 [6]. This new device was cumbersome to use and had low freezing capacity and limited applicability [7]. Further developments on cryosurgery had to await the availability of cryosurgical agents that were capable of producing extremely low temperatures.

Later around 19th century several major progresses were observed in the field of cryogenics. Louis Cailletet, a French mining engineer produced liquid oxygen droplets by adiabatic expansion system [8] [9]. James Dewar in 1892, designed the first vacuum flask. This facilitated the storage and handling of liquefied gases. Von Linde established commercial liquefaction of air in 1895-1896. In the subsequent years, methods to liquefy gases like oxygen, nitrogen and hydrogen were developed. Providing extreme cold cryogenics agents and the means of storage and handling in therapy, these progresses in cryogenics greatly stimulated the development of cryosurgery [3] [10].

Figure 1.1 A man self-administering hydrotherapy [11]

Dr. Campbell White in 1899, used liquid air in treatment of skin disease along with Professor Charles Tripler [12]. Liquid air was reported to treat warts, varicose leg ulcers, chancroids, boils, carbuncles, herpes, zoster and epitheliomas [10]. As a clinical cryofluid, liquid air was later on replaced by solid carbon dioxide due to its wide availability [13]. In later years, liquid oxygen was alternatively used in skin treatments. This option however was not viable due to fire hazards [14]. In early 1940s large scale liquefaction of hydrogen and helium were developed and liquid nitrogen, a byproduct,

available in abundance and low cost. Liquid nitrogen performed much better than carbon di oxide and gained popularity in the cryosurgical procedures.

1.1.2 Modern Day Cryosurgery

Modern cryosurgery began through the collaborative work of a physician, Irving Cooper and an engineer Arnold Lee [15]. They built a prototype from which every subsequent cryoprobe was developed. This prototype was made of three concentric long tubes. They used pressurized liquid nitrogen as the cryofluid as seen in Figure 1.2. The innermost tube served as a conduit for liquid nitrogen flow to the tip of the probe whole the space in between the middle and innermost tube served as the annulus and provided a path for the return of gaseous nitrogen from the tip of the probe. The space between the middle and the outermost tube was vacuum insulated and had a radiative shield [15]. Thus the field of cryosurgery experienced a fast growth.

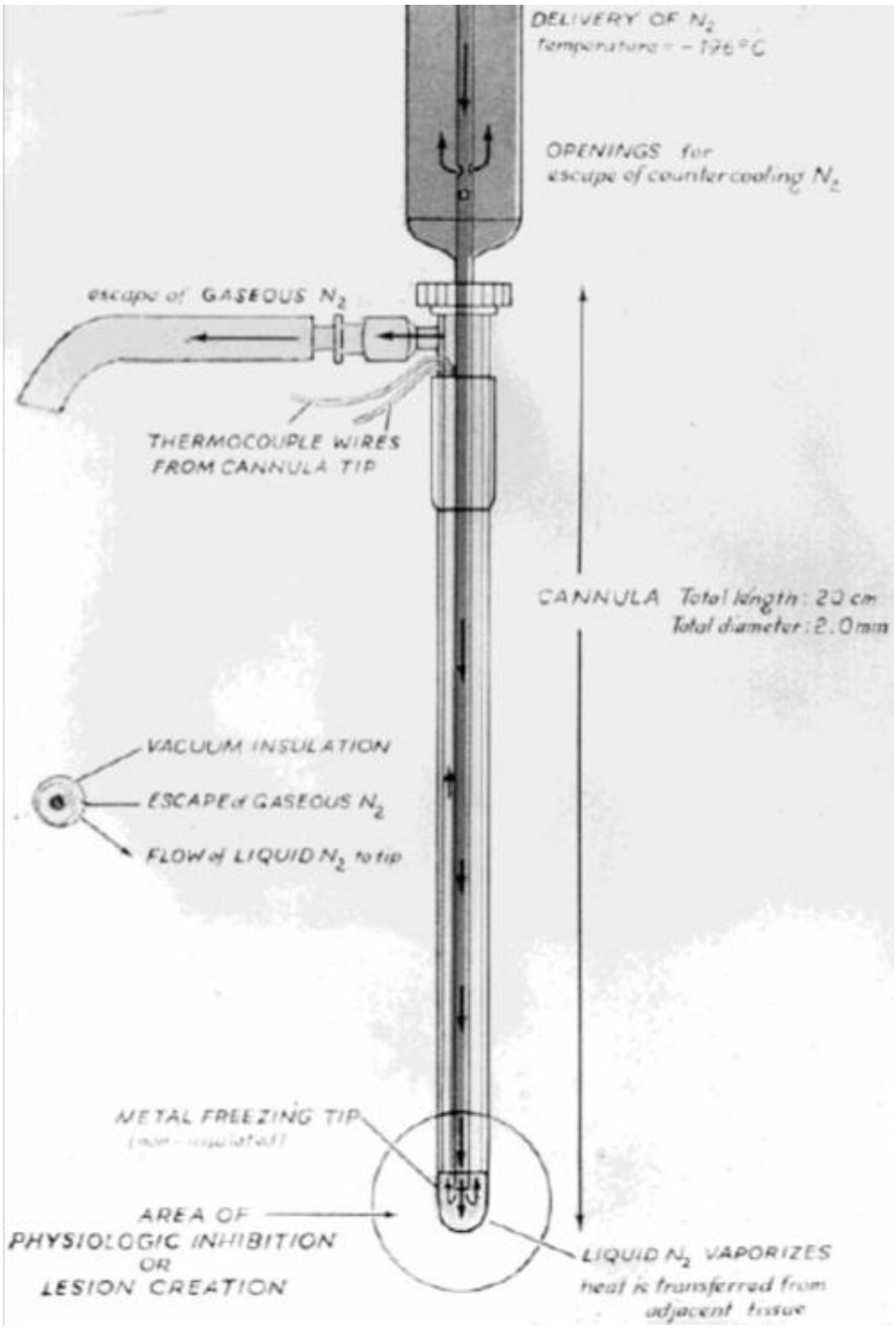

Figure 1.2 Schematic of the first cryoprobe developed by Cooper and Lee for the treatment of Parkinsonism [16] [11].

Cryosurgery was also used in the field of neurology by Rand and his colleagues in 1964 [17], in the treatment of prostate disease by Gonder and his colleagues 1964 [18], in the area of orthopedics by Marcover and Miller [19], and in the treatment of cutaneous surgery by Zacarian [20] and Torre [21]in 1966 and 1970 respectively. In 1964, Cahan [22] and his colleagues developed a heating element for the easy release of the probe from the frozen tissue and applied cryosurgery in treatment of diseased uterus.

Unlike traditional surgical procedures, the issue with cryosurgical procedures is that the physician cannot visually determine the extent to which the frozen front advances during the procedure. This could lead to a possibility of either insufficient freezing or over-freezing. If insufficient freezing occurs, then there is a high risk of incomplete treatment. For example, in case of cancer treatments there is a possibility that not all cancer cells get necrosed, in case of ablation procedures for atrial fibrillation the irregular beating of heart continues etc. Over-freezing during the procedure however could cause serious problems to the healthy tissues resulting in various complications post-procedure. Due to the above mentioned issues, cryosurgery lost its popularity in the 1970s. Several efforts have been made in the last couple of decades to increase the efficacy of the procedures by developing advanced monitoring and imaging techniques.

For example, advancements in the local thermal measurement techniques as seen in Figure 1.3 helped ensure proper monitoring of the temperatures during tissue destruction. However, there are drawbacks even to these methods [23]. Even though cryosurgery is minimally invasive, monitoring the temperature involved inserting a thermocouple directly on the targeted tissue. Also, the measurements were restricted to the sites where the thermocouple was mounted which are insufficient when freezing the entire cluster of targeted tissue. Another drawback was that the temperatures measured had relatively large errors due to the influence of the thermocouple shaft [24]. However, cryosurgery experienced rapid growth in many fields around 1980’s in the field of dermatology and gynecology.

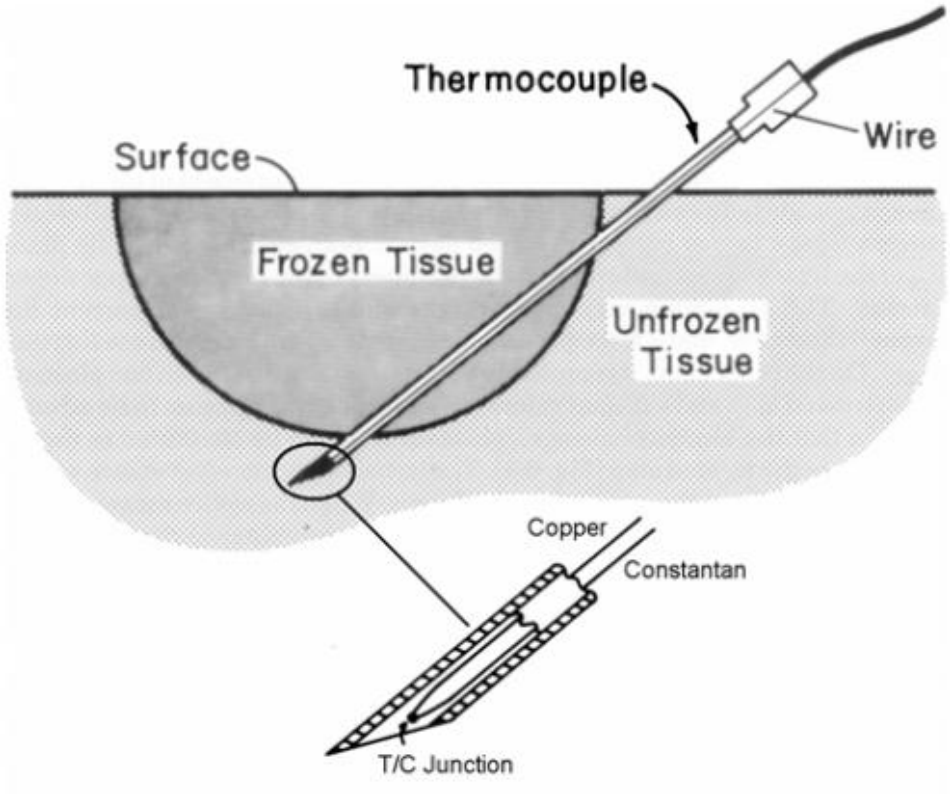

Figure 1.3 Schematic of temperature monitoring using thermocouple needle that is inserted into the tissue to be necrosed [3]

Table 1.1 History of Cryosurgery

History of Cryosurgery			
Time (Year)	**Inventer**	**Cryosurgens**	**Application**
3500 years ago	Old Greece	Ice	Treatment of infected wounds
11th century	Avicenne	Ice	Anesthesia

1650	Whenry	Ice	Treatment of gout
1845	Faraday M.	Ice and salt water	Freezing tumors
1851	Arnott	Mixure of salt and crushed ice	Freezing advanced cancers
1877	Caillete, France; Pietet, Swizerland	Liquid oxygen and nitrogen	Making low-temperature
1892	Dewar,UK	Deveopment of the first vacuum flast for facilitated storage and handling of liquefied gases	
1895	Linde, Germany; Hampson, UK	Use of the Joule_Thomson effect to produce continuously operating air liquefiers	
1899	Campbell White	First to use refrigerants for medical practice	
1907	Whitehouse	Use of liquid air for epitheliomata	

1907	Pussey William	Solid carbon dioxide	Establishment of cryotherapy
1911	Hall-Edwards	Described carbon dioxide collection model	
1940s	Kapitsa, Collins	Liquid hydrogen and nitrogen	Making liquid nitrogen
1945 1950	Jarnott Allington	Low temperature Liquid nitrogen	Treatment of tumors Use of treatment in dermatology and gynecology
1959		Mixture of ethanol	Cryosurgery
1961	Cooper, USA	Liquid nitrogen	Treatnement of diseases of central nervous sysem
1967 1968	Amoils	Liquid nitrogen probe Liquid nitrogen	Cryoextraction Treatment of prostate cancr and liver cancer
1976	Wright	Nitrous oxide cryo-	Treatment of

		apparent	benign prostate hyperplasia
1985	Zacarian	Developing copper probe	Treatment of deep lesions
1090s	USA,China	Liquid nitrogen	Treatment of tummors of prostate, liver and kidney
1998	USA	Argon - based cryosurgical system	Treatment of prostate cancer and liver cancer approved by FDA, USA
1999 - 2000	Israel	Argon - based cryosurgical system	Clinical use approved by CE, 1999, and by FDA , USA, 2000
After 2000	USA, China	Argon - based cryosurgical system	Treatment of tumors of liver, lung, kidney and pancreas

1.2 Cryosurgery using Cryoprobes

Cancer is one of the major causes of mortality in our modern fast-paced society and has taken over cardiovascular diseases to become the number one killer disease in the world. According to American Cancer Society 2013 report, about 1,660,290 new cancer cases are expected to be diagnosed in 2013, and in 2013 about 580,350 Americans are projected to die of cancer, almost 1,600 people a day. Cancer remains the second most common cause of death in the US, accounting for nearly 1 of every 4 deaths [25]. Common treatments of cancer include surgical removal, radiation therapy and chemotherapy which have devastating effects on the cancer patients [26]

1.2.1 In-depth background

As previously discussed, cryosurgery is based on the freezing of dysfunctional tissue by means of a low-temperature fluid contained within a cryoprobe that is brought in thermal contact with the target tissue [27]. This fluid extracts heat from the surrounding tissue and within several minutes after the cooling begins, the temperature of the tissue in contact with the probe reaches the phase transition temperature and begins to freeze. The freezing interface propagates outward until the flow of the coolant fluid in the cryoprobe is stopped. At that time, the frozen tissue has a temperature distribution that ranges from a low cryogenic temperature at the tissue surface in contact with the probe to the phase-transformation temperature on the outer edge of the frozen lesion [28, 29]. As a consequence, there is a steep temperature gradient across the thickness of the ice [30]. This gradient gives rise to differential expansion and to concomitant thermal stresses. It appears that these stresses are held in check during the freezing process because the ice does not crack [31] [32].

The freezing process of the tissue is followed by the heating of the cryoprobe by passing a room-temperature fluid through it [33] . The heating does not affect the already-necrosed tissue. In the case in which argon is used to create the cryo-temperatures, the heating of the ice layer is accomplished by circulating gaseous helium through the same flow passages that previously accommodated the argon [34] [35]. Helium is chosen because it has the highest thermal conductivity of any gas, aside from hydrogen whose use requires special handling precautions. The value of the Joule-Thomson coefficient for helium is very smaller and of different sign than that of argon [35] [36] so the temperature of the flowing helium does not experience a drop. The combination of a freezing process followed by a thawing process gives rise to thermal stresses. These stresses are relieved by the cracking of the ice. [37].

The consequence of the elevated cryoprobe temperature is the thawing of the iceball. During warming, the ice has a tendency to recrystallize at high subzero temperatures to minimize the Gibbs free energy [38]. This recrystallization causes disruption of the extracellular space and also macroscopic structure of the tissue [39]. In the process of thawing, the ice melts and the tissue can be briefly hypotonic causing the water to enter some cells and expand them thus rupturing them to cause damage [40]. Furthermore, rupture of blood vessels and platelets aggregation lead to cell injury due to thrombosis, vascular occlusion and necrosis [41] [27] [42] [43]. A detailed description of the factors affecting the procedure is discussed in the further sections of this chapter. There are various devices used in the cryosurgical procedure for eg- cryoprobes (also called as cryoprobes), cryoablation-catheters (also known as focal-point cryocatheters), cryoballoons, cryosprays which are used in the treatment of various diseases. A detailed discussion of the construction, operation, shortcomings and the resulting motivation for this work is discussed further.

1.2.2 Structure and Working

A display of cryosurgical probes is shown in Figure 1.4. The ice ball [44] created by the freezing of the intercellular fluids is also displayed along with its typical dimensions.

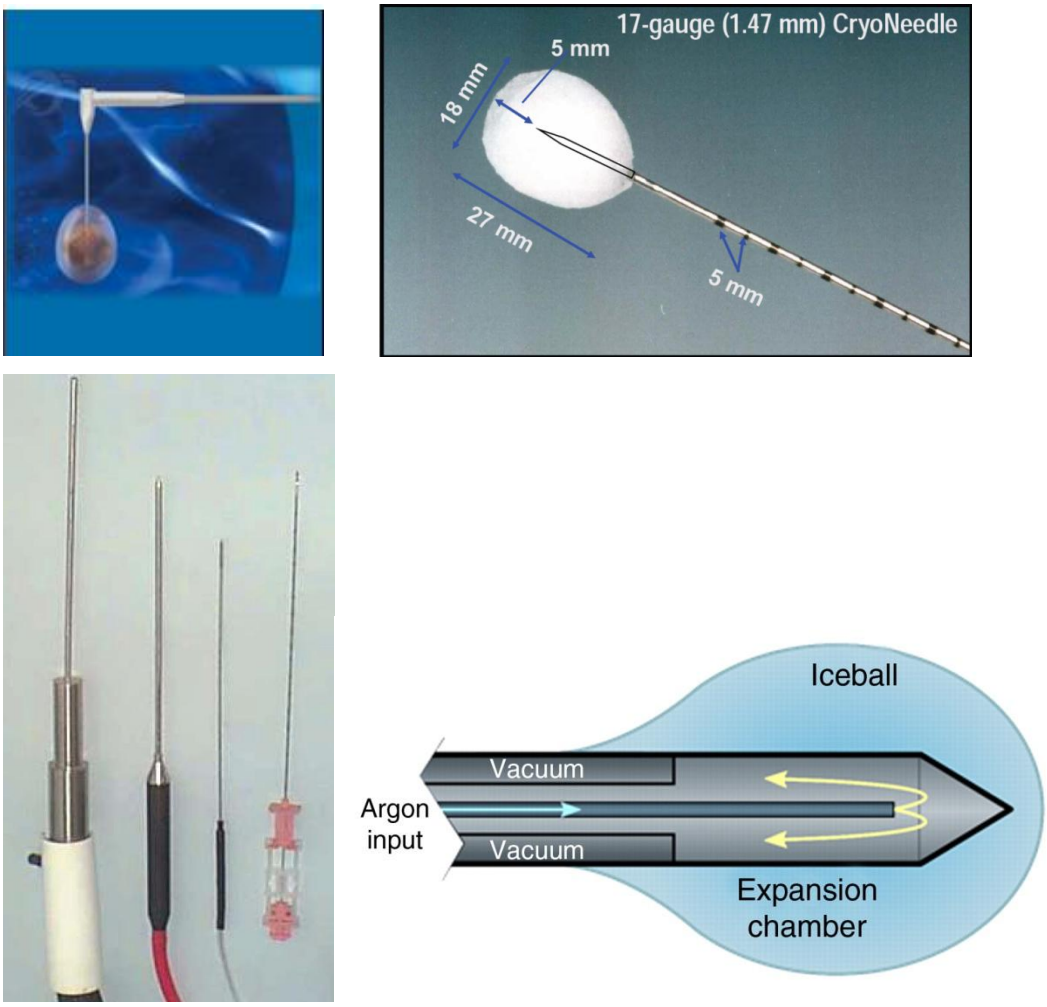

(a) (b)

Figure 1.4(a) Typical shape of ice ball. (b) Several shapes of cryosurgical probes [26] [45] [46].

A schematic diagram, taken from the literature, of a typical therapeutic setup is shown in Figure 1.5. The figure shows the presence of a high-pressure argon tank used during the

tissue-freezing portion of the therapeutic process. The cryofluid is stored in a high-pressure cylinder, typically 6000psi that supplies enough gas for 8-10cryoprobes [47]. The pressurized gas is then transferred to regulator system that controls the gas flow rate to the cryoprobes. The gas is transferred to the cryoporbe where it is allowed to decompress inside the cryoprobe and then released to the atmosphere in its return flow path.

The argon pressure is controlled by a pressure-reducing valve, where after the argon is ducted to a capillary tube that is situated along the axis of the cryoprobe. [The colors are to be ignored because they do not have any connection with the either temperature or pressure]. Not shown in this diagram is the flow path used to convey the spent argon from the cryoprobe.

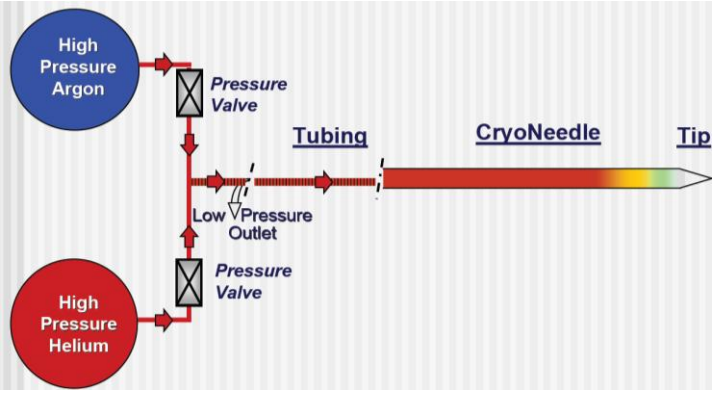

Figure 1.5 Schematic diagram of a typical therapeutic setup using a cryosurgical probe [47]

Figure 1.6 is another diagram taken from the literature [35] [36] [48]. It also shows the use of argon as a cryofluid. The figure is to be regarded as highly schematic and does not necessarily represent the most common configurations of currently used cryoprobes. In particular the colors are those the reference from which the figure was taken and do not

carry any specific message. Note that the argon which flows in the central tube must execute a 180-degree turn after it exits the downstream end of the tube through a constriction. Thereafter, the argon in the annulus external to the central tube exchanges heat not only with the external surface of the cryoprobe but also with the central tube. Due to the J-T effect in gases like argon, nitrogen and oxygen, the rapid decompression results in the cooling effect. The cooled gas is vented out to the atmosphere at room temperature

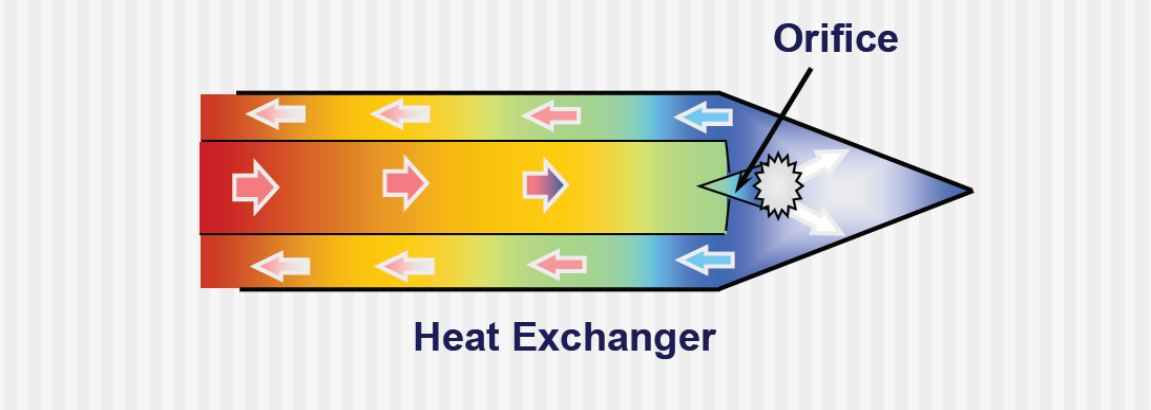

Figure 1.6 Schematic cartoon of a cryoprobe with argon as the cryofluid

Once an ice ball has been created and necrosis has been achieved, the internal channels of the cryoprobe are used to facilitate the sloughing off of the ice ball by means of a fluid which does not experience the J-T effect. In this regard, helium is the gas of choice because of its high thermal conductivity and because its J-T effect is negligible. The heating of the ice coating at the end of the necrosis process creates a temperature distribution across its thickness. In the direction outward from the exterior surface of the tool, the temperature may decrease at first, reach a minimum, and then increase. The induced thermal stress pattern is superposed on the already existing stress pattern.

There are three ways in which the thermal energy is transferred from one volume to another (a) conduction-by the transfer of heat or energy from the tissue at a high temperature (37C) to a the iceball at a lower temperature (-150C) by virtue of physical contact (b) convection-by the transfer of energy from the iceball to the body fluids (c)

radiation- by removing radiant energy from all bodies above absolute zero temperature [49] [50]. No significant radiation losses are seen in cryotherapy so the study focuses on the conduction and convection phenomena. The removal of the energy from the surrounding tissue is affected the J-T cooling of the cryofluid. The probe shape depends on the size and shape of target lesion. The resultant isotherms for different probes are graphically represented in Figure 1.7.

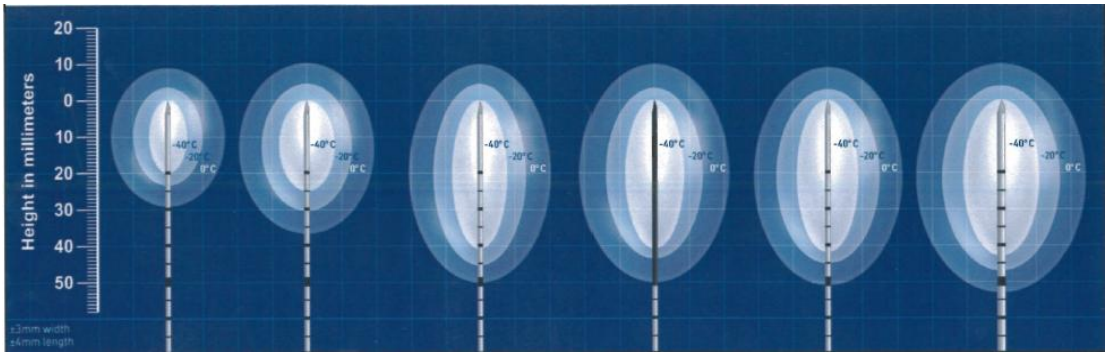

Figure 1.7 Graphical representation of isotherms for different probes

As seen in Figure 1.8 there are two competing phenomena (sum of conduction and convection) occurring in the cryoablation procedure- the rate of heat transfer in $\dot{Q}_{in}$ and out $\dot{Q}_{out}$ of the ice ball. The diameter of the iceball depends on the difference between the heat transfer rates.

At the beginning of the procedure the $\dot{Q}_{out}$ is more than $\dot{Q}_{in}$ and the ice ball keeps growing in size. The surface area of the ice increases thus $\dot{Q}_{in}$ increases. $\dot{Q}_{out}$ is stable and depends only on the flow rate of gas that expands in the needle. At equilibrium $\dot{Q}_{out}$=$\dot{Q}_{in}$ and the iceball growth stops. This is the steady state portion of the cryoablation procedure.

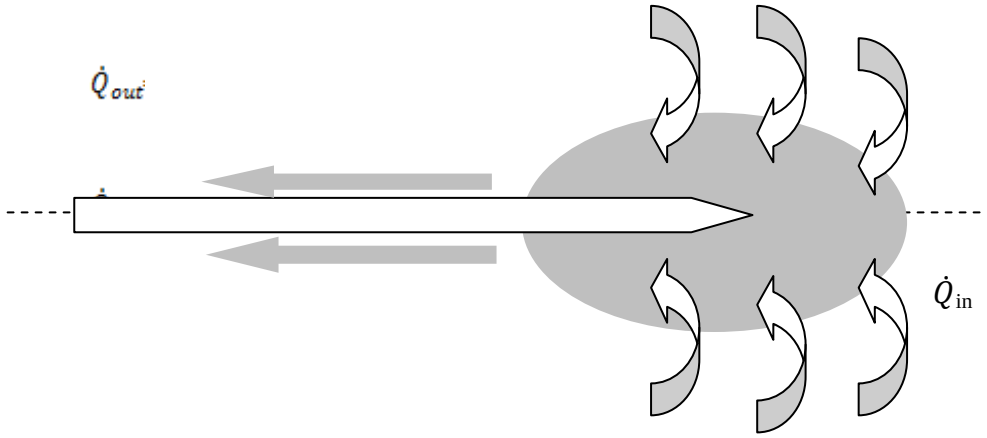

Figure 1.8 Schematic of the heat transfer phenomena in a cryoprobe [46]

As discussed earlier, the diameter of the iceball depends on the flow rate of the cooling gas. The length of the iceball depends on the uninsulated part of the cryoprobe as seen in figure. The temperature rises quickly as a function of distance from the needle, and it reaches zero at the edges of the iceball. The schematic shown in Figure 1.9 displays the flow of argon gas into the cryoprobe and the temperature variation across the iceball. The internal mechanisms like Joule-Thomson effect, shockwaves, 180 degree turns, conjugate heat transfer phenomena in the needle etc., depend greatly on the cryofluid used in the procedure. The external thermodynamic mechanisms of cooling may vary significantly depending on the medium surrounding the cryoprobe and the internal mechanisms [51].

Depending on the surrounding media, needle combinations, and type of cryofluid, will draw different amount of heat loads and can produce different temperature gradients on and surrounding the cryoprobe. The prior art in this area can generally be grouped into boundary conditions that prevail on the external surface of the needle [46] [52]. This includes constant surface temperature, constant heat flux, and surface convection conditions. The temperature profile along the center of the ice ball is seen in Figure 1.9.

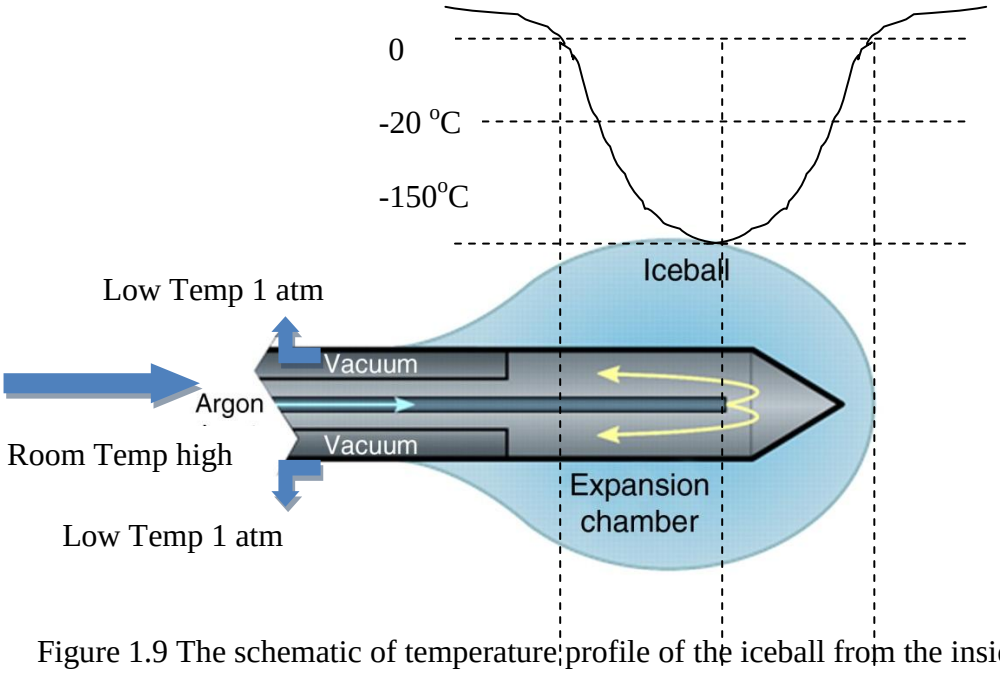

Figure 1.9 The schematic of temperature profile of the iceball from the inside end touching the outerwall of the probe to the surrounding medium in contact [46]

1.3 Cryosurgery Using Cryoballoons and Cryoablation Catheter

1.3.1 Atrial Fibrillation

1.3.1.1 In-depth background

The electrical signals in the heart control the rhythm of the heartbeat. An electrical signal begins in the group of cells called the sinus or sinoatrial node located in the upper right atrium as seen in Figure 1.10 [53], new heart beat begins here. As signal travels through the right and left atria, the atria contracts and pumps the blood into the ventricles. The electrical signal slowly moves to the next group of cells called the atrioventricular node

located between the atria and the ventricles. As soon as the ventricle is filled with blood, the electrical signal leaves the artioventricular node and travels to the ventricles. This causes the ventricles to contract and pump blood to the lungs and the rest of the body. One heart beat cycle completes here.

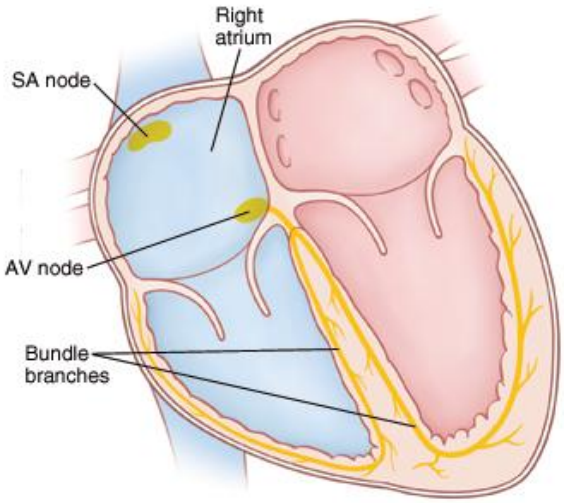

Figure 1.10 Path travelled by electrical signal in the heart

A normal heart beats about 60-100 time each minute (100,000 times/day) in a steady and even rhythm. Irregular disturbances in the heartbeat occur when the electrical impulses in the heart that coordinate the heartbeat don't function in a synchronized manner. This too fast, too slow or irregular heart beat causes cardiac arrhythmia. A heart beat that is too fast or too slow is called tachycardia and a heartbeat that is too slow is called bradycardia. Arrhythmia occurs in the upper(atria) or lower (ventricles) chamber of the heart. Atrial Fibrillation is the most common type of arrhythmia. The word *atrial* is derived from *atria*, two upper chambers of the heart and *fibrillation* means very fast and irregular contraction.

In patients suffering from atrial fibrillation, the electrical signals do not start at the sinus node. Instead these signals originate from another part of atria or in the nearby pulmonary

veins. These randomly generated signals spread throughout the atria in a rapid and disorganized way causing the atria to fibrillate. These faulty signals reach the atrioventricular node triggering the ventricles to beat faster. However, the atrioventricular node cannot send the signals to the ventricles at the same rate as they arrive. Hence, even though the ventricles beat faster than the normal, they are not as fast as the atria. Thus, there is a lack of coordination between the atria and the ventricles. This creates a fast and irregular heart rhythm. In atrial fibrillation, the ventricles beat around 100-175 times a minute in contrast to the normal rate of 60-100 times per minute. The blood is not pumped in to the ventricles at the same rate as the normal heart. The blood that stays in the atria can clot resulting in circulatory instability or stroke.

1.3.1.2 Atrial Fibrillation: Treatment

Atrial fibrillation(AF) is the most commonly sustained cardiac rhythm disturbance that has increasing prevalence with age [54]. Pulmonary vein isolation using a catheter-based device is the one of the primary treatments for AF [55]. A discussion on catheter-based technique was used as early as 1982 [56].

Depending on the severity of the condition, several different treatments are available for the treatment of atrial fibrillation. Some of them include anticoagulation drugs used to prevent blood clots to reduce the risk of stroke, rhythm controlling drugs within a normal range, restore a normal heart rhythm with drugs, cardioversion, maze procedure, surgery, and catheter ablation procedures. Ablation is a minimally invasive technique that is used in removal or necrosis of unwanted body of tissue. Catheter ablation involves advancing several flexible catheter or thin tubes extruded from biocompatible materials into the patients' blood vessels either in the femoral vein (location), or subclavian vein (location). These catheters are then advanced towards the heart. Ablation procedure in atrial fibrillation can be accomplished using several different techniques like the radio frequency ablation around the pulmonary vein i.e, heating of the tissue cells, cryoablation

i.e., freezing the abnormal tissue cells to prevent them from causing the disturbances, percutaneous ethanol injection (PRI), microwave, laser, and focused ultrasound. Each of these techniques have their strengths and weaknesses with unique issues to tackle. For example, there are inherent risks involved in using radio frequency energy [57] on a thin-walled atrium that can injure the adjacent structures including the pulmonary veins (stenosis), oesophagus, nerve plexi, aorta, bronchi, pericardium, phrenic nerve, and lungs. Although all the methods cause death of cells by coagulation necrosis, the knowledge and understanding of the underlying mechanism of thermal ablation of the tissue and the effect of the specific heats on the tissue can help improve the efficacy of the procedures [58].

Cryoablation was initially introduced as another point-by-point ablation technique. Subsequently, a balloon based platform was introduced with the theoretical advantage that they may be able to apply a simpler, faster and more effective means of achieving pulmonary vein isolation.

1.3.2 Cryoabaltion catheter and cryoballoon

1.3.2.1 Cryoablation Catheter: Structure and Working

Focal cryoablation procedures are carried out using a cryoablation catheter as seen in Figure 1.11. The basic design is similar to the cryoprobe. The liquid refrigerant is delivered under pressure to the tip through a hollow injection tube. The refrigerant (N2O) then undergoes phase change to a gas and the tip cools. The gas is removed under vaccum through the catheter shaft. The working of this device is very similar to the cryoprobe. Unlike the cryoprobe where the tip of the probe is sharp to provide assistance during insertion of the needle, the tip of the focal-point catheter is blunt.

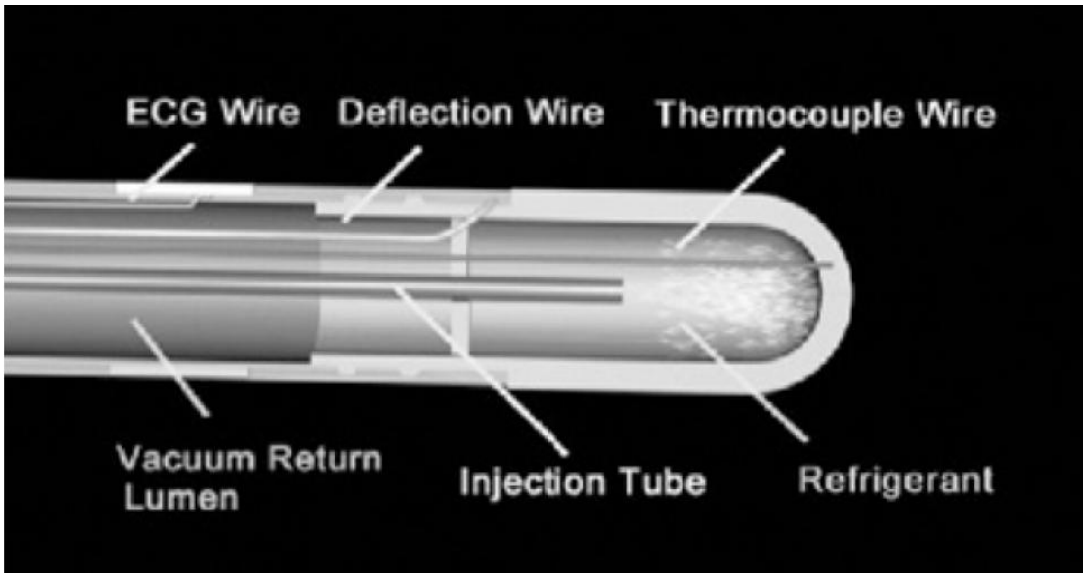

Figure 1.11 Schematic of cryoablation catheter. [59]

1.3.3.2 Cryoballoon: Structure and Working

Catheter cryoballoon ablation procedures are performed by circulating a cryofluid through a catheter that is inserted into the body and positioned at the site of the arrhythmia. The concept of using a cryoballoon for treatment of atrial fibrillation was set forth in early 2000's [60] and is shown in Figure 1.12. During period 2005-2013, 974 results were found with the keywords " cryoballoon for atrial ablation". The cryoballoon catheter in contrast with the focal-point catheter represents a more appealing system for pulmonary vein isolation. It is hoped that the balloon can help achieve the goal of electrical isolation with potentially one single application [61]. Currently, only one balloon design is available for clinical use [62].

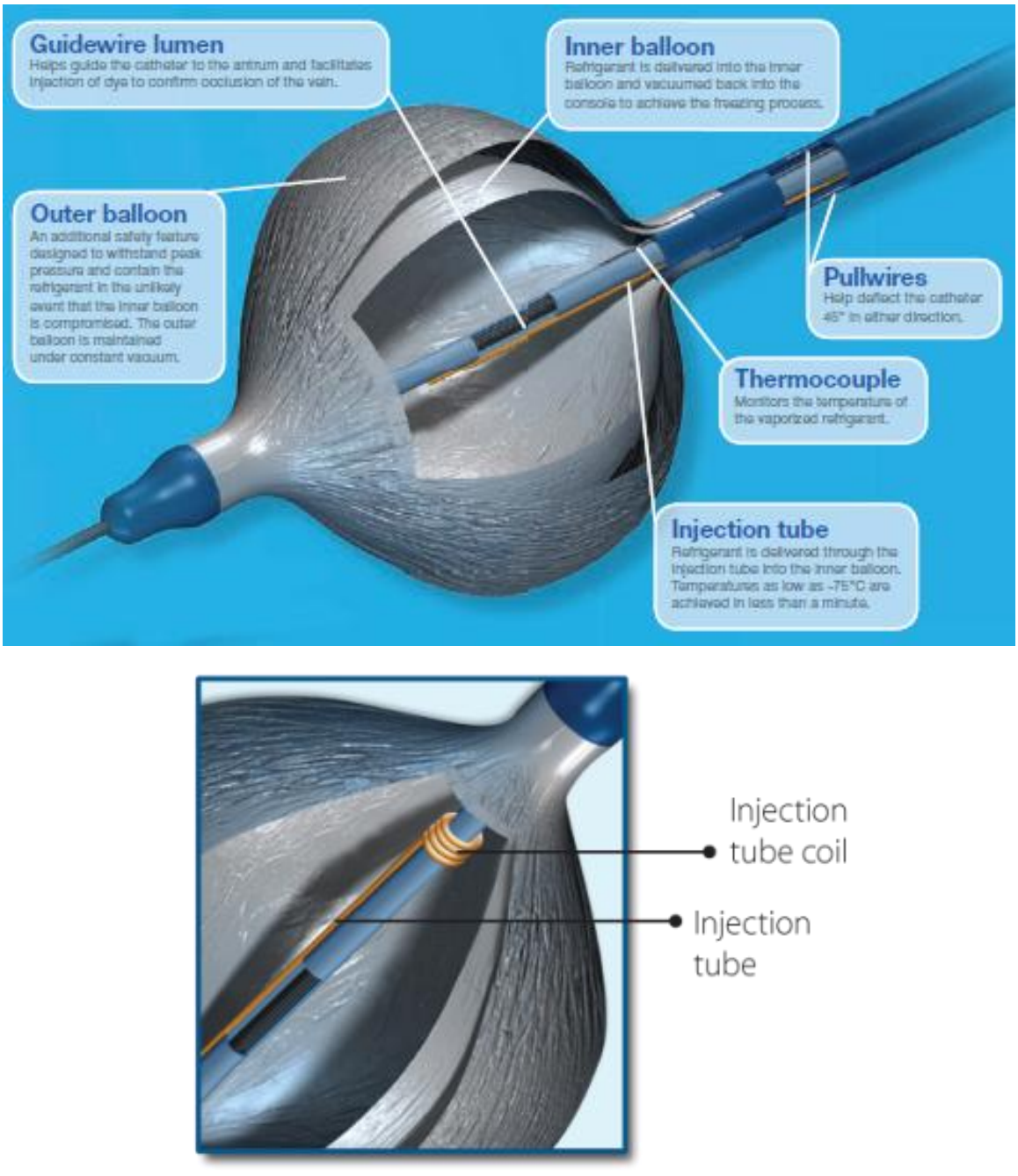

Figure 1.12 Cryo balloon [63]

The actual dimensions of the balloon are seen in Figure 1.13. The balloon is first inflated and then it is positioned next to the part where the ablation procedure is to be performed

as seen in Figure 1.14. A cryoballoon catheter consists of an injection tube that permits the injection of cryorefrigerant to the inner balloon, an exhaust lumen that facilitates its removal, a lumen in the center that permits a guide wire for proper positioning and support, a thermocouple on the central shaft near the proximal end of the balloon to facilitate the inner balloon temperature measurements, pullwire mechanism to steer the catheter deflections, an d vacuum insulated outer polyurethane balloon [64].

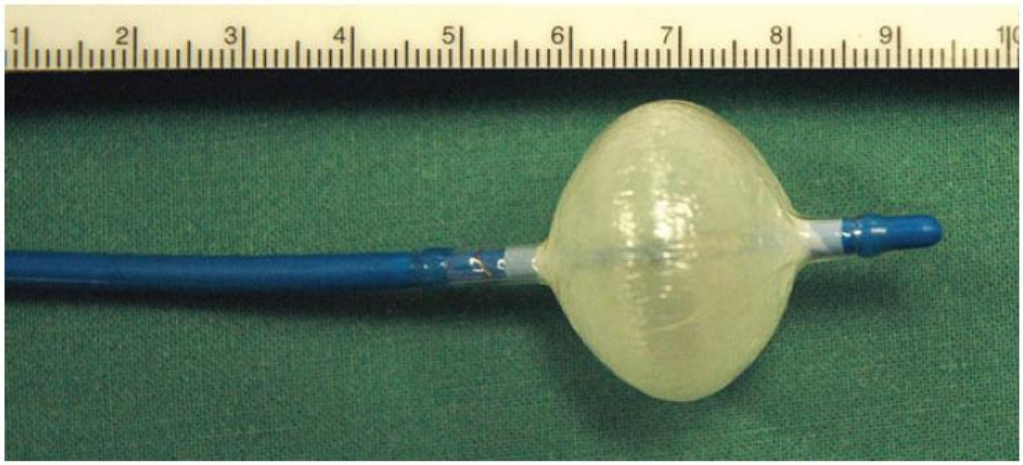

Figure 1.13 Distal end of a 23 mm, 10.5 F, double lumen cryoballoon catheter after inflation [65]

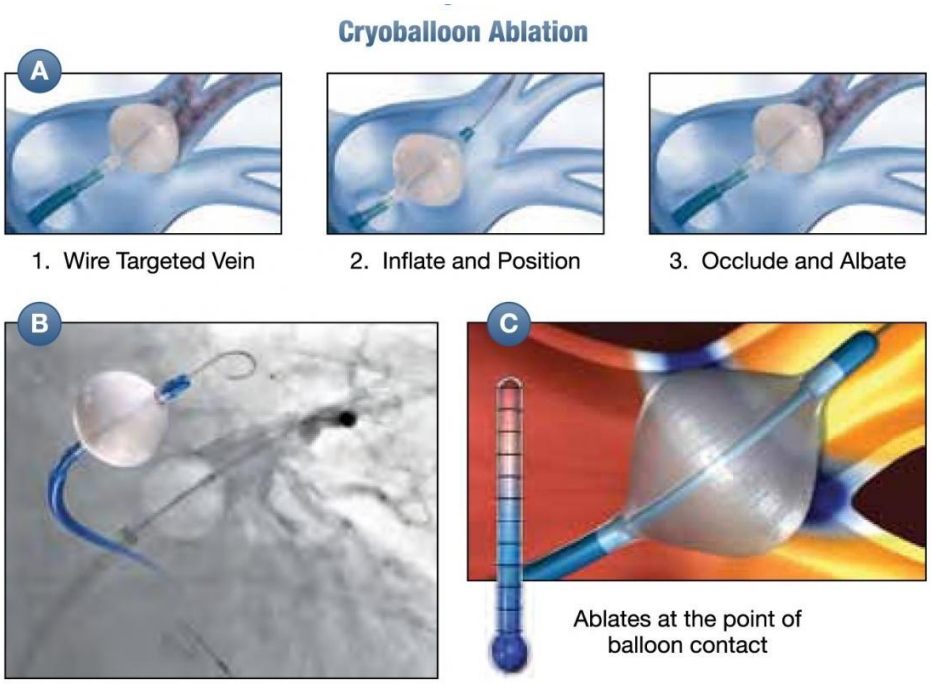

Figure 1.14 Cryoablation procedure [66]

A coaxial tube carries the cryofluid (N2O) [67] [68] to and from the balloon as seen in Figure 1.12. This high pressure cryofluid circulated through a centrally positioned ultra-fine lumen is injected in to the balloon [69]. At the point, the cryofluid experiences a huge change in pressure and it thus causes a decrease in the temperature (-80C). The inner lumen is helically wound on the inner diameter of the catheter. This helical coil has exit ports to eject the cryofluid inside the balloon. Due to the Joule-Thomson effect, the fluid temperature drops even further as it experiences sudden expansion through the exit ports while entering the balloon. The jets impinge on the periphery of the balloon.

Cooling occurs on the spots where the jet impinges the balloon. The cooling zones gradually increase to cause a frozen circumferential area. The cryofluid changes its phase from liquid medium to gas due to sudden expansion. The spent fluid in the gaseous media is carried through the coaxial annulus and collected back in the console.

Similar to the cryoprobe, the cryoballoon lesions occur in three main phases. The first phase is characterized by immediate effect of freezing the cardiac tissue by forming ice crystals in both the extracellular and intracellular space. When the temperature reaches lower than -20to -25C ice formation occurs in the extracellular space. When the temperature reaches lower than -40C, cellular damages is initiate by means of intracellular ice formation. Irreversible cellular death occurs when the temperature reaches below -70C. When the cryothermal energy is stopped, a rapid vasolidation and a state of augmented vascular permeability is reached, which causes hemorrhage and edema and leads to further tissue injury. This phase is also characterized by the microthrombus formation in the tissue and it leads to further damage [62].

1.4 Other Modalitites of Cryosurgery

The cotton tipped dipstick method of liquid nitrogen has been popular for treating many benign lesions. This method was later supplanted by the liquid nitrogen spraying technique. It is easy to use technique for external benign, premalignant and malignant lesions Figure 1.15 .

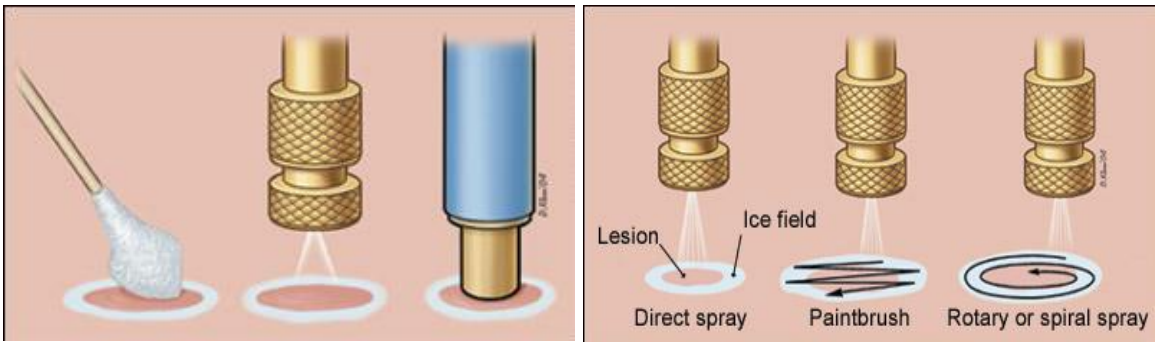

a. dipstick method b. spray tecnique c. timed spot freeze technique [70]

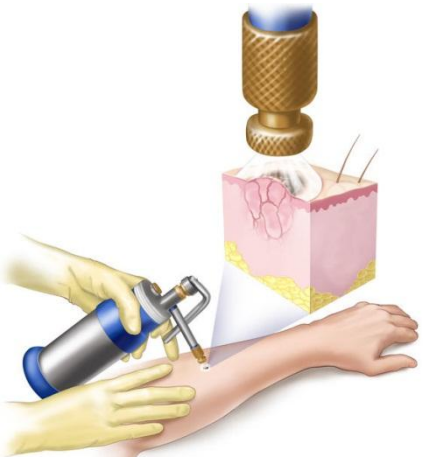

Figure 1.15 Other modalities of cryosurgery

The times spot freeezing technique allows greater standardization of the cryofluid delivery. The spray gun holds 300ml-500ml of cryofluid through a nozzle. Some other techniques include direct spraying in a rotary or spiral pattern and paintbrush method.

1.5 Merits of Modern Day Cryosurgery

With advances in technology modern cryosurgery has been used in treatment of various cancers, cardiovascular disorder, ophthalmology, and several other benign and malignant lesions. It is primary using tissue freezing to destroy any undesirable tissue. According to the National Institue of Cancer, cryosurgery is used treat several types of cancer, and some precancerous or noncancerous conditions. In addition to prostate and liver tumors, cryosurgery can be an effective treatment for the following:

- Retinoblastoma (a childhood cancer that affects the retina of the eye). Doctors have found that cryosurgery is most effective when the tumor is small and only in certain parts of the retina.
- Early-stage skin cancers (both basal cell and squamous cell carcinomas).

- Precancerous skin growths known as actinic keratosis.
- Precancerous conditions of the cervix known as cervical intraepithelial neoplasia (abnormal cell changes in the cervix that can develop into cervical cancer [47]).

Cryosurgery is also used to treat some types of low-grade cancerous and noncancerous tumors of the bone. It may reduce the risk of joint damage when compared with more extensive surgery, and help lessen the need for amputation. The treatment is also used to treat AIDS-related Kaposi sarcoma when the skin lesions are small and localized.

Researchers are evaluating cryosurgery as a treatment for a number of cancers, including breast, colon, and kidney cancer. They are also exploring cryotherapy in combination with other cancer treatments, such as hormone therapy, chemotherapy, radiation therapy, or surgery [25].

Unlike traditional open surgeries, cryosurgery is minimally invasive and has some of the following merits-

- As compared to the traditional surgeries, cryosurgery is performed with the intent of minimally destroying any of the surrounding healthy tissue. This makes cryosurgery very appealing for treatment of various diseases of heart, lung, liver, uterus, brain, bone etc [71]
- Since the excision of the tissue is avoided, the possibility of hemorrhage is potentially reduced. Thus the bleeding control for wide areas in surgery is also not necessary in cryosurgery [71]. Thus the recovery time is faster with minimal operative trauma. This lowers the hospital stays , hospital costs, and increases the quality of life for the patients
- The time duration for the procedure is very short. It is a quick and simple method to treat tumor
- Anesthesia is usually not required for some of the procedures as the cold itself serves as an anesthetic

- As there are no cuts involved in the surgery, scars are largely avoided, especially for skin related treatments
- This is a focal treatment, hence there is prevention of metastasis at the time of treating the tumor as the procedure requires no cutting
- Both benign and malignant tumors can be easily treated

1.6 Insufficiencies of Modern Day Cryosurgery

In cancer treatment, cryosurgery does have side effects, although they may be less severe than those associated with conventional surgery or radiation therapy. One of the issues is the precise monitoring of the ice front. In order to visualize tumors, guide cryoprobe and monitor tissue freezing, intra-operative ultrasound is used [71]. However, there are limitations to this procedure. The ice ball cases acoustic shadowing and obscures the details at the frozen front. Thus there is a need to monitor the freezing zone from various locations. To date, this is a difficult task. Next issue is that the tissue undergoes complex, multistate, simultaneous and significant changes during the freezing process which are yet to be fully understood. Every factor in this change plays a role in the outcome of the procedure. There are extensive and ongoing studies for *in vitro* and *in vivo* experiments to understand the mechanisms of cryosurgical procedures [72] [73].

The next area of ongoing research is cryosurgical treatment planning [74] [75]. A highly integrated model that is capable of predicting the thermal history of the target tissue, microscopic and macroscopic biophysical variations in the physical and chemical properties, and the cryosurgical outcome.

Some of the other disadvantages of the procedure are discussed next. Cryosurgery of the liver may cause damage to the bile ducts or major blood vessels, which can lead to heavy

bleeding or infection. Cryosurgery for prostate cancer may affect the urinary system. It also may cause incontinence (lack of control over urine flow) and impotence (loss of sexual function), although these side effects are often temporary. Cryosurgery for cervical tumors has not been shown to affect fertility, but this possibility is under study. More studies must be conducted to determine the long-term effects of cryosurgery as a cancer treatment approach [76].

To place the motivation for the present investigation in context, it is necessary to provide sufficient background to highlight the relevant issues. A count of the number of publications found using Google Scholar for the cryoprobe and cryoballoon is seen in Figure 1.16. In recent years, there is an increase in research efforts in understanding the working of the cryosurgical devices studied in this work.

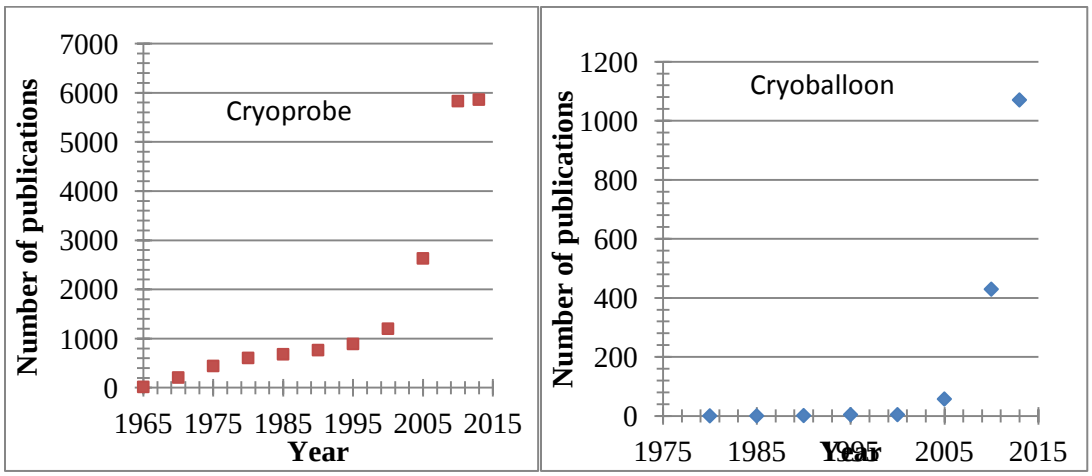

Figure 1.16 Number of publications (including citations and patents) for cryoprobe and cryoballoon

A large volume of efforts have been focused in the following fields to promote the applications of cryosurgery

- Macro-scale and micro-scale variations in tissue freezing
- Mechanisms involved in cryosurgery

- Parameters affecting cryosurgery

To this end, a review of the relevant literature focusing on the fields mentioned above will be presented in the following sections.

1.7 Macro-Scale and Micro-Scale Variations in Tissue Freezing

An in-depth understanding of the tissue mechanisms plays a vital role in the development of advanced mathematical models, development of new cryosurgical devices and optimization and improve efficacy of the treatment. This section discusses various macro-scale and micro-scale physical and physiological variations occurring during tissue-freezing.

1.7.1 Macroscale variations in tissue freezing

The study of bioheat transfer processes in the tissue has attracted the interestsof researchers as early as 1876 [77]. The works of Gage [78] ,Hardy [79],Bazett [80], Mendelson [81], and Bernard [77]were focused on quantifying the effects of blood perfusion and metabolism on tissue heat transfer. However, Pennes [82]published an experimental study in 1948 on temperature distribution of tissue with the first qualitative model. This model combined the conventional heat conduction equation with two new terms that represented the thermal effects of blood perfurion and metabolism. Pennes equations is applied widely as the foundation of bioheat transfer models [83].

1.7.2Microscale variations in tissue freezing

Extracellular ice formation, cellular dehydration and intracellular ice formation constitute the microscale variations in tissue freezing. Extracellular ice formation always occurs prior to intracellular ice formation. The phenomena of cell dehydration has been studied extensively by Mazur [30] [84] [85] [86] [87] [88] [89] [90] [91] [92]. Cell dehydration occurs when the cell freezes with a slow cooling rate. Intracellular ice formation occurs when cooling rate is relatively high. Higher cooling rates allow little time for water transport through the cell membrane and ice nucleates and grows in the intracellular region. A detailed discussion on the mechanisms involved in cryosurgical procedures and the parameters affecting them will be made in the following sections.

1.8 Mechanisms Involved in Cryoablation/Cryosurgery

There are intermediate cellular effects as well as late effects that determine the lesions produced during cryosurgery as seen in Figure 1.17.

1.8.1 Direct cell injury

1) Extracellular ice: The cells are cooled at a very slow rate. Thus extracellular ice beings to form. This results in a hyperosmotic extracellular environment that in turn withdraws the water from the surrounding cells. This mechanism starts taking effect when temperatures around -20C are applied very slowly to allow the water shifts from intracellular to extracellular zones. Hypertonic stress causes the cellular shrinkage and damages the membrane and cellular constituents. During thawing process, the reversal of the above process takes place and causes cellular swelling that is sufficient to disrupt the cellular membranes. If the duration is sufficient, cooling to

this level will cause cellular death. If these effects are small by cooling to mild temperatures (0C to -10C), fully reversible effects can be produced.

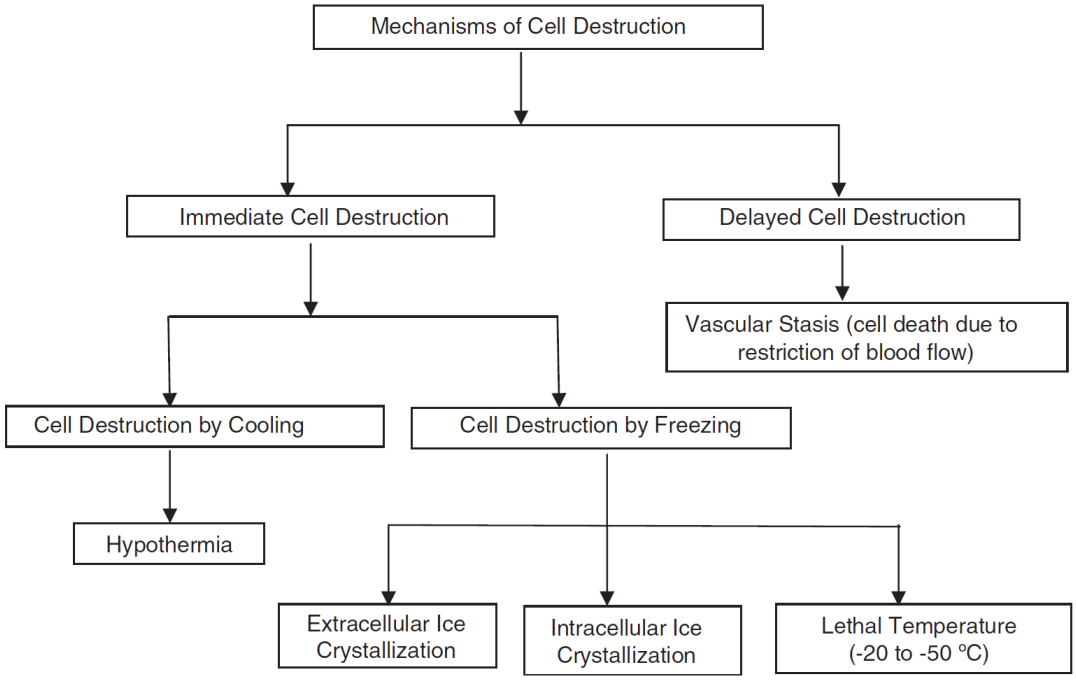

Figure 1.17 Flow diagram illustrating the mechanism of tissue destruction [43]

2) Intracellular ice: If the temperature is dropped to -40 or below, at a faster cooling rate, intracellular water will freeze to form intracellular ice. This is lethal to the cells, as it causes major or irreversible damage of intracellular organelles and cellular membranes. As seen in Figure 1.18, in the early thawing phase, coalescence of ice crystals into larger crystals causes further disruption of intracellular organelles and cellular membranes.

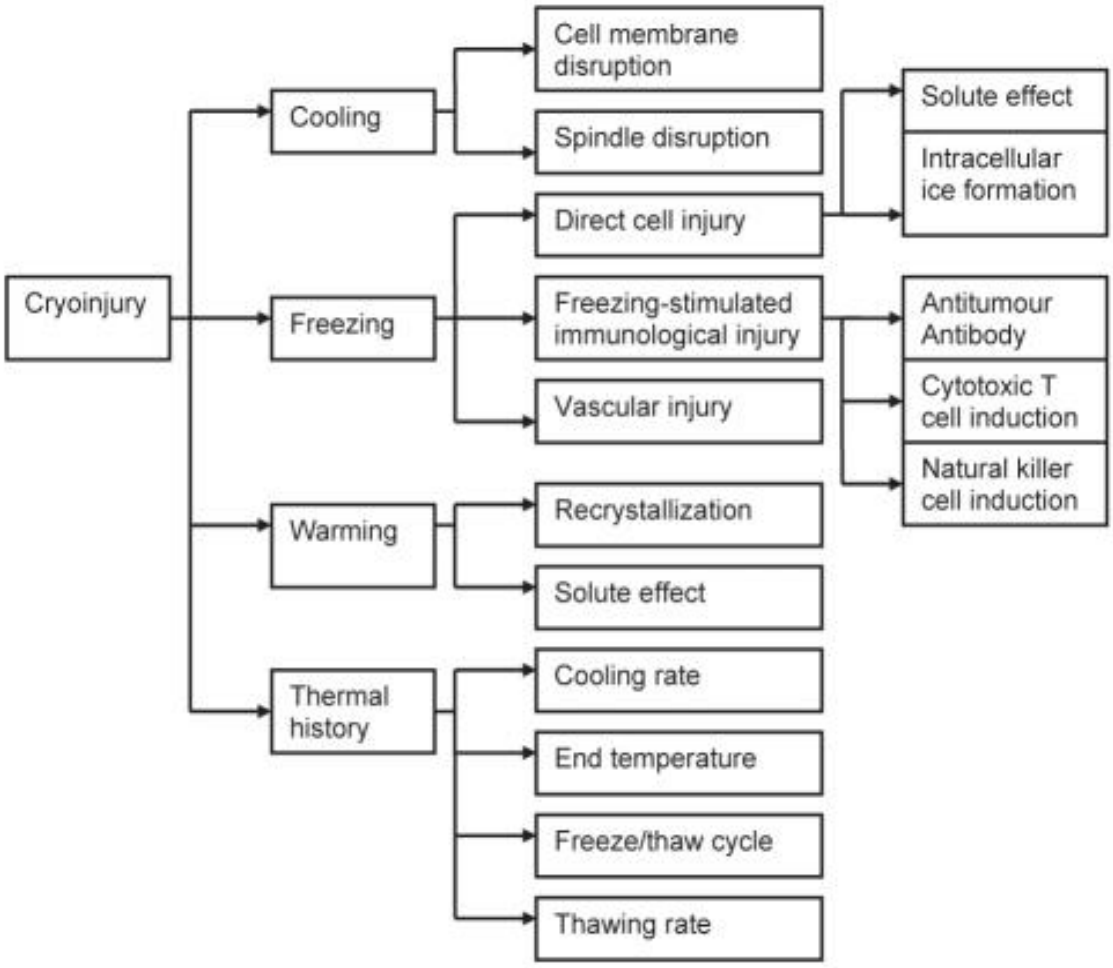

Figure 1.18 Mechanisms of cryoinjury [16]

1.8.2 Vascular injury

Within the zone of the frozen tissue, cryothermy is known to have significant effects on microvasculature. As tissue is cooled, vasoconstriction occurs and as the tissue freezes, circulation ceases altogether within the frozen tissue. Upon re-warming there is a hyperemic vasodilation, with increased vascular permeability and localized edema. Damage to the endothelium within the frozen tissue results in micro-level thrombus formation and microcirculatory arrest within the lesion. By 4 hours after thawing, small blood vessels are occluded. This loss of blood supply results in ischemic necrosis and a

dense uniform lesion. It is generally accepted that this is a major mechanism of cryolesion formation during tissue freezing, although it is impossible to distinguish this mechanism of cell death form that of intracellular ice formation [93]. A sketch of the injury mechanisms during freezing is seen in Figure 1.19.

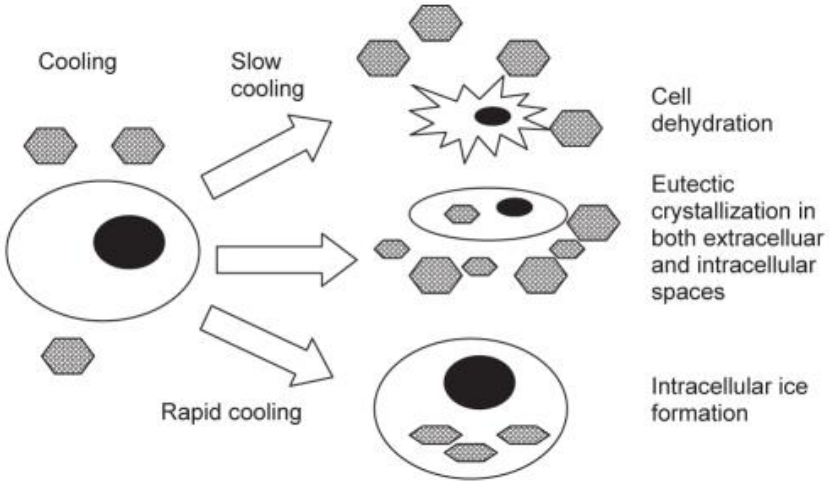

Figure 1.19 Injury mechanisms during freezing

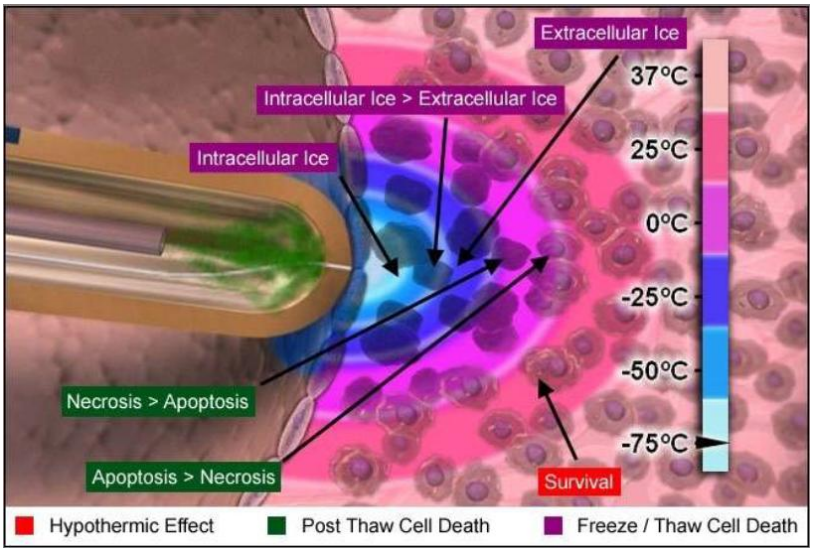

Figure 1.20 Freezing mechanism

1.9 Parameters Affecting Cryosurgery

Tissue response varies with intensity of cryogenic injury. Less cryogenic injury produces inadequate tissue destruction while more cryogenic injury may extend deleterious effects to surrounding normal tissue. For optimal treatment of the diseased tissue, it is necessary to be concerned on following controlling parameters:-

1.9.1 Cooling rate

A rapid cooling rate of more than 50 degree C/min produces intracellular ice crystals that are more destructive. A background review suggested that cooling rates of 3degreeC/min, 22degree C/min, and 50degreeC/min are required in order to induce intracellular ice in neoplastic cells [42]. These higher cooling rates can be achieved in the proximity of the cryodevice and the effects fades away from the contact area. Thus the whole tissue is not subjected to rapid cooling. Studies performed by Mazur, Walter and Farrant suggest that the cells are exposed to diverse thermal profiles for different times and cooling rate is not the prime factor [30] [84].

1.9.2Temperature

The lethal effect of the tissue temperature increases as the temperature drops lower and lower. The lethal temperature range is less than -50 degree Celsius [30]. Studies have shown that the temperature of -20C applied for 1 minute is sufficient to cause necrosis [94] [95] [96]. The treatment of tumor requires a tissue temperature at which all the

abnormal cells are certainly dead.

First Author	Year	Cell/Tissue	Lethal Temperature(^{0}C)
Gage	1966	Osteocytes, bone, dog	-2
Gage	1979	Melanocytes, skin, dog	-4
Smith	1974	Liver, rat	-15
Rivoire	1996	Liver, pig	-15
Lefebvre	1975	Cheek pouch, hamster	-18
Dow	1970	Prostate, dog	-20
Gage	1982	Skin, dog	-40
Yamada	1976	Skin,mouse	-40
Gage	1978	Palate, dog	-40
Neel	1971	Sarcoma,mouse	-60
Steren	1997	Adenocarcinoma, rat	-70

Table 1.2 Lethal temperatures for cell experiments in Vivo for single freeze thaw cycle [44-46]

Lethal tissue temperature is very crucial especially for the treatment of cancer. However, varieties of experiments have provided many range of lethal temperature for corresponding type of tissue. Due to variations in sensitiveness and thermophysical properties of normal and cancerous tissue, it is quite complex to achieve the lethal temperature of the diseased tissue. From the review of experimental studies the temperature below -40C has been considered prime factor for tissue destruction [97].

1.9.3 Hold time and freeze time

As mentioned in the preceeding discussion for the other parameters, Mazur stated that the rate of cell death is greatest when the tissue temperature is above -30C [84]. Experimental studies show that longer duration of frozen tissues could produce more damage [97]. Studies have suggested that the duration of freezing is unimportant if the tissue is held at temperatures colder than -50C. However, more damage is achieved with temperature around -40C [41] [97].

1.9.4Thawing rate

Slow and long rate of thawing causes complete necrosis. Rapid rates on the other hand allow cell survival. If the tissue is held between -20C to -25C for longer duration, the necrosis is effective due to recrystallization process which produces large ice crystals [42] [98]. Rapid freezing and slow thawing do not guarantee effective cell destruction. Therefore, the cryosurgery process should be programmed in such a way to produce appropriate lethal effect to certain volume of tissue. Now freeze-thaw cycle came into concept, each of which cycle is injurious to cells [98]. During repetition of cycles, several times cells undergo through disturbed thermal conditions than the thermal conditions for their survivability, this leads to more volume of cell death. Freeze-thaw cycle is more destructive if repetition is performed within temperature range of -20C to -30C. Intracellular ice formation is progressive in repeated cycles, which causes tissue abrasion. Use of repeated freeze-thaw cycle is also beneficial in treatment [99].

1.10 Cryoprobe Study

Cryotechnology in the latest years has spawned from reduced size needles to image-guided procedures, percutaneous cryoablations have carved out an ever-expanding niche. Generally a tumor is irregularly shaped and the iceball formed by a single needle cannot optimally cover the tumor without causing excessive damage to the surrounding tissue. This detrimental freezing becomes even more concerning when the diseased region is located in proximity to the critical organs and blood vessels. Unnecessary freezing can lead to a host of lethal and chronic conditions. Solving this issue requires more than good surgical judgement or reliance on visual monitoring. A deeper understanding of the impact of the phenomena occurring internal to the cryoprobe on the iceball formation would be of value.

1.10.1 Freezing of Tissue and Cell Necrosis

The earliest predictive work on the formation of an ice layer, commonly called an iceball, on the external surface of a cryoprobe appears to be due to Cooper and Trezak [100] [101]. By means of a simplified model, they were able to obtain analytical solutions for the rate of formation of frozen regions around spherical and cylindrical cryoprobes. Their models included blood profusion and metabolic heat generation; the latter was also taken into account by Warren and co-workers [102]. In more recent times, numerical simulation has been used extensively to study iceball evolution; for example, by Rewcastle and coworkers [103], who used both finite-difference and finite-element computational methods. Another feature of the immediately foregoing investigations is the use of multiple cryoprobes to service a large volume of dysfunctional tissue. The determination of the optimal placement of the individual probes in a multi-probe array [104]was a natural follow-on to Rewcastle [103]. A recent [2013] study highlights the

maxmimum destruction of diseases tissue and also minimize injury to the healthy tissue [105] [106]. The velocity of the freezing front is a key factor in the duration of the cryotherapy, and its determination in an *in vitro* simulation using glass capillaries proved to be effective [107]. The cooling rate of the tissue was found to be the most important factor in determining the final outcome of the cryosurgical process [108]

The temperature gradients incurred in the formation of the ice ball naturally give rise to differential thermal expansion and thermal stresses [109], Another factor contributing to thermal stresses is the density change that accompanies phase change [110]. Possible differences between thermal expansion of freezing tissues and that of pure water were definitely established [111]. Experiments were conducted by Xiao-Zhao [112] to evaluate fracture toughness of an ice ball. He [113] experimentally determined the thermal stress distribution in the cryosurgery of a kidney using a multiphysics finite-element model.

Some attention has been given to the geometrical and thermal configurations of iceballs. A cryoprobe tip was analyzed to identify the locations of the highest and lowest temperatures and how they affect the shape of the iceball [114]The thermal profile and the size of the ice ball produced were definitely related to the efficacy of the probes [115]. Deng [116]studied the irregular shape of the frozen region, the direction of the ice growth, and the temperature distribution within the ice ball during the freezing process. The thermal history within the ice ball needed to ensure the necrosis of cancerous cells was established [117].

1.10.2 Cryoprobe Internal Processes

Attention will now be turned to literature in which issues that relate to the cryoprobe proper might have been considered. In a very recent paper [118] where the last 30 years of cryoprobe literature was reviewed, the only mention of cryoprobe internals is among

the recommendations for future work: "3. improved technical means to control the temperature variations of the cryoprobe ....." An even more recent paper [119] described an *in vitro* experiment in which a cryoprobe was situated in a vacuum chamber. The experiment was accompanied by a highly oversimplified model in which the actual fluid mechanics within the cryoprobe was ignored. Instead, a friction factor based on an incompressible-flow model was used, and the heat transfer calculation was based on a formula for a fully developed, low-speed, incompressible flow. In reality, the model of [119] ignores the dominant effects of compressibility, acceleration, and the Joule-Thompson effect on a flow which ultimately becomes sonic as well as the ensuing multiple shocks, compressibility, high rates of acceleration, strong expansion waves, 180-degree turns, non-uniform boundary conditions, and high rates of heat transfer which affect thermophysical properties. As a matter of fact, it is impossible for a compressible gas flow in a tube to become fully developed.

In [120] an in vitro experiment is described in which human tissue is replaced by water containing an additive. A sketch of a cryoprobe is displayed without any discussion of its operation and its dimensions. In what appears to be the beginning stage of development of a cryoprobe, consideration was given to liquid nitrogen flowing in a tube which is open at both ends [121]The authors promise later usage of a coaxial setup and admit that "direct injection of a cryogen (in tissue) is not possible. No consideration is give to fluid mechanic phenomena.

From the literature cited in the foregoing paragraphs which deal with cryoprobe internals, two major conclusions may be drawn. The first is that there is no open-literature studies of neither the physical phenomena nor the mathematical modeling that occur within a cryoprobe. The second conclusion is that among the few attempts to consider cryoprobe internals, there is no case in which any attempt was made to link with in vivo phenomena. This state of affairs clearly indicates that the investigation here is altogether novel both with respect to the in-depth treatment of internal phenomena.

Cryogen	Temperature [C]	Pressure [psi]	Principle of cooling
Nitrous oxide	-89.5	~760	Joule-Thomson
Argon	-189	~3600	Joule-Thomson
Liquid nitrogen	-196	Atmospheric	Cold gas

Table 1.3 Temepratures and pressures for cryogenic medium

1.10.3 Theory of the Joule-Thomson Effect

Since the J-T effect is central to the utilization of a gaseous medium as a cryofluid, it is relevant to explore the genesis of the effect. In particular, the thermodynamic analysis is intended to relate the J-T coefficient to the degree by which a gas departs from ideal behavior. The definition of the J-T coefficient is

$$\mu_{JT} = \left(\frac{\partial T}{\partial p}\right)_h \tag{1.1}$$

This equation identifies the change of temperature *dT*with respect to a change of pressure *dp* at constant enthalpy *h*. The restriction to constant enthalpy will become apparent as the theory of the J-T effect is presented. The forerunner of this equation is the First Law of Thermodynamics for a flowing fluid, which is

$$0 = \dot{Q} - \dot{W} + \dot{m}(h + \frac{V^2}{2} + gz)_{in} - \dot{m}(h + \frac{V^2}{2} + gz)_{out} \tag{1.2}$$

In this equation, the quantity $\dot{Q}$ is the rate of heat transfer to the flowing fluid, $\dot{W}$ is the rate at which the fluid does work on the surroundings, and$\dot{m}$ is the mass flowrate. The other symbols are the specific enthalpy *h*, velocity *V*, gravitational acceleration *g*, and elevation *z*.

For a flow that is adiabatic, $\dot{Q} = 0$. Furthermore, since $\dot{W}$ represents either shaft work or electrical energy flow, it can be omitted from the equation. However, the flow work has been incorporated into the enthalpy. In an ideal situation, the kinetic energy terms at the inlet and the exit cancel out. On the other hand, if there is a change in kinetic energy, its significance is minimized by rationalizing its units, $(m/s)^2$, with the units of the specific enthalpy, which are kJ/kg. This rationalization gives rise to a factor of 0.001 as a multiplier of the kinetic energy term. With regard to the gravitational term, the change in elevation is typically small enough so that it can be neglected without loss.

When these considerations are imported into Eq. (1.2), there results

$$h_{in} = h_{out} \tag{1.3}$$

If the flowing medium were to be an ideal gas, it would follow from Eq. (1.3) that the temperature would be constant. On the other hand, for a non-ideal gas, the temperature will vary although the enthalpy is constant. In particular, enthalpy for an ideal gas depends on both pressure and temperature. Since the pressure is changing, constant enthalpy is maintained by compensating changes of temperature. This characteristic is the basis of the J-T effect and motivates interest in Eq. (1.1).

To continue, it is convenient to make use of the second *Tds* equation, where *v* is the specific volume, and *s* is the specific entropy.

$$Tds = dh - vdp \tag{1.4}$$

After dividing through by *dp* and then applying Eq. (1.4) at constant temperature, there follows

$$\left(\frac{\partial h}{\partial p}\right)_T = T\left(\frac{\partial s}{\partial p}\right)_T + v \tag{1.5}$$

To eliminate $\left(\frac{\partial s}{\partial p}\right)_T$, the following Maxwell equation [122] was used. In general, the Maxwell equations provide connections between thermodynamic properties.

$$\left(\frac{\partial s}{\partial p}\right)_T = -\left(\frac{\partial v}{\partial T}\right)_p \tag{1.6}$$

with the result

$$\left(\frac{\partial h}{\partial p}\right)_T = -T\left(\frac{\partial v}{\partial T}\right)_p + v \tag{1.7}$$

To proceed, it is useful to regard the enthalpy as a function of *T* and *p* and to use the chain rule

$$dh = \left(\frac{\partial h}{\partial T}\right)_p dT + \left(\frac{\partial h}{\partial p}\right)_T dp \tag{1.8}$$

Since the derivative of the enthalpy with respect to temperature at constant pressure is the definition of the specific heat and, after making use of Eq. (1.7), there is obtained

$$dh = c_p dT + \left[v - T\left(\frac{\partial v}{\partial T}\right)_p\right] dp \tag{1.9}$$

Further, if the foregoing equation is divided through by *dp* while holding *h* constant, the J-T coefficient emerges as

$$\left(\frac{\partial T}{\partial p}\right)_h = \frac{1}{c_p}\left[T\left(\frac{\partial v}{\partial T}\right)_p - v\right] \tag{1.10}$$

Another form of the J-T coefficient can be obtained by making use of the compressibility factor Z,

$$Z = \frac{Mpv}{RT} \tag{1.11}$$

where*M* is the molecular weight, and *R* is the universal gas constant. The combination of Eqs. (1.10) and (1.11) yields

$$\mu_{JT} = \frac{RT^2}{pc_pM}\left(\frac{\partial Z}{\partial T}\right)_p \tag{1.12}$$

Equation (1.12) is the commonly used formula for the calculation of the J-T coefficient. The essence of Eq. (1.12) is that the J-T effect is directly linked to the property Z which is a measure of the departure of a gas from the ideal.

1.10.4 Cryofluid

The foregoing theory of the J-T coefficient requires numerical values for its implementation. This information is scattered throughout a literature extending from the 1920s to the present. For the respective fluids of interest, the relevant J-T information is: (a) argon [123], (b) helium, [124] [125] [126], (c) nitrogen, [122] (d) carbon dioxide, and [127] [34] [128] mixtures of the aforementioned gases [125] [129].

A figure, Figure 1.21, is presented to show the values of the J-T coefficient for several at low pressures. It can be seen from the figure that argon is an attractive gas for low-temperature applications because of its relative high values of the J-T coefficient. It is relevant to note that while argon and nitrogen have J-T coefficients that are positive, those for helium and hydrogen in the relevant temperature range are negative. Also of interest is that the magnitudes of the coefficients for argon are larger than those for nitrogen (nitrous oxide). It can be observed that helium and hydrogen display negative values of the J-T coefficient at temperatures in the relevant range. With regard to carbon dioxide, the information provided in the figure does not encompass the temperature range of interest so that its relevance to cryosurgery is uncertain. The cryofluid used in this study is argon.

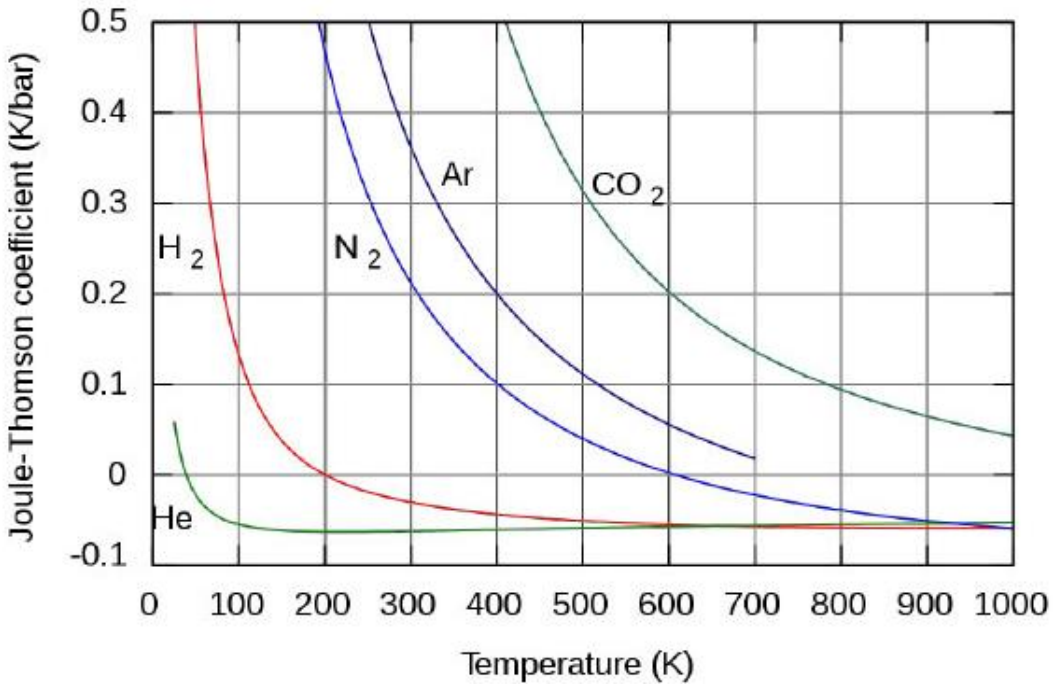

Figure 1.21 Values of the Joule-Thomson coefficient for several gases at low pressures (effectively, zero)

It is relevant to observe that the constant enthalpic J-T coefficients of Figure 1.5 are an approximation to the actual behavior of the gaseous medium in a flow configuration such as that pictured in Figure 1.6. In that figure, it is seen that the gas flowing into the system via the central tube exchanges heat with the same gas flowing through the annular space that surrounds the tube. As for now be demonstrated the isenthalpic J-T coefficient is an upper bound to the effective value of the J-T coefficient in the presence of heat transfer.

The effect of the presence of heat transfer as discussed in the foregoing paragraph can be qualitatively analyzed. It is believed that the gas flowing within the central tube is losing heat to the surrounding annular flow. For that case, it is relevant to review the foregoing analysis of the J-T coefficient to determine the impact of the heat loss. If the starting point of the analysis is Eq. (1.2) and if $\dot{Q}$ is retained, there emerges

$$0 = \dot{Q} + \dot{m}(h)_{in} - \dot{m}(h)_{out} \tag{1.13}$$

or

$$h_{in} - h_{out} = -\frac{\dot{Q}}{\dot{m}} > 0 \tag{1.14}$$

Inspection of this equation indicates that there is a decrease in enthalpy as the gas passes through the central tube.

Next, attention will be focused on Eq. (1.9). After dividing through this equation by *dp*, there is obtained

$$\frac{dh}{dp} = c_p \frac{dT}{dp} + \left[v - T \left(\frac{\partial v}{\partial T} \right)_p \right] \tag{1.15}$$

so that

$$\frac{dT}{dp} = \frac{1}{c_p} \left[T \left(\frac{\partial v}{\partial T} \right)_p - v \right] - \frac{1}{c_p} \frac{dh}{dp} \tag{1.16}$$

Since, in the presence of heat loss, *dh/dp* is positive, it follows that *dT/dp* is smaller than its value for the isenthalpic flow. This leads to the conclusion that the temperature drop when heat loss is present is smaller than for the isenthalpic case.

1.10.5 Scope of Research

The major areas of this research are focused on all aspects of the J-T flow within a cryoprobe, including strong compressibility superposed on the J-T effect, expansion waves and shocks, a 180-degree turn in the shock-affected zone.

This work was motivated by the fact that never before has there been any attempt to deal with the complex physical phenomena that occur within the cryoprobe. Furthermore, as demonstrated by the literature search, there has been no previous attempt to bring together the physical processes that occur within the cryoprobe with those that occur in the tissue external to the probe surface. All of the previous work has neglected these internal processes and has focused exclusively on the phenomena occurring external to the probe body.

This work has been divided into two situations based on the boundary conditions on the outer wall of the probe. In the first situation the cryoprobe was insulated and the fluid flow and heat transfer analysis studies. For the second situation, the cryoprobe placed in a surrogate medium was studied. The temporal progression in the shape of the iceball and the corresponding temperatures were considered for the purpose of the study.

Three different turbulence models were compared to provide a rationale for the choice turbulence models. A series of studies were performed to comprehend the effect of the thermal interactions between the tube flow and the annular flow within a J-T system, and

the interactions between a J-T system and an external environment for two situations discussed in the foregoing paragraph.
One of the objectives was to carry out a complete analysis of all of the physical processes which occur within the cryoprobe. This means dealing with the incoming argon flow entering the central capillary tube where the J-T effect and compressibility conspire to both lower the fluid temperature and bring about sonic flow.

Special focus was directed to heat transfer to the virgin cryofluid entering and passing through the central capillary tube. There is no past history relating to bringing together the processes internal to the cryoprobe with those in the contiguous medium.

The numerical modeling is performed using various features of ANSYS software. These features included compressible CFX coupled with convective heat transfer and conduction in solid walls. The processes involved in the iceball formation are unsteady and require that the heat capacity of all the participating media be taken into account.

The equations governing the physical processes external to the cryoprobe have been the subject of intense study starting with the pioneer work of Cooper in 1971 [130]. The intention of the work was to examine each of the physical processes and to create models of the highest fidelity to those processes. The resolution of fine, but significant details such an array of shocks requires an extremely fine mesh.

1.10.5.1Complete characterization of all the internal cryoprobe physical processes

This part deals with the physical processes that take place in both the J-T capillary tube and in the annular flow that surrounds the tube. Of particular interest in this regard are the interactions between the accelerating J-T compressible flow in the tube with those of the spent cryofluid in the annulus. The straight capillary depends on length and diameter to effect the pressure drop.

The conjectured flow situation in the geometry of Figure 1.22 is a developing, increasing-Mach-number flow in the central tube. The increase of the Mach number is related to an increase of the momentum of the flowing fluid. That momentum increase induces a major decrease in pressure. In addition, friction provides additional pressure drop. The fluid flowing in the capillary tube must experience a pressure drop that is sufficiently great to trigger the J-T effect. At the exit of the central tube, the shock-expansion wave complex [131] were resolved in great detail by the simulation model.

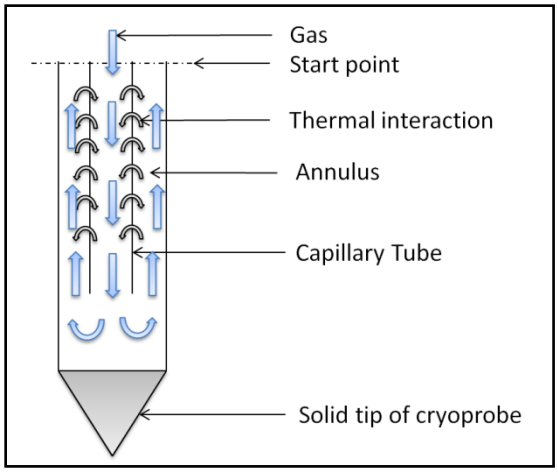

Figure 1.22 Thermal interactions between the gas flowing through a straight capillary and an annulus

The reality and complexity of the situation lies in part in the conjugate nature of the temperature distribution [132]. In this context, *conjugate* refers to the interaction of two processes governed respectively by different phenomena which are coupled by the means of interface continuity conditions.

1.10.5.2 J-T effect in the presence of heat transfer

To help identify the impact of the heat transfer on the J-T effect as well as on the fluid flow in both the central tube and its enveloping annulus was investigation was performed where the wall separating the incoming fluid with annulus was specified as adiabatic. Subsequently, heat was allowed to flow freely between the central tube and the annulus as another comparison. Note was taken of the temperature variations encountered and in the realistic situation where heat must flow between the central tube and the surrounding annulus. By this approach, the extent of the heat transfer impact on both the J-T effect and the compressible gas flow was demonstrated.

1.10.5.3 Interactions between the J-T system and an external environment

The J-T systems that have been discussed in the preceding sections were ultimately intended to interact with an external environment. In particular, if a J-T system is used as a cryosurgical tool, it will interact with the surrounding medium whose initial temperature is considerably elevated compared with that of the cryosurgical tool. As noted earlier, there is no previous work in which the processes internal to a cryoprobe are simultaneously matched with the thermal events occurring in the enveloping medium. The universally employed approach has been to altogether neglect the physical processes within the probe proper.

The mating of the J-T system with the external environment is an enormous undertaking. It involves solving the highly complex fluid flow internal to the cryoprobe along with the heat transfer that occurs therein with the phase change and heat conduction processes in the tissue. Furthermore, all of these interacting processes were modeled in the transient state. No such undertaking has ever been attempted.

In the tissue that surrounds the cryoprobe, a number of simultaneous, time-dependent thermal processes occur. In the literature relating to these thermal processes, it is standard

to subsume the processes of cell necrosis into a moving phase front. That front is characterized as a mushy zone wherein phase change occurs over a range of temperatures rather than at a single specific temperature. The enthalpy method [133], and another by [134] is employed to facilitate taking account of the latent heat that is released by the solidification process.

1.11 Cryoballoon Study

1.11.1 Background

The phenomena occurring after the application of cryothermal energy using cryoballoon is similar that of the cryoprobe. The issues discussed in the foregoing sections regarding the cryoprobe and the cellular damage prevails for the cryoballoon-based surgery as well. As discussed earlier, when the temperature reaches lower as -40C, cellular damages is starts by means of intracellular ice formation. Irreversible cellular death occurs when the temperature reaches below -70C. When the cryothermal energy is stopped, a rapid vasolidation and a state of augmented vascular permeability is reached, which causes hemorrhage and edema and leads to further tissue injury. This phase is also characterized by the microthrombus formation in the tissue and it leads to further damage [62].

Achieving pulmonary vein isolation is very critical in order to have an effective cryoablation procedure. If this goal is not achieved a focal tip catheter is used in the treatment of gaps to complete the isolation process [62]. A successful pulmonary vein isolation with the cryoballoon is highly dependent on a perfect contact to the atrial wall at the ostium of the pulmonary vein. Achieving a uniform and continuous jet impingement pattern is one of the crucial objectives fin successful completion of the treatment [55].

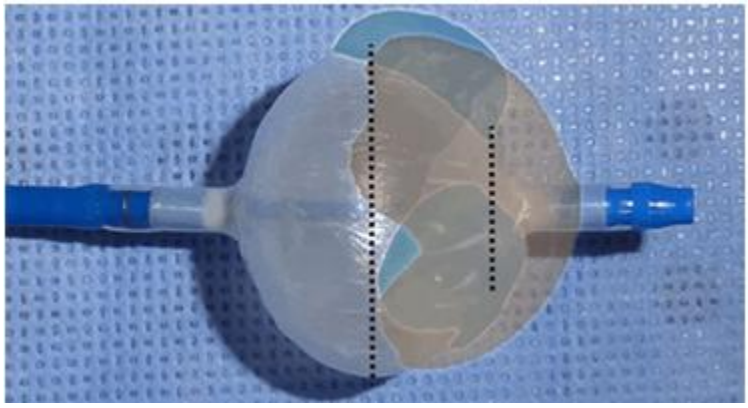

Figure displaying the jet impingement on the circumference of the balloon [135]

From the literature review it can be concluded that the cryoballoon technology potentially represents a very quick, simple and safe approach to the treatment of AF, however, there are some shortcoming yet to be answered. A lot of effort has been focused in studying the effectiveness of pulmonary vein isolation [67], efficacy, methods and safety, in patients of varying age, gender, sex, chronic conditions [57]etc. A literature review reveals that no open literature has been found that numerically analyses the internals of the cryoballoon. This work would also help in furthering the development with better understanding of the existing device [61].

1.11.2 Scope of Research

1.11.2.1 Complete characterization of the umbilical, catheter, balloon and return flow for two boundary conditions

The goal of this work is to model all of the physical processes that occur throughout all the components of the system. The system was subdivided into its functional parts, starting with the inlet to the umbilical and proceeding downstream to the distal end of the system. An in-depth numerical simulation of the mode of operation of the balloon-catheter system and of the components that enables the functions of the system to be

implemented. Those simulations take into account all the complex process that occurs in the balloon-catheter system and its components. The outcome of this model is necessary to continue the simulation through the manifold. These results were further used in the simulation of the balloon which subsequently led to the calculations for the temperatures and the mass flow rates for two boundary conditions for the return flow model.

1.11.2.2 Interactions of the balloon with the surrounding medium

The primary tool used to facilitate this fundamentals-based analysis is computational fluid dynamics, including fluid flow, convection heat transfer, phase change, and jet impingement. A similar approach as before was implemented for the study of interactions of the balloon with the surrounding medium.

1.12 Organization

A brief discussion of the layout of this work has been provided in this section. Chapter 1 highlights an overview of the literature review and the subsequent scope of research for the cryoprobe and cryoballoon studies. Chapter 2 discusses the all of the physical processes that occur throughout all the components of the cryoballoon system and their corresponding numerical simulations. A description of the experimental setup will be seen in Chapter 3. Chapter 4 discusses the numerical simulations for the cryoprobe study. A comparison of the experimental results and the outcomes of the numerical simulations is provided in Chapter 5. Chapter 6 provides concluding remarks for the study performed in this thesis.

Chapter 2 Cryoballoon Ablation

2.1 Introduction

There are numerous approaches to eliminate dysfunctional tissue from the body. Aside from the traditional scalpel-based surgery, other less invasive procedures have been developed and are now in common use. One category of procedures is thermal-based. These procedures function either as elevated-temperature or reduced-temperature means for creating tissue necrosis. As has been set forth in Chapter 1, the research of this thesis is focused on cryosurgery. Furthermore, note has already been taken of the different modalities by which cryosurgery is performed. In this chapter, focus will be directed to balloon-based cryosurgery. Although there are different applications of balloon cryosurgery, the most developed equipment to implement its use is focused on treating artial fibrillation.

To illustrate the use of cryoballoon therapy in treating atrial fibrillation, Figure 2.1 has been prepared. The figure shows the balloon wedged in place between the various arms

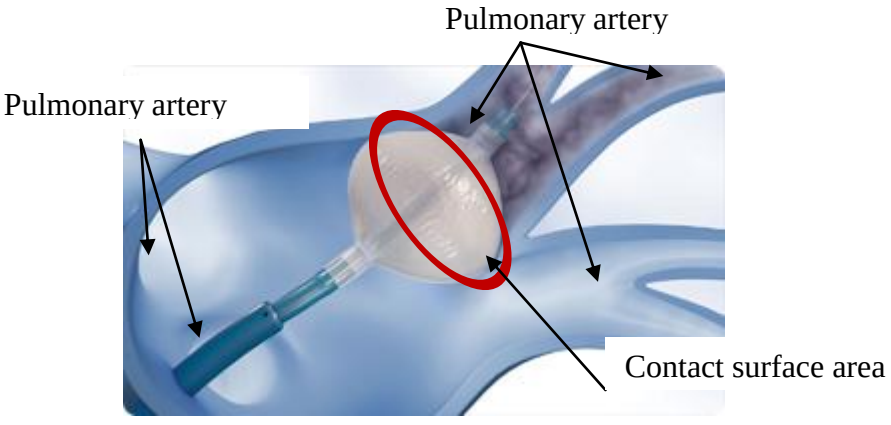

Figure 2.1 Schematic diagram of a cryoballoon in place. The gray color is a contrast medium used to identify complete occlusion of the pulmonary artery. The cryoballoon creates a ring-shaped lesion.

In this chapter, a multi-faceted, in-depth numerical simulation will be formulated of the mode of operation of the balloon-catheter system and of the components which enable the functions of the system to be implemented. Those simulations will take account of the complex physical processes which occur in each component of the equipment. The primary tool used to facilitate this fundamentals-based analysis is computational fluid dynamics, including fluid flow, convection heat transfer, phase change, and jet impingement. The participating physical processes will be modeled without approximation. Wherever possible, comparisons between the results of the analysis and those of relevant experiments will be made.

2.2 Experimental Equipment

A photographic view of the cryosurgical system in question is conveyed in Figure 2.2. The working fluid which enables the therapeutic function to be performed is nitrous oxide. The components of the system will be identified by following the path of the nitrous oxide as it leaves the console in liquid form and passes through various components and finally changes phase to vapor in the cryoballoon. The vapor phase persists in the return path of the nitrous oxide to the console.

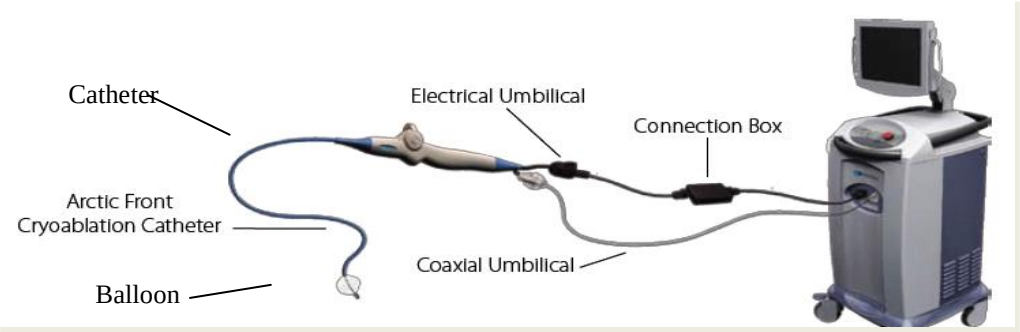

Figure 2.2 Photograph of the Arctic Front cryosurgical system

The console stores nitrous oxide and also provides electric power to the system. The conduit through which the nitrous oxide is conveyed from the console to a downstream-located catheter is a circular tube called the umbilical. En-route, the fluid passes through the handle of the catheter. The catheter delivers the nitrous oxide to a distribution manifold situated within the cryoballoon. The fluid exiting the manifold experiences a phase change and impinges on the bounding walls of the balloon as jets of a two-phase mixture. The spent fluid is returned to the console through an annulus which surrounds the circular tubing which conveyed the virgin fluid to the catheter.

2.2.1 The Umbilical

The nitrous oxide supplied by the console through the system is in liquid form. It passes through a coaxial pipe, termed the umbilical, which is shown schematically in cross-sectional view in Figure 2.3. As seen in the figure, the circular polyimide tube at the core of the pipe carries the liquid phase which is drawn from the console. That tube is surrounded by three concentric circular layers that are intended to serve as thermal insulators.

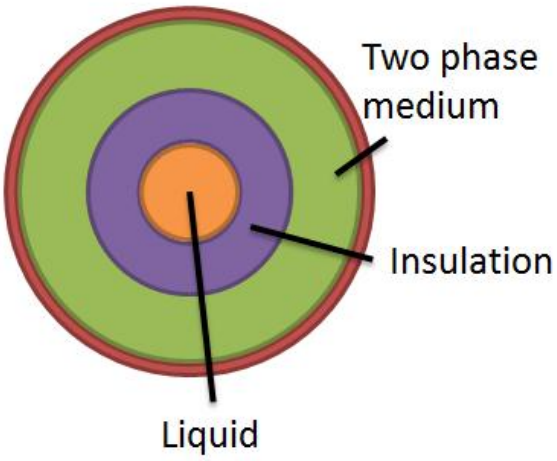

Figure 2.3 Schematic diagram of the cross section of the umbilical pipe (not to scale)

A two-phase mixture of nitrous oxide vapor flows in the outer annulus en-route from the cryoballoon to the console. It is discharged into the console. At the downstream end of the umbilical, the pipe assembly experiences an approximate 10% reduction in the inner and outer diameter.

2.2.2 The Handle

As seen in Figure 2.1, the downstream end of the umbilical is attached to the upstream end of the handle of the catheter. In turn, the downstream end of the handle is mated to the catheter proper.

2.2.3 The Catheter

The proximal end of the catheter is attached to the downstream end of the handle. The catheter is, in fact, a double-tube configuration in which the central tube carries the liquid medium to the cryoballoon while the annulus conveys the spent two-phase mixture from

the balloon to the console. With regard to dimensions, the external tube, the corresponding dimensions 2.0 mm and 3.3 mm. The length of the catheter is approximately 100 cm.

2.2.4 The Balloon

The distal end of the catheter mates with the proximal end of the cryoballoon. At that point, the central tube and the annulus of the catheter separate, with the central tube penetrating the balloon and extending along its length to the distal end. A schematic diagram of the distal end of the balloon is displayed in Figure 2.4. Inspection of the figure shows the presence of a rigid support tube which originates at the downstream end of the handle. That tube supports the central tube of the catheter. The central tube delivers the working fluid to a coiled manifold, whose function is to distribute the working fluid to the internal cavity of the balloon. The dispersion of the fluid is accomplished by means of eight exit ports deployed along the length of the coil. The maximum diameter of the balloon used for the numerical simulations is 28mm.

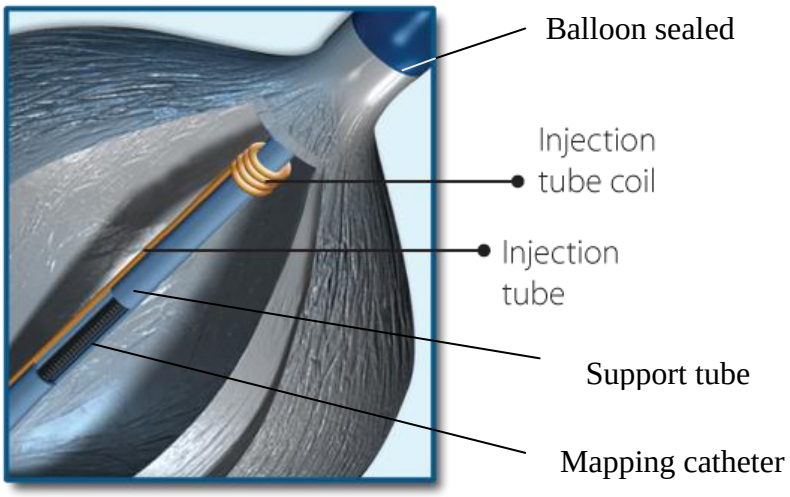

Figure 2.4 Helically wound injection tube [136]

A more extensive view of the support tube, central tube and coil, balloon, and two-phase return flow passage is presented in Figure 2.5.

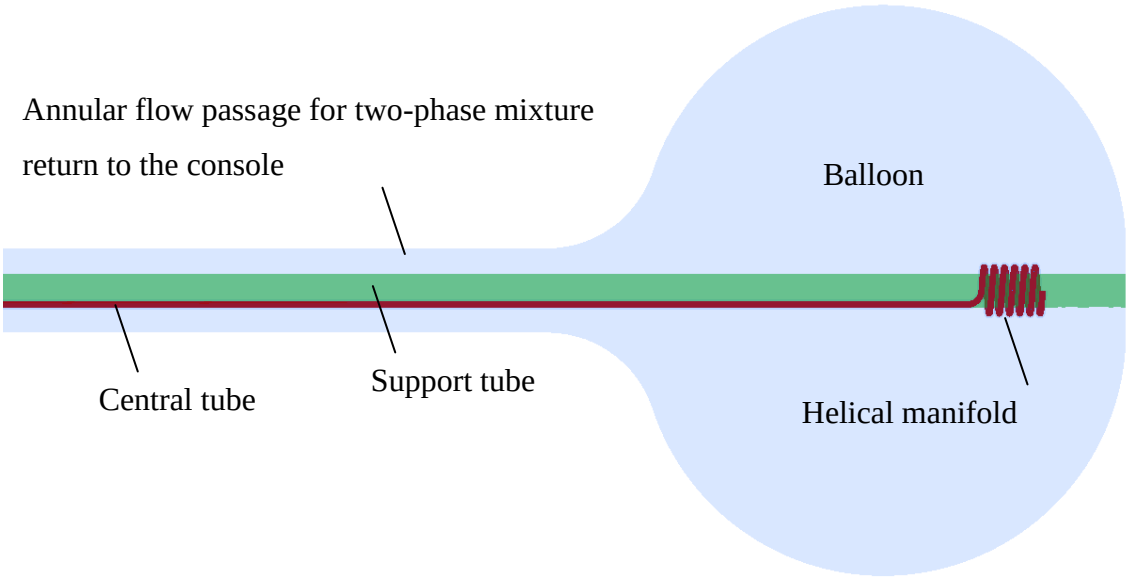

Figure 2.5Longitudinal view showing the central tube and coil, balloon, and two-phase return flow passage

2.2.5 Laboratory Setup

In a laboratory setup of the Arctic Front device, the cryoballoon was situated in a water bath whose temperature was approximately 37^{o}C. Heat transfer between the outer surface of the balloon and the water bath was by natural convection. This situation differs from that in which the system is used for therapeutic purposes, a typical application being that shown in Figure 2.1.

2.3 Simulation Model

The physical processes to be dealt with involve three-dimensional fluid flow, convective heat transfer, phase change, and two-phase flow. These processes are governed by conservation equations which, in total, constitute an interlocking set of nonlinear partial differential equations. To solve problems of this complexity, numerical simulation is necessary. In that regard, it is necessary to descretized the differential equations to achieve a transformed set of algebraic equations. There are several means by which the discretization can be performed: finite difference, finite element, and finite volume. Since fluid mechanics is dominant in the physical processes being considered here, the finite volume approach will be adopted. That adoption limits the choice of software to three major codes, FLUENT, CFX, and STAR-CCM. Since the research licenses are available for CFX, that code was used for the present solutions. The latest versions of that code, 14.0 and 14.5, were employed.

The transformation of the governing differential equations to algebraic equations creates a non-continuum solution domain. The solutions of the algebraic equations are sought at a set of discrete points in the solution domain called nodes. The accuracy of the numerical solution is intimately connected with the number of nodes and their deployment.

The nodes are related to small, finite volumes which fill the solution domain. There are various geometric forms of the volumes. Also, there may be different numbers of nodes associated with elements of different shapes. Therefore, it is common that the number of nodes and the number of elements that constitute the solution domain are different. Typically, the number of elements exceeds the number of nodes.

Although there is considerable emphasis in the literature on the importance of the number of elements, it is believed that the number of nodes and their deployment is the critical factor in the accuracy of the solution. In particular, the density of the nodes must be greatest in those parts of the solution domain characterized by the steepest gradients of the dependent variables.

2.3.1 Physical Model And Governing Equations

To enable an unprejudiced approach to the fluid flow problem, a constitutive model was adopted which auto-determines the flow regime, encompassing laminar, intermittent, and fully turbulent. This multi-regime model is based on three interlocking sets of equations. The first set consists of the Reynolds-Averaged Navier-Stokes equations (RANS) and the equation of mass conservation. The RANS equations represent a first-stage introduction of turbulence into the traditional Navier-Stokes equations by means of the turbulent viscosity μ_{turb}.

The second set of equations is that which is needed to obtain values of the turbulent viscosity. There are several such equation sets that have been developed over the years to represent various turbulence models. The set selected here is the Shear Stress Transport (SST) model [138]. In general, the applicability of one or the other turbulence model has to be confirmed by information from experimentation. In this connection, the Shear Stress Transport (SST) model has received considerable support [139] [140] [141] [142]. It represents a merging of two previously developed models, the k-ε and k-ω models. The quantity k is the turbulence kinetic energy, ε is the turbulence dissipation, and ω is the turbulent eddy frequency. The k-ε model has been demonstrated to give satisfactory descriptions of the velocity field at locations that are distant from bounding walls, and the k-ω model provides a good characterization of velocities in the near neighborhood of the wall.

A third set of equations was created to provide a means of dampening the turbulence kinetic energy predicted by the SST model [143] [144]. The dampening functions to diminish turbulence in the intermittent regime that is the transition between laminar and turbulent. A further functioning of the dampening is to suppress turbulence altogether in order to achieve purely laminar flow. The SST-based dampening model is the only one that has been specifically adapted to internal flows.

The starting point of the analysis is the RANS generalization of the Navier-Stokes equations. These equations, as used here, are

$$\left(\frac{\partial \rho u_j u_i}{\partial x_i}\right) = -\frac{\partial p}{\partial x_i} + \frac{\partial}{\partial x_i}\left(\left(\mu + \mu_{turb}\right)\frac{\partial u_j}{\partial x_i}\right) \quad j = 1,2,3 \tag{2.1}$$

These equations are augmented by the conservation of mass, which is

$$\frac{\partial \rho u_i}{\partial x_i} = 0 \tag{2.2}$$

The Reynolds stresses are represented in Eq. (2.1) by the turbulent viscosity μ_{turb}.

The equations of the SST model are

$$\frac{\partial\left(\rho u_i \kappa\right)}{\partial x_i} = \gamma \cdot P_\kappa - \beta_1 \rho \kappa \omega + \frac{\partial}{\partial x_i}\left[\left(\mu + \frac{\mu_{turb}}{\sigma_\kappa}\right)\frac{\partial \kappa}{\partial x_i}\right] \tag{2.3}$$

$$\frac{\partial\left(\rho u_i \omega\right)}{\partial x_i} = A\rho S^2 - \beta_2 \rho \omega^2 + \frac{\partial}{\partial x_i}\left[\left(\mu + \frac{\mu_{turb}}{\sigma_\omega}\right)\frac{\partial \omega}{\partial x_i}\right] + 2\left(1 - F_1\right)\rho \frac{1}{\sigma_{\omega 2}\omega}\frac{\partial \kappa}{\partial x_i}\frac{\partial \omega}{\partial x_i} \tag{2.4}$$

The solution of Eqs. (2.3) and (2.4) yields the values of k and ω, which give the turbulent viscosity μ_{turb} from

$$\mu_{turb} = \frac{\alpha\rho\kappa}{\max(\alpha\omega, SF_2)} \tag{2.5}$$

Turbulence Dampening Model

$$\frac{\partial(\rho u_i \gamma)}{\partial x_i} = P_{\gamma,1} - E_{\gamma,1} + P_{\gamma,2} - E_{\gamma,2} + \frac{\partial}{\partial x_i}\left[\left(\mu + \frac{\mu_{turb}}{\sigma_\gamma}\right)\frac{\partial\gamma}{\partial x_i}\right] \tag{2.6}$$

and

$$\frac{\partial(\rho u_i \Pi)}{\partial x_i} = P_{\Pi,t} + \frac{\partial}{\partial x_i}\left[\sigma_{\Pi,t}(\mu + \mu_{turb})\frac{\partial\Pi}{\partial x_i}\right] \tag{2.7}$$

The nomenclature that appears in Eqs. (2.1) – (2.7) is:

A	model constant
$E_{\gamma 1}$, $E_{\gamma 2}$	intermittency destruction terms
F_1, F_2	blending functions in the SST model
P_k	production term for the turbulent kinetic energy
$P_{\gamma 1}$, $P_{\gamma 2}$	intermittency production terms
$P_{\Pi,t}$	production term for the transition onset Reynolds number
S	absolute value of the shear strain rate
u	local velocity
x_i	tensor coordinate direction
α	SST model constant

β_1, β_2	SST model constants
ω	turbulent eddy frequency
μ	molecular viscosity
μ_{turb}	turbulent viscosity
σ	Prandtl-number-like diffusion coefficient
γ	damping factor
ρ	fluid density
Π	turbulent adjunct function

It is relevant to discuss the manner in which the turbulence is damped. In that regard, reference may be made to Eq. (2.3), and, in particular, to the term involving P_k which represents the rate of production of turbulence kinetic energy. In the native form of Eq. (2.3), the multiplying factor γ does not appear. It is only when the total model of turbulence that includes intermittency and laminarization that γ is employed. It is, in fact, a damping factor which diminishes the rate of turbulence production.

Heat transfer also occurs and is governed by

$$\frac{\partial\left(\rho u_i h_{tot}\right)}{\partial x_i} = \frac{\partial}{\partial x_i}\left(\left(k + k_{turb}\right)\frac{\partial T}{\partial x_i}\right) + \varphi \tag{2.8}$$

where

$$h_{tot} = h + \frac{1}{2}u_i u_i \tag{2.9}$$

In these equations, u_i represents the three velocity components, respectively in the x, y, and z directions. The thermophysical properties ρ, μ, k, and c_p correspond to the fluid density, viscosity, thermal conductivity, and specific heat, respectively. The temperature of the fluid is represented by T and the pressure by p. In the energy equation, the quantity φ is the viscous dissipation term.

Note that these equations are coupled together so that they must be solved simultaneously. Furthermore, since these equations are nonlinear because of terms like u^2 and Tu, they cannot be solved mathematically. Therefore, a numerical solution is mandatory.

In these equations, the quantities ρ and u_i are as before. The new variables are the total enthalpy h_{tot}, the thermal conductivity k, the turbulent conductivity k_{turb} and the dissipation function φ. The turbulent thermal conductivity is deduced from the turbulent viscosity μ_{turb} by means of the turbulent Prandtl number Pr_{turb}, which is defined as

$$Pr_{turb} = c_p \frac{\mu_{turb}}{k_{turb}} \tag{2.10}$$

It is widely accepted for computational purposes to set Pr_{turb}= 0.9 as a default.

It is expected that as the working fluid moves through the system, it will experience a total or partial change of phase from liquid to vapor. This process will be regarded as a local equilibrium process. For nitrous oxide, there is an equation connecting the vapor pressure and the temperature for equilibrium phase change [145].That equation has been evaluated and is plotted in Figure 2.6. The figure provides information for temperatures starting as low as 140K and extends to room temperature. This choice of temperature range corresponds to the present focus on cryogenics. The equation for the curve exhibited in the figure has been used as an input for the numerical simulations. Note that the critical point occurs at a temperature of approximately 310K. In the physical situation to be dealt with here, any issues related to the critical point are not relevant.

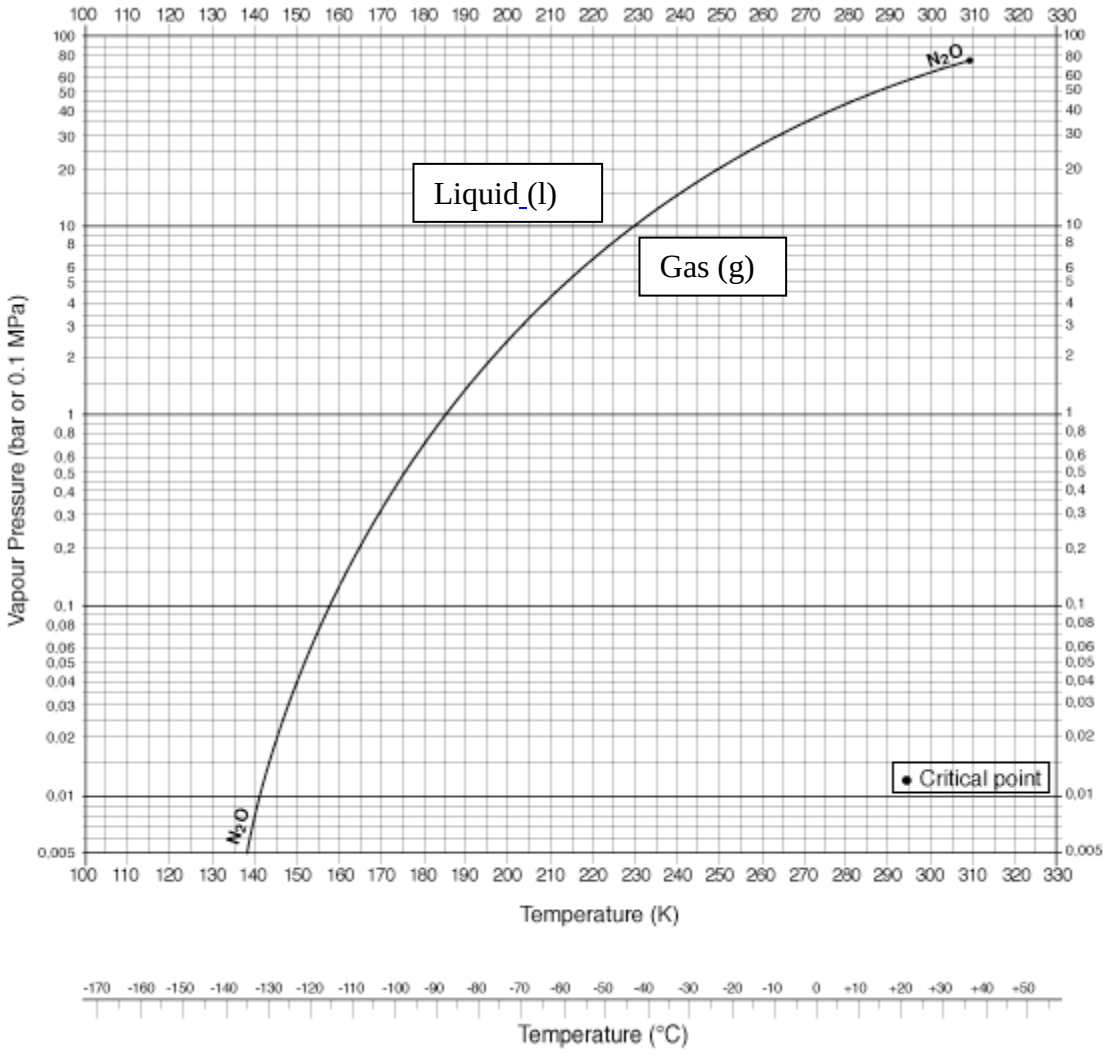

Figure 2.6Vapor-pressure line for nitrous oxide [146]

A major process that occurs in the present treatment is the phase change between the liquid nitrous oxide and its vapor. A related issue is the identification of the volume fractions of these two components. To deal with both of these issues, the VOF (Volume of Fluid) model is used. To implement this model, it is first necessary to select which of the two phases is to be regarded as the continuous phase and which is selected as the dispersed phase. In that regard, it appeared natural to have the liquid be the continuous

phase and vapor be dispersed. It was then necessary to select a heat transfer correlation for the interphase heat transfer, and the well-established Ranz-Marshall correlation was selected. The last critical selection was the mean diameter of the dispersed phase. In this endeavor, focus was directed to the zone of major phase change; that zone being the balloon proper.

The ultimate selection of the mean diameter of the dispersed phase was based on the specification that the surface temperature of the balloon is in the range suitable for cryosurgery. To this end, parametric values of the mean diameter were selected as input to the VOF equations which were solved simultaneously with those for fluid flow and heat transfer. Those solutions required a realistic thermal boundary condition at the surface of the balloon. That thermal boundary condition, a heat flux, was deduced from auxiliary information to be described shortly. This protocol established a suitable value for the mean diameter.

It was also necessary to take account of changes in the distributions of the two phases in the flow from the exit of the balloon to the console. As for the balloon, the VOF equations were solved along with the others and with the mean diameter deduced for the balloon as described in the preceding paragraph.

The results obtained from this modeling effort will be described along with all of the others that were extracted from the numerical simulation of the entire system.

2.3.2 Protocol

In general, it would have been necessary to deal with all of the components in a single simulation, starting with the fluid supplied by the console to the umbilical and terminating with the fluid emptying into the console from the return loop. This

undertaking, while possible in principle, would have involved a simulation which encompassed about 20 million nodes. Although the capacity to accommodate this nodal number was available, the time to achieve a single solution with the available computer power would have been on the order of months. Furthermore, multiple solutions are needed, so that the total computational enterprise would have been unrealistic.

In this light, an approach was sought which would enable the problem to be solved in a more realistic time frame. Information extracted from experimental work was used at two locations in the system: (a) the pressure at the inlet of the umbilical, (b) the pressure at the exit of the umbilical, and (c) the mass flow through the system. This information facilitated the solution to be performed serially along the path of fluid flow, starting with the inlet to the umbilical and terminating at the return flow entering the console.

2.4 Numerical Simulation and Results for Each of the Components of the System

2.4.1 The Umbilical

The fluid flow problem in the umbilical is posed as a pressure-driven flow using known values of the pressures at the inlet and exit provided by experiment.The major unknown is the mass flow rate and/or the volumetric flow rate. The formulation of the problem requires that simultaneous consideration be given to the fluid flow and heat transfer. The need to consider heat transfer comes from the dependence of the thermophysical properties of the liquid on the temperature. The fluid model for the umbilical was based on the flow being totally liquid. This assumption was verified *a posteriori*.

It is also necessary to specify the boundary conditions prior to undertaking the solution of the equations. The pressure ratio across the umbilical is approximately. Furthermore, the velocity components at the tube wall are zero. These specifications are sufficient for the velocity problem. For the temperature, the inlet value is approximately -20^{o}C. At the downstream end of the balloon, the software imposes a very weak boundary condition in the form $\partial^2 T/\partial x^2 = 0$.

It still remains to specify a thermal boundary condition at the wall of the tube. Examination of Figure 2.3 indicates that the liquid flowing in the central tube can exchange heat with the fluid that passes in counterflow in the surrounding annulus. Between these two fluids, the multiple layer thermal resistance provides a thermal barrier. One of the elements of the thermal resistance is a heat transfer coefficient at the interface of the external surface of the tube wall and the flowing medium in the annular return leg of the system. In principle, the heat transfer characteristics of the vapor-phase fluid flow could be determined by means of a separate numerical simulation and, if so, it would not be necessary to use values of the heat transfer coefficient from the literature. That would be the preferred approach because it is a rare event that literature information is directly applicable. However, since focus is being directed to the liquid flow in the tube, it was deemed sufficient to defer the numerical simulation of the flow in the annulus to a later time, and to utilize literature-based information for the heat transfer coefficient for that flow.

The software has provision for the specification of a surface boundary condition which involves a heat transfer coefficient. However, for the situation depicted in Figure 2.3, the heat transfer coefficient can be regarded as a thermal resistance and that interpretation enables account to be taken of all of the participating thermal resistances. The manner of accounting for the participating resistances will now be described.

It is well established that the overall resistance between two flowing fluids is the sum of the series resistances that are encountered along the heat flow path. If the resistances are numbered consecutively from inner to outer, then the summed overall resistance is

$$R = R_1 + R_2 + R_3 + R_4 + R_{fluid} \tag{2.12}$$

From the theory of heat conduction, the resistance for conduction through an annulus of insulating material is

$$R_{ins} = \frac{ln\left(\frac{r_{i+1}}{r_i}\right)}{2\pi L k_{ins}} \tag{2.13}$$

in which L is the length of the tube. Furthermore, the established manner of expressing a resistance based on convection, when applied to the return flow, follows as

$$R_{vapor} = \frac{1}{Ah_{fluid}} \tag{2.14}$$

where A is the surface area of the inner bounding wall of the annulus. When Eqs. (2.12-2.14) are brought together, the expression for the overall thermal resistance becomes

$$R = \frac{ln\left(\frac{r_2}{r_1}\right)}{2\pi L k_1} + \frac{ln\left(\frac{r_3}{r_2}\right)}{2\pi L k_2} + \frac{ln\left(\frac{r_4}{r_3}\right)}{2\pi L k_3} + \frac{ln\left(\frac{r_5}{r_4}\right)}{2\pi L k_4} + \frac{1}{2\pi r_5 L h_{fluid}} \tag{2.15}$$

To evaluate the resistance as expressed by Eq. (2.15), numerical values of the thermal conductivities, the dimensions, and the heat transfer coefficient for the return flow are necessary. To obtain a value of the latter, the literature was consulted. The literature values for the heat transfer coefficient are necessarily approximate, with expected accuracies of the order of ± 10%. This level of uncertainty is acceptable since the ratio of the convective resistance is 3% of the total resistance of the insulating layer.

Since the software does not accept the value of the overall thermal resistance *R* as an input, Eq. (2.15) must be transformed to have the appearance of a heat transfer coefficient. For this purpose, let

$$2\pi r_1 L\hat{h} = R \tag{2.16}$$

where $\hat{h}$ can be regarded as an overall heat transfer coefficient. In addition to the $\hat{h}$ deduced from Eq.(2.16), the temperature of the fluid flowing in the annulus is also required. From results obtained later in this analysis, the temperatures at each end of the annular flow passage are available: 180K at the inlet of the annulus (corresponding to the location of the exit of the umbilical) and 220K at the exit of the annulus (corresponding to the location of the inlet of the umbilical). Linear interpolation between these two values was used to determine temperatures at intermediate locations.

The foregoing paragraphs have described the thermal boundary condition for the case in which there is heat flow from the fluid in the annulus to the liquid passing through the tube. In view of the stated uncertainties, it was deemed relevant to perform a sensitivity study of the impact of the uncertainties by making use of a different boundary condition. That other condition that was selected is an adiabatic wall bounding the liquid flow. In the following presentation of results, these two thermal boundary conditions will be considered, and the resulting axial distribution of the bulk temperature in the umbilical will be compared.

For the present work, research licenses were available, and a mesh consisting of approximately 2,000,000 nodes was used for the solution of the umbilical. Inasmuch as the fluid flow and heat transfer were modeled as being axisymmetric, it was not necessary to extend the solution domain across the entire cross section of the tube. In fact, it is sufficient to select a pie-like wedge and focus on solving the relevant equations in that wedge. For the calculations in question, a wedge with a two-degree opening angle

was selected, and the approximately 2,000,000 nodes were deployed within that space. With respect to a solution which would have encompassed the entire 360-degree geometry, an equivalent node count would have been 360,000,000 nodes! A representative display of a portion of the mesh is presented in Figure 2.7. Note that the density of the mesh is made progressively smaller in the neighborhood of the inner surface of the tube wall. In fact, in the immediate neighborhood of the wall, the mesh is so dense that it cannot be distinguished.

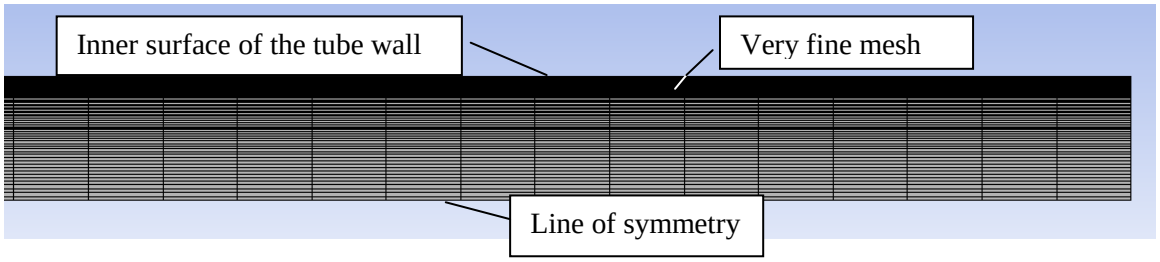

Figure 2.7 Representative portion of the discretized mesh

2.4.1.1 Results and discussion for the umbilical

The quantities of practical interest include the mass and volumetric flow rates, temperature and pressure distributions, and volumetric fractions of the liquid and vapor.

The rate of mass flow through the entire cross-section of the umbilical was extracted from the numerical simulations and was found to be 2.269e-04 kg/sec. Two different turbulence models discussed in the preceding sections were implemented for this study. The outcomes of both the models are in excellent agreement with that of [147]. Further inspection of the table reveals excellent agreement between the mass

SST	RNG k-ε
2.269 e-04 kg/sec	2.270e-04 kg/sec

Table 2.1 Comparison of the mass flow rates in the umbilical using two turbulence models

flow rates obtained by application of the two turbulence models.

The mass flow rate is constant along the entire length of the umbilical. On the other hand, the volumetric flow is not necessarily constant along the length. If $\dot{m}$ denotes the mass flow rate and $\dot{q}$ represents the volumetric flow rate, their relationship is

$$\dot{q} = \frac{\dot{m}}{\rho} \tag{2.17}$$

where ρ is the density of the flowing medium. Since that medium is a liquid, its density can be determined from a correlating equation provided by NIST [2]. That correlating equation shows that ρ is a function of temperature. For the problem under consideration, the temperature varies both across the section of the tube and along its length. As a consequence, ρ will experience similar variations. Therefore, before evaluating Eq. (2.17), it is relevant to display and interpret the temperature results.

Figure 2.8 displays the variation of the temperature across the cross section of the tube

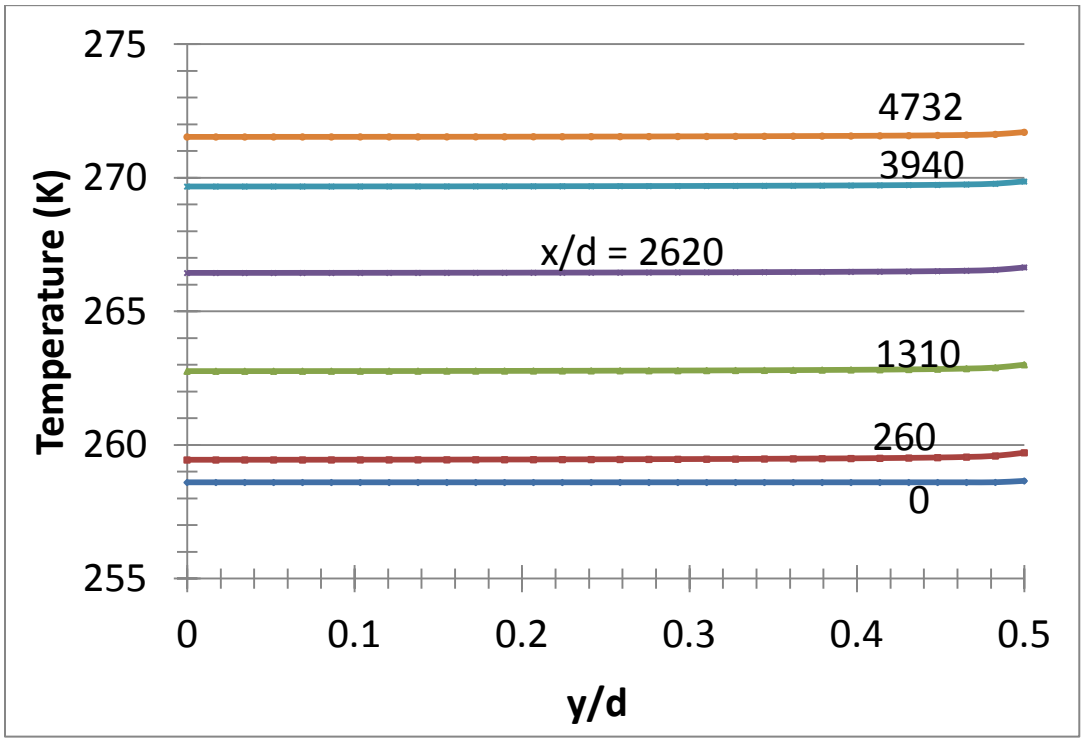

Figure 2.8 Cross-sectional variation of the temperature at several axial locations for the case in which there is heat transfer between the countercurrent liquid flow in the umbilical and fluid flowing in the annulus

for the case of wall heat transfer. This information is displayed for parametric values of *x/d* that represent different locations along the length of the umbilical. The radial location is made dimensionless by the coordinate *y/d*, where *y* is the radial coordinate measured outward from the axis, and *d* is the tube inner diameter.

It can be seen from the figure that the radial temperature distribution is virtually uniform in the immediate neighborhood of the inlet (*x/d* = 0). With increasing downstream distance, the departure from radial uniformity is confined to the near-wall region. In view of the strong relationship between the density and temperature, a graph of the density

distribution would display trends similar to those shown in Figure 2.8, except reversed because density decreases as temperature increases.

Since it does not appear that there is a single value of ρ that would serve for the evaluation of Eq. (2.17), attention was turned to the bulk temperature. That temperature is commonly encountered in studies involving heat transfer. It is the mass-weighted average temperature at each cross section. Since the bulk temperature is widely accepted as a valid representation of the average fluid temperature at each cross section, it will be used to determine an average density for any selected cross section.

Figure 2.9 displays the variation of the bulk temperature as a function of axial distance for two cases, respectively for wall heat transfer and for an adiabatic wall. It can be seen from the figure that for both of these cases, the bulk temperature increases along the length of the umbilical. Intuitively, it might be expected that in the absence of wall heat transfer, there is no reason for the bulk temperature to increase. However, in reality, the friction between the wall and the flowing liquid gives rise to dissipation of the mechanical energy of fluid motion into thermal energy. This transformation of energy is typically referred to as *viscous dissipation*. Both the cases of wall heat transfer and adiabatic wall are affected by the viscous dissipation. The very small temperature difference between these two cases that is seen in Figure 2.9 is due to the heat transferred from the annulus to the umbilical. Clearly, this is a very small effect. From this recognition, it may be concluded that the details of the heat transfer are not very important. In particular, the uncertainty in the annulus heat transfer coefficient is of no practical significance.

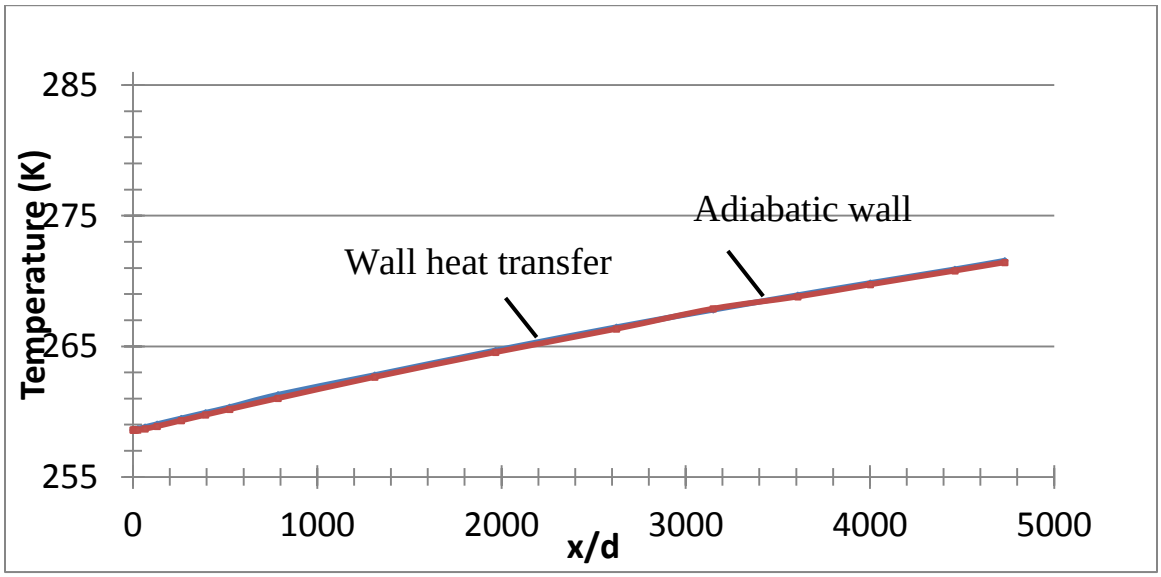

Figure 2.9Variation of the fluid bulk temperature along the length of the umbilical

The increase of the bulk temperature from the inlet to the exit of the umbilical is approximately 13-14K for both cases.

With the bulk temperature distributions as input, the corresponding density variations (hereafter referred to as the bulk density variations) were readily determined from the NIST [2] correlating equation. The bulk density variations obtained in this way are shown in Figure 2.10.

It can be seen from the figure that the axial variations of the bulk density are moderately significant. For the two cases in question, the changes in density from end to end are

about 6%, respectively.

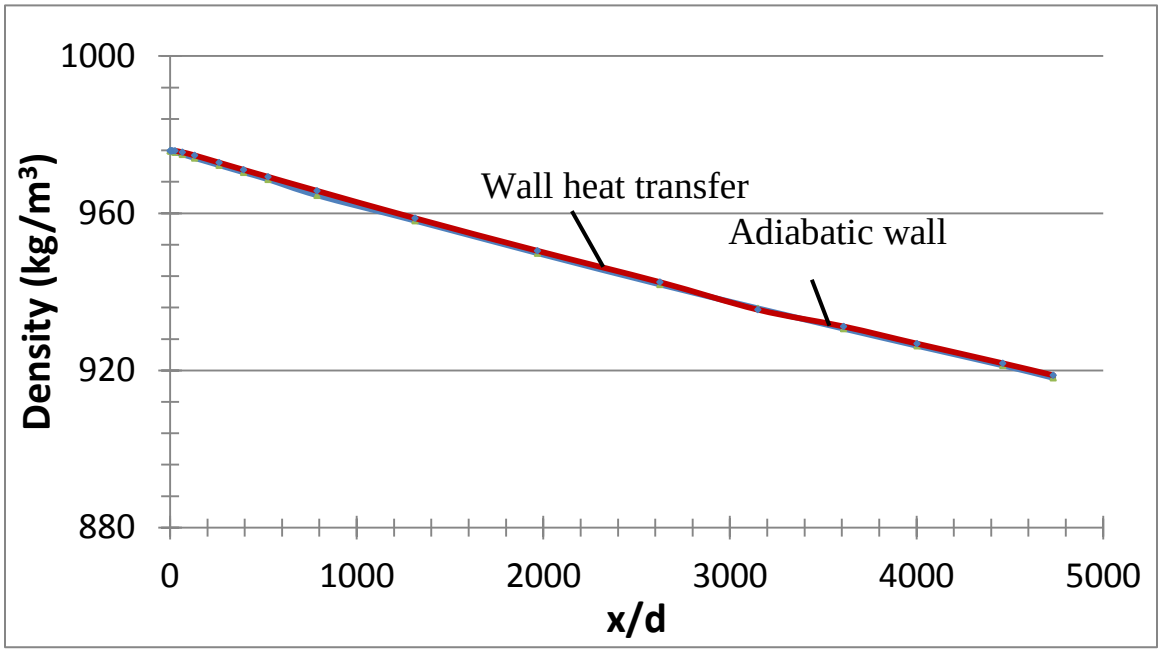

Figure 2.10 Variation of density corresponding to the bulk temperature variations along the length of the umbilical

Equation (2.17) provides the axial variations of the volumetric flow rate corresponding to the bulk density distributions. Those variations are displayed in Figure 2.11. The

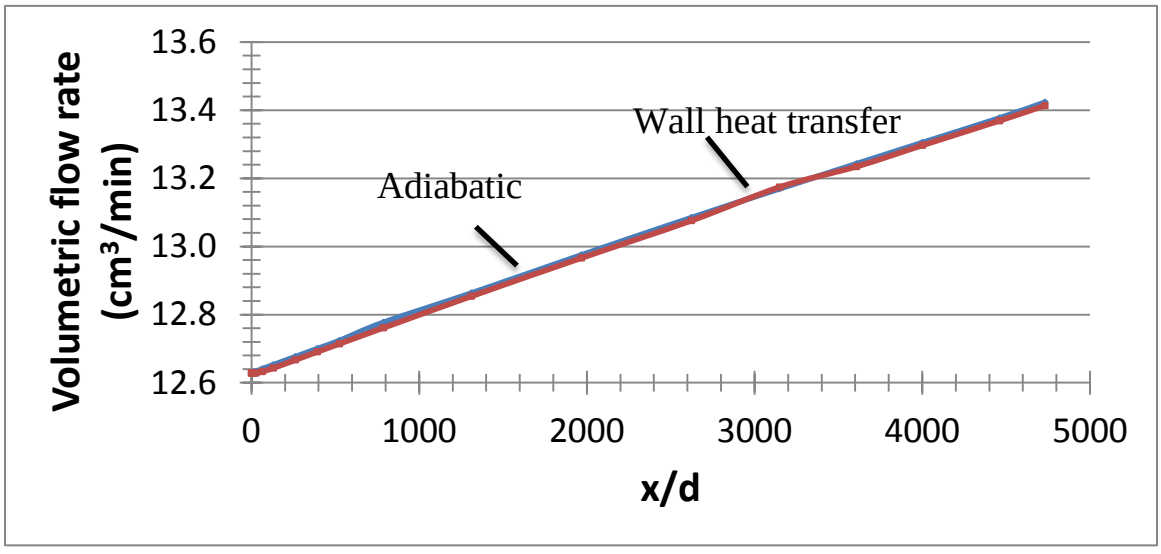

Figure 2.11 Variations of the volumetric flow rate along the length of the umbilical

volumetric flow rate is seen to increase more or less linearly along the length of the umbilical, the variation being about 6%. The extent of the variation of the volumetric flow rate is sufficiently great to suggest that is inadvisable to use this quantity as a descriptor of the magnitude of the flow.

Attention will now be focused on the flow development in the umbilical tube. Near the inlet of the tube, the momentum carried by the flowing fluid changes in accordance with the changes in the shape of the velocity profile. With increasing downstream distance, the changes in momentum decrease steadily and, ultimately, the momentum carried by the fluid becomes constant. Correspondingly, a force balance between the pressure drop and the retarding friction at the wall is established. This flow condition is denoted by the term *fully developed*.

To support the foregoing description of the flow development, the variation of the velocity across the cross section of the tube is exhibited in Figure 2.12 for parametric values of x/d that represent different locations along the length of the umbilical. This information is intended to be illustrative, so that only the case of wall heat transfer is considered. The velocities have been made dimensionless by normalizing them with the mean velocity of the flow at the inlet of the umbilical. Here again, the coordinates x and y have been made dimensionless with respect with to the inner diameter of the tube. The slope of the velocity profile at the surface of the tube wall is proportional to the friction-based wall shear stress. Inspection of the evolution of slopes displayed in the figure indicates that the wall shear diminishes with increasing downstream distance. Although the successive velocity profiles do not quite become congruent, it is seen that they are approaching congruency.

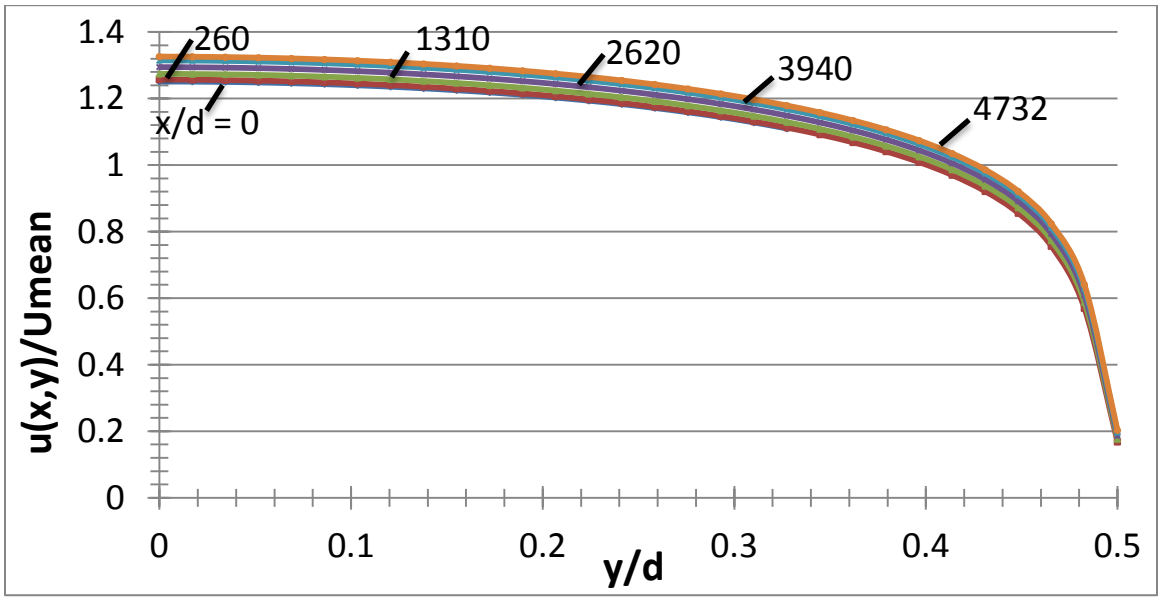

Figure 2.12 Velocity profile development for wall heat transfer

The viscous effects are caused by the shear stress between the flowing fluid and the wall of a pipe. Since the shear stress retards the flowing fluid, a pressure drop is necessary to maintain the motion of the fluid. The variations in the bulk viscosity along the length of the umbilical are shown in Figure 2.13. It can be clearly seen that the viscosity decreases in the downstream direction as the temperature increases along the length of the umbilical.

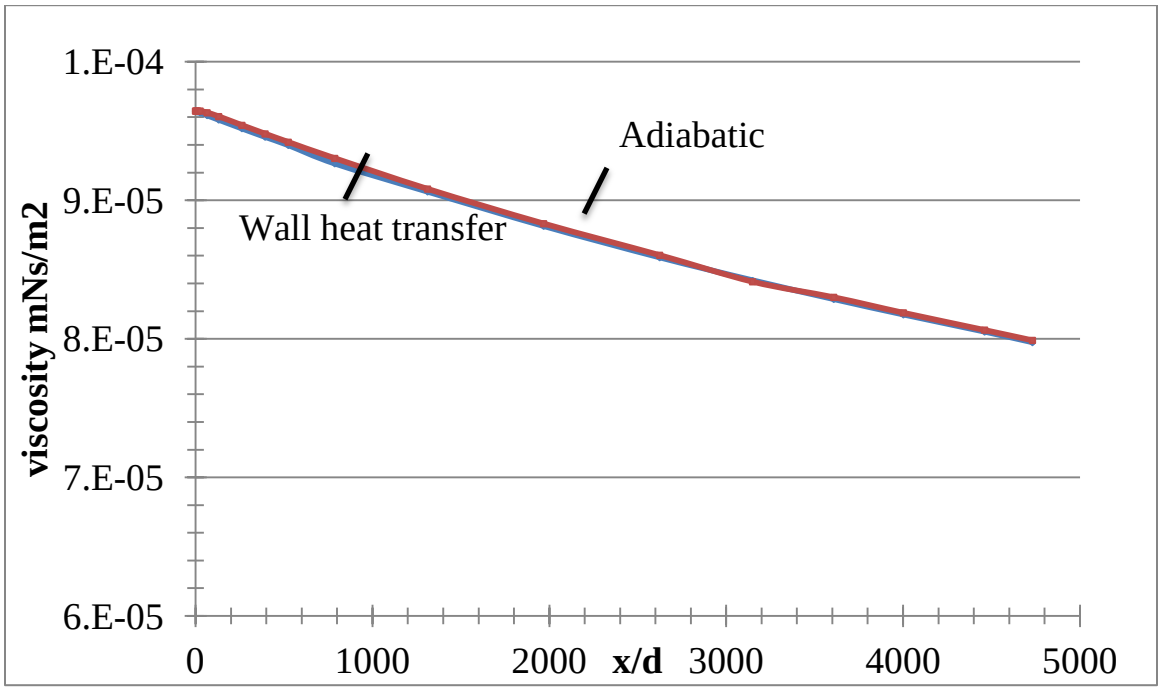

Figure 2.13 Variations in bulk viscosity along the length of the umbilical for the cases of wall heat transfer and adiabatic wall

The pressure drop along the length of the umbilical can be seen in Figure 2.14. This pressure difference was prescribed since the fluid flow was modeled as pressure driven.

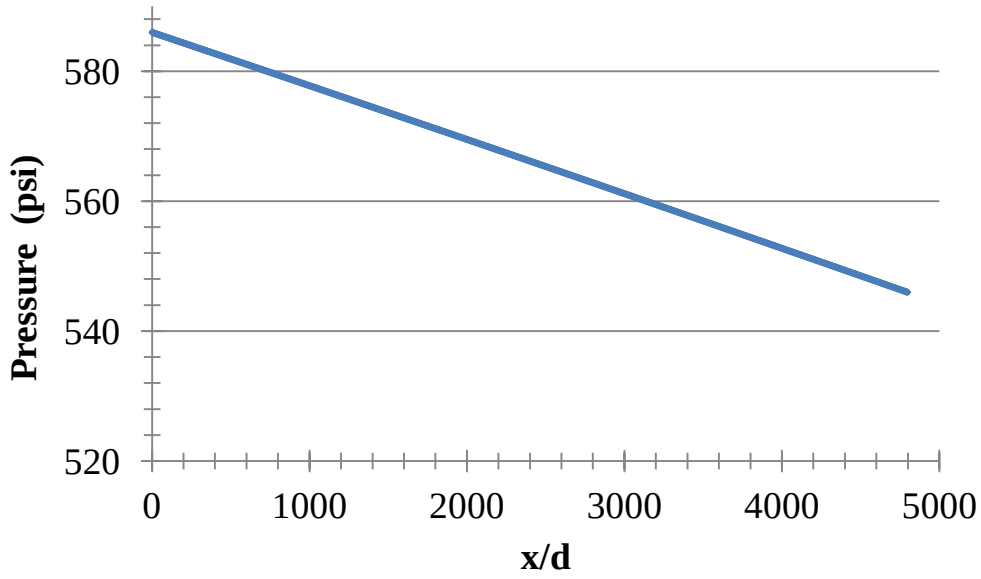

Figure 2.14 Pressure variation along the length of the umbilical

The fluid flow in the umbilical has been modeled as a liquid flow, without phase change. To support this contention, Figure 2.15 has been prepared. That figure displays the liquid-vapor saturation curve taken from NIST [2]. Also shown in the figure is a line that represents the bulk temperature and pressure variations along the length of the umbilical taken from the numerical simulation. Since the latter line does cross the saturation curve, there is no phase change, and the fluid remains in the liquid phase all along the length of the umbilical.

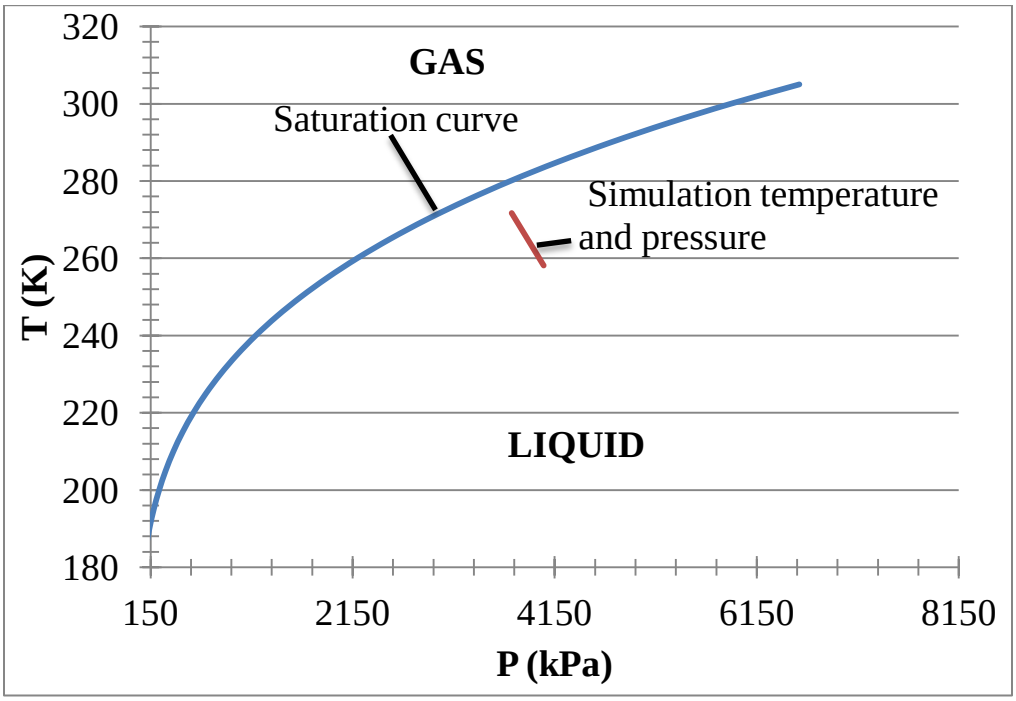

Figure 2.15 Saturation curve and the actual temperature and pressure comparisons

2.4.2 The Handle

An approximate calculation was made of the pressure drop experienced by the flowing liquid from the inlet to the exit of the handle. That calculation yielded 6437 Pa (0.933 psi). When compared to other pressure drops in the system, the pressure drop across the handle can be neglected.

2.4.3 The Injection Tube

The simulation was first focused on the fluid flow and heat transfer in the injection tube as shown in Figure 2.16. The length of the straight section of the inlet pipe is approximately 100cm, and the inner and outer diameters are around 0.3mm and 0.4 mm

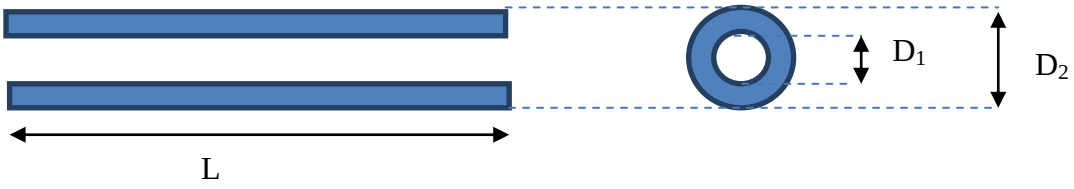

Figure 2.16 The injection tube (a) longitudinal view, (b) cross section

respectively. The mass flow rate, pressure, and temperature obtained from the solution of the umbilical were used as inlet conditions for the injection tube. With these inputs, a numerical solution based on an adiabatic boundary condition was performed for the injection tube. The imposition of the adiabatic condition was based on the findings displayed in Figure 2.9. The solution for the injection tube was extended from its inlet to a location just upstream of the beginning of the coiled manifold. It was found that the temperature and pressure at the latter location were (a) p = 3447kPa and (b) T = 271K.When this information is plotted on a temperature-pressure saturation diagram, similar to Figure 2.15, the outcome is displayed in Figure 2.17. Inspection of this figure reveals that the state of the fluid just upstream of the injection tube is liquid.

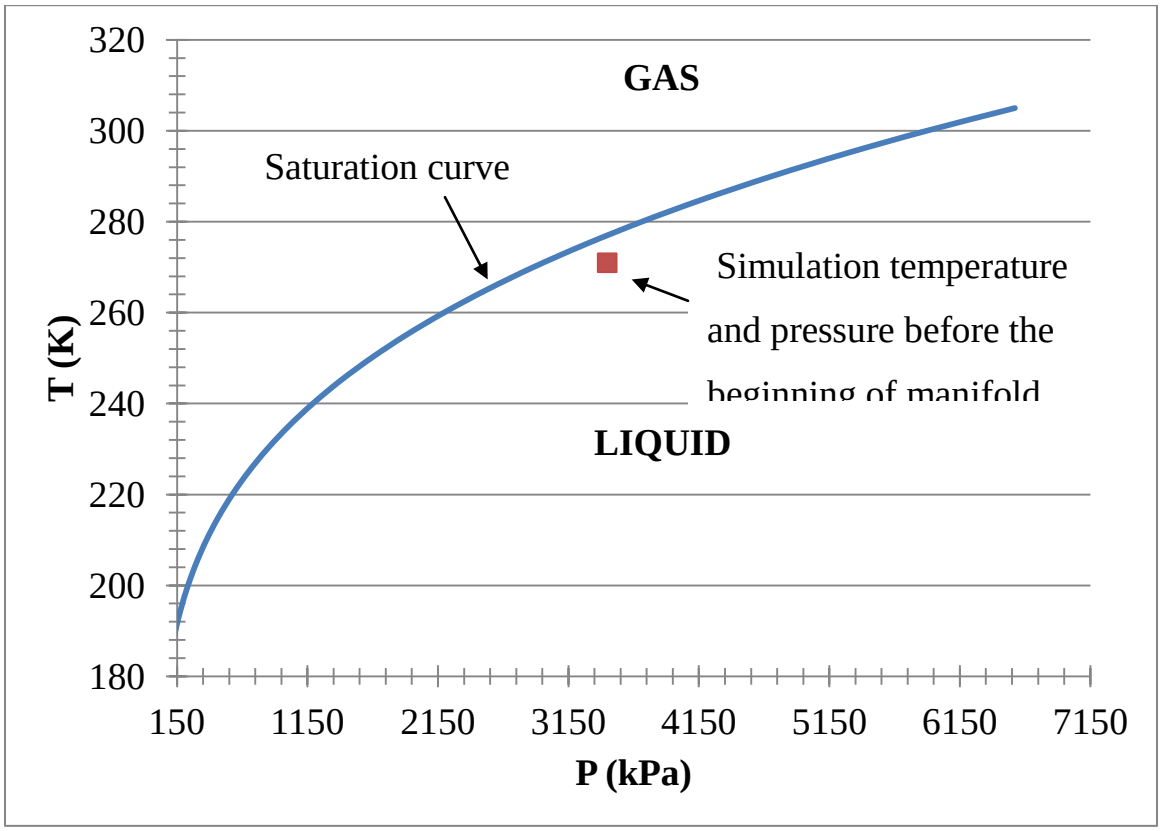

Figure 2.17 Saturation curve and the actual temperature and pressure at the beginning of the manifold

2.4.4 The Manifold and the Balloon

Based on the foregoing identification of the fluid state before the beginning of the coiled inlet as liquid, a simulation model as seen in Figure 2.5 was extended through the coiled manifold and into the balloon volume.

For the continuation of the numerical simulation into the balloon proper, it is first necessary to select a solution domain. The next two figures, Figures 2.18 (a) and (b) were prepared to illustrate the solution domain.

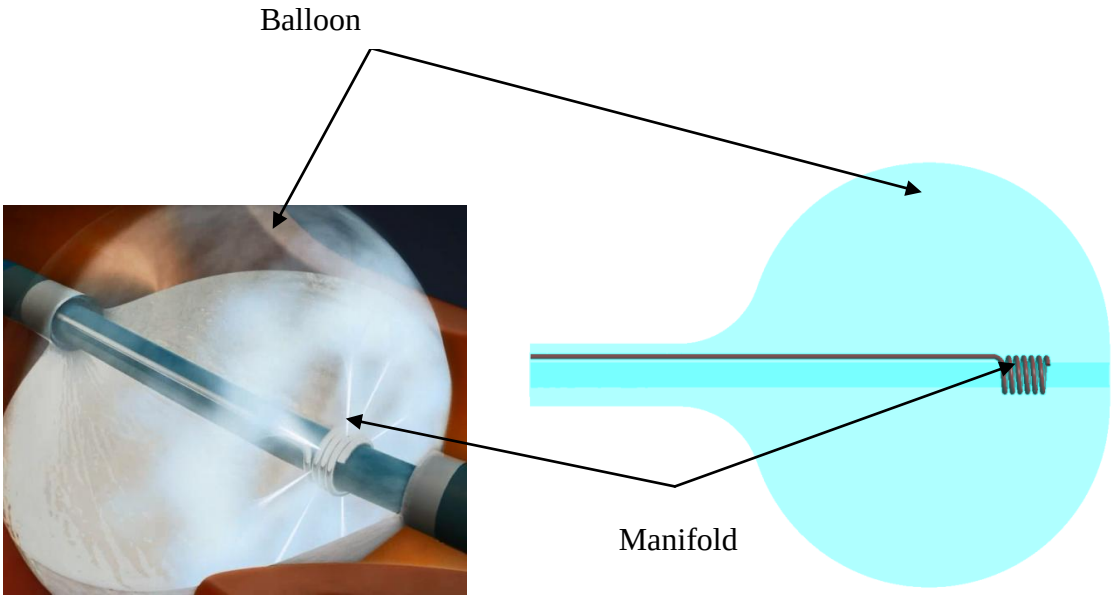

Figure 2.18 (a) Photograph of the jet discharging into the balloon. (b) A side view of the balloon which displays the solution domain from a longitudinal vanatge point.

The mesh in the cross-sectional area of the balloon is shown in the Figure 2.19. The nodal deployment along the steep gradients was created to facilitate better convergence. An approximate mesh size of 8.5 million nodes was used for the manifold-balloon analysis.

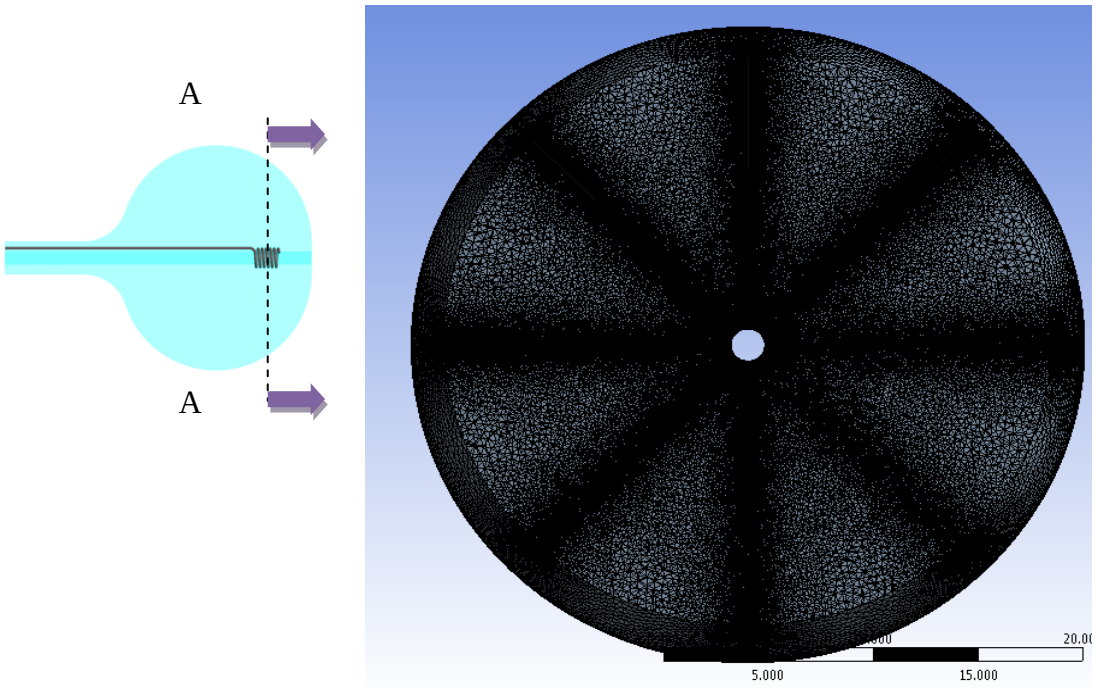

Figure 2.19 Representative cut section of the discretized mesh displaying nodal deployment

2.4.4.1 Results and discussion for the manifold and the balloon

The first result of significance is the variation of the rates of mass flow emerging from the eight apertures in the manifold. This information is conveyed in Figure 2.20. The mass flow rates along the length of the manifold are very nearly constant at a value of approximately 2.8 e-05kg/sec. This outcome suggests that the manifold design is satisfactory.

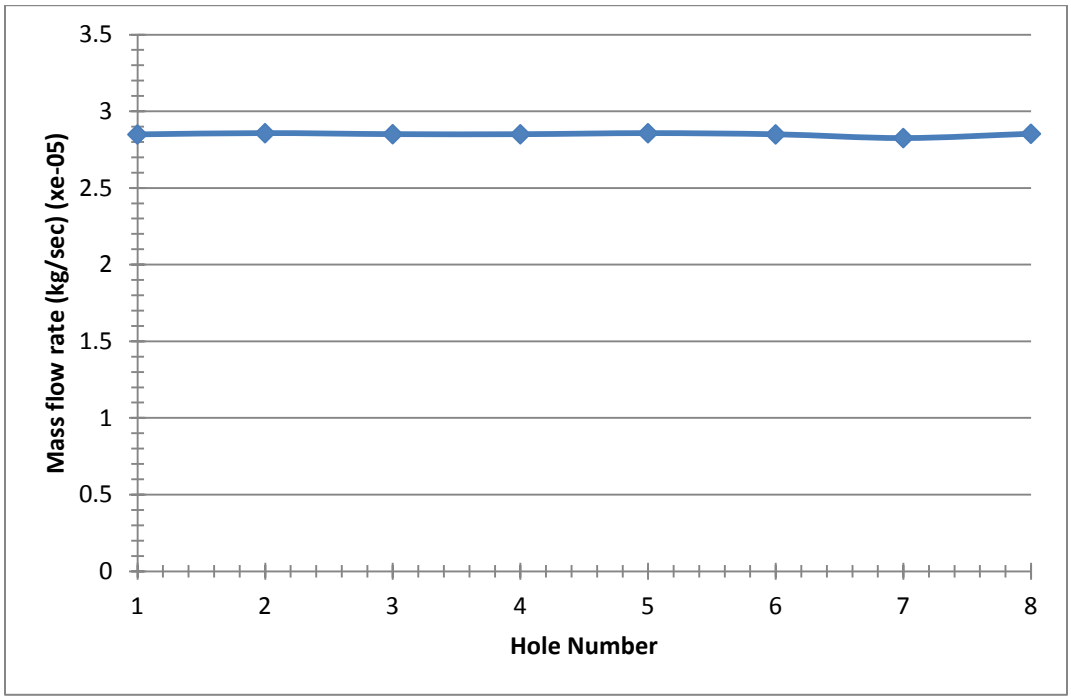

Figure 2.20 Mass flow rates emerging from the eight apertures of the manifold

The second result to be presented is the jet impingement pattern on the inner surface of the balloon. Two models were used for the analysis of the manifold/ balloon solution domain. For the first case, the balloon outer boundary was modeled as adiabatic, and a second model with a more realistic boundary conditions was also studied. The end results for an adiabatic boundary on the outer wall of the balloon are displayed in Figure 2.21(a).

It is seen that the temperature distribution on the surface of the balloon is not strictly uniform in view of the approximately 10 K temperature variations. It may be reasoned that the temperature distribution reflects the pattern of jet of impingement. From this point of view, it may be argued that the impingement pattern is quite uniform.

To provide prospective for the adiabatic-wall temperature pattern exhibited in Figure 2.21(a), it is appropriate to identify the zone of contact between the balloon and the tissue to be necrosed. That contact zone is clarified by inspection of Figure 2.21(b), which

shows the balloon wedged into the tissue needing treatment.

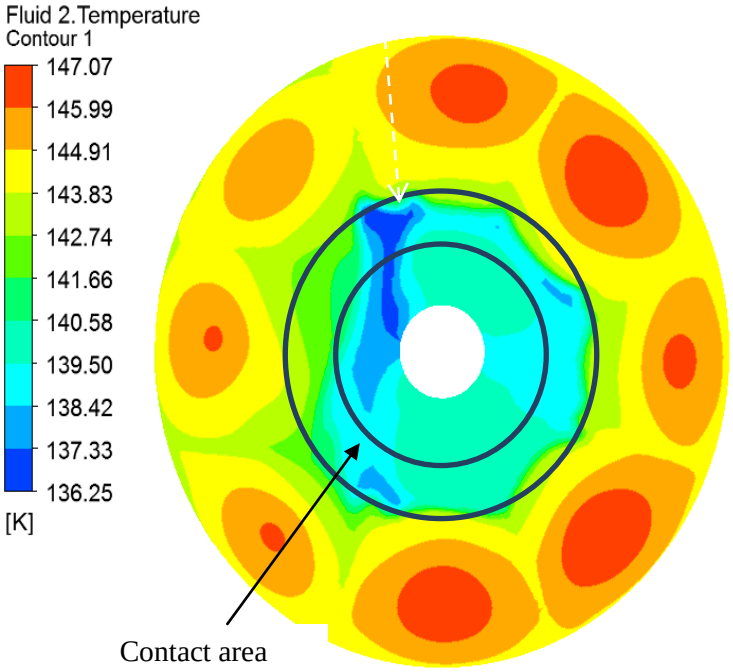

(a)

Contact area

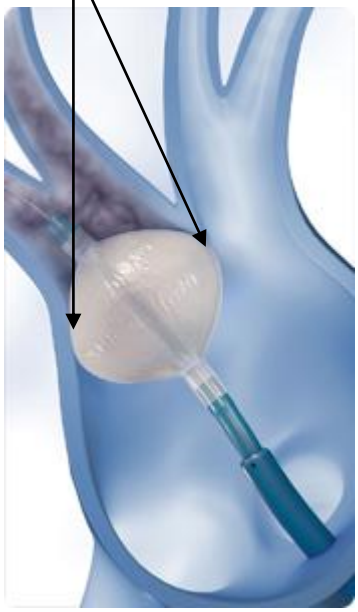

(b)

Figure 2.21 (a) Temperature pattern of the jet impingement on the wall of the balloon for the adiabatic boundary condition. (b) Display of the area of contact between the balloon and the tissue to be necrosed

The pattern of fluid flow within the balloon for the adiabatic-walled case is presented in Figure 2.22. The jets streaming from the discrete openings in the manifold entrain the

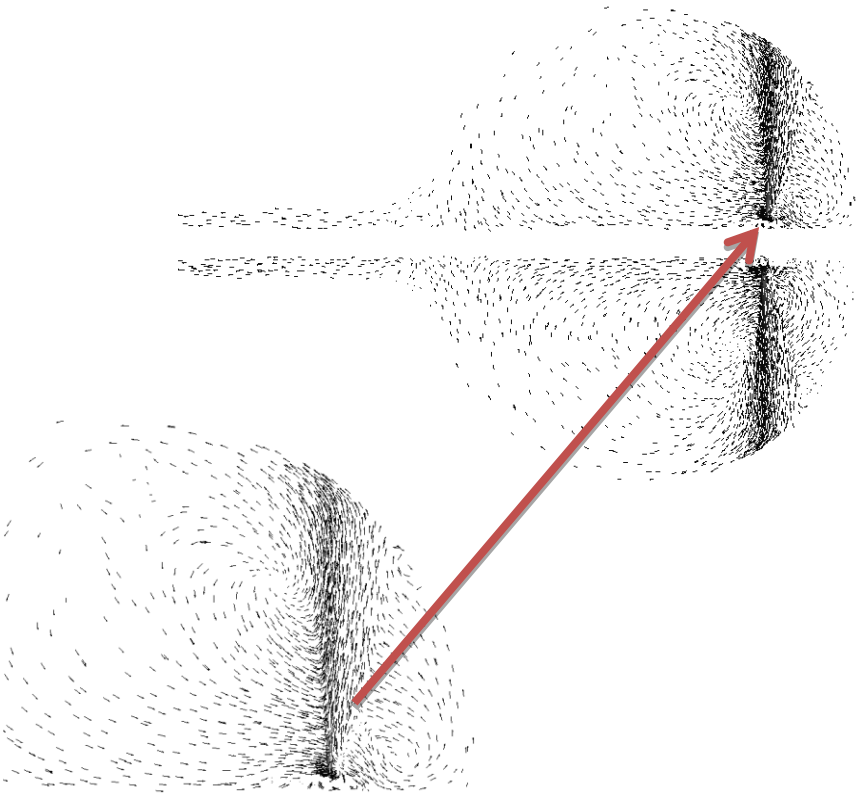

Figure 2.22 Pattern of fluid flow within the balloon for the adiabatic-wall case

otherwise quiescent fluid within the balloon, and this action creates recirculation zones. A close-up of a jet is displayed in the inset at the lower left of the figure.

The next case to be considered is that in which heat is conveyed to the outer surface of the balloon from an external source. In particular, in *ex vivo* experiments, the balloon was surrounded by a water bath whose temperature was maintained at 37^{O}C. In order to calculate the rate of heat transfer from the water bath to the surface of the balloon, it is necessary to make use of the standard equation for convective heat transfer, which is

$$\frac{Q}{A_{surface}} = h\,(T_{waterbath} - T_{balloon\,surface}) \qquad (2.18)$$

In order to apply this equation, a value of the convective heat transfer coefficient *h* is needed. A suitable value of around 25.4W/m^{2}K is used for *h*. Equation (2.18) was used as the thermal boundary condition at the surface of the balloon.

The balloon surface temperature corresponding to this thermal boundary condition is shown in Figure 2.23. If focus is directed to the part of the balloon surface that lies in the contact zone, it is seen that the temperatures are more or less the same as the measured temperatures of about -80^{O}C to -100^{O}C for cryosurgical procedures [148].

To provide perspective for this result, it is relevant to clarify the thermal boundary condition at the surface of the balloon. That boundary condition was chosen to correspond to the experimental setup. In that setup, the balloon was situated in a water bath whose temperature was maintained at 37^{o}C. In that connection, it is significant to note that water is an outstanding heat transfer medium. In another environment external to the balloon, the temperatures would undoubtedly be different.

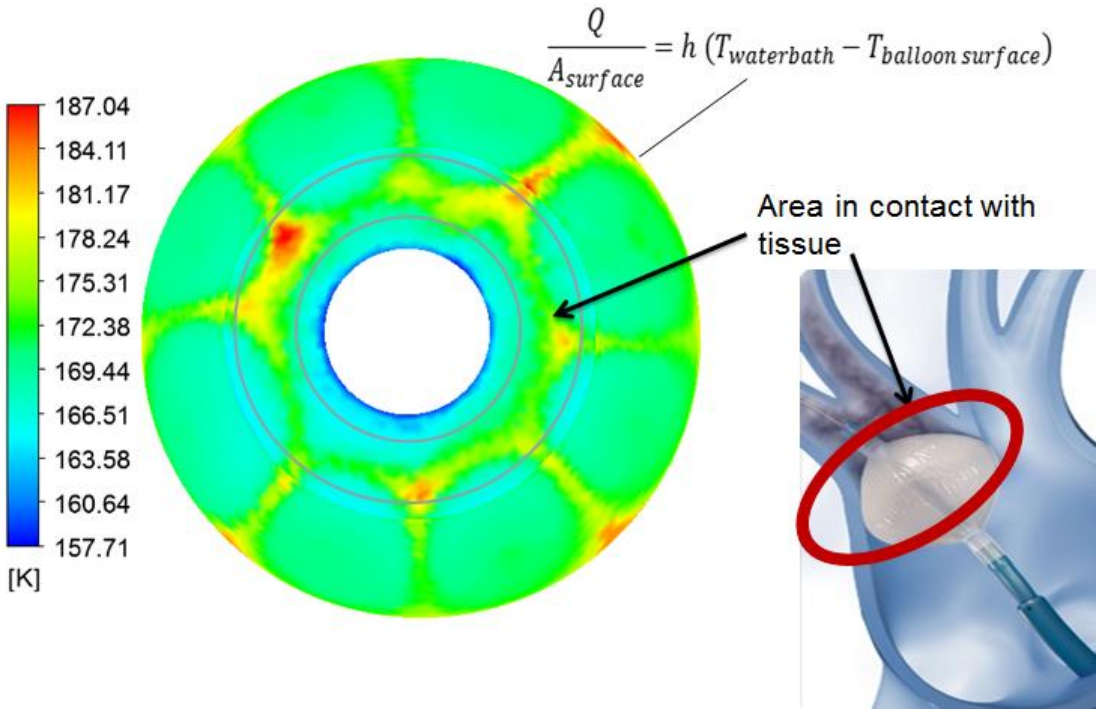

Figure 2.23 Temperature pattern of the jet impingement on the wall of the balloon for a convective heat heat transfer boundary condition

Another result of interest is the distribution of the volume fractions of the two phases throughout the balloon, and Figure 2.24 is presented for this purpose. To clarify the information conveyed in the figure, the colors are keyed to the volume fraction of the liquid phase. The figure corresponds to a longitudinal cut through the balloon. For this cut, only one of the manifold distribution ports is shown to be distributing fluid. The fluid within the manifold is clearly seen to be totally liquid. However, almost immediately upon leaving the fluid-distributing port, phase change is initiated. Away from the jet, the volume fraction of the liquid is relatively uniform.

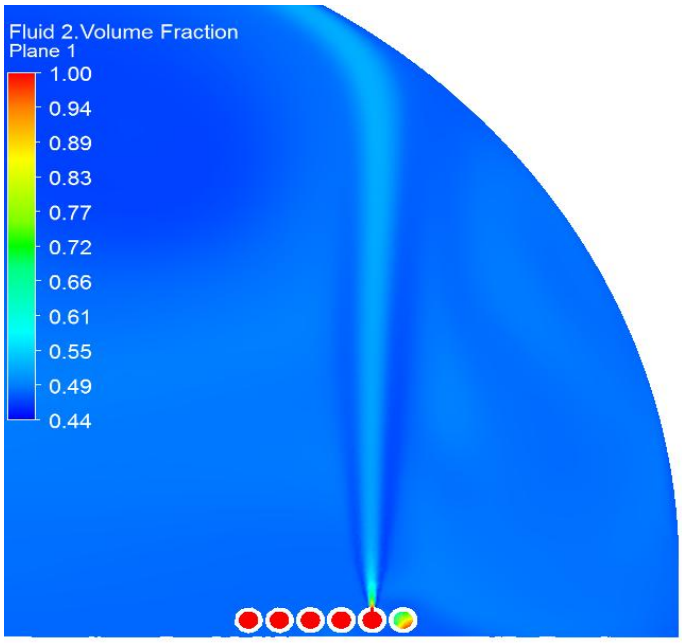

Figure 2.24 Volume fraction of the liquid leaving one exit manifold

2.4.5 The Return Flow Model

The spent nitrous oxide exits through the annulus which surrounds the injection tube. It then passes through the handle and flows back to the console through the annulus of the umbilical tube. The close loop system is thus complete. Figure 2.25 shows the annular flow of the vapor-liquid mixture back to the console. The inner and outer diameters of the annulus surrounding the injection tube are approximately 2mm and 3mm respectively, while the inner and outer diameters of the annulus surrounding the umbilical are approximately 3.5mm and 5mm respectively.

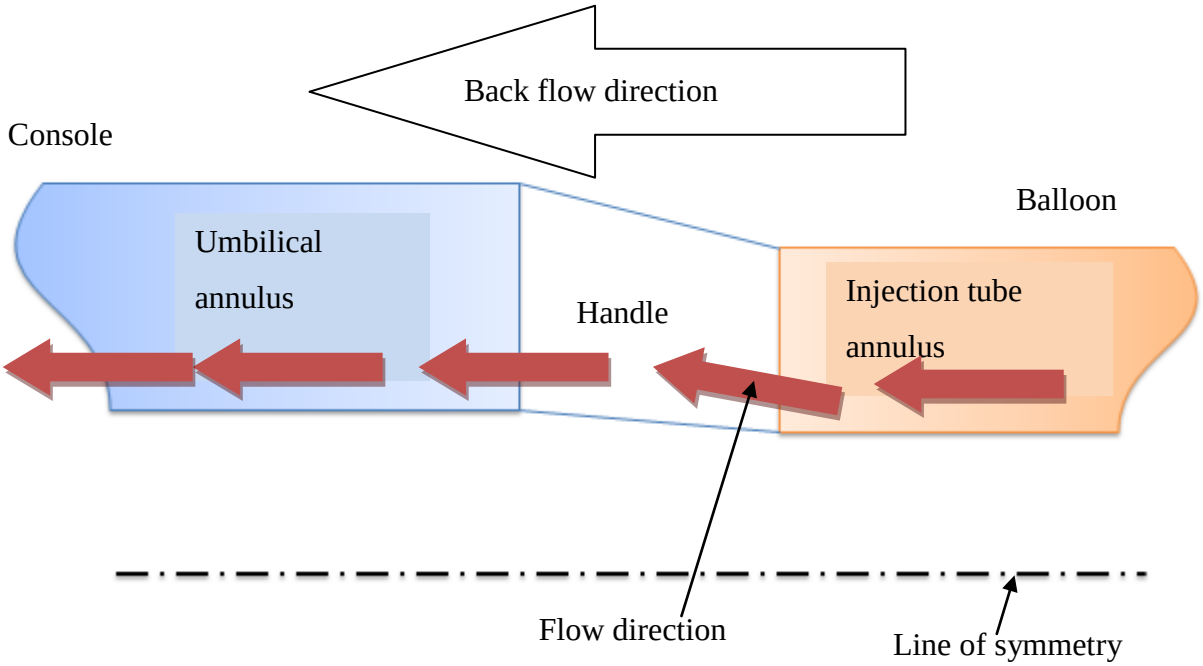

Figure 2.25 Longitudinal view of the vapor annulus for the return flow (units are in mm)

The fluid flow in the return flow model was modeled as being axisymmetric. Consequently, it was not necessary to extend the solution domain across the entire cross section of the tube. It is, in fact, sufficient to select a pie-like wedge and focus on solving the relevant equations in that wedge. For the calculations in question, a wedge with a two-degree opening angle was selected, and the over 3,500,000 nodes were deployed within that space.

A heat transfer coefficient of 22.5 W/m^{2}K was calculated for natural convection from the surrounding air medium to the outer wall of the annular return flow using Eqs. (2.19-2.21)

$$Ra = \frac{g\beta\Delta T\, D^3}{\nu^2} Pr \qquad (2.19)$$

$$\bar{h}_{convective} = \frac{k}{D}\left[0.6 + \frac{0.387\, Ra^{\frac{1}{6}}}{\left[1+\left(\frac{0.559}{Pr}\right)^{\frac{9}{16}}\right]^{\frac{8}{27}}}\right]^2 \tag{2.20}$$

$$h_{total} = h_{convective} + h_{radiation} \tag{2.21}$$

2.4.5.1 Results and discussion for the return flow model

Figure 2.26 displays the variation of the fluid bulk temperature as a function of axial distance for an adiabatic wall. As expected, the bulk temperature remains constant for an adiabatic outer wall boundary. This information is displayed for x that represents different locations along the return flow path. The origin of the geometry is placed at the downstream end where the handle is mated to the catheter proper.

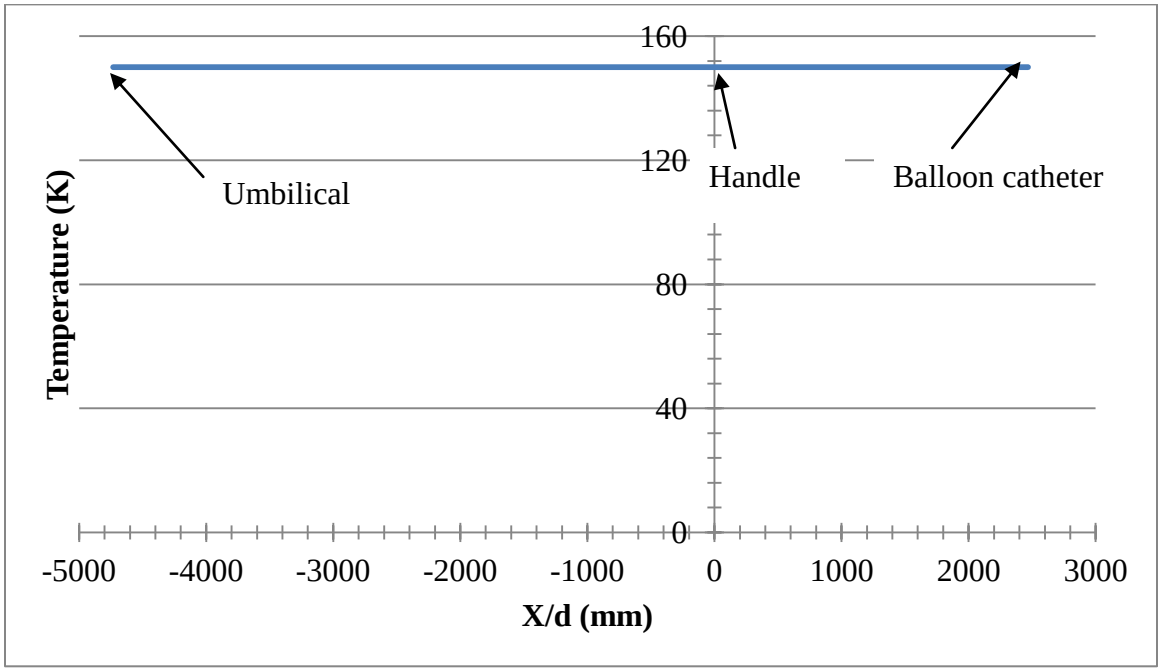

Figure 2.26 Bulk temperatures for return flow in the annulus along the length of the injection tube-handle-umbilical for the adiabatic-wall boundary condition. In the figure, the axial dimension x is normalized by the diameter d of the umbilical

To take into account the heat transfer between the surrounding medium and the return flow, a convective boundary condition (Eq. (2.21)) was imposed on the wall of the return flow through the annulus. Figure 2.27 represents the bulk temperature of the fluid leaving the balloon and returning to the console. The temperature difference between those displayed in Figures 2.26 and 2.27) is due to the heat transfer from the ambient into the return flow. The increase of the bulk temperature from the inlet to the exit of the flow path is approximately 70^{O}K.

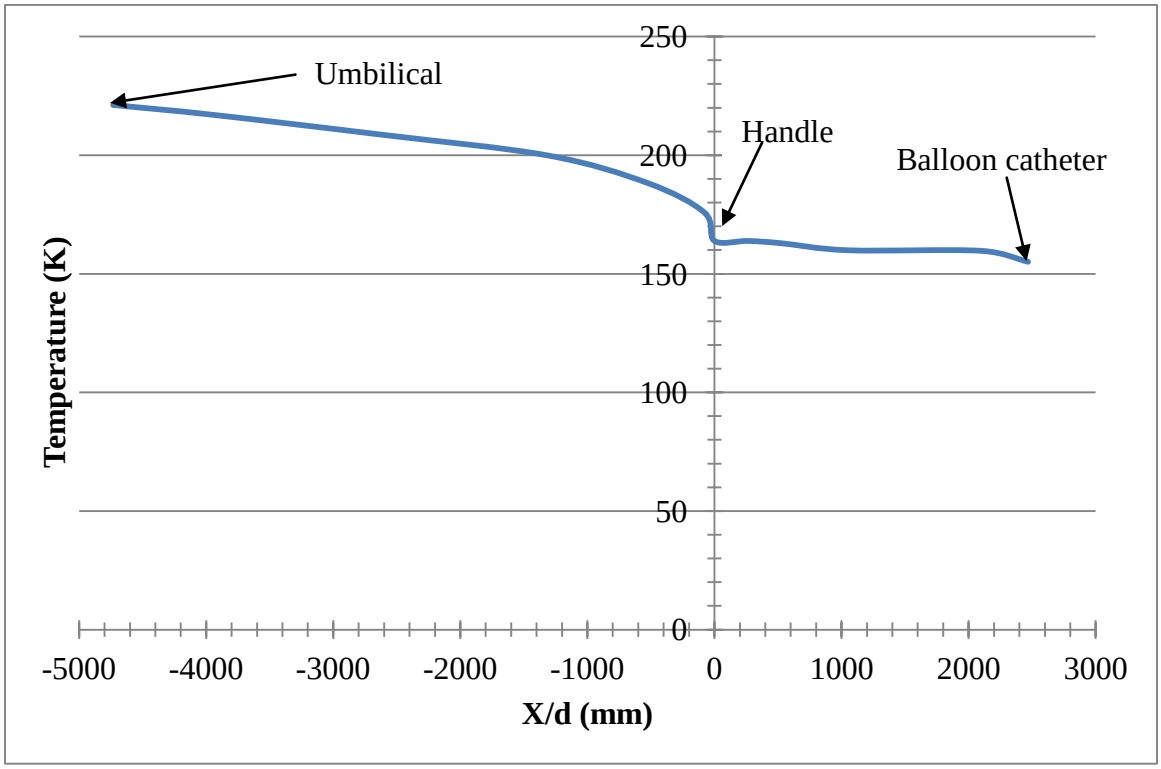

Figure 2.27 Bulk temperature plot for return flow in the annulus along the length of the injection tube--handle-umbilical for the heat transfer boundary condition. In the figure, the axial dimension x is normalized by the diameter d of the umbilical

Another result of significance is the volume fraction of the fluid returning to the console. The volume fraction of the liquid entering the return flow path is 44.5%. Figure 2.28 show color contour plots of the cross-sectional variations of the liquid volume fraction of the return flow close to the inlet, at the handle, and close to the outlet. The monotonic decrease of the liquid volume fraction ranges from 0.44 to 0.025.

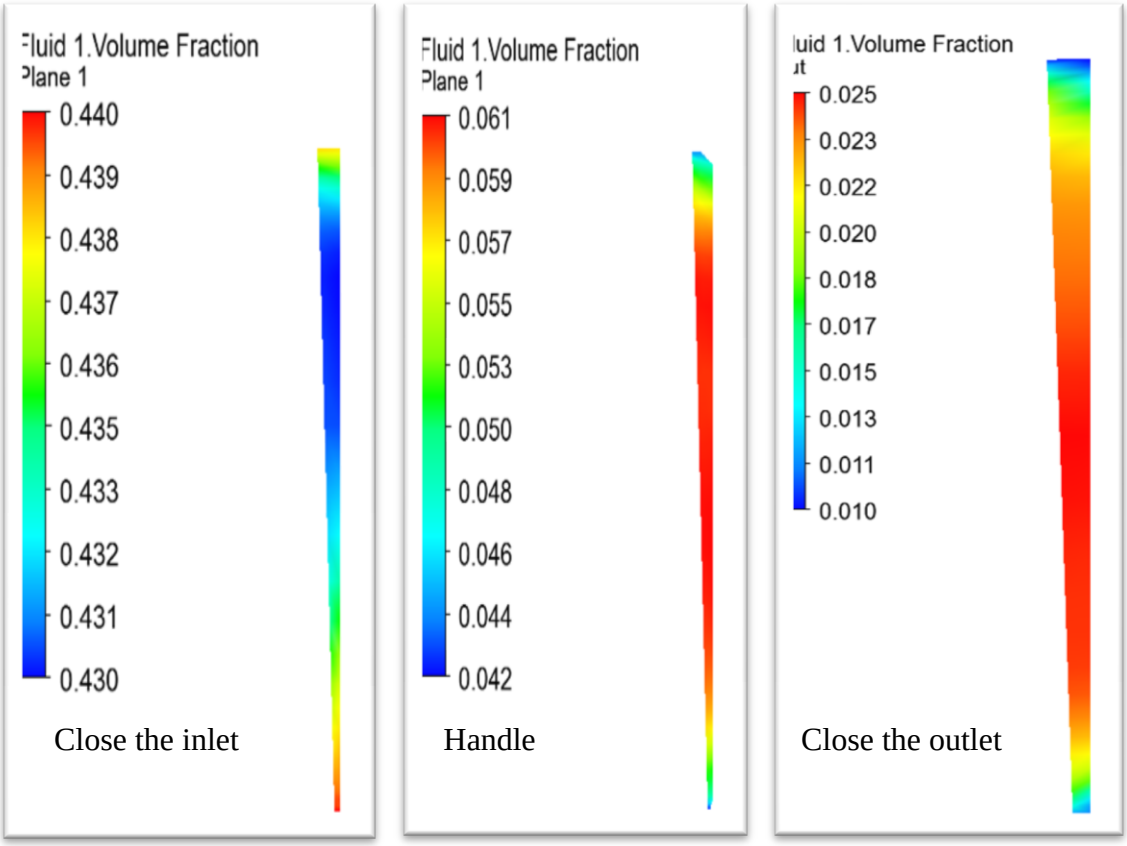

Figure 2.28 Volume fraction contours diagrams at different cross sections in the return flow path

Figure 2.29 shows the continuous variation of the maximum volume fraction at cross sections along the return flow path. The maximum volume fraction reduces to ~2.5% close to the console. Figure 2.30 displays the variation in the pressure along the return flow path.

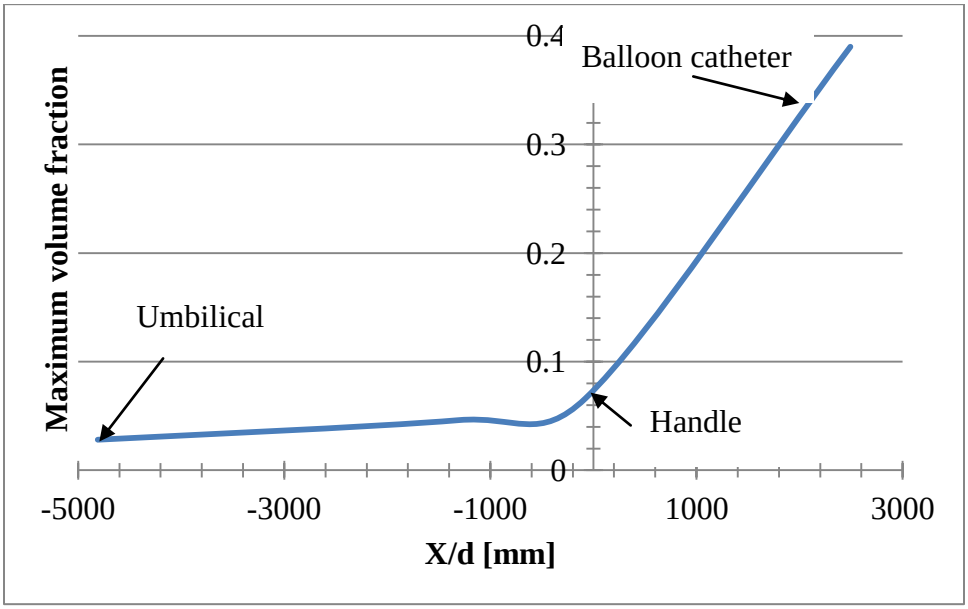

Figure 2.29 Maximum volume fractions at different cross sections along the return flow path. In the figure, the axial dimension x is normalized by the diameter d of the umbilical

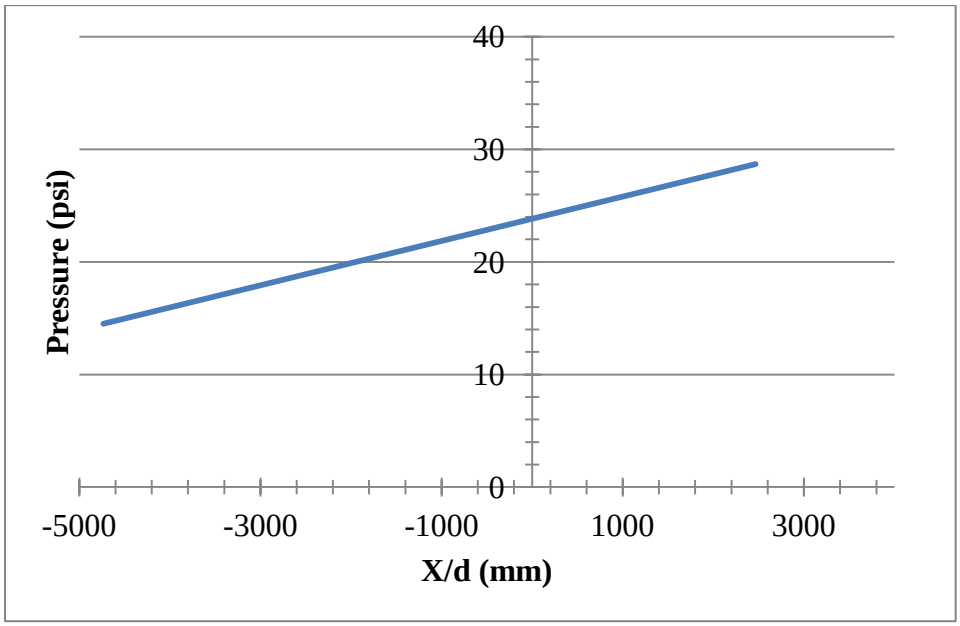

Figure 2.30 Pressure variations in the return flow path. In the figure, the axial dimension x is normalized by the diameter d of the umbilical

2.5 Conclusion

The goal of the research presented in this chapter was to model all of the physical processes that occur throughout all the components of the cryoballoon system. To facilitate the analysis, the system was subdivided into its functional parts, starting with the inlet to the umbilical and proceeding sequentially to the distal end of the system. Numerical simulation was used to facilitate the solutions of the partial differential equations that describe the participating physical processes which occur in the cryoballoon therapy system. The modeled functional components are, starting at the upstream end, the umbilical, the handle, the injection tube, the coiled manifold, and the cryogenic balloon and the return path.

The results extracted from the numerical simulation of the umbilical include the mass flow rate of the fluid and the streamwise variations of temperature, pressure, and fluid state. The predicted mass flow rate value was compared with that determined from experiment and exact agreement was obtained to within two significant figures. It was also demonstrated that the fluid remained in the liquid state throughout the entire length of the umbilical.

The pressure drop sustained by the fluid in passing through the handle was calculated and found to be negligible compared to the other pressure drops in the system.

The balloon inlet tube, which extends downstream from the handle to the inlet of the coiled manifold, was next subjected to simulation. The simulation of the flow in the injection tube also verified the perpetuation of the liquid phase. That solution provided inputs for the study of the fluid flow phenomena in the coiled manifold. That investigation demonstrated that the liquid state was maintained throughout the manifold. Of great importance is the finding that the mass flow rates of the fluid exiting the eight apertures of the manifold were almost uniform.

The continuation of the numerical simulations into the manifold and cryoballoon proper provided the temperature distribution on the surface of the balloon. For the simulations, a thermal environment similar to that of the experiments of [1] was utilized. That environment consisted of a water bath at a temperature of approximately 37^{O}C. It is well established that water is an excellent heat transfer medium and is, therefore, able to impose its temperature on adjacent media. Hence, the temperature variations observed will be different from those of actual cryosurgery applications. The volume fraction of the fluid at the exit of the balloon was found to be 44.5% liquid.

The final part of the analysis involved the return flow path. The fluid returning to the console is 97.5% vapor.

Chapter 3 Cryoprobe Experiments

3.1 Experimental Apparatus

To support the numerical simulations for the cryoprobe, a synergistic experimental program was formulated and executed. A not-to-scale schematic diagram of the cryoprobe that was used for the experiments is shown in Figure 3.1. Its primary features, all of stainless steel, are conveniently identified by following the path of fluid flow. The working medium is gaseous argon whose initial pressure is 3500psi. It passes through an eight-foot-long tube which delivers it to the upstream end of the cryoprobe proper. The delivered argon gas passes into a straight circular tube whose length and internal diameter are, respectively, 17.5cm and 0.4mm, yielding a length-to-diameter ratio of 437.5 The downstream end of the tube opens into a relatively large space whose end is bounded by a solid conical tip.

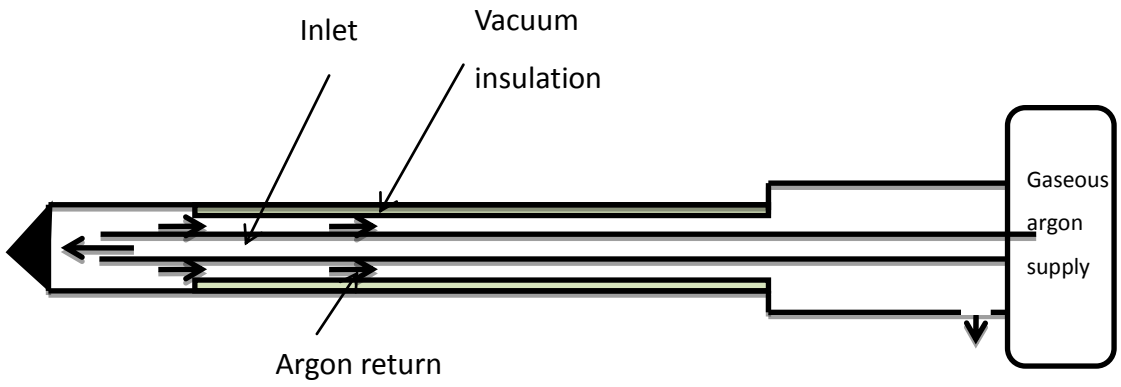

Figure 3.1 Schematic of cryoprobe used in the experiments

The flowing medium experiences a 90-degree flow reversal in the enlarged space and thereafter enters an annulus that envelops the inlet pipe. Its internal and external

diameters are around 0.5and 1.35mm, respectively, and its axial length is 15mm approximately. The outer surface of the argon-flow annulus is girdled by another annulus which constitutes a vacuum space and is intended to serve as an excellent insulator. The vacuum annulus has internal and external diameters of 1.35 and 2 mm, respectively. When the cryoprobe is inserted into the malfunctioning tissue, necrosis occurs over a length extending from the tip of the probe to the upstream end of the vacuum space.

The downstream end of the insulated argon-flow annulus is mated with an uninsulated continuing annular space which conveys the spent fluid to an exhaust site situated just upstream of the argon supply.
A photograph showing a bank of argon storage tanks and the console used to control the experiments is displayed in Figure 3.2.

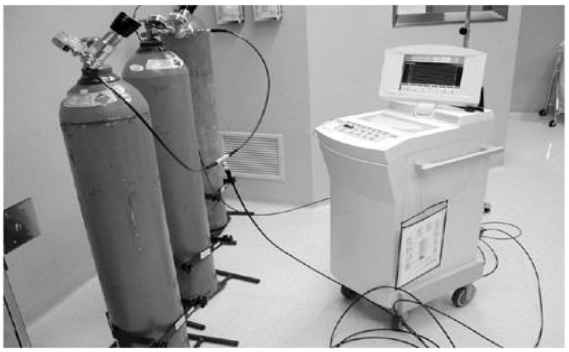

Figure 3.2 Photograph of the argon storage tanks and the control console

3.2 Thermocouple Installation

The primary instrumentation that was used to extract experimental data is thermocouples. In order to facilitate the installation of the thermocouples, it was necessary to take apart a portion of the apparatus. The first step of disassembly is shown in Figure 3.3(a). That step

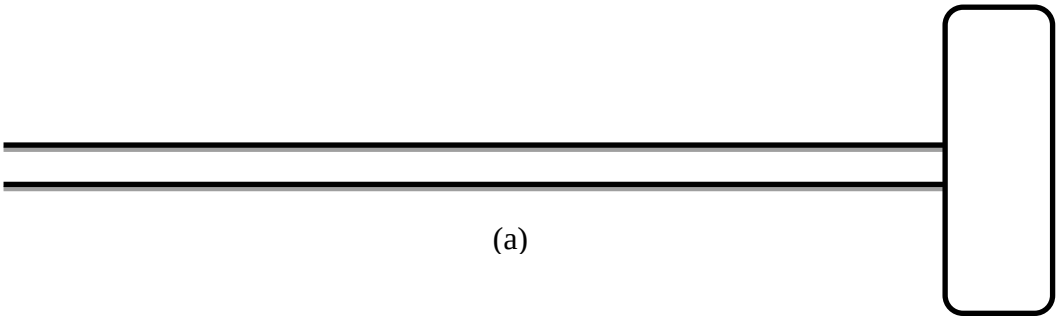

(a)

exposes the inlet tube from end to end. A tight fitting helically coiled spring was put in place as shown in diagram (b). As will be seen shortly, the spring acts as a set of fins to enhance the heat transfer. With the spring in place, thermocouples were soldered to the inlet tube at locations that correspond to the two ends of the spring, as seen in diagram

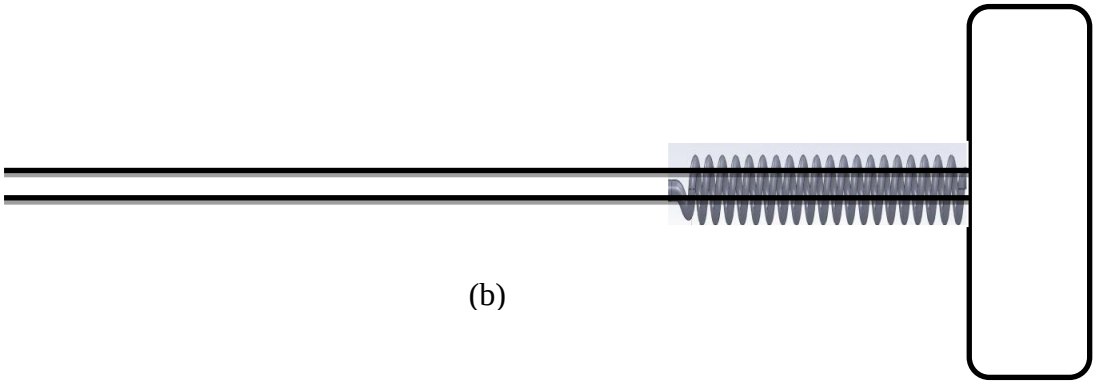

(b)

(c). The thermocouple wire was Type K, with the individual wires, chromel and alumel, being 0.010 inches in diameter and 36 inches in length. The soldering was accomplished by means of a lead-free solder (alloy of 95% tin and 5% silver).

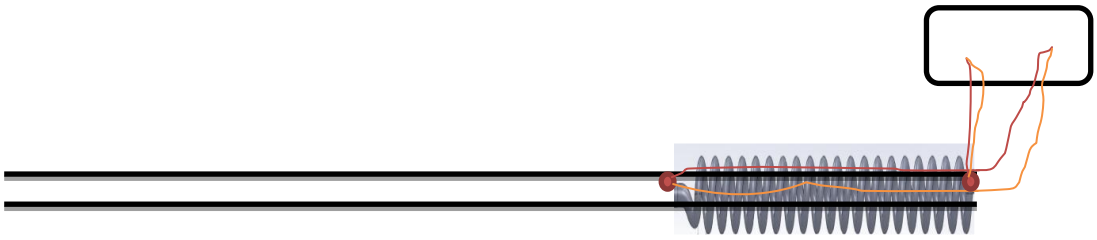

(c)

The next to the last step in the instrumentation installation is the re-assembly to restore the probe to its initial configuration. The re-assembled probe is shown in diagram (d). That diagram enables the description of the function of the coiled spring. Note that the spent fluid, still below the room temperature passes over the coils, thereby cooling the external surface of the inlet pipe. In turn, the pipe extracts heat from the incoming argon gas. The final step is the

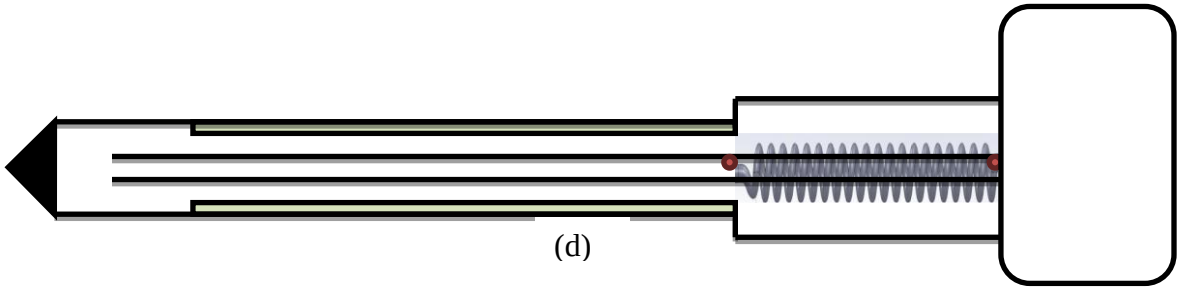

(d)

installation of another thermocouple whose positioning is illustrated in diagram (e). In particular, the thermocouple is placed on the outside surface of the annular sheath in-line with the upstream end of the vaccum jacket.

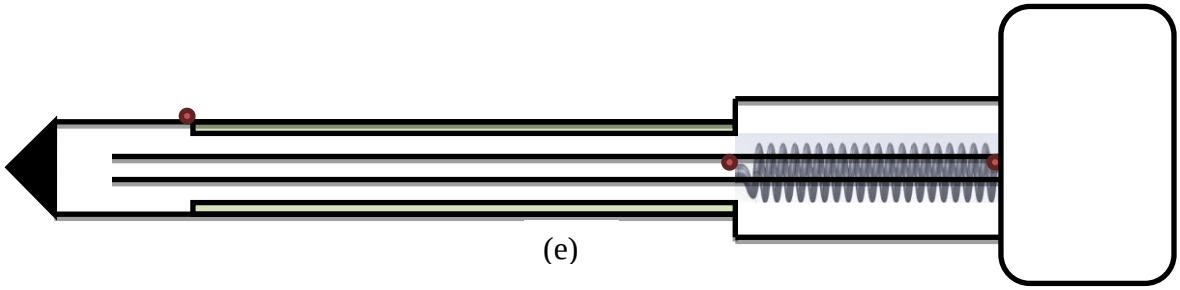

(e)

Figure 3.3 The successive steps in the installation of the thermocouples

A photographic view of the external surface of the fully assembled cryoprobe is displayed in Figure 3.4.

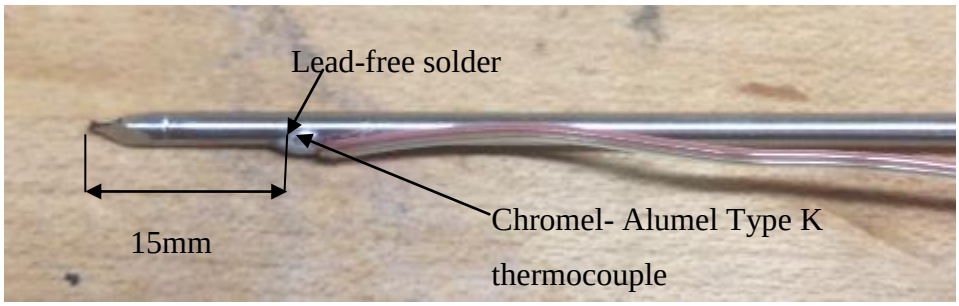

Figure 3.4 External photographic view of the fully instrumented cryoprobe

3.3 Operational Modes

Two types of experiments were performed utilizing the cryoprobe that was described in the foregoing paragraphs. In the first type, to be designated as Experiment I, the exterior surface of the probe was swathed in insulation. As shown in Figure 3.5, the insulation was in two sections. The forward part, which enveloped the probe proper, consisted of several layers of bubble wrap, whereas as the rearward part was a rubber sleeve. A

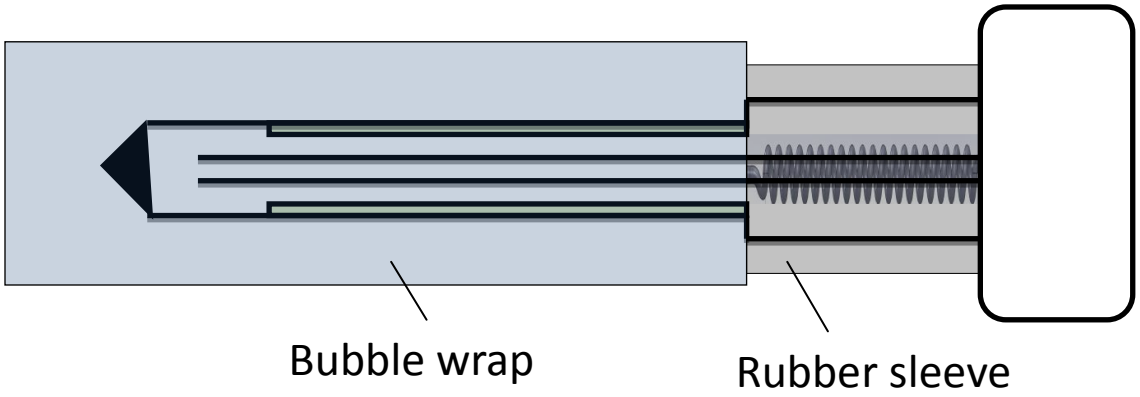

Figure 3.5 Configuration of the probe for Experiment I

photograph of the probe configuration for Experiment I is pictured in Figure 3.6.

Figure 3.6 Photograph of the probe configuration for Experiment I

Experiment II involved the use of a gel as a surrogate for human tissue. For this experiment, the insulations for Experiment I were removed. Additionally, the thermocouple that had been used to determine the temperature of the inlet tube just upstream of the probe proper was removed. Instead, a surface-mounted thermocouple was installed at the junction of the conical tip of the cryoprobe (T_1) and its mating cylindrical surface. A photograph of the surface mounted thermocouples for Experiment II is presented in Figure 3.7.

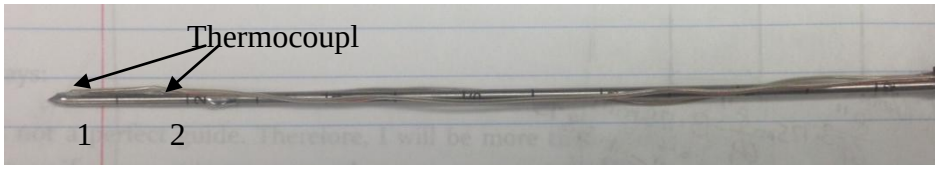

Figure 3.7 Photograph of surface mounted thermocouples for Experiment II

The test setup for Experiment II is pictured schematically in Figure 3.8. The cryoprobe proper is immersed in a beaker containing ultrasound gel, a medium that has seen frequent use as a surrogate for human tissue, and its thermophysical properties are well known. The beaker of rectangular planform served to enable the freezing process to be observed without distortions that are associated when viewing through a curved surface. The dimensions of the beaker are 20cm x 17cm in cross section and 17cm in height. The beaker was partially filled with the surrogate medium to a height that enabled the probe proper to be fully immersed.

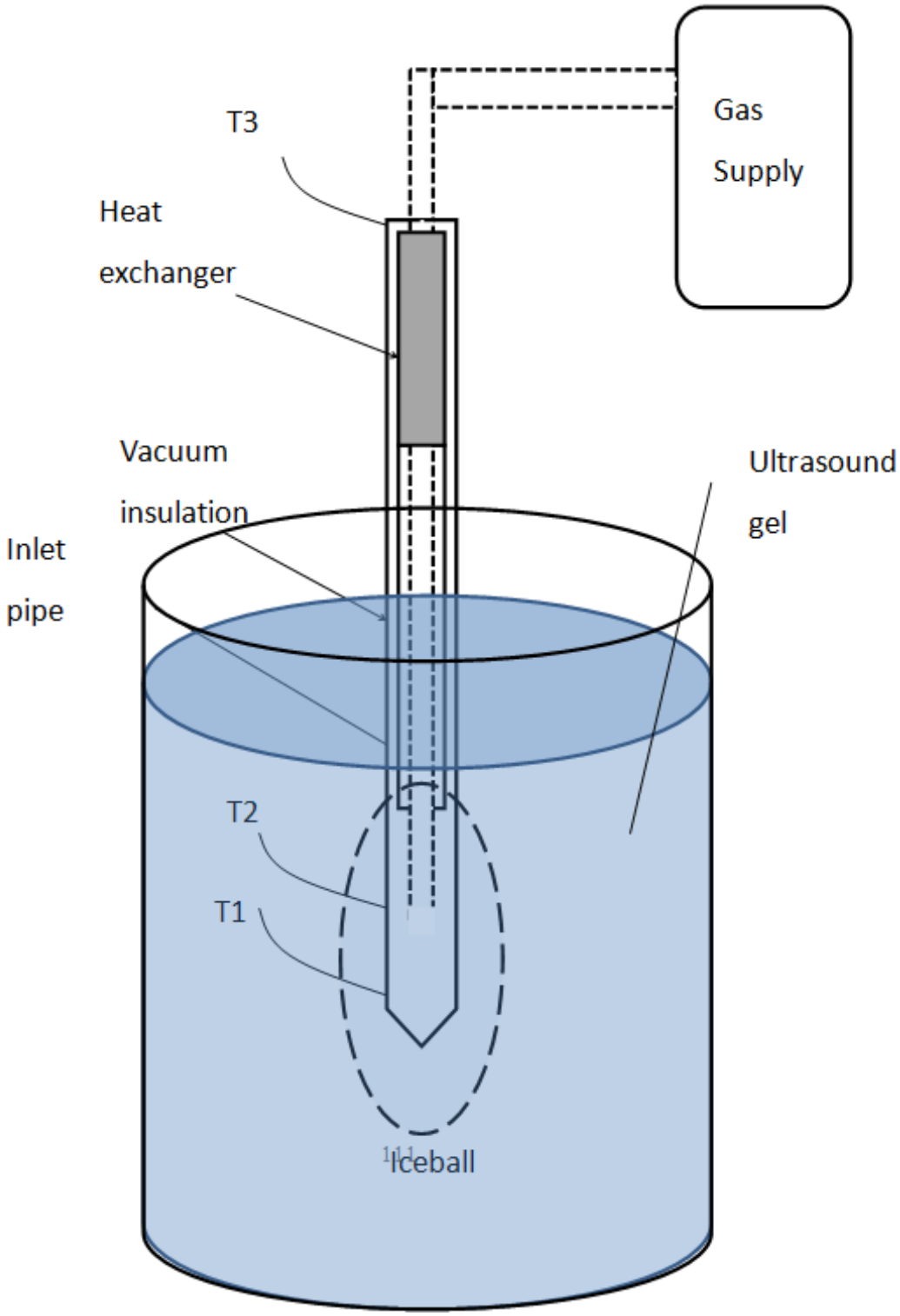
Gas
Supply
T3
Heat
exchanger
Vacuum
insulation
Ultrasound
gel
Inlet
pipe
T2
T1
Iceball

Figure 3.8 Test setup for Experiment II

A photograph of the test setup of Figure 3.8 is displayed in Figure 3.9.

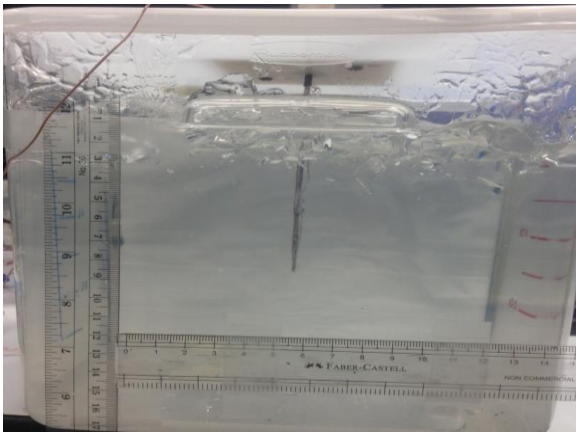

Figure 3.9 Photograph of the test setup of Experiment II

3.4 Experimental Procedure

3.4.1 Experiment I

The goal of the experiment was to determine steady-state temperatures at the thermocouple locations 1 and 2 that are identified in Figure 3.2(e). Thermocouple location 3 was not monitored because it is situated outside of the domain that used for the subsequent numerical simulations.

A number of preparatory steps were executed prior to the initiation of the experiments. A pressure regulator controls the flow of argon gas into the cryoprobe. Although the available argon gas is listed as 99.99% pure, there are residual impurities and condensables present to cause contamination problems during operation of the probe. These impurities caused a blockage in the expansion space just downstream of the exit of

the inlet tube. Another potential cause of blockage somewhere in the system is related to the fact that the apparatus was open to the surrounding ambient prior to its final assembly. In the likely event that ambient air had penetrated the apparatus, any humidity in that air would be subject to condensation when it interacted with low-temperature argon.

To overcome the possible blockages, a purge procedure was performed prior to the beginning of the final data runs. The purging is performed by introducing argon into the apparatus at a pressure of 100-200psi above ambient and maintaining this argon flow for approximately five minutes. This pressure is sufficiently high to sweep all blockage media out of the apparatus. The total extraction of blockage media was identified by a change in the sound of the argon as it passed through the system. At the conclusion of the purge procedure, the temperatures at sites 1 and 2 were virtually identical and equal to 24 ^{o}C. These temperatures at the were monitored by means of a HH309A Omega Data Logger Thermometer as shown to the right.

The completion of the purge process corresponded to a slow manual change in the argon control valve which ultimately resulted in a pressure of 3500psi. Subsequently, temperatures were monitored every second during the duration of the data run. A steady- state was attained in about four minutes as indicated by the temperature measurements. The steady-state temperatures at sites 1 and 2 were -150.8 and -110.1^{o}C, respectively.

3.4.2 Experiment II

Experiment II closely represented the operation of the cryoprobe in biomedical applications. The major deviation from reality was the use of a surrogate to replace human tissue. The preparatory purge procedure was executed as described for Experiment I. It was performed on the bench top prior to the installation of the cryoprobe in the surrogate medium. At the conclusion of the purge, the probe assembly was introduced into the surrogate bath and secured in place. This setup, which was completed in approximately five minutes, is shown in Figure 3.10. As seen in the figure, a stopwatch

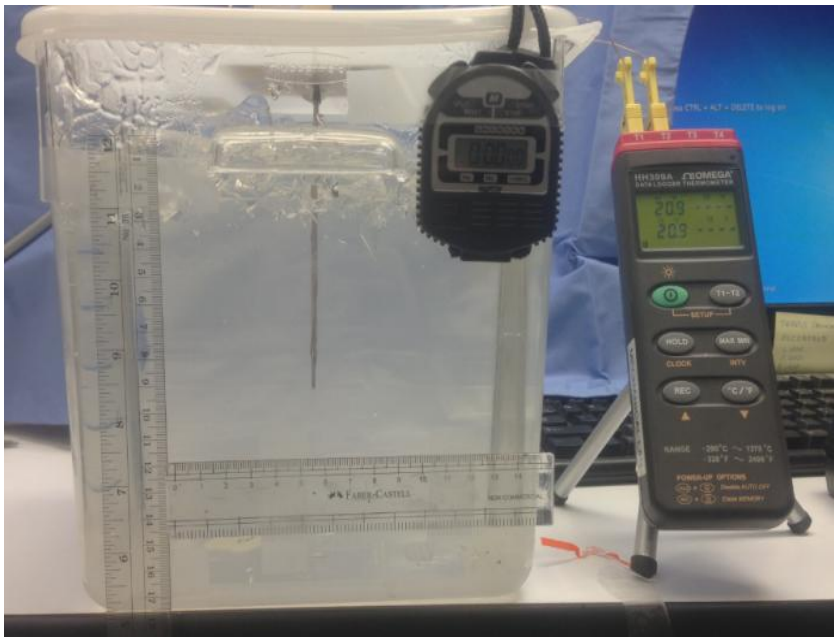

Figure 3.10 Setup for Experiment II

and a temperature data logger were put in place to enable convenient simultaneous observation of the instruments and the iceball formation that was in progress.

To initiate the experiment, the pressure was ramped up to 3500psi and the temperatures were recorded at every second at sites 1 and 2. The cooling of the cryoprobe creates an ice layer over its surface. This layer gradually grows thicker and ultimately achieves a

steady state that depends on the balance between the supply of refrigerant from the cryoprobe on one hand and of the heat extracted from the surrounding medium. The attainment of the steady state was validated by the constancy of measured temperatures. Approximately four minutes were required for the achievement of the steady state. The steady state temperatures were -112 .6 and - 127.3^{o}C at sites 1 and 2, respectively.

3.5 Results

3.5.1 Experiment I

The temperature data collected during the duration of the Experiment I are displayed in Figure 3.11. The figure conveys a graph of temperature as a function of time at the locations 1 and 2. It is seen that there is a start-up transient which eventually leads to a steady state at about 200 seconds of operation. The steady-state temperatures are T_1 = -150.6 and T_2 = -110.1^{o}C. These results will be used later in connection with the numerical simulations.

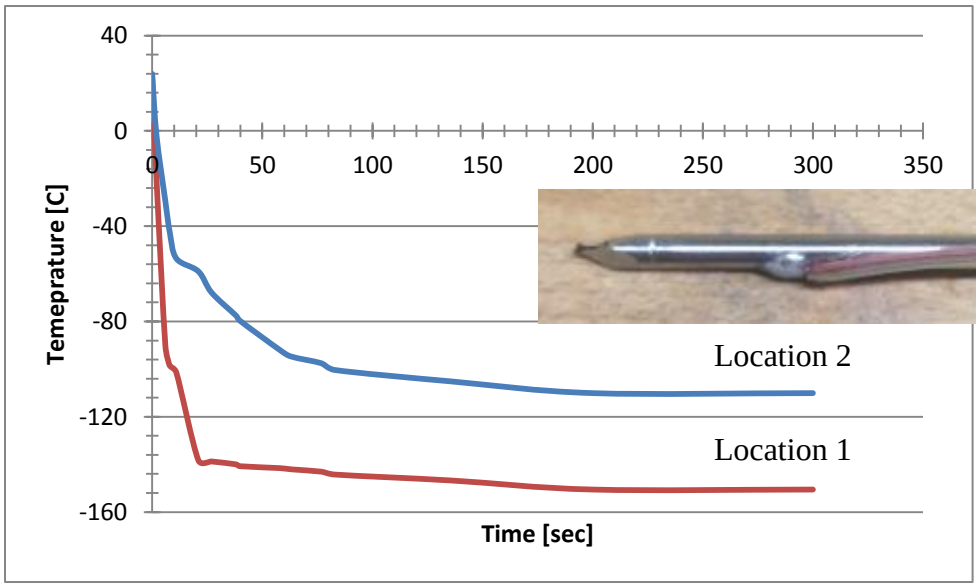

Figure 3.11 Temperature vs. time data at locations 1 and 2 for Experiment I

3.5.2 Experiment II

The motivation for Experiment II is to have a means of determining the evolution of the volume of the iceball during the freezing process. The selected means was based on photographic evidence collected at every second during the duration of the experiment. A post-processing procedure developed to quantify the coordinates of the outer surface of the iceball. For this purpose, a typical photograph, that corresponding to 30 seconds duration after the initiation of the experiment, will be used to describe the step-by-step processing procedure.

Figure 3.12 was extracted from a video of the events that occurred during the entire course of the experiment. Inspection of that photograph provides a moderately clear definition of the shape of the solidified region. Careful inspection, however, indicates that the lighting was not uniform, so that the instantaneous location of the left edge of the iceball was better defined than that of the right edge. The iceball was magnified, and then a procedure was undertaken to try to make the edges of the iceball sharper. The first attempt consisted of varying the gray scale and the brightness of the photograph. The result of this work is exhibited in Figure 3.12.

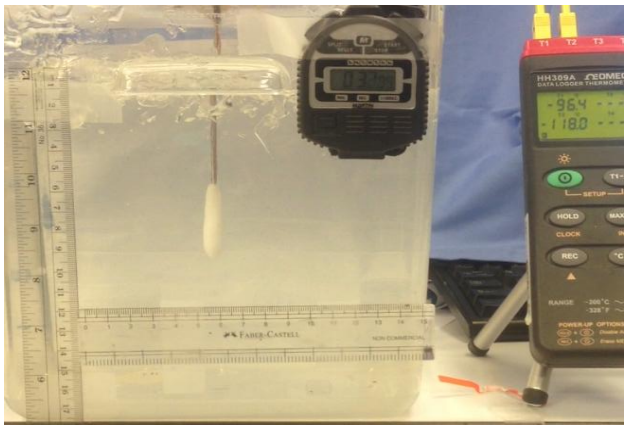

Figure 3.12 Photograph of the experimental setup at 30 seconds subsequent to the initiation of the experiment

Figure 3.13 conveys three levels of information. At the left is shown the iceball at a moderate stage of enlargement. Subsequent to this stage, further enlargement was performed and a square grid was overlaid. That grid provided a means for quantitative evaluation of the coordinates of the left-hand boundary of the iceball. The vertical and horizontal coordinates are determined by inspection of the figure. Clearly, it was not possible to get similar data for the right-hand boundary. The coordinate information was then plotted as the blue diamond symbols on the graph in the right side of the figure. It can be seen that there is a considerable length of the iceball surface whose boundary is almost vertical, flanked by receding thicknesses both above and below. At this point, it was decided that this procedure was too dependent on human perception and that a more objective approach was necessary.

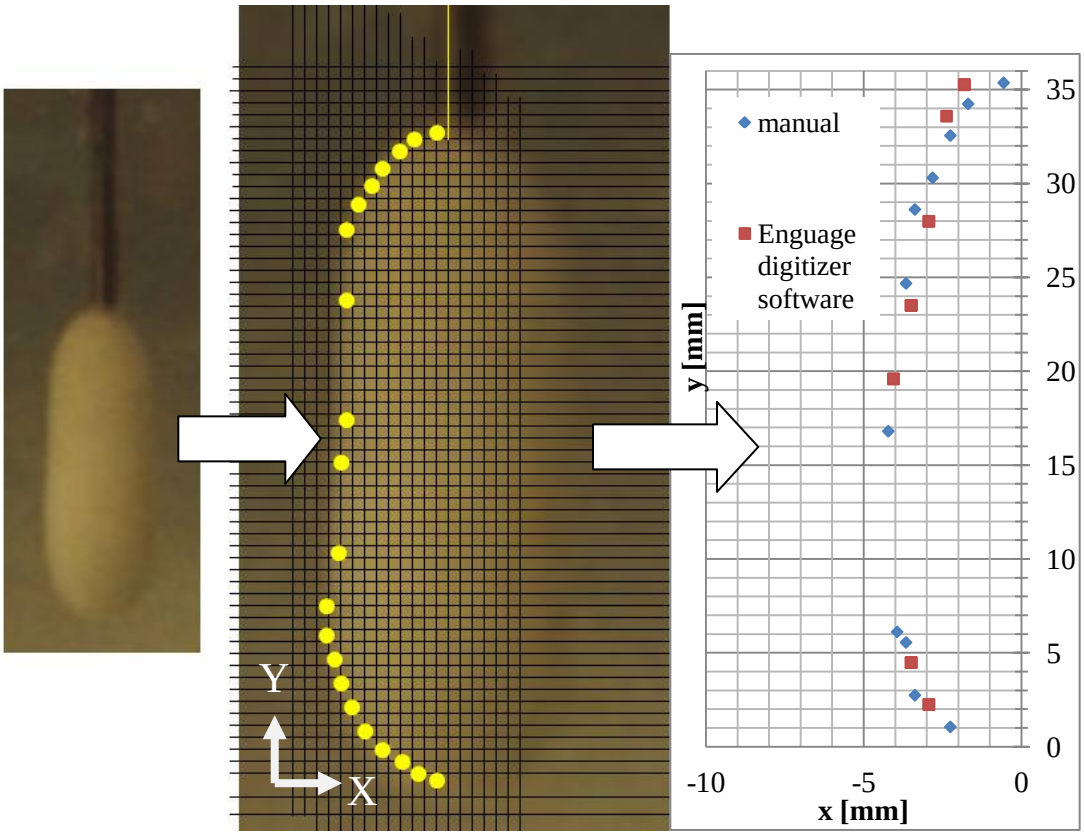

Figure 3.13 Display of the first procedure for determining the coordinates of the edge of the iceball

The selected objective procedure was based on already existing open-source software Engauge Digitizer. A main feature of that software is the capability of highlighting significant features by manipulation of color at a far more sophisticated level than gray scales and brightness. A photograph of the iceball surface after being subjected to color manipulation is presented in Figure 3.14. It can be seen that the color manipulation is successful in producing sharp edges at both the left and the right edges of the iceball.

In order to achieve high accuracy in determining the coordinates of those edges, the view shown in Figure 3.14 was enlarged by a factor of 500. The edge coordinates of the enlarged image are read automatically by the software. Those coordinates are recorded as

the red data symbols in Figure 3.13. Inspection of the figure indicates satisfactory agreement between the two means of data extraction. It is the opinion of the writer that the digitally processed information is more accurate.

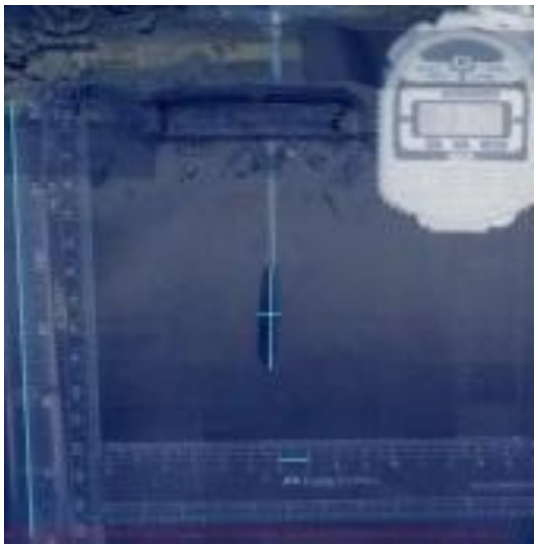

Figure 3.14 Color-altered form of the iceball at 30 seconds

The foregoing procedure was applied at times t = 0, 30, 60, 90, 120, 150, 300 and 595 seconds. The subsequent pictures of the iceball surfaces are seen in Figure 3.15-22.

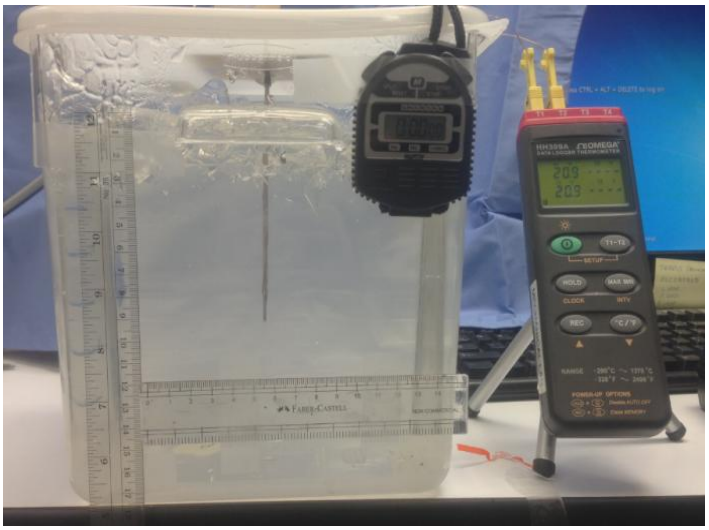

Figure 3.15 Photograph of the experimental setup at 0 seconds

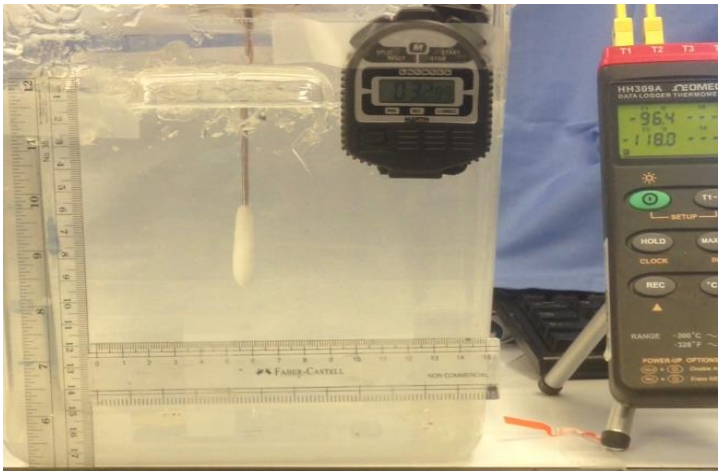

Figure 3.16 Photograph of the experimental setup at 30 seconds subsequent to the initiation of the experiment

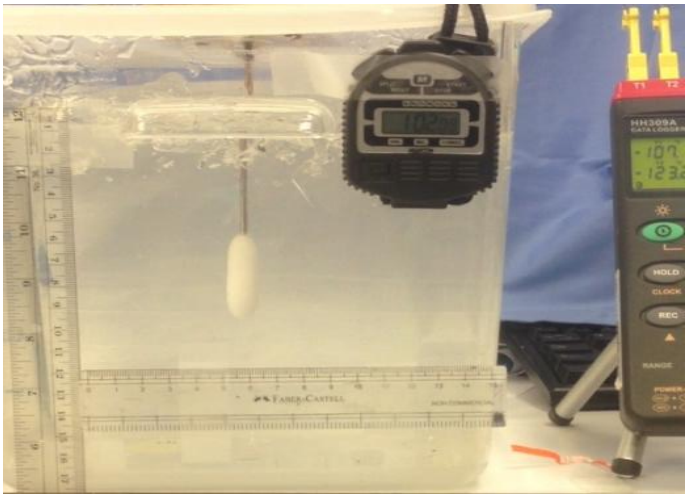

Figure 3.17 Photograph of the experimental setup at 60 seconds subsequent to the initiation of the experiment

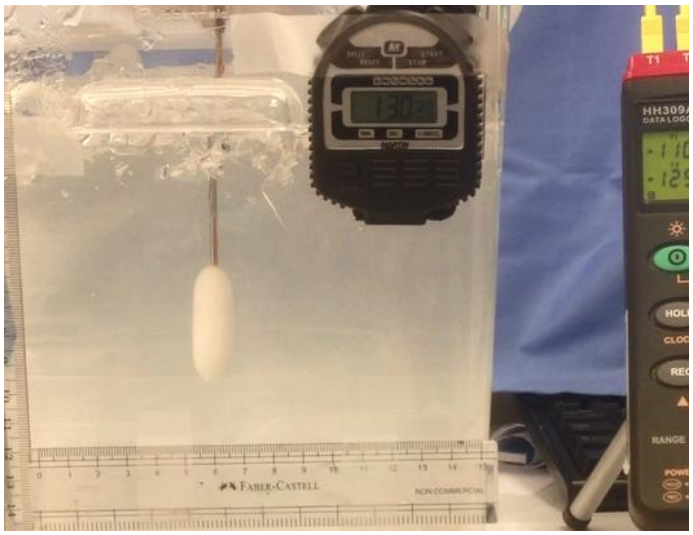

Figure 3.18 Photograph of the experimental setup at 90 seconds subsequent to the initiation of the experiment

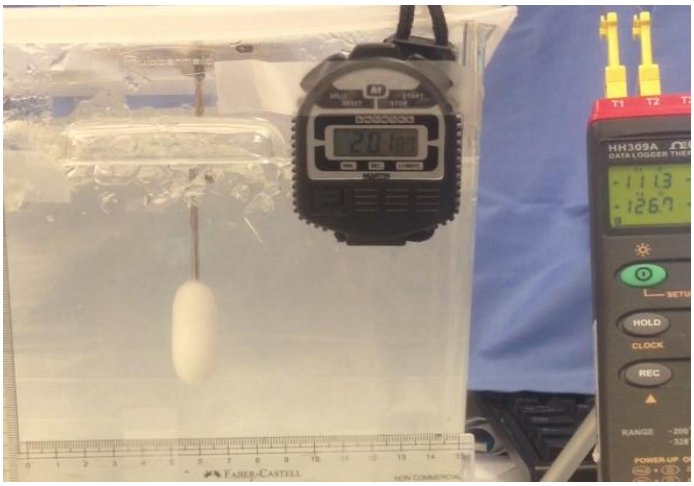

Figure 3.19 Photograph of the experimental setup at 120 seconds subsequent to the initiation of the experiment

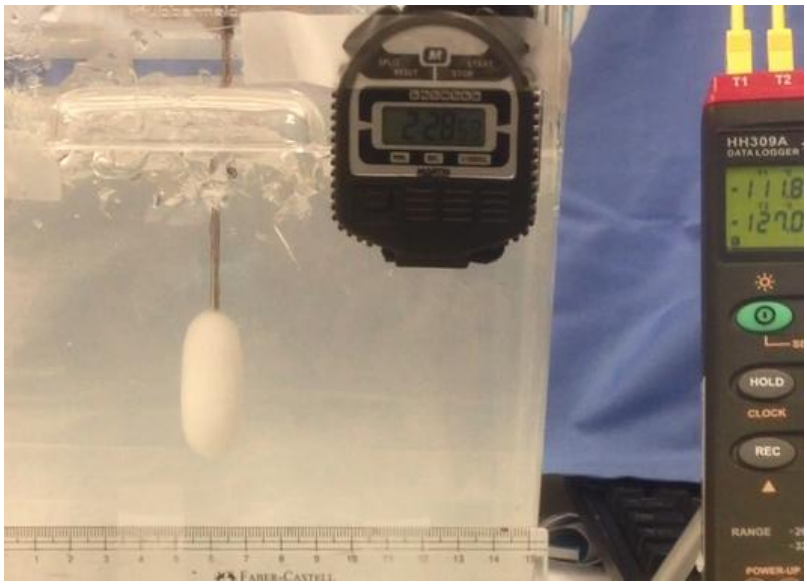

Figure 3.20 Photograph of the experimental setup at 150 seconds subsequent to the initiation of the experiment

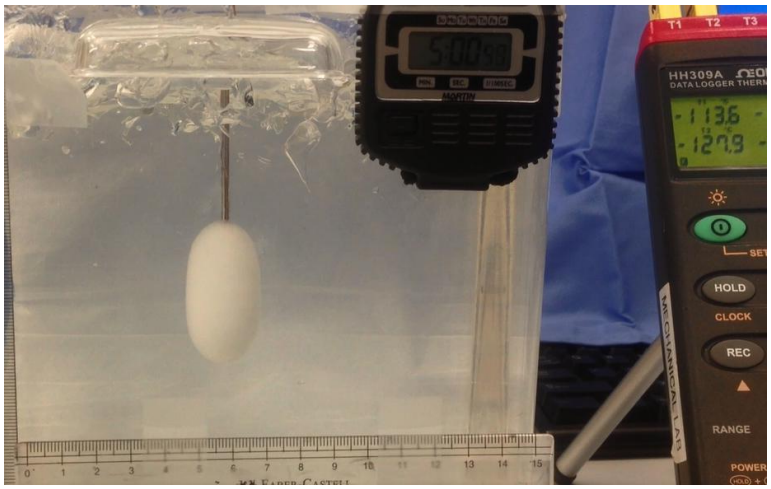

Figure 3.21 Photograph of the experimental setup at 300 seconds subsequent to the initiation of the experiment

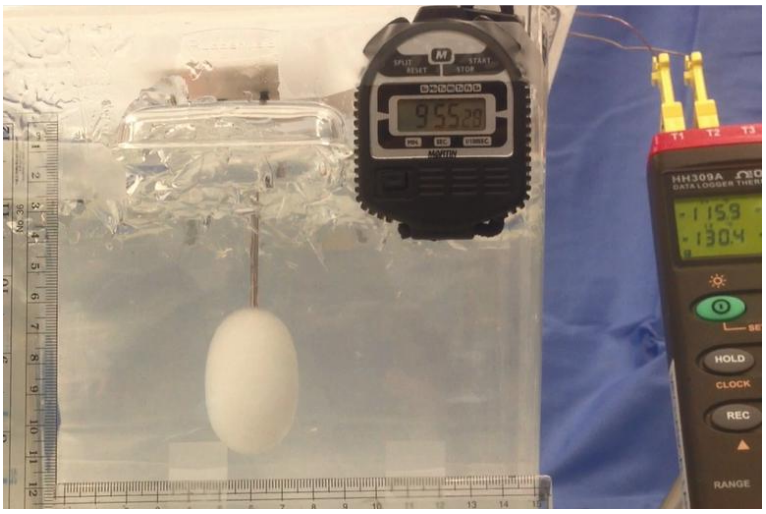

Figure 3.22 Photograph of the experimental setup at 595 seconds subsequent to the initiation of the experiment

The coordinates of the iceball surfaces at those times are displayed from left to right in Figure 3.23. The growth of the iceball is sharply delineated in these figures. Globally, the height of the iceball changes only slightly with the passage of time, while its lateral dimensions increase monotonically. In geometric terms, the iceball shape may be regarded as an ellipsoid whose major axis is relatively unchanged with time while its minor axis achieves a significant growth.

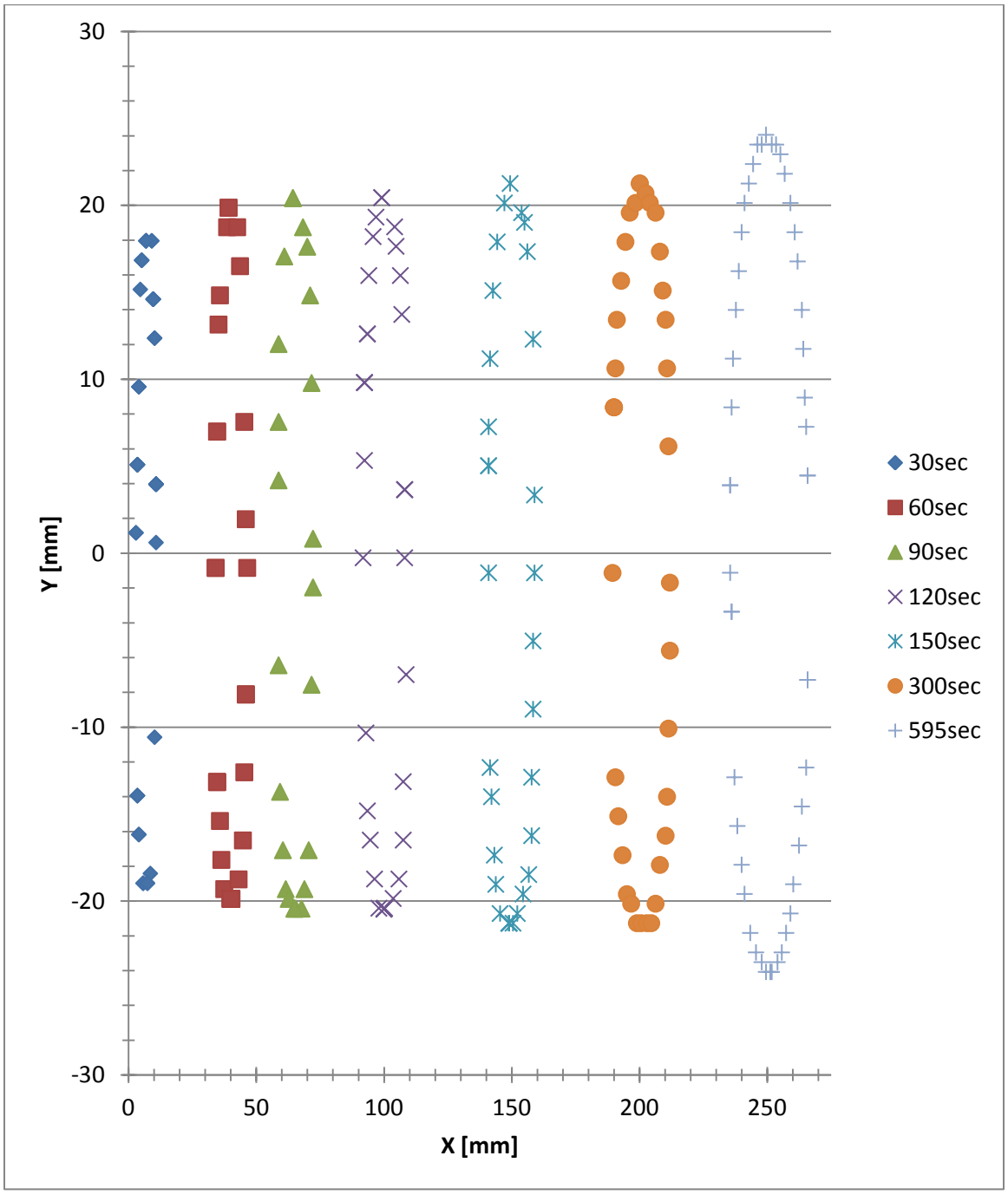

Figure 3.23 Iceball surface cooridnates at 30, 60, 90,120, 150, 300 and 595 seconds

The temperature data collected during the duration of the Experiment II are displayed in Figure 3.24. The figure conveys a graph of temperature as a function of time at the locations 1 and 2. It is seen that there is a start-up transient that eventually leads to a steady state at about 200 seconds of operation. These results will be used later in connection with the numerical simulations.

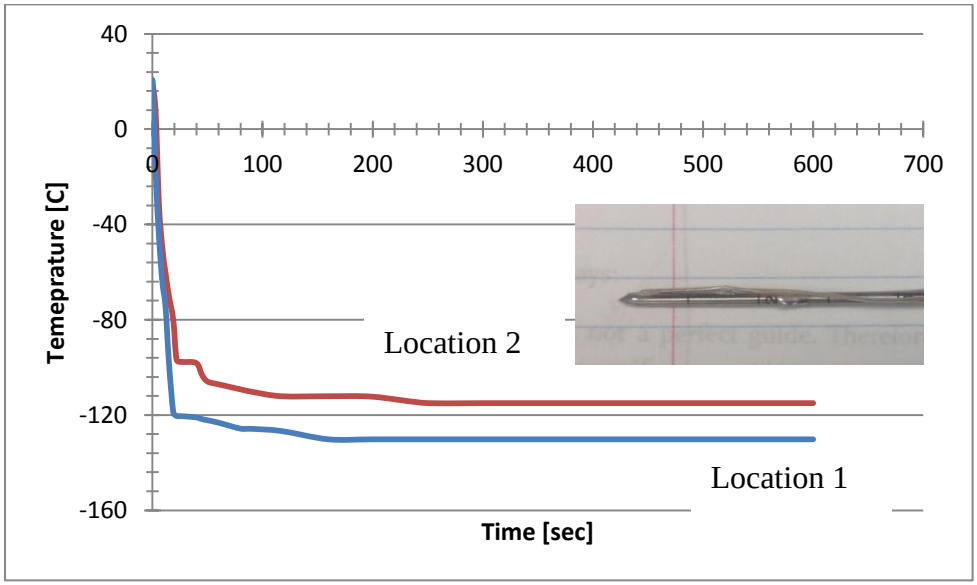

Figure 3.24 Temperature vs. time data at locations 1 and 2 for Experiment II

Chapter 4 Cryoprobe Simulations

4.1 Introduction

The foregoing experiments represent one portion of a synergistic study of the performance of a cryoprobe equipped with a straight delivery tube. The other portion of the study is the numerical simulations that are set forth in this chapter. To enable a definitive comparison between the experimental and simulation results, the geometry of the simulated cryoprobe was made identical to that of the experimental apparatus. Simulations were performed for both the situations of Experiments I and II.

The fluid flow and heat transfer processes which occur within the cryoprobe are governed by Eqs. (2.1) through (2.9). These equations are sufficient to solve the limiting case in which the outer bounding walls of the cryoprobe are assumed to be adiabatic. However, for the situation in which the cryoprobe is immersed in a phase change medium, these equations must be coupled with those which are needed to describe the thermal processes that govern the formation of the iceball.

The heat conduction within the iceball is governed by

$$\frac{\partial(cT)}{\partial t} = \frac{\partial}{\partial x_i}\left(k\frac{\partial T}{\partial x_i}\right) \tag{4.1}$$

in which c is the specific heat of the solidified medium and k is its thermal conductivity. Information was available for the variations of both c and k with temperature [Satish paper]

4.2 Physical models

4.2.1 Model Corresponding to Experiment I

The physical model used for the numerical simulation of Experiment I is shown in Figure 4.1. It can be seen from the figure that axisymmetry has been assumed. As a consequence, the solution domain can be restricted to the space contained within the red dashed boundary. The solution domain spans the longitudinal space between the fluid inlet at the left and the tip of the cone of the probe at the right. Of significance for the simulation model is the adiabatic boundary condition which is extended over the entire external surface of the apparatus. The locations of the two thermocouples that were affixed to the cryoprobe for the experimental work are indicated by the blue circles. The forward most of the thermocouples is designated by the temperature T_1 and that at the exit of the spent argon is labeled T_2. For the simulations, two models were employed for the thermal characteristics of the wall of the delivery tube. In one case, the wall was accorded its actual thermal conductivity, while in the second, the thermal conductivity was set equal to zero. The motivation for performing such a computational experiment was to study the effect of heat transfer between the incoming argon flow in the delivery tube and the outgoing spent argon flowing in the annulus. The root of this experiment was to examine one of the tenets of the Joule-Thomson effect. In its purest form, the Joule-Thomson effect is designated as being applicable to an adiabatic flow.

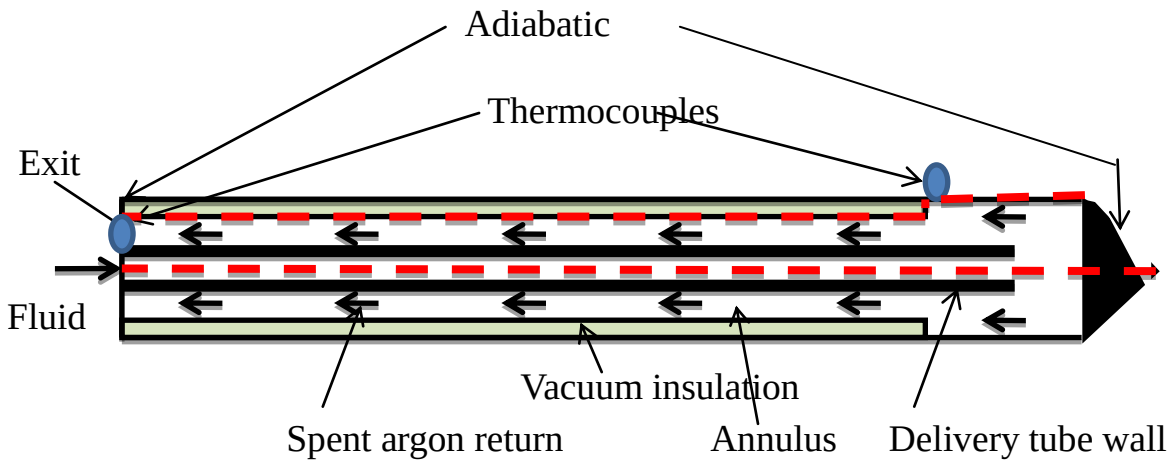

Figure 4.1A physical model for numerical simulation of Experiment I

4.2.2 Model Corresponding to Experiment II

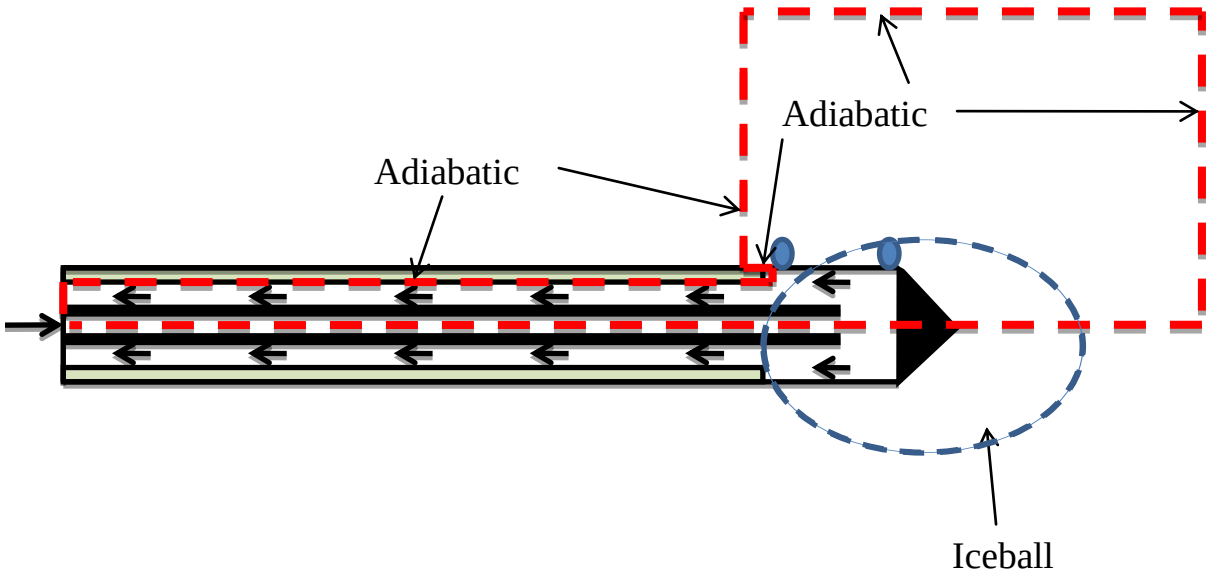

Figure 4.2 A physical model for numerical simulation of Experiment II

The geometric model of Experiment II is displayed in Figure 4.2. This figure maintains some of the features that were shown in Figure 4.1, but there are a number of important differences. The most significant change is in the nature of the solution domain. In order

to account for the phase change in the surrounding medium, the solution domain had to be extended into the space occupied by that medium. Furthermore, to avoid a situation in which the solution domain boundaries would have to be altered with the passing of time due to the growth of the iceball, the domain was extended far into the liquid phase of the medium. As a consequence, the expanding iceball was contained well within the solution domain. Another consideration in the selection of the solution domain is the need to apply realistic boundary conditions to its surface. It was reasoned that if the boundaries of the domain were positioned sufficiently far from the solidification process, those boundaries could be modeled as being adiabatic.

The external surface of the cryoprobe forward of the zone of vacuum insulation is no longer adiabatic as was the case in Experiment I. Rather, heat conduction across the outer wall of the probe and within the cone were fully taken into account. A significant point to be noted is that the nature of the present simulation did not require the specification of values of a heat transfer coefficient, as was true in some of the previous investigations of the performance of cryoprobes.

4.2.3 Meshing

For the purpose of this study, the fluid flow and heat transfer were modeled as being axisymmetric so that it was not necessary to extend the solution domain across the entire cross section of the probe. In fact, it is sufficient to select a pie-like wedge and focus on solving the relevant equations in that wedge. For the calculations in question, a wedge with a two-degree opening angle was selected, and the approximately 9,900,000 nodes were deployed in that wedge. A representative display of a portion of the mesh is seen in the following figures. The mesh density is higher closer to the wall and so it is difficult to distinguish from the figures. To enable a better display of the mesh, the mesh in particular zones has been magnified, and Figure 4.3 displays the different sections of the probe where the mesh will be exhibited.

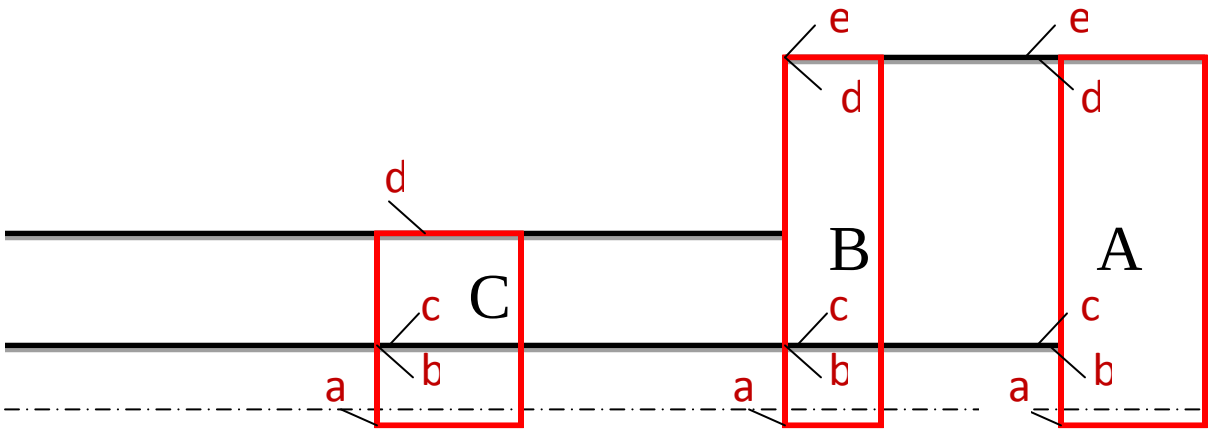

Figure 4.3 Axisymmetric cross sectional view of the 2 degree wedge of the cryoprobe

Figure 4.4 represents section A of Figure 4.3. The mesh shown here is in the expansion region of the cryoprobe just downstream of the delivery tube. In order to capture the shock waves in the immediate vicinity of the exit of the delivery tube, a finer mesh was deployed in that region. The figure also indicates the direction in which the bias was introduced while deploying the nodes. The mesh is so fine that it was deemed appropriate to rotate it by 90 degrees to enable a more advantageous orientation for discerning the details. Note the letters a, b,…, e. These identify locations at the left hand edge of the section A in Figure 4.3. These same letters appear at the upper edge of section A as it is displayed in Figure 4.4. The use of this nomenclature enables easy reference to the geometry of the mesh of Figure 4.4.

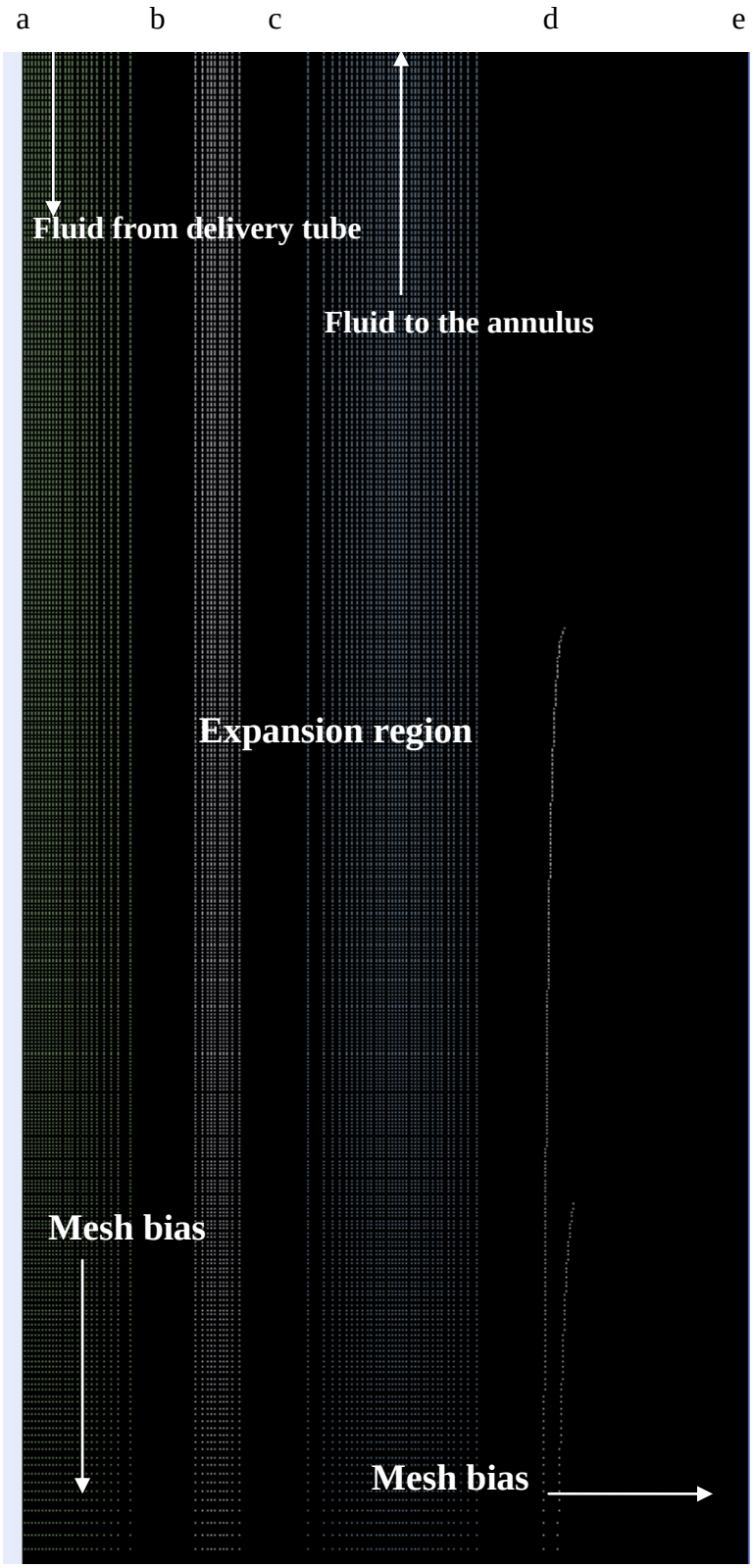
a
b
c
d
e
Fluid from delivery tube
Fluid to the annulus
Expansion region
Mesh bias
Mesh bias

Figure 4.4 Mesh for section A

Figure 4.5 shows the mesh in section B of Figure 4.3. The mesh is seen to be finer in the region close to the wall. A large bias was introduced in the nodal deployment seen in the dark sections of the figure. The a,b, …, e symbols have the same meaning as before

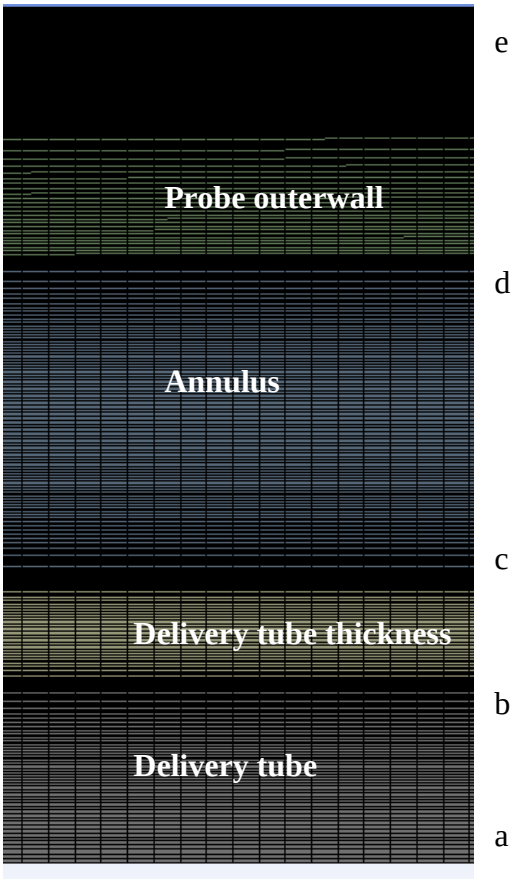

Figure 4.5 Representative mesh for section B

Figure 4.6 displays the mesh in section C of Figure 4.3. This section cuts across both the delivery tube and the return-flow annulus. Note that the mesh is considerably finer adjacent to the bounding walls relative to that at locations away from the walls.

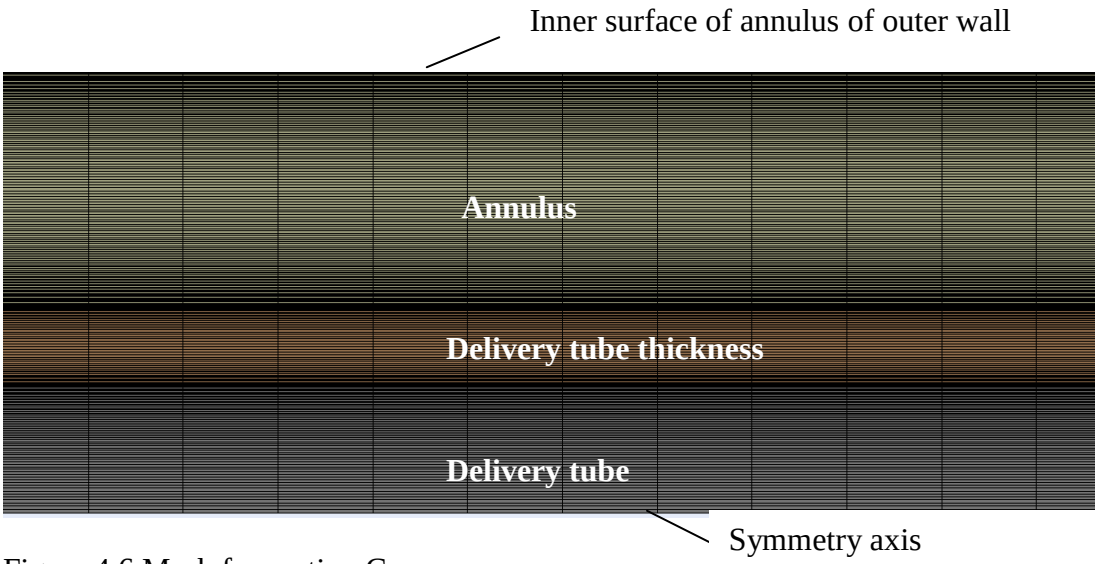

Figure 4.6 Mesh for section C

4.3 Results for Adiabatic Outerwall of Cryoprobe

The first set of results that were extracted from the numerical simulations is those that correspond to an adiabatic outer wall of the cryoprobe. It is expected that the temperatures obtained from these solutions would be lower than those for the case in which an iceball was formed on the probe surface. In effect, the results presented in this section of the report correspond to a lower bound on the temperature field.

The quantities of physical interest include the temperature distribution on the outermost wall of the cryoprobe proper. Three different turbulence models, SST, k-ε, and RNG k-ε, discussed in the preceding sections were implemented for this study. Figure 4.7 shows a comparison of the temperature of the fluid adjacent to the outer wall of the probe using three different turbulence models. The outcomes of both the models are in close agreement with each other. The temperature distributions are essentially uniform ~-150C . A small variation is seen in the temperature of the fluid in the expansion region and the region close to the beginning of the vacuum insulation.

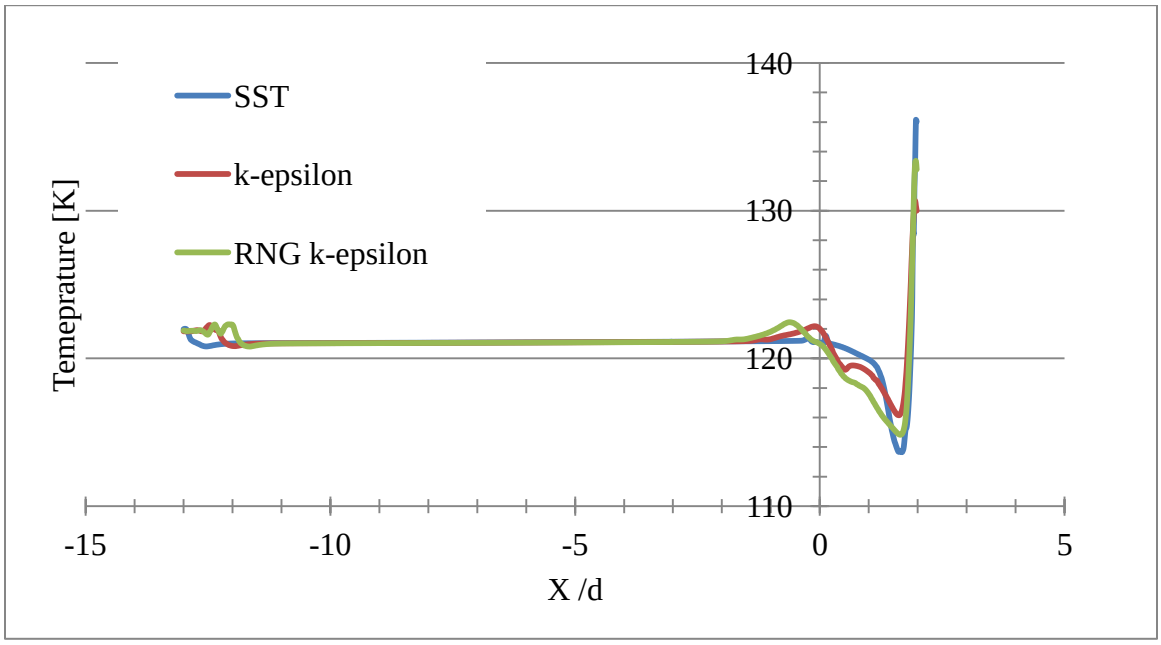

Figure 4.7 Temperature distribution on the outerwall of cryoprobe

A similar comparison was made for the bulk temperature of the argon gas flowing through the delivery tube as a function of the axial distance as seen in Figure 4.8.

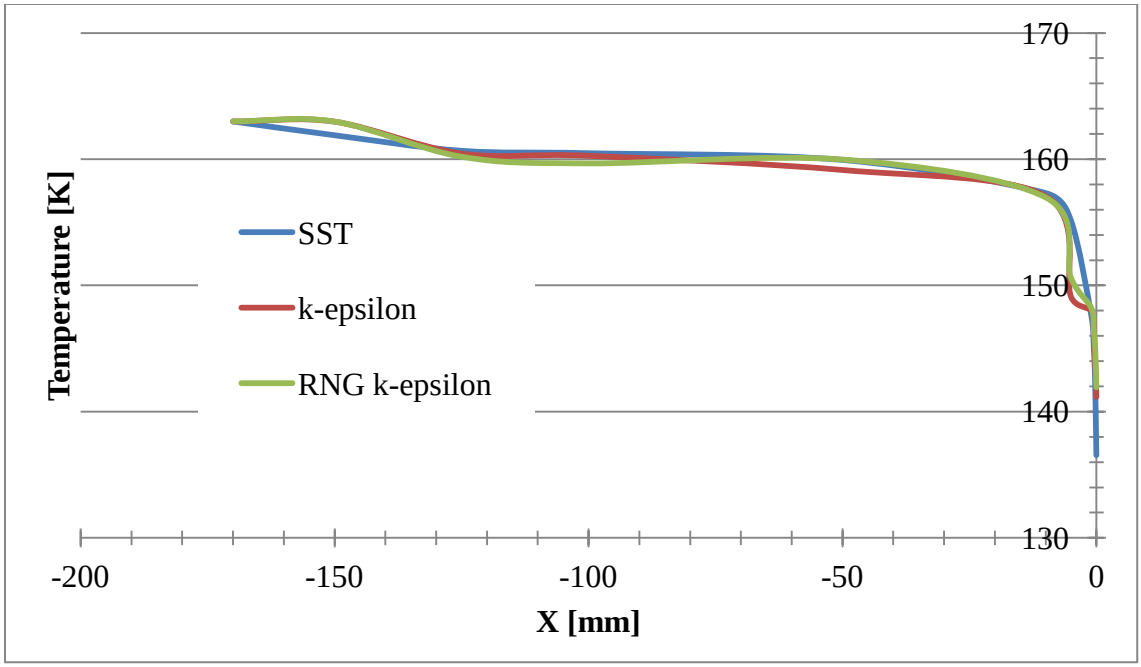

Figure 4.8 Bulk temperature of the argon gas flowing through the delivery tube

The temperatures on the outer surface of the probe that correspond to the adiabatic boundary condition are presented in Figure 4.9. In this figure, the surface temperature is plotted against the dimensionless axial coordinate X/d, where d is the inner diameter of the outer wall of the probe, and the origin of X is at the downstream end of the delivery tube. The location X/d = -13 corresponds to the downstream end of the vacuum insulation section. The end of the expansion space is at X/d = 2, and the cone is extended downstream from that location. The figure consists of both a graph and a color contour diagram. It is also relevant to note that the entire range of temperatures displayed in the figure is approximately 9C, so that the situation is virtually isothermal.

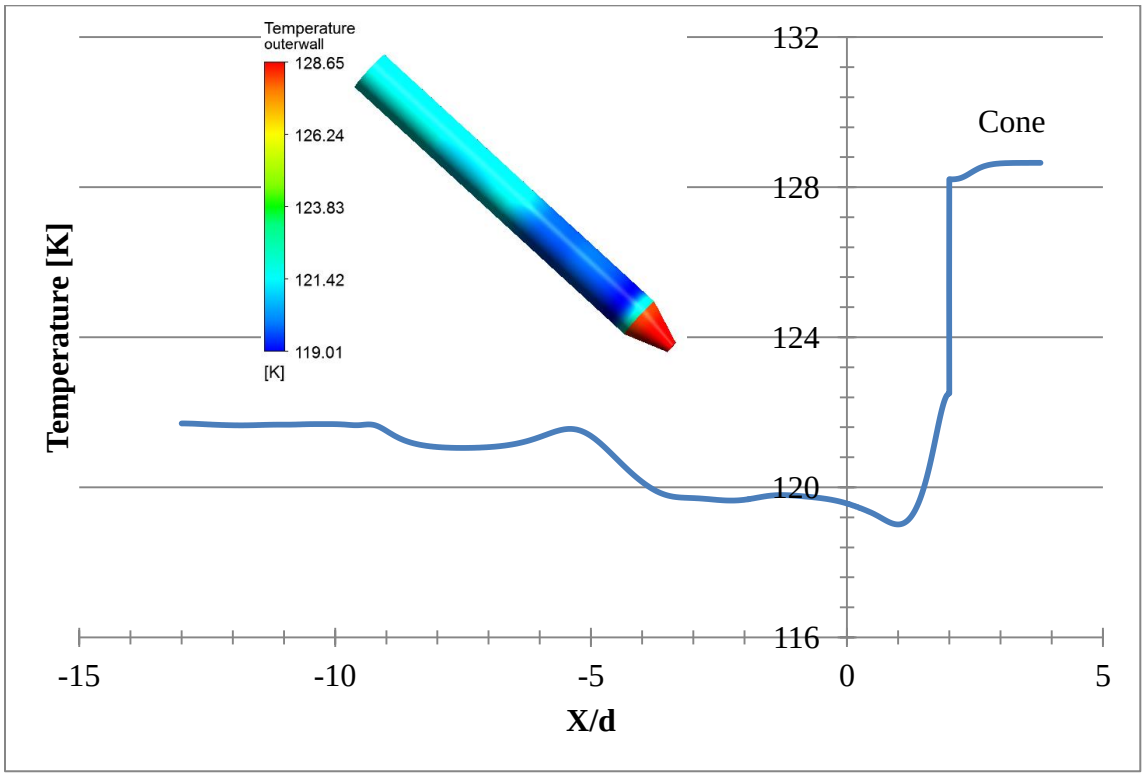

Figure 4.9 Color diagram of the temperatures on the outer surface of the probe and a corresponding graphical display

The temperature distribution in the fluid adjacent to the outer wall of the probe is displayed in Figure 4.10. It can be seen from the figure that the temperature is essentially uniform (-150C) from the insulation space to the expansion tube end. Downstream of the exit of the delivery tube, in the expansion space, a complex flow pattern is encountered which gives rise to a rapid drop in the fluid temperature followed by an even sharper increase.

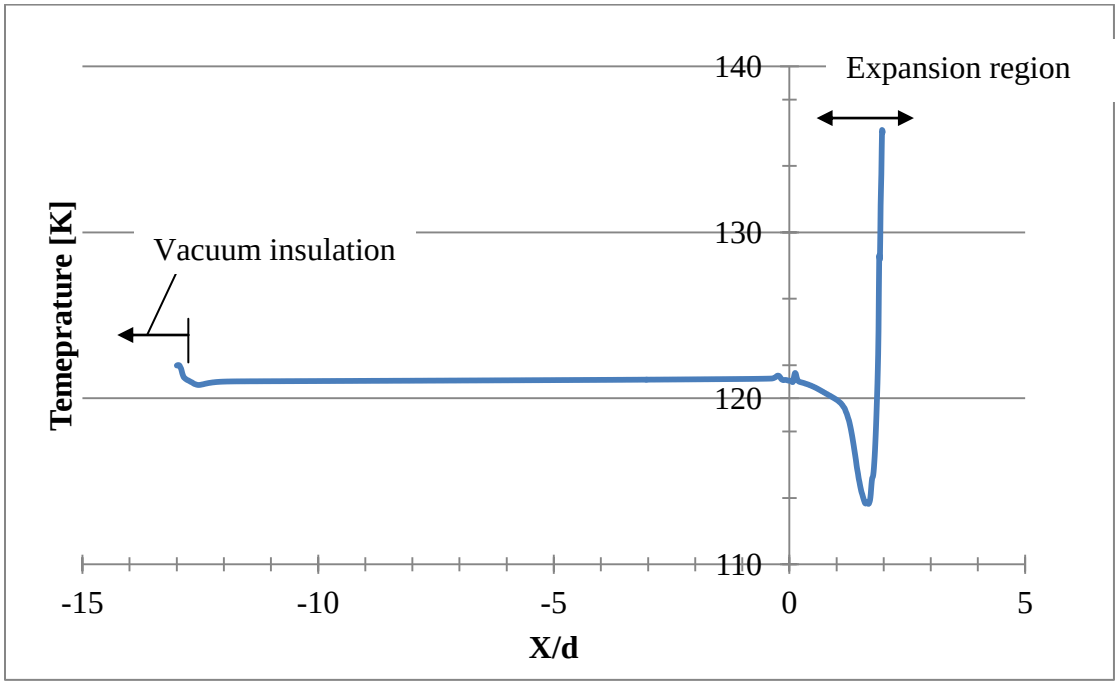

Figure 4.10 Temperatures of the argon adjacent to the probe wall

The next result to be presented relates to the effect of heat conduction between the fluid in the delivery tube and that in the return-flow annulus. The motivation for this consideration is that the traditional Joule-Thomson effect is restricted to adiabatic flow, and there may be heat transfer in the present situation. Figure 4.11 displays the axial variation of the bulk temperature in the delivery tube fluid both in the presence and absence of cross conduction between the two fluids. Observation of the figure clearly shows that any heat conduction is of negligible significance.

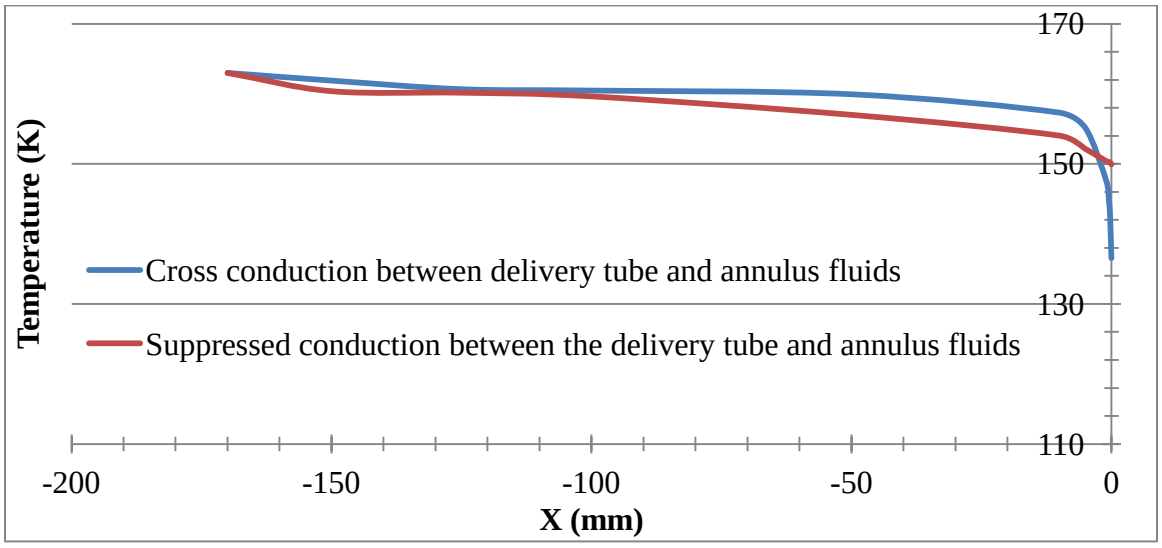

Figure 4.11 Bulk temperature of the fluid in the delivery tube corresponding to: (a) cross conduction between the fluids in the delivery tube and in the return-flow annulus and (b) suppressed cross conduction

Since the problem involves high-speed compressible flow, the Mach number distribution is of particular relevance. The flow exiting the delivery tube enters an enlarged space and undergoes a sequence of shocks. The Mach number distribution along the axis of the probe is displayed in Figure 4.12. An overview of this figure indicates that the flow field is partitioned into a sequence of shocks which give rise to an undulating Mach number distribution where M > 1. Only at the downstream end of the expansion zone does the Mach number decrease sharply as the flow impinges on the wall of the cone.

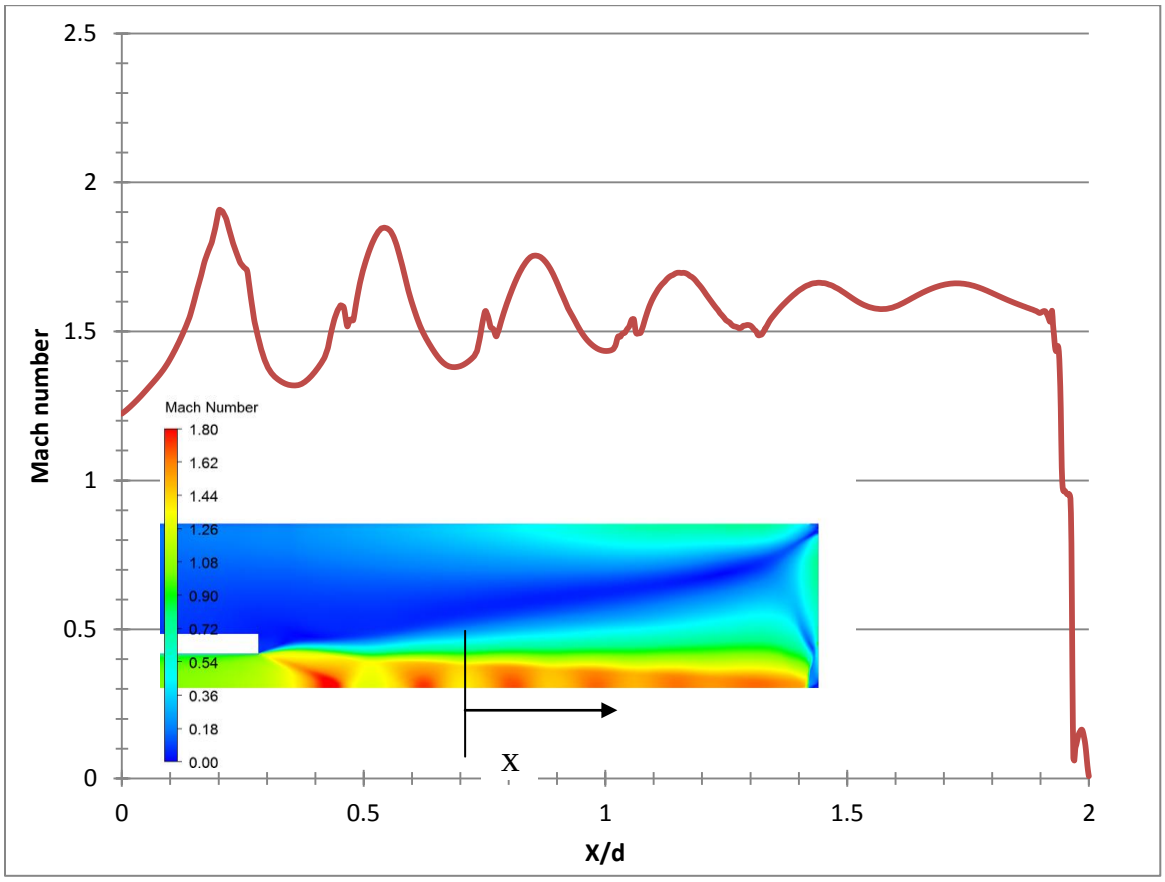

Figure 4.12 Color contour diagram of the Mach number distribution and graphical display of the variation of the Mach number along the axis

Evidence of a recirculating flow can be identified by inspecting a vector diagram which is focused on the expansion space. Figure 4.13(a) displays an overall view of the vector field, and Figures (b) and (c) are close ups of selected zones of the expansion space. Attention will first be focused on Figure 4.13(a). Inspection of the figure reveals three large-scale features: (a) a jet that extends downstream of the delivery tube in which the flow is always in the forward direction, (b) a large recirculation zone whose eye is situated adjacent to the blocked end of the expansion space, and (c) a back flow which hugs the upper wall of the expansion space. Figure 4.13(b) enlarges the flow field at the

downstream end of the expansion space. That figure highlights the eye of the eddy and exposes a well-ordered recirculation.

Figure 4.13(c) enlarges the flow field upstream of section B-B of Figure 4.13(a). The lower part of the vector diagram displays the formation of first shockwave, the tail of eddy, and the return flow path close to the outer wall of the probe.

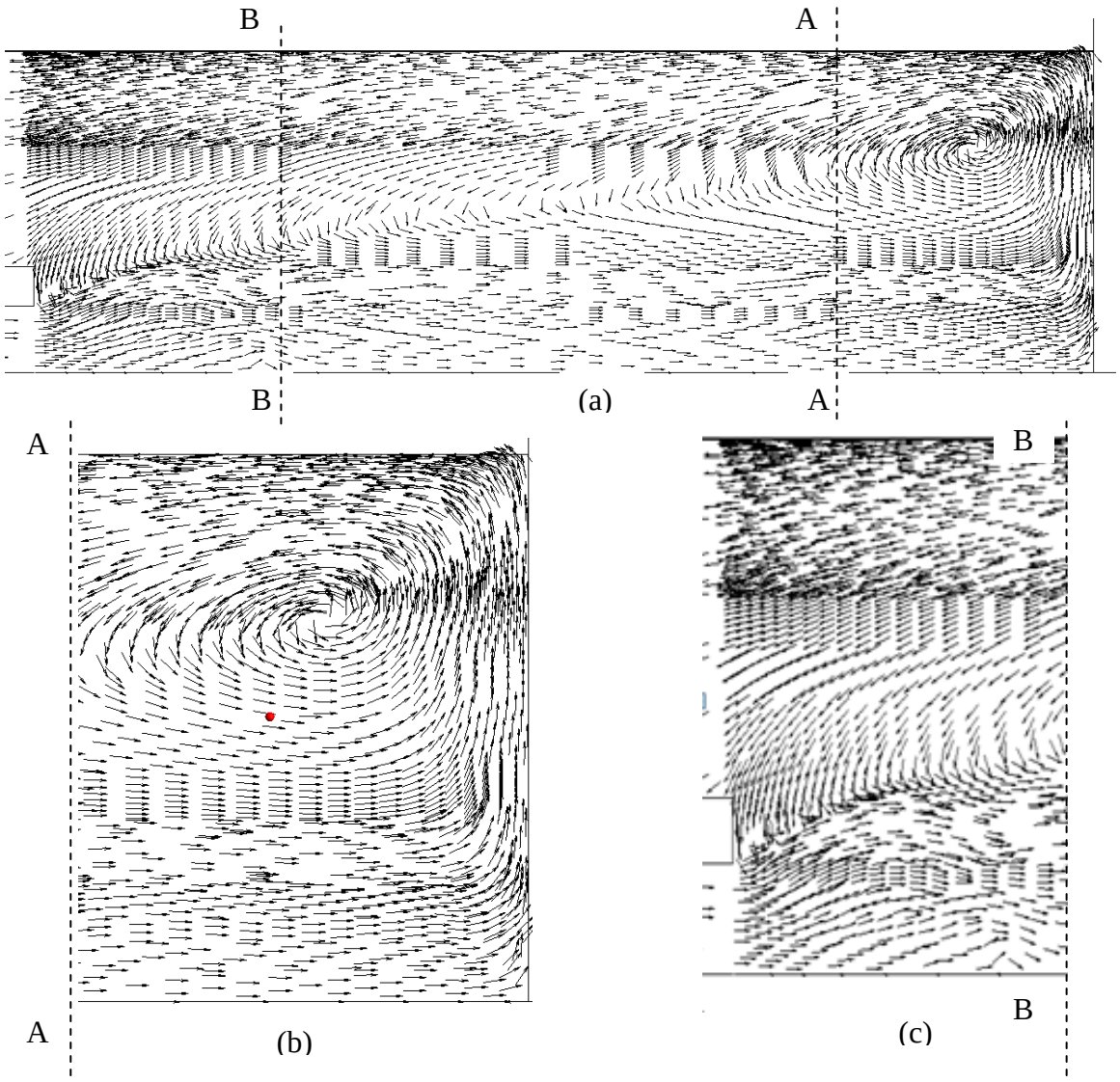

Figure 4.13 Vector diagram on the cross sectional view of the cryoprobe in the expansion region

Figure 4.14 shows the recirculating zone at the corner where the vacuum insulation begins. This recirculation zone is responsible for the rise in the temperature near the point of confluence.

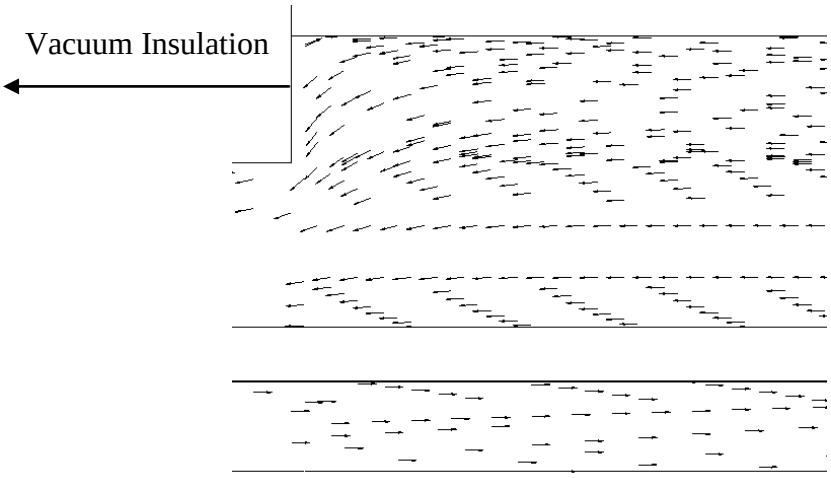

Figure 4.14 Vector diagram near vacuum insulation

The argon gas has a high pressure when it is introduced into the needle assembly, and the pressure undergoes a severe reduction as it passes through a capillary tube. This large reduction in pressure is accompanied by a significant temperature drop. Figure 4.15 shows a graphical representation of the pressure drop experienced by the fluid through the delivery tube. The pressure drops from an initial value of 3350 psi to 528 psi at the exit of the delivery tube.

The pressure in the expansion space is seen to change rapidly by 300psi in the expansion region where the shock waves appear. The contour diagram in Figure 4.16 shows the shock wave pattern in the expansion region.

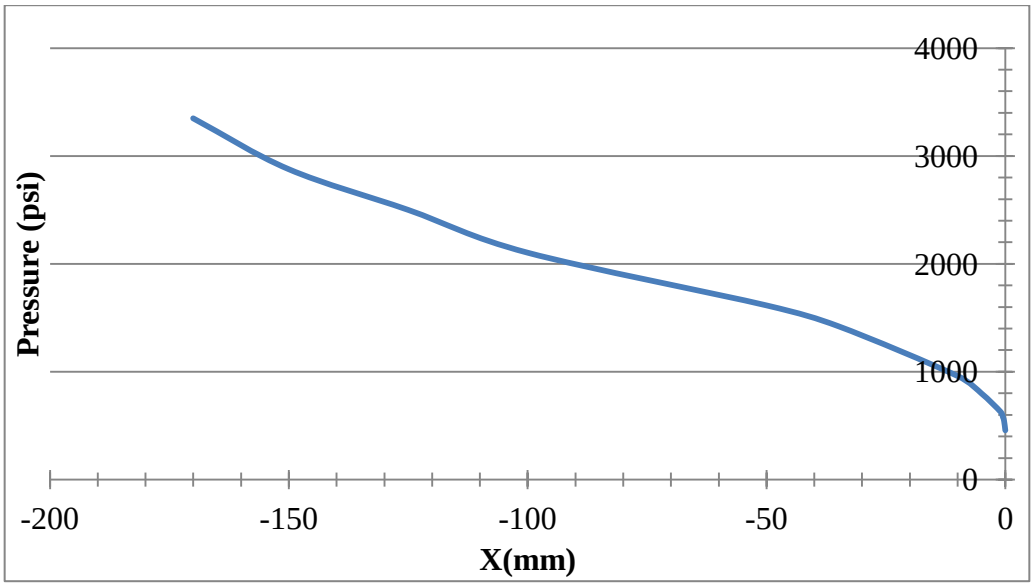

Figure 4.15 Pressure variation along the length of the delivery tube

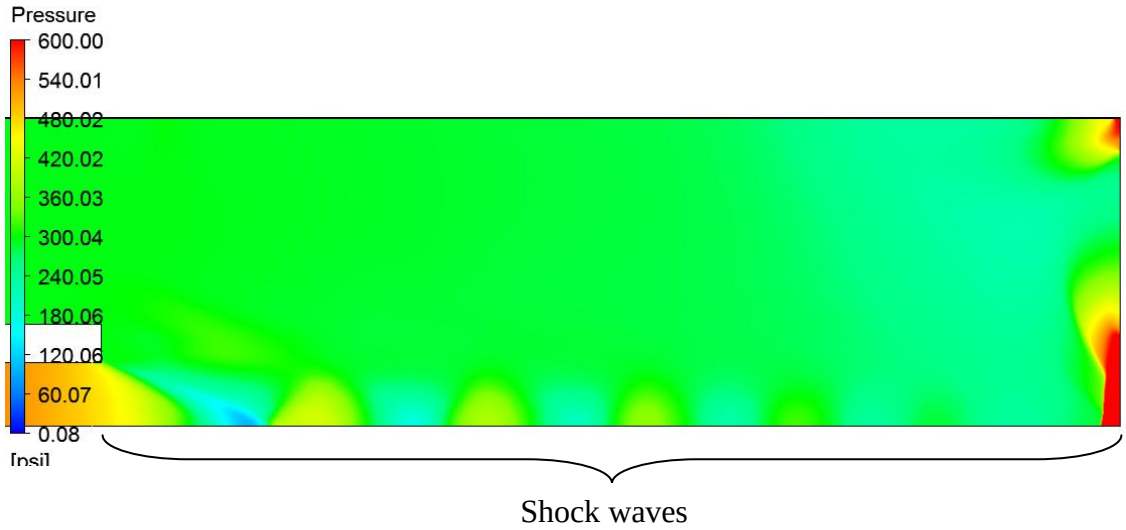

Figure 4.16 Pressure contour in the expansion region

Attention will now be directed to the sensitivity of the results with respect to the nature of the fluid properties that were used in the simulations. In this regard, two cases will be considered. In one, the real gas properties for density, viscosity, and thermal conductivity

were incorporated into the simulation model. In the other, the density variation was modeled by means of the ideal gas law, while both the thermal conductivity and density were taken to be constant at a temperature of 25C and 1atm.

Figure 4.17 displays the response of the bulk temperature in the delivery tube to the two aforementioned property models. It can be seen from the figure that the bulk temperature is totally unresponsive to the difference in the properties except in the immediate neighborhood of the delivery tube exit. At the exit proper (X = 0), the difference in the bulk temperatures for the two cases is approximately 19K, with the ideal gas result being lower.

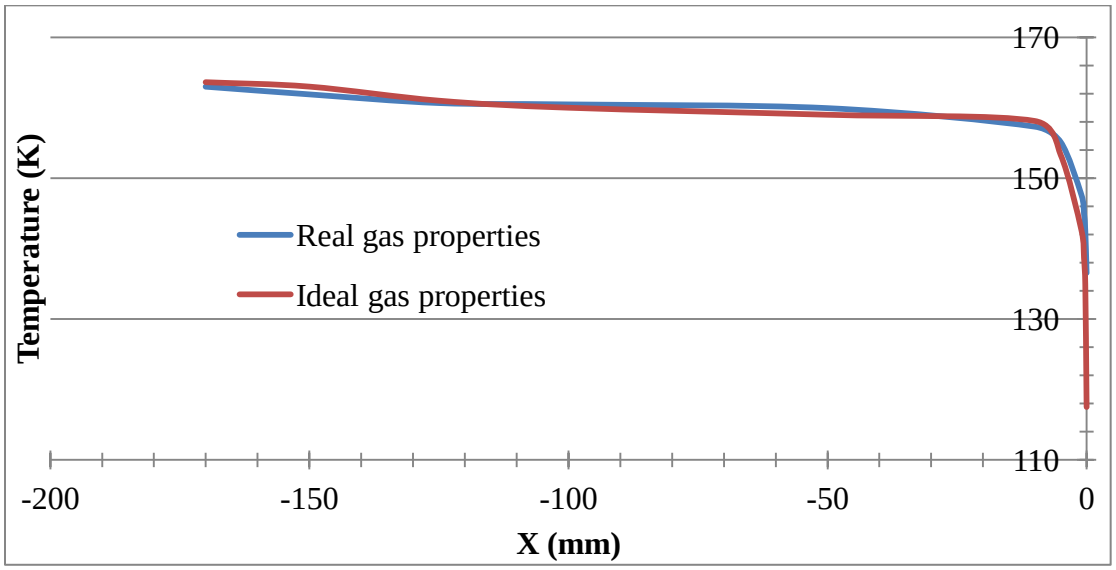

Figure 4.17 Response of the bulk temperature in the delivery tube to two property models: (a) real gas properties and (b) ideal gas law for the density and constant values of the viscosity and thermal conductivity. The values of the latter correspond to a temperature of 25C

Another perspective relevant to the impact of the property values is exhibited in Figure 4.18. That figure compares, by means of color contour diagrams of the temperature, the

results for the range of X between -2 and +2 mm. In this range, there are significant differences of temperature. These differences are as great as 55K. This finding makes a clear statement about the necessity of using real gas properties.

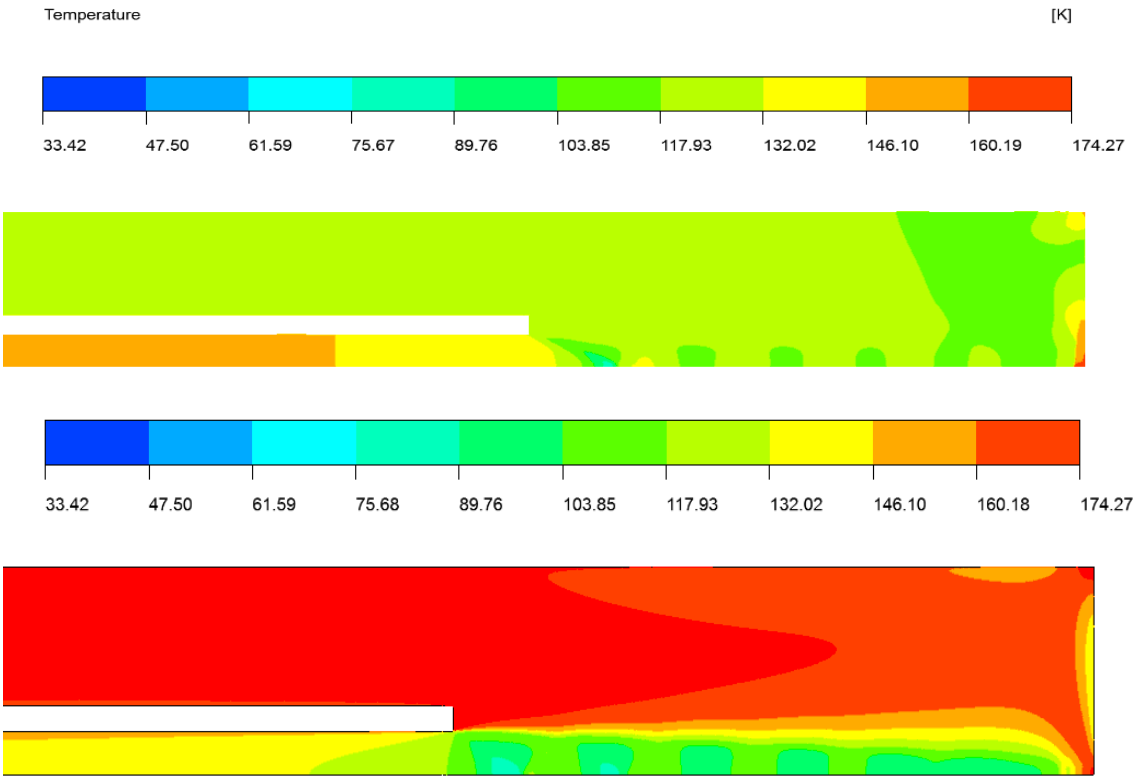

Figure 4.18 Comparison of temperature results for the two models of gas properties in the range of X between -2 and +2mm

The next issue to be explored in the context of different property models is the values of the Mach number. Figure 4.19 has been prepared for this purpose. Although there is some difference in detail, the general configuration of the Mach number distributions is more or less the same for the two models.

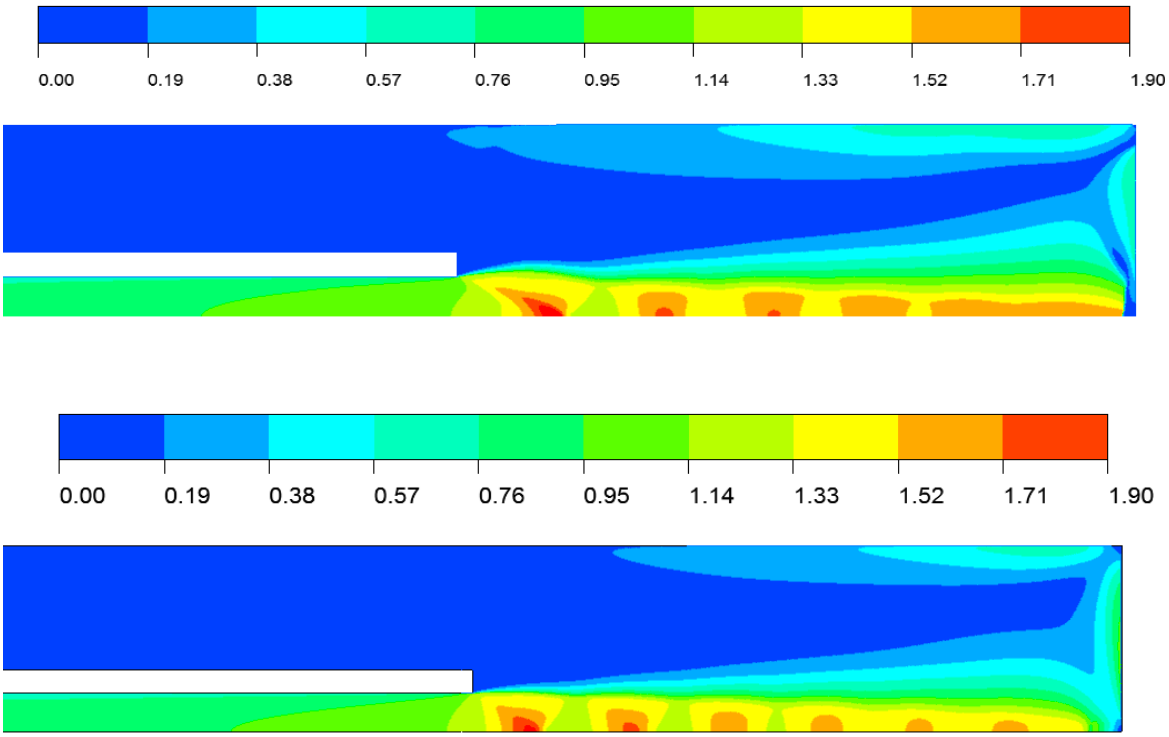

Figure 4.19 Color contour diagrams comparing the Mach number distributions for the two models of the fluid properties

The graphical displays of the Mach number distribution for the real gas and the ideal gas property models are shown in Figure 4.20. These results pertain to axis of the probe. The profiles of the Mach number distribution along the axis of the probe are seen to be qualitatively similar for both the property models.

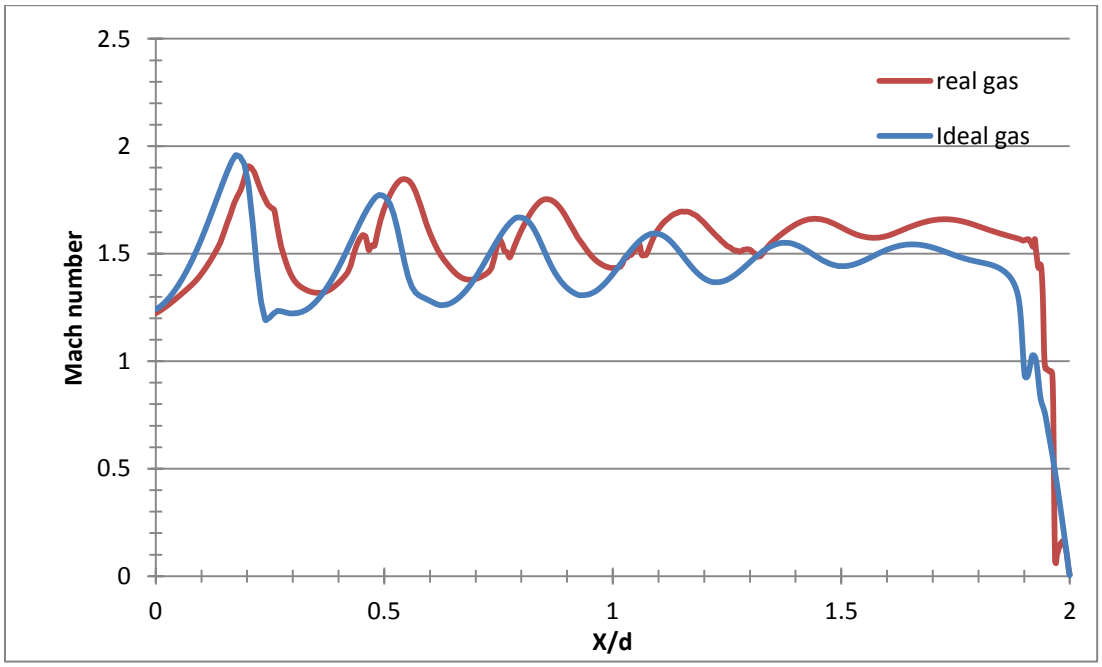

Figure 4.20 Centerline Mach number distribution for the two fluid property models in the range of X between 0 and 2

4.4 Results During Period of Iceball Formation

The second set of results that was extracted from the numerical simulations is those that correspond to an actual situation of iceball formation on the cryoprobe. This simulation was modeled as a transient, conjugate heat flow problem. In the present context, conjugate means that the temperature problems within the cryoprobe and in the surrogate phase change medium had to be solved simultaneously. Another issue that required consideration is that the thermophysical properties of argon substance depend on temperature so that the velocity solution could be affected due to the property variations. If the property effects were substantial, the velocity solution would be altered as the phase change process progressed.

4.4.1 In-probe Velocity Effects

To deal with the velocity problem, the following strategy was adopted. A first pass at the conjugate heat transfer problem was made with the velocity solution frozen at its state corresponding to the adiabatic wall boundary condition. With this velocity solution as input, the solidification process was solved from its initiation to duration of approximately 600 seconds. Focus was then directed to the computed temperature field in the argon within the cryoprobe corresponding to a time of 90 seconds after the onset of solidification. The argon properties corresponding to this temperature field were evaluated, and the velocity problem was solved anew.

This updated velocity solution was fixed, and the conjugate heat transfer problem was solved from scratch over the range between t = 0 and 600 seconds. The in-probe temperature field at 600 seconds was then employed to evaluate the argon properties and, once again, the velocity solution was performed. This renewed velocity solution was frozen and the conjugate heat transfer problem was re-solved.

To assess the possible effect of the different velocity solutions, the 90-second-based and the 600-second-based heat transfer results were compared. To enable a quantitative comparison, values of the in-probe local heat transfer coefficients, respectively deduced from the two velocity solutions, were evaluated. The evaluation of the local heat transfer coefficient was performed as follows. At a given moment of time, the bulk temperature T_b of the spent argon flowing in the external annulus of the probe was evaluated as a function of axial position. At that same moment of time, the heat flux q and the surface temperature T_s as a function of axial position at the external surface of the annulus were extracted from the numerical solution. Then, the local coefficients were determined from

$$h = q/(T_s - T_b) \qquad (4.2)$$

For purposes of comparison, heat transfer coefficients were determined at times t = 90 and 595 seconds during the solidification process. At each of these times, both the in-probe velocity fields corresponding respectively to in-probe temperatures at times t = 90 and 595 seconds were employed.

The thus-determined results are plotted in Figure 4.21. As seen there, there is very little difference in the values of the heat transfer coefficient corresponding to the different velocity bases. The graph also shows a substantial spatial variation of the coefficient values, with the highest values in the neighborhood of the inlet of the annulus and the lowest values at the downstream end. The time dependence of the results is also substantial.

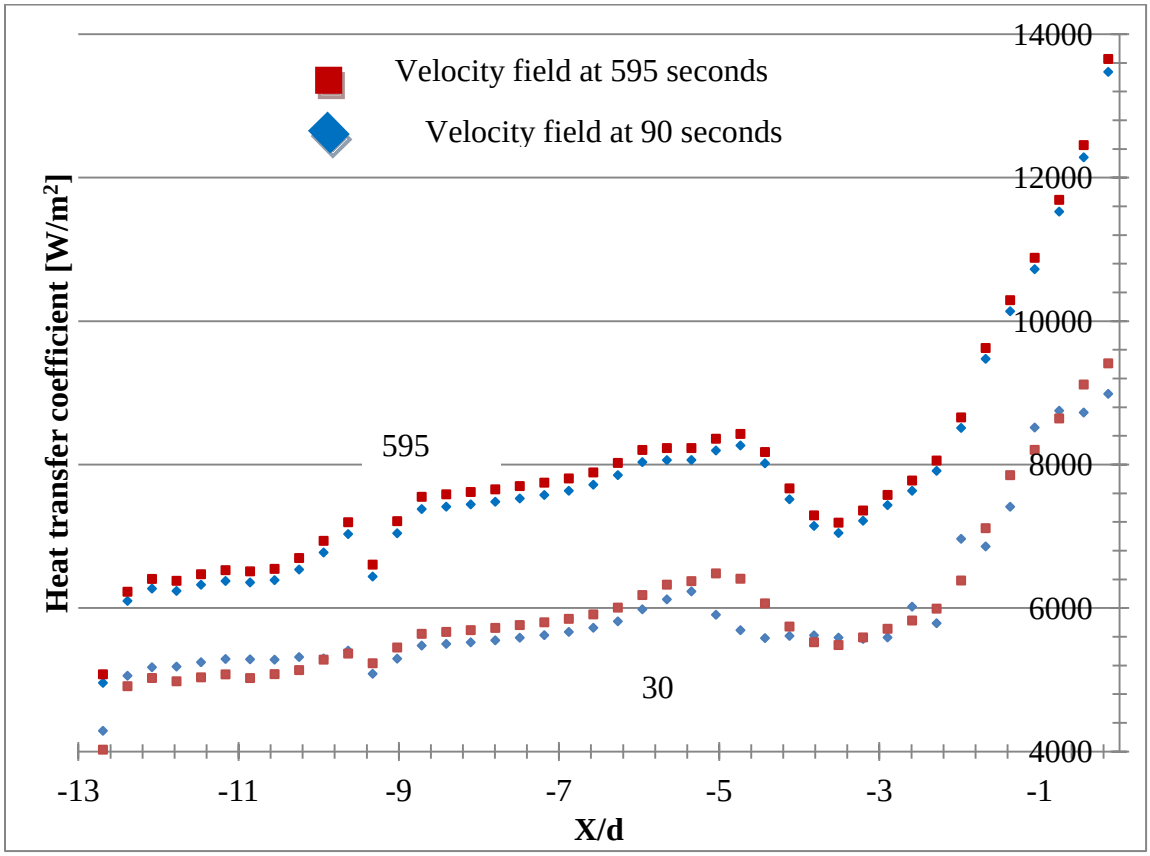

Figure 4.21 Heat transfer coefficients corresponding to the 90-second-based and 600-second-based velocities

4.2.2 Heat Transfer Coefficients

Figure 4.22 displays a schematic of the cryoprobe that will be used in the discussion of the next set of results. Region A represents the outer surface of the probe starting at the exit of the delivery tube and extending leftward to the beginning of the vacuum insulation. Region B represents the outer surface of the probe starting at the exit of the delivery tube and extending rightward up to the beginning of the conical tip. The next set of results address the sections of the probe designated as region A and region B.

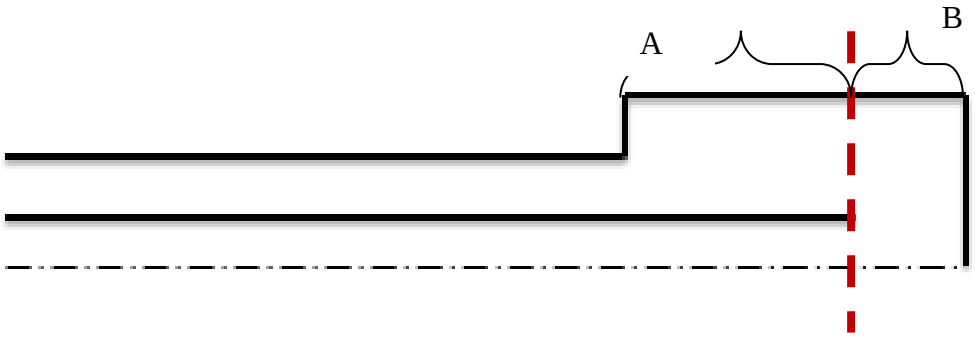

Figure 4.22 Schematic of the cryoprobe

4.2.2.1 Coefficient results for Region A

A graphical representation of the spatial variation in the bulk temperature for region A for times t = 30, 60, 90, 120, 150, 300 and 595 seconds is seen in Figure 4.23. In appraising the results displayed in the figure, it is important to note the highly expanded ordinate scale. Of the seven times that serve as curve parameters, five are essentially coincident. Only two are separated from the pack and only in a limited spatial region. The change in the bulk temperature is very insignificant with respect to time. In particular, only a 2K change in bulk temperature with time is seen for region A.

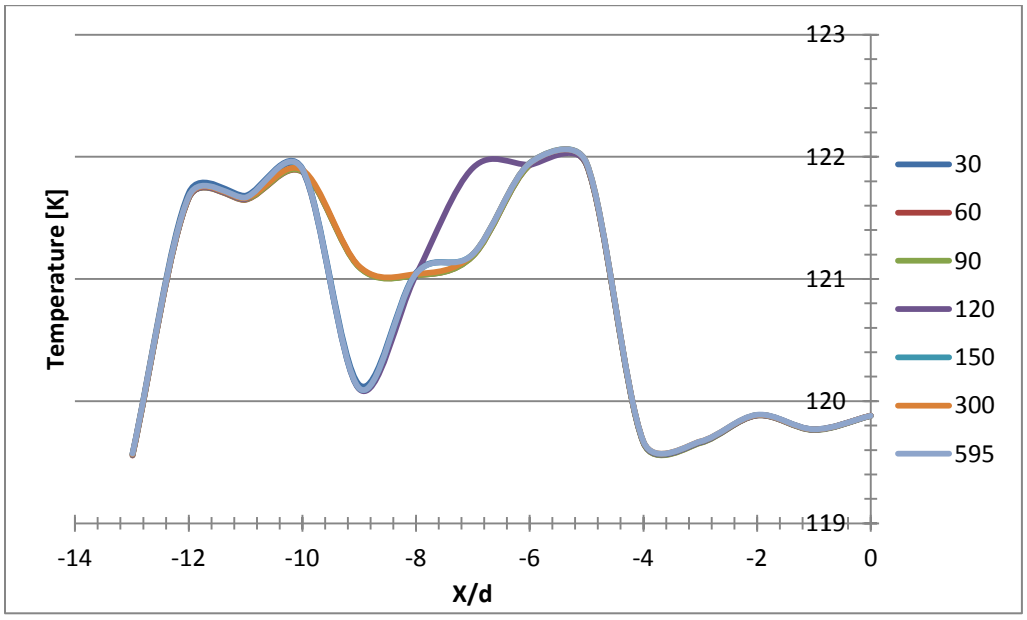

Figure 4.23 Spatial variation of the bulk temperature for region A at various times during the phase change period

The spatial variation of the wall heat flux for region A at times t = 30, 60, 90, 120, 150, 300 and 595 seconds is presented in Figure 4.24. Not unexpectedly, the wall heat flux decreases with time from the onset of the solidification process to 595 seconds. Generally, between times t = 30 and 595 seconds, the heat flux decreases by approximately 40,000W/m^2 . There is also a spatial variation which extends from the highest values at the downstream end of the annulus to the lowest values at the inlet.

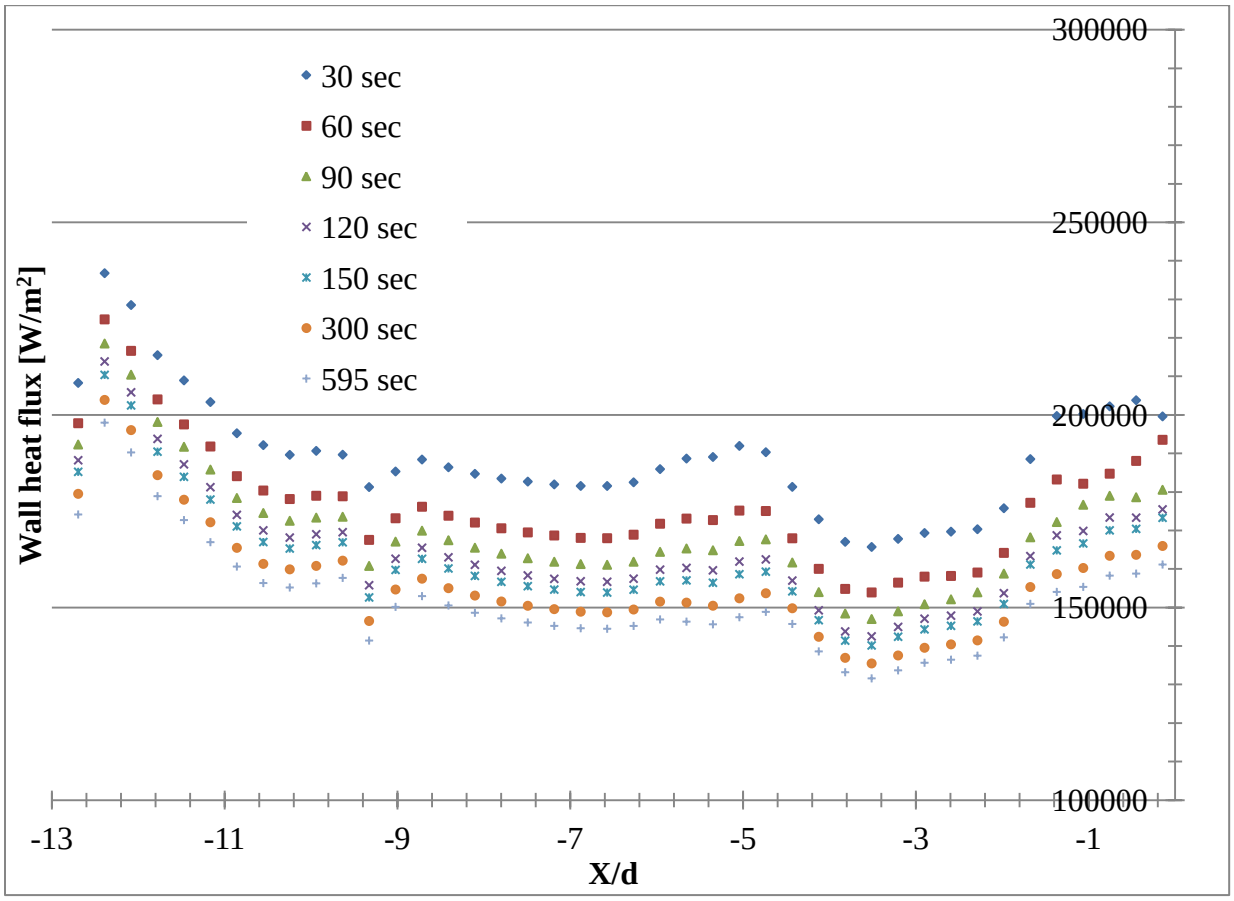

Figure 4.24 Spatial variation of the wall heat flux in region A for times t = 30, 60, 90, 120, 150, 300 and 595 seconds

To complete the display of the basic data, the counterpart of Figure 4.24 for the surface temperature in region A is presented in Figure 4.25. There is a spatial variation, with the highest temperatures at the downstream end of the annulus and the lowest temperatures at the annulus inlet. The greatest spatial variation, about 40K, corresponds to t = 30 seconds. At the other times, the spatial variation is about 25K.The temperatures drop rapidly between t = 30 and 60 seconds but more slowly thereafter.

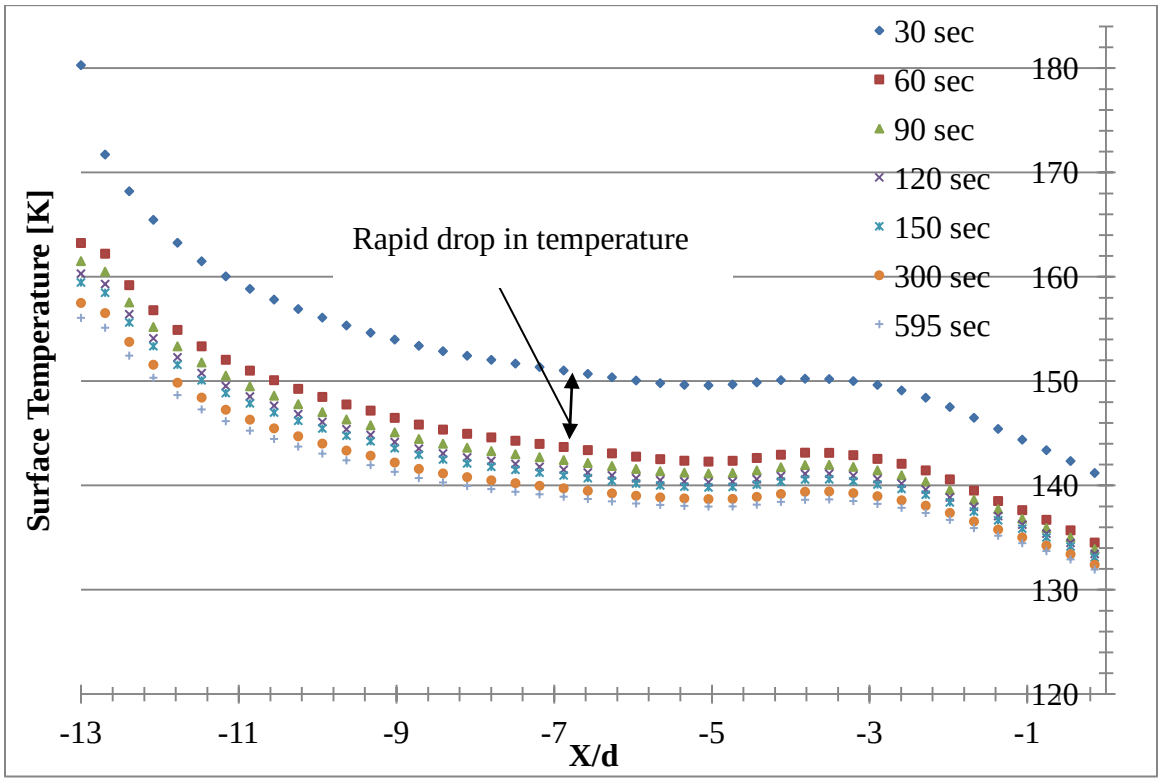

Figure 4.25 Spatial variation of the surface temperature in region A for times t = 30, 60, 90. 120, 150, 300 and 595 seconds

The information conveyed in Figures 4.23, 4.24, and 4.25 was used in conjunction with Eq. (4.2) to calculate the heat transfer coefficients on the outer surface of the probe in region A . These results are shown in Figure 4.26. Generally, the lowest coefficients are at the far end of the annulus and the highest ones are at the inlet of the annulus. The overall spatial variation extends from about 5000 to almost 14,000 W/m^2-K. The largest temporal variations are at early times. Thereafter, the coefficient values continue to decrease, but more slowly.

With respect to the just-determined heat transfer coefficient, it is noteworthy that they represent information never before available in the present context. In prior research, the need for heat transfer coefficient information was recognized, but was determined on a

ad hoc basis. In [149], it was assumed that the venerable Dittus-Boelter equation for the average heat transfer coefficient for fully developed pipe flow could be employed. The argon properties were evaluated at a mean temperature between 20 and -140^{o}C. (The 20^{o}C temperature is not encountered in the annulus.) The authors of [reference] utilized a spatially and temporally constant value of 8400 W/m^2 for the heat transfer coefficient. If this value is compared with those of Figure 4.26, it is clear that substantial errors were made in [149].

In [150], the adopted local heat transfer coefficient decreased precipitously from 40,000 at a location upstream of the annulus to a value of 3000W/m^2 at the inlet of the annulus. In the annulus proper, the heat transfer coefficients ranged 3000 to 2000 W/m^2. Finally, in a 3-mm length at the downstream end of the annulus, the heat transfer coefficient increased from 2000 to 6000 W/m^2. These values are clearly low when compared with those of Figure 4.26 except at the downstream end of the annulus.

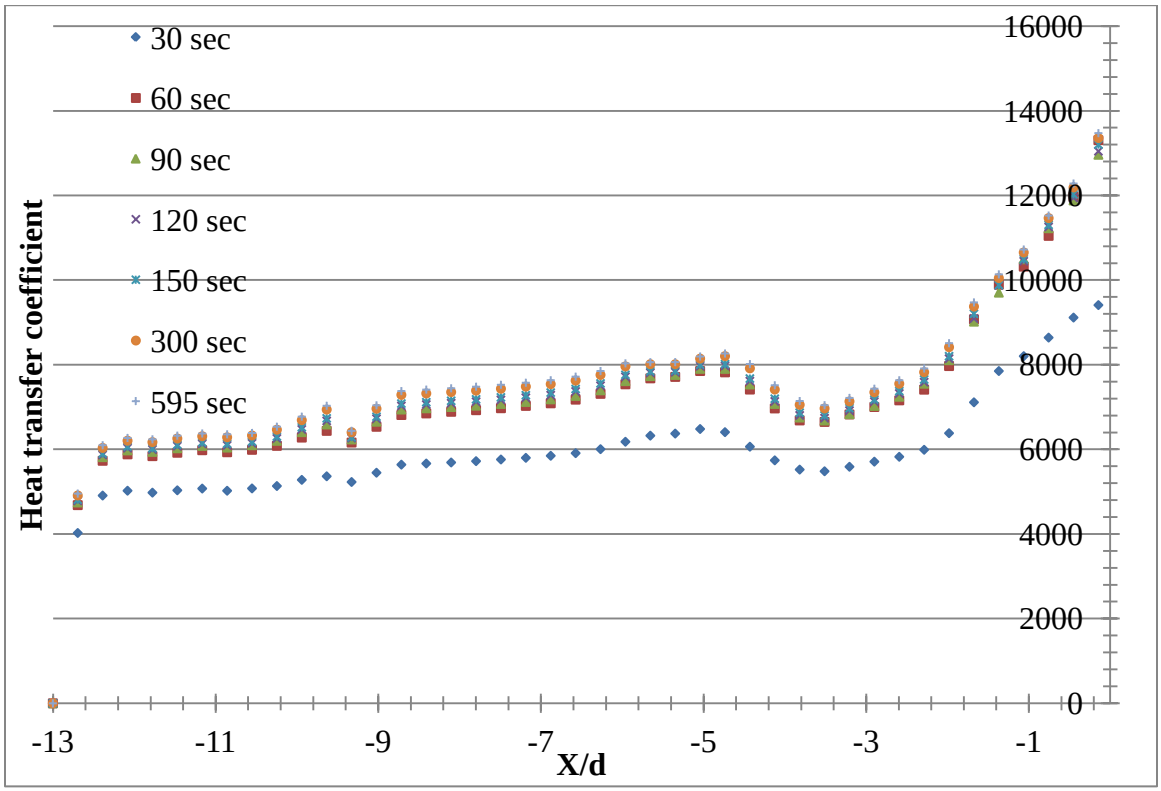

Figure 4.26 Spatial variations of the heat transfer coefficient in region A for times t =30, 60, 90. 120, 150, 300 and 595 seconds

4.2.2.2 Coefficient Results for Region B

Another objective was to determine heat transfer coefficients in region B (see Figure 4.22). An impediment to this effort is the absence of bulk temperatures in that region. However, reference to Figure 4.23 shows that the spatial and temporal variations of the bulk temperature in region A are very modest, on the order of 2K. In particular, in the range of *X* where regions A and B meet, the region A bulk temperatures are approximately 120K. This value was adopted in order to facilitate the determination of heat transfer coefficients in region B.

The heat flux values for region B were extracted from the numerical solutions and are plotted in Figure 4.27. From the figure, it appears that the heat flux increases monotonically from X = 0 (the location of the annulus inlet) to X = 1.8. Thereafter, there is a sharp decrease due to an eddy occupying the corner where the side and the end walls meet. At any location, the expected decrease of the heat flux with the passing of time is validated from the results.

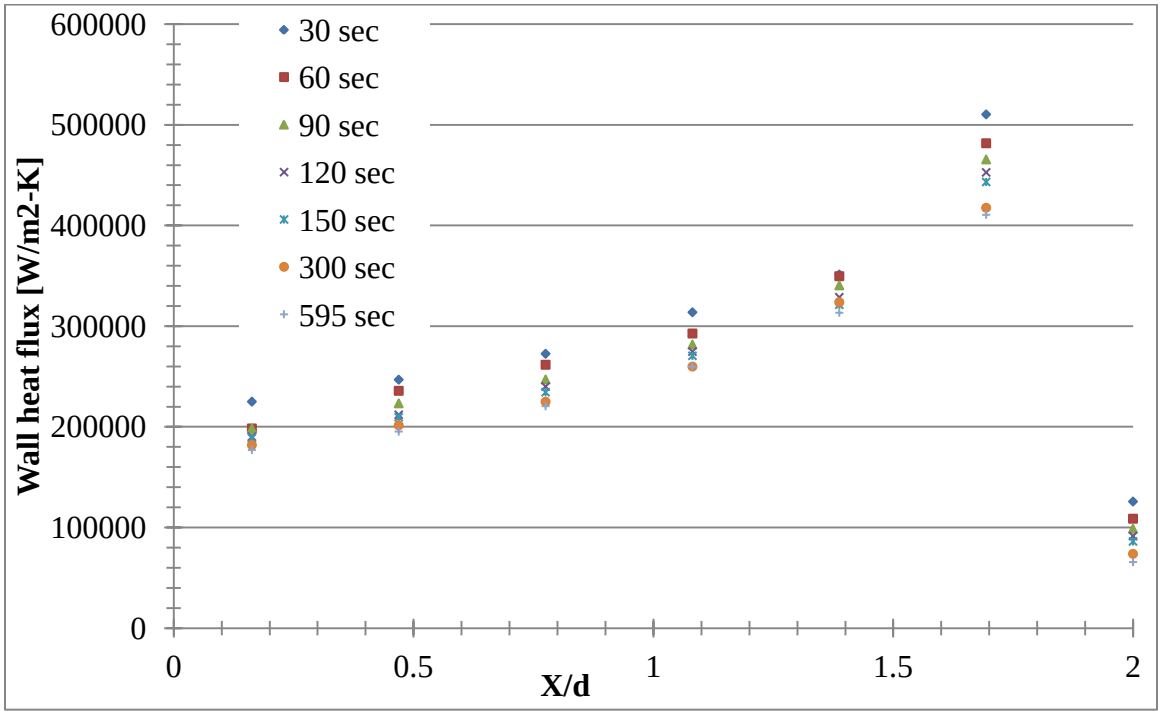

Figure 4.27 Spatial variations of wall heat flux for times t = 30, 60, 90, 120, 150, 300 and 595 seconds

The surface temperature for region B is presented in Figure 4.28. The rapid increase at the rightmost end of region B can be related to the presence of the aforementioned eddy. Aside from that, the wall temperature is relatively spatially uniform. Here again, there is a rapid drop in the temperature from time t = 30 to 60 seconds with slower changes thereafter.

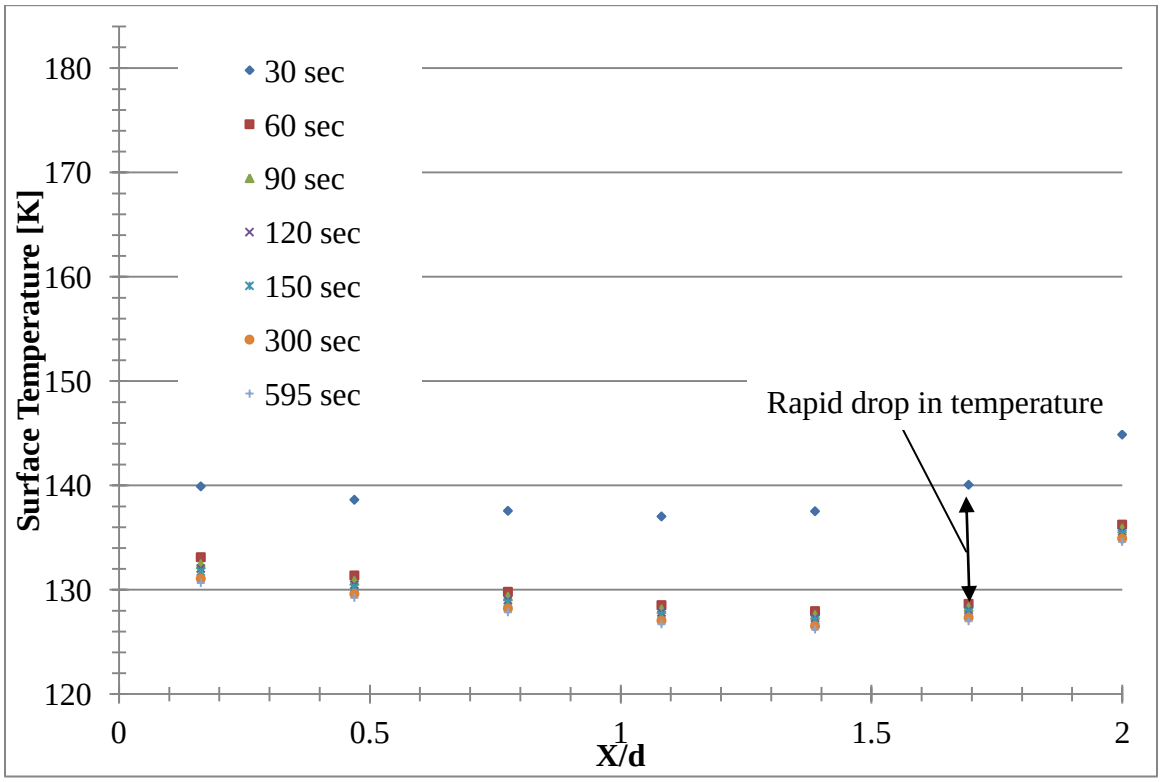

Figure 4.28 Spatial variations of surface temperature for time t=30, 60, 90. 120, 150, 300 and 595 seconds

Using the information conveyed in Figure 4.27 and Figure 4.28 and the bulk temperature as 120K, the heat transfer coefficients were calculated and are presented in Figure 4.29. There is a clear trend of increasing heat transfer coefficient in the direction from the annulus inlet to the corner. The highest heat transfer coefficient achieved was almost 60,000 W/m^2. However, at the corner proper, there is a spectacular drop-off owing to the low velocities required by the no-slip boundary condition at the juncture of the two walls. A high change in the heat transfer coefficient is seen from time t = 30 to 60 seconds; thereafter, the change slows with time.

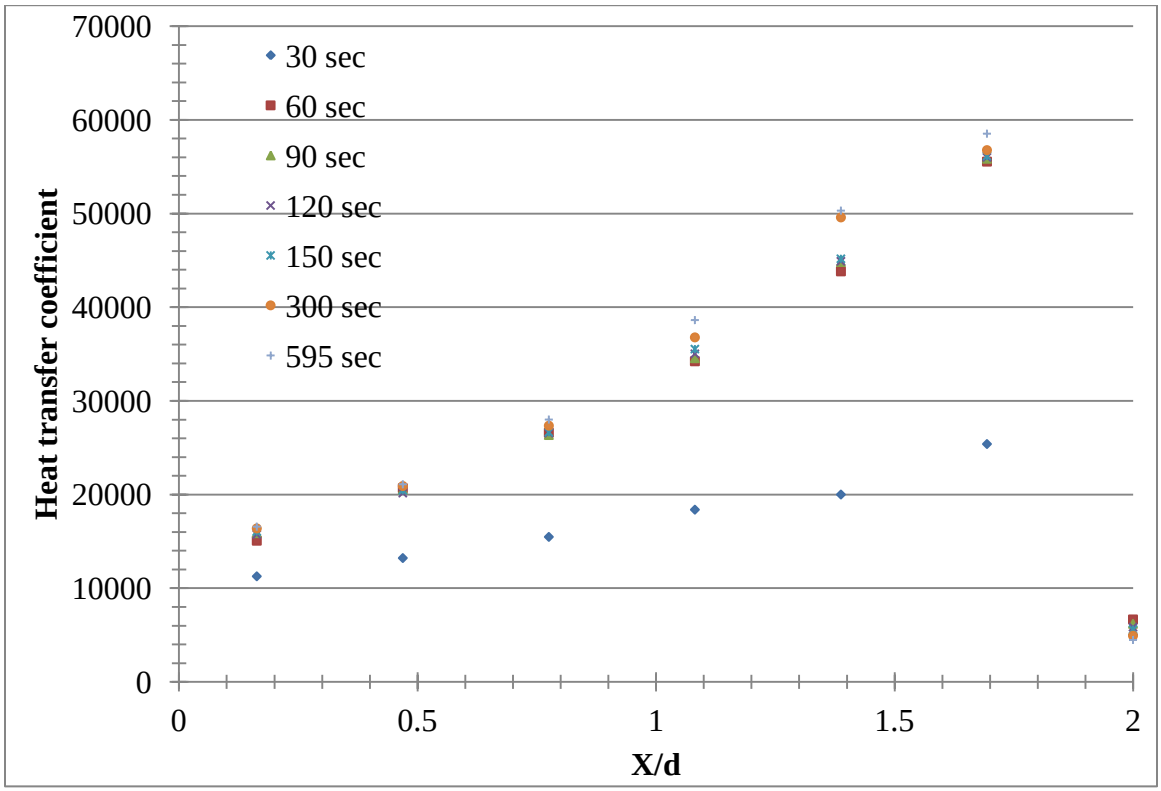

Figure 4.29 Graphical representation of heat transfer coefficient for time t=30, 60, 90. 120, 150, 300 and 595 seconds

4.3 Iceball Growth with Time

A color contour diagram of the temperature distribution on the longitudinal section of the iceball for times t = 30, 60, 90, 120, 150, 300 and 595 seconds is seen in Figure 4.30. The outer boundary of the outermost contour represents the outer surface of the iceball. In general, the iceball geometry is an ellipsoid whose major and minor axes evolve with time. At the earliest time of observation, t = 30 seconds, the major axis is approxiamtely one and a half times the minor axis. As time proceeds, the two axes become more equal in length. The minor axis of the iceball at time t = 595 seconds is approximately 3.5 times that at time t = 30 seconds. The major axis of the iceball at time t = 595 seconds is 1.2 times that at time t = 30 seconds.

More quantitative information will be presented in the next chapter when comparisons are made between the predictions of the simulations and the experimental data.

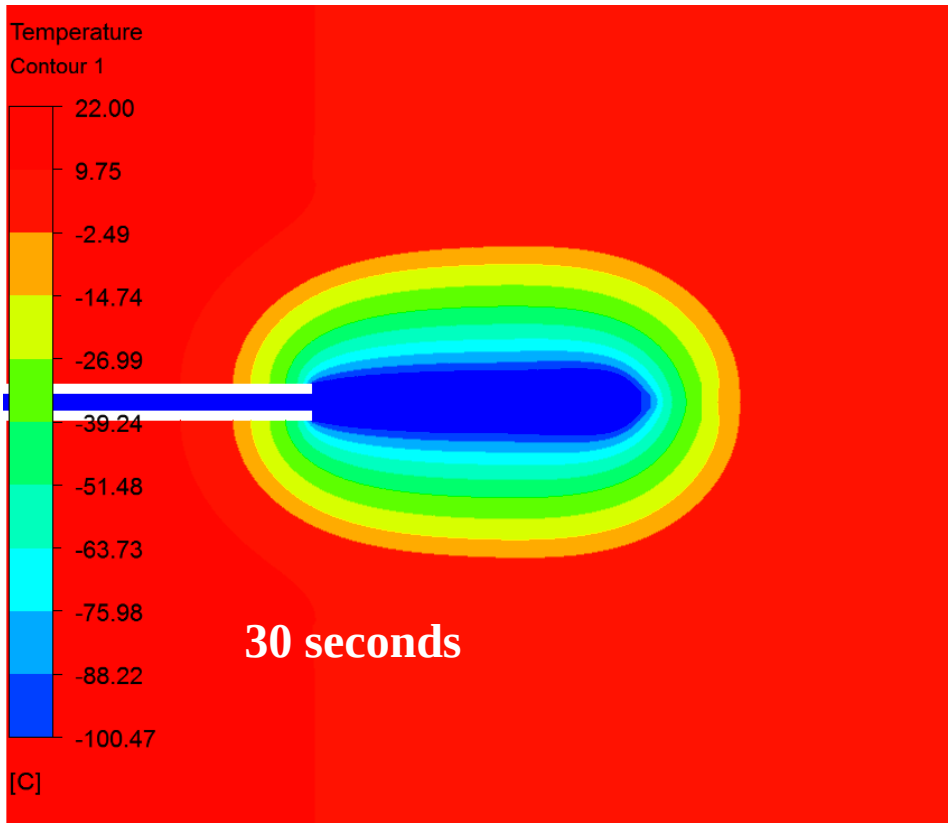

(a)

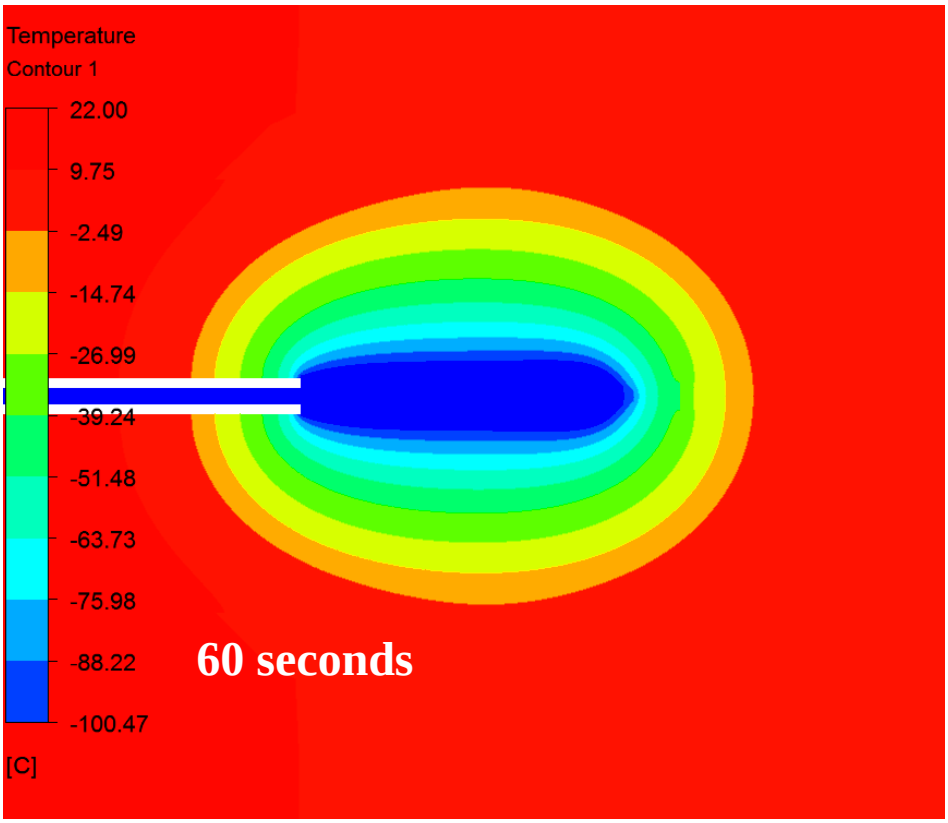
Temperature
Contour 1
22.00
9.75
-2.49
-14.74
-26.99
-39.24
-51.48
-63.73
-75.98
-88.22
-100.47
[C]
60 seconds

(b)

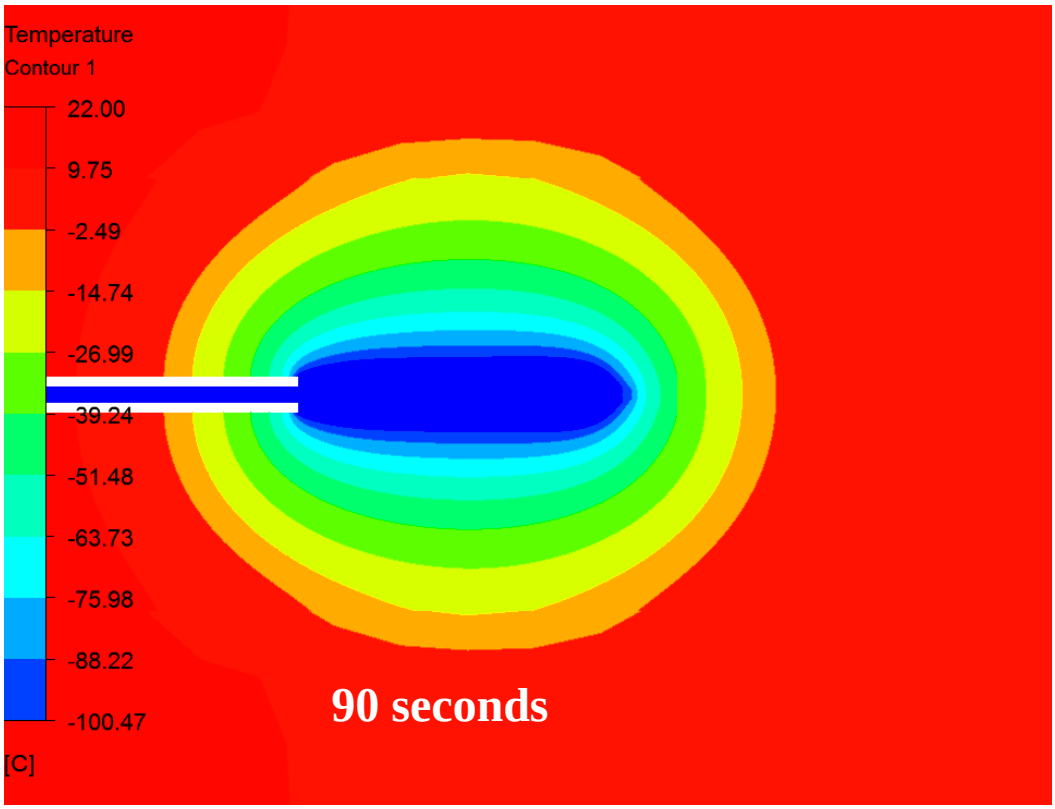
Temperature
Contour 1
22.00
9.75
-2.49
-14.74
-26.99
-39.24
-51.48
-63.73
-75.98
-88.22
-100.47
[C]
90 seconds

(c)

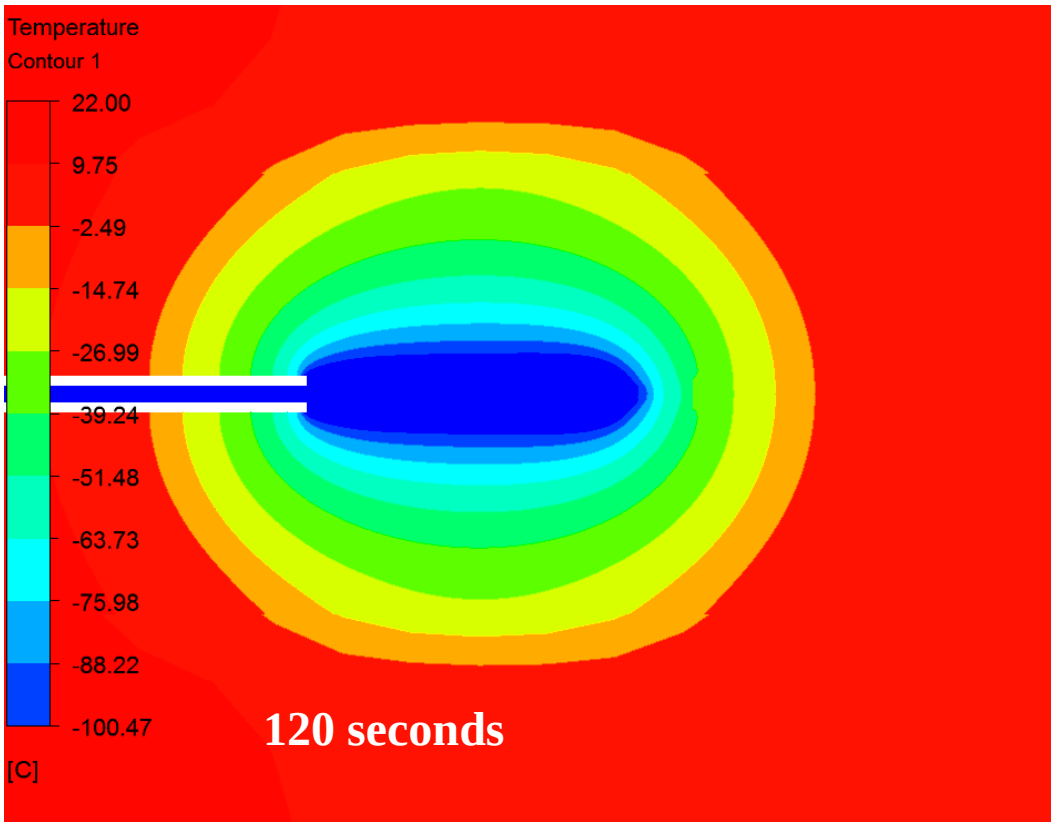
Temperature
Contour 1
22.00
9.75
-2.49
-14.74
-26.99
-39.24
-51.48
-63.73
-75.98
-88.22
-100.47
[C]
120 seconds

(d)

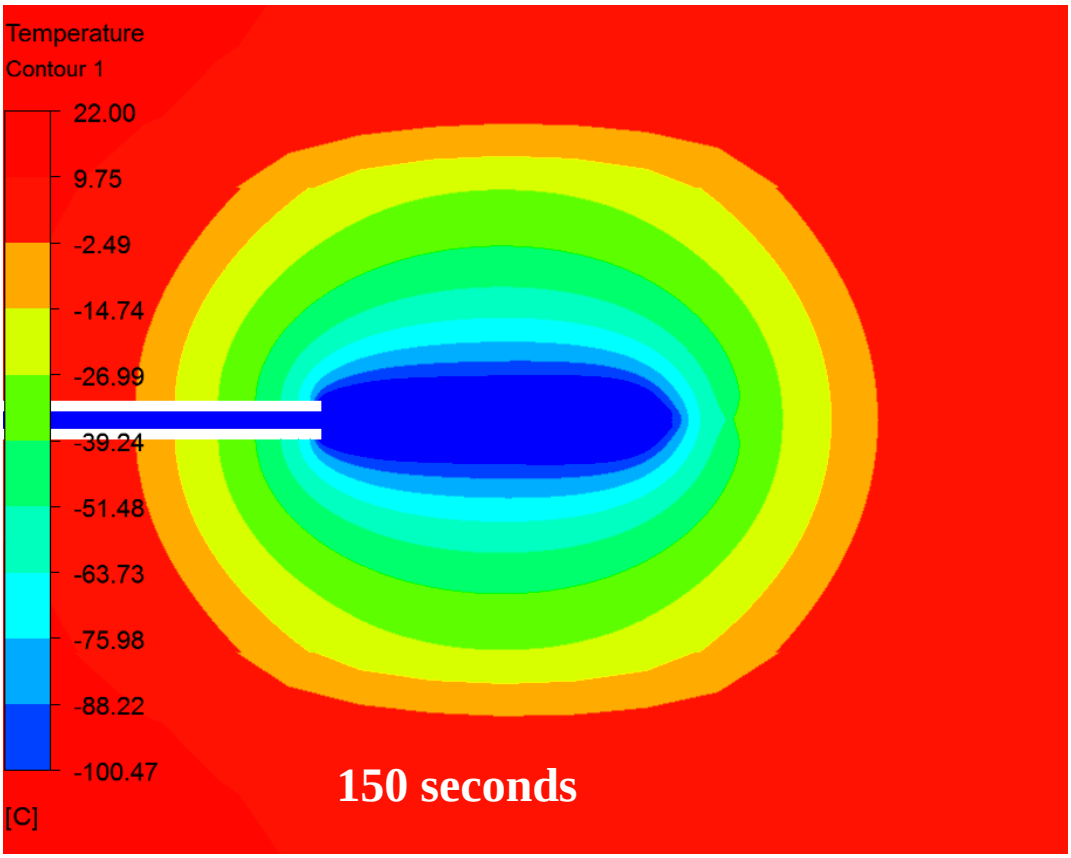
Temperature
Contour 1
22.00
9.75
-2.49
-14.74
-26.99
-39.24
-51.48
-63.73
-75.98
-88.22
-100.47
[C]
150 seconds

(e)

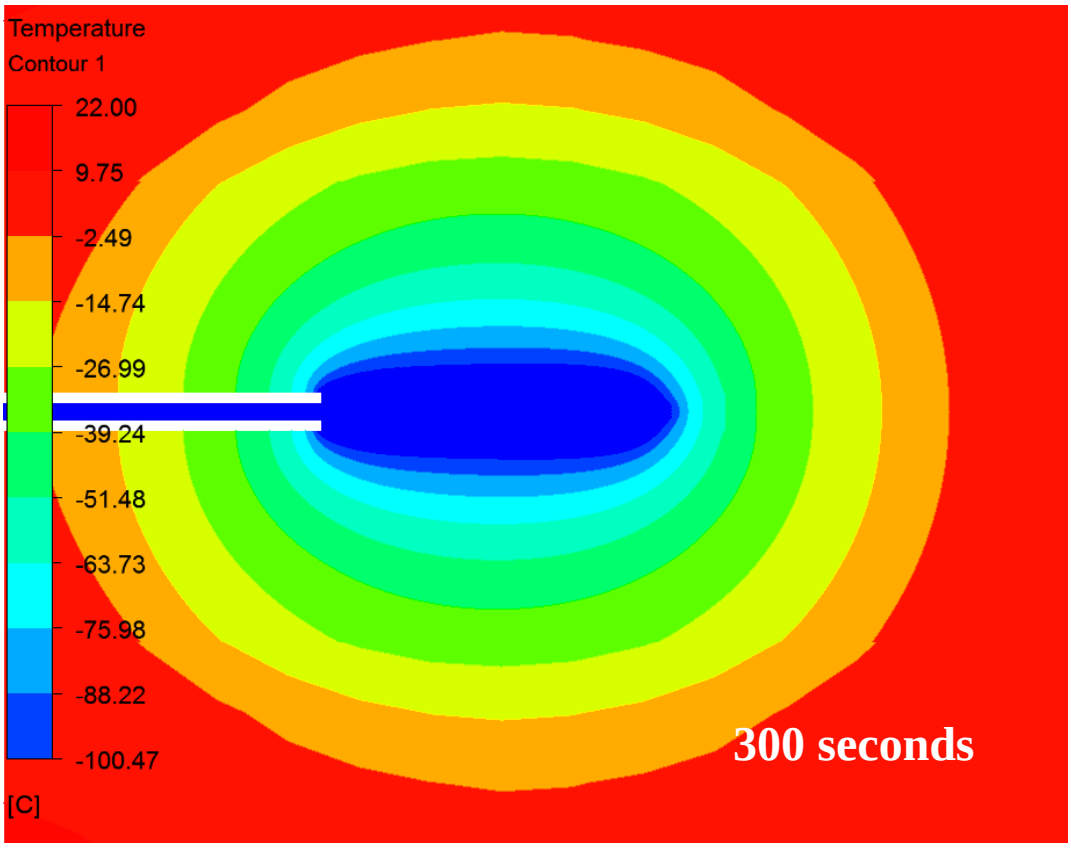
Temperature
Contour 1
22.00
9.75
-2.49
-14.74
-26.99
-39.24
-51.48
-63.73
-75.98
-88.22
-100.47
[C]
300 seconds

(f)

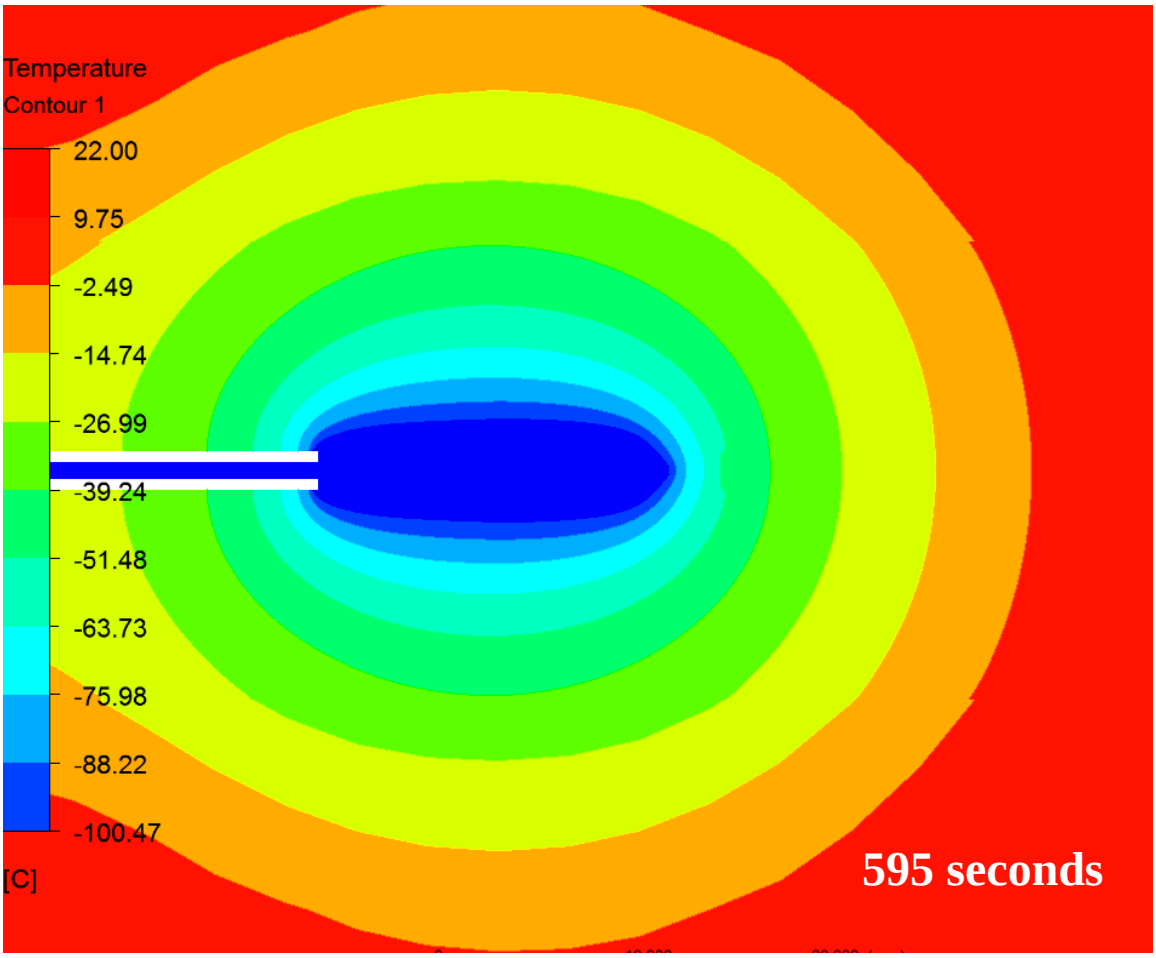

(g)

Figure 4.30 Color contour diagrams of the temperature distribution along the cross section of the iceball at 30, 30,90, 120,150,300 and 595 seconds

Chapter 5 Comparison of Experimental and Simulation Results

5.1 Introduction

The two foregoing chapters individually highlighted the experimental and the simulation efforts involved in the study of the performance of a cryoprobe equipped with a straight delivery tube. The present chapter is a comparison of the experimental and the simulations results discussed in the foregoing chapters.

5.2 Experiment I

The temperatures on the outer surface of the cryoprobe that correspond to the adiabatic boundary condition are presented in Figure 5.1. Recall that the numerical simulation for the adiabatic case was performed under steady state conditions. The figure contains three distinct pieces of information. The continuous curve is from the numerical simulations, as is the inserted color contour diagram. The third piece of information is the experimental data recorded when steady state had been achieved.

Special focus is directed to the comparison of the numerical prediction and the corresponding experiment. From the figure, it is clear that excellent agreement prevails. To provide a more exacting comparison, a table situated just beneath the figure has been prepared. As seen in the table, the measured value of temperature is 120K and value predicted by the simulation is 119.6 K. This level of agreement is a strong support for the simulation model and its implementation.

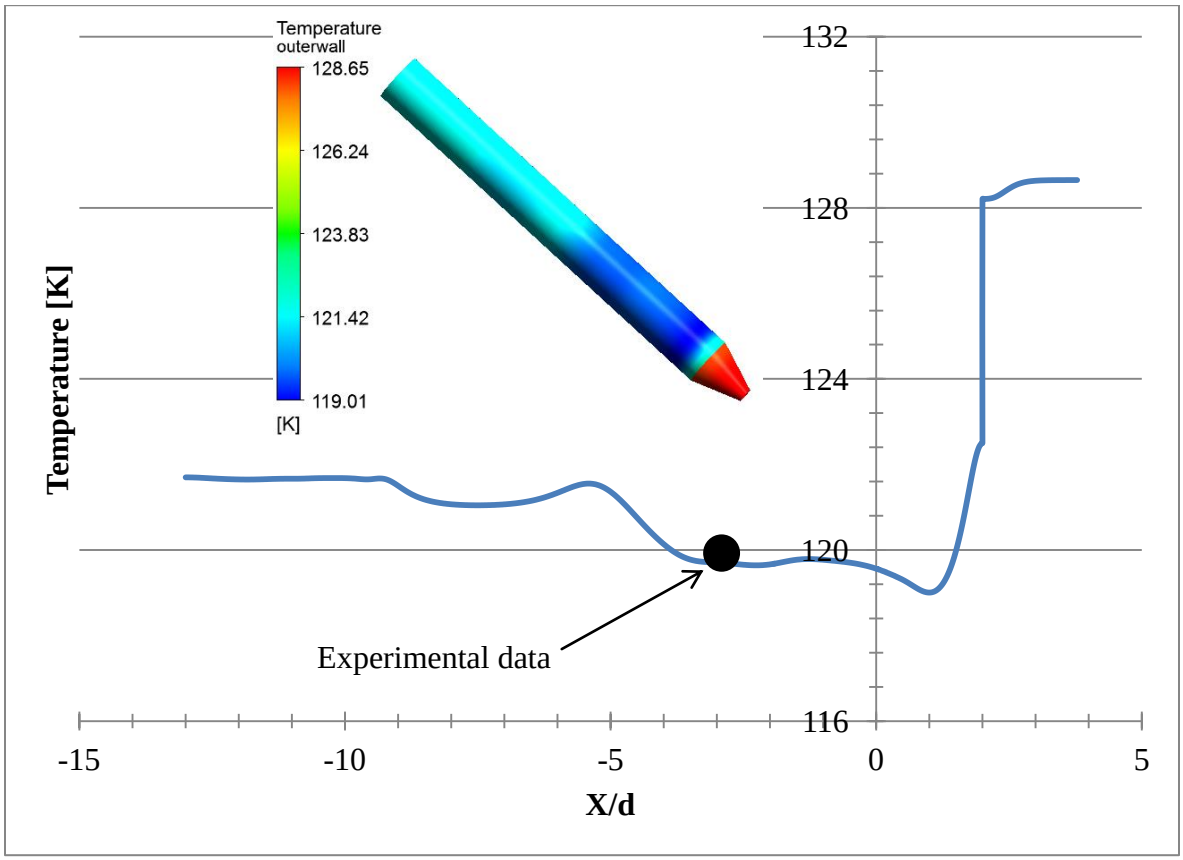

Simulation value [K]	Experimental value [K]
119.6	120

Figure 5.1 A comparison of the experimental and simulation results for the temperatures on the outer surface of the probe

5.3 Experiment II

Figure 5.2 displays the comparison of simulation results and experimental data for the temporal variations of the temperature at locations 1 and 2 as seen in Figure 3.7. The dashed lines represent the results obtained from the simulation and the solid lines correspond to the data during the experimental work. It can be seen that the both the results are in close agreement at location 1. The agreement is not as good at location 2.

This deviation can be attributed to a degree ambiguity that prevails at that location. In that regard, note should be taken that that location 2 is at the junction of nominally insulated and fully uninsulated regions of the surface.

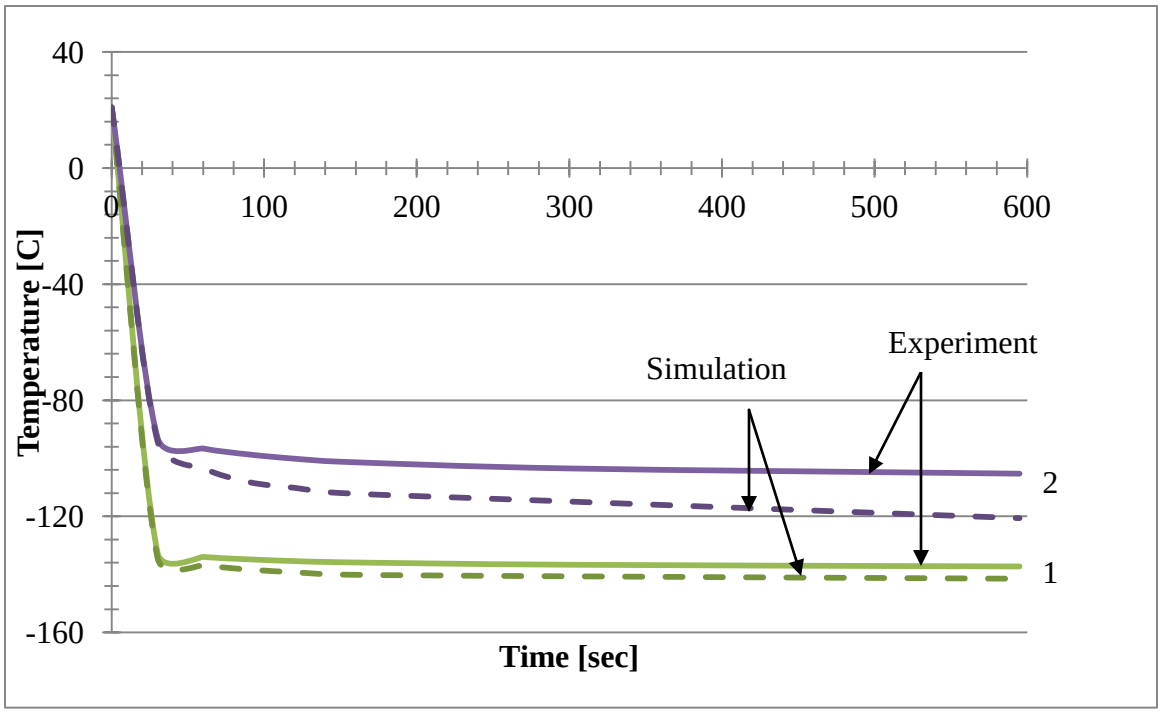

Figure 5.2 Temporal temperature variations at thermocouple locations measured experimentally and compared with those from numerical simulations

The next set of results displays the shape of the iceball with time for both the numerical simulations and the experiments. This information is conveyed in Figures 5.3(a)-(g). The successive graphs correspond to observation times t = 30, 60, 90, 120, 150, 300 and 595 seconds.

In each of the graphs, the continuous curve represents the numerical prediction while the experimental data are delineated by the black squares. An overview of Figures 5.3 indicates excellent agreement between the predicted and measured results. Further

inspection of the figures provides detailed information about the growth of the iceball. For instance, at t = 30 seconds, the radius of the iceball 3.8mm, while at t = 595 seconds, the radius has grown to 15.4mm. During the same time interval, the height of the iceball has grown from about 37 to 47mm.

The excellent agreement between the predicted and the measured iceball dimensions lends strong support to the simulation model, the implementation of the model, and the experimental technique and data acquisition. It is noteworthy that the results presented in Figures 5.3 represent the first instance where information obtained from two assumption-free sources has been compared without compromise.

Further details of the iceball growth are presented in Figure 5.4 and 5.5.

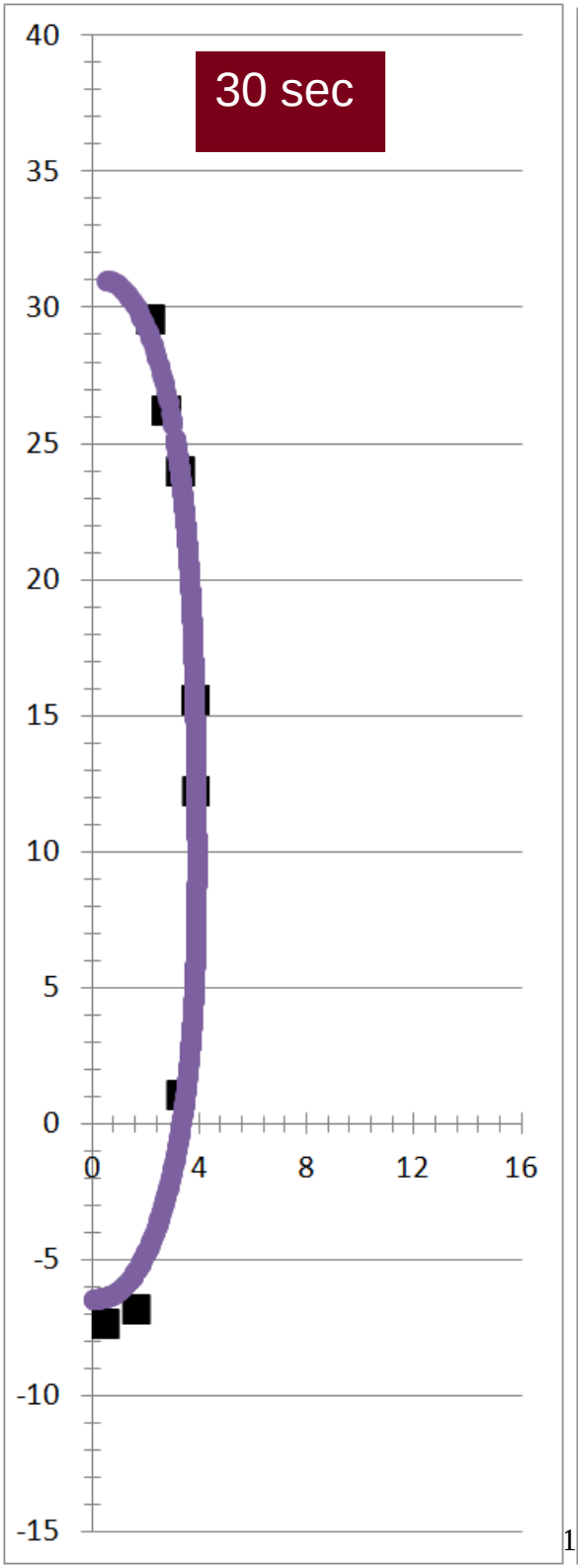
30 sec
40
35
30
25
20
15
10
5
0
-5
-10
-15
0
4
8
12
16

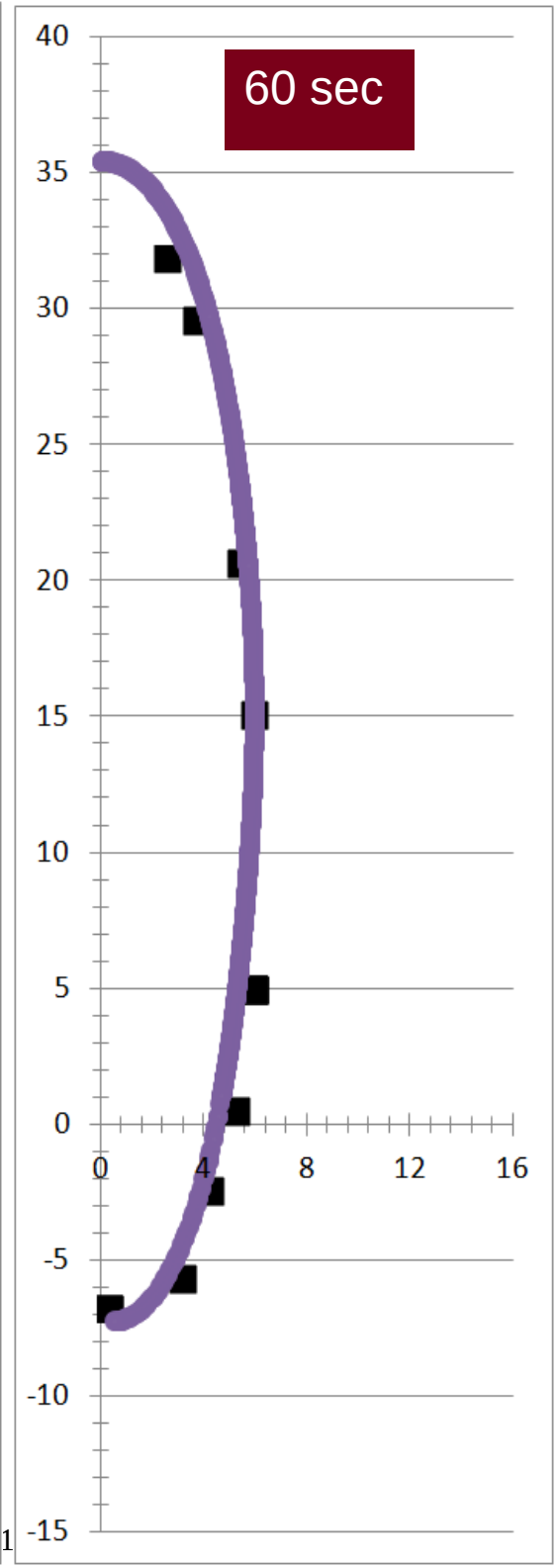
60 sec
40
35
30
25
20
15
10
5
0
-5
-10
-15
0
4
8
12
16

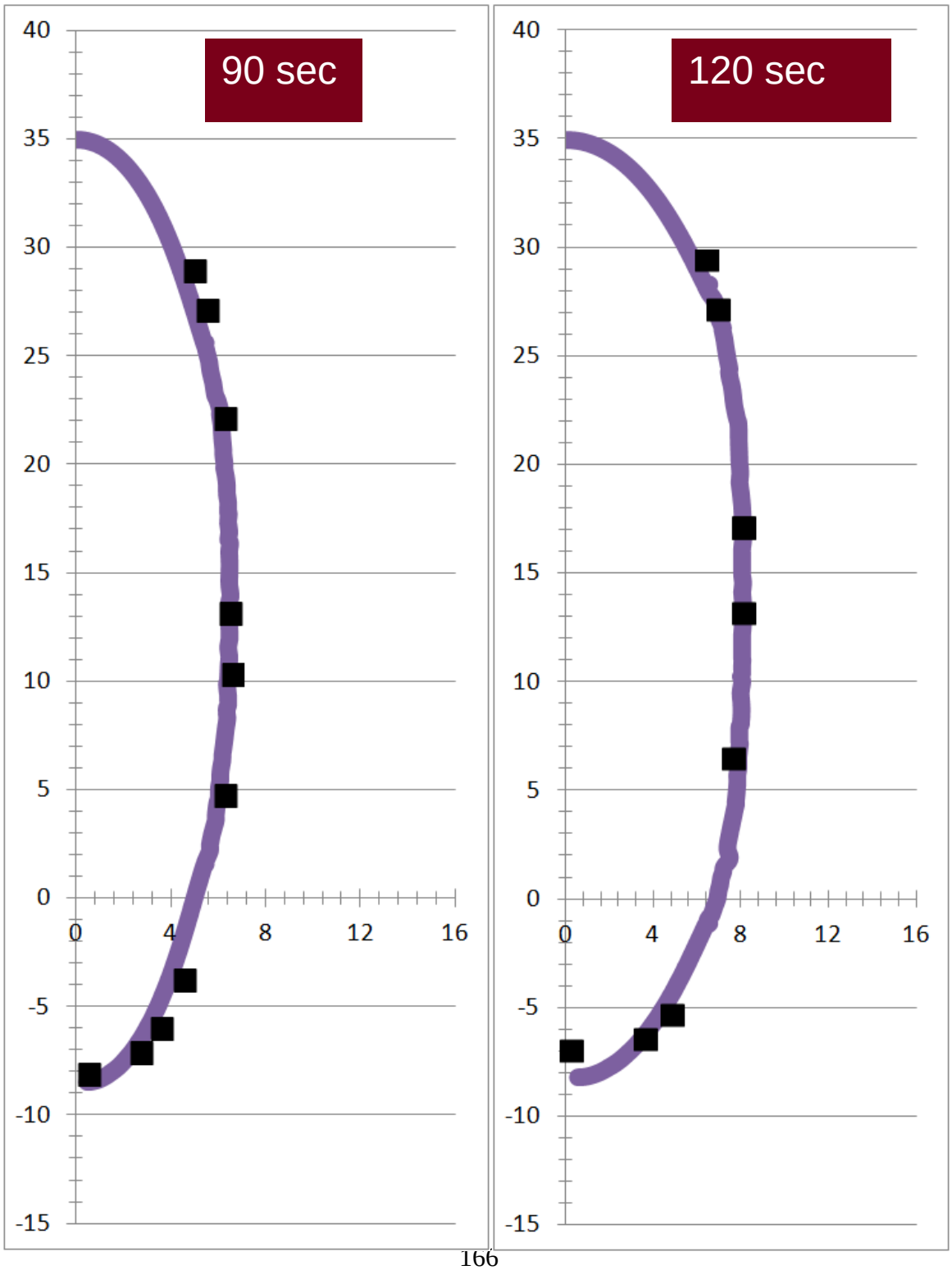
90 sec
120 sec
40
35
30
25
20
15
10
5
0
-5
-10
-15
0
4
8
12
16

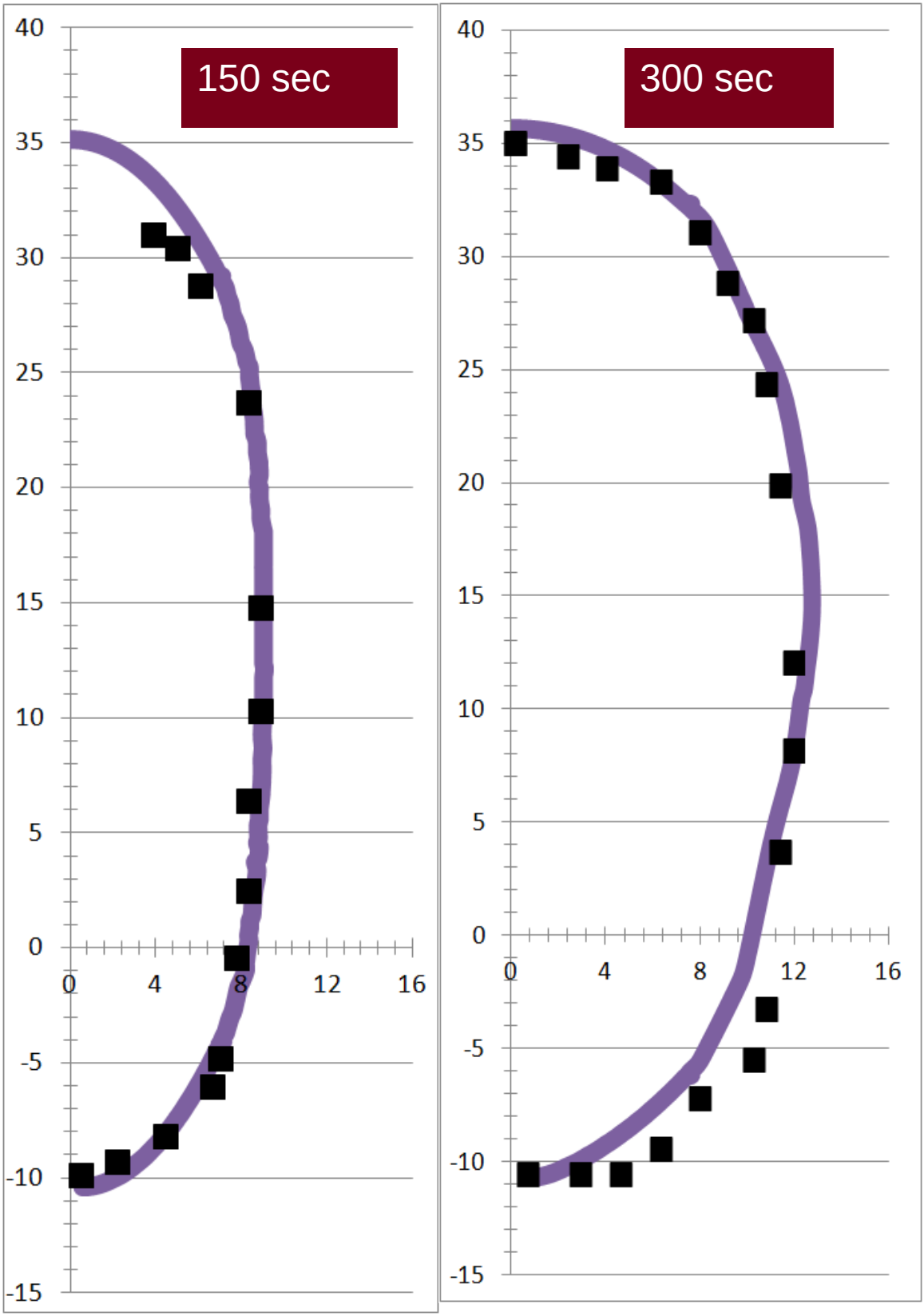
150 sec
300 sec
40
35
30
25
20
15
10
5
0
-5
-10
-15
0
4
8
12
16

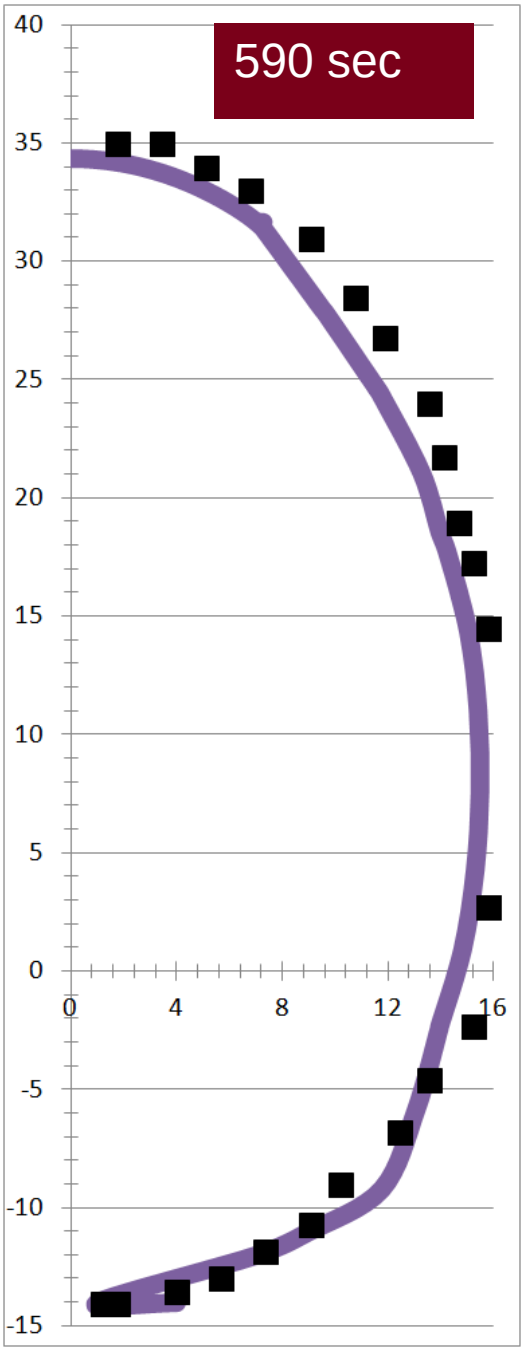
590 sec
40
35
30
25
20
15
10
5
0
-5
-10
-15
0
4
8
12
16

Figure 5.3Graphical representation of iceball at 30, 60, 90, 120, 150, 300 and 595 seconds.

The first of these figures displays the temporal evolution of the minor axis of the iceball. The figure features information from both the numerical simulations and the experiments. The agreement between the two sets of results is excellent. Attention will next be turned to a similar comparison showing the evolution of the major axis, and this information is presented in Figure 5.5. Once again, excellent agreement exists. It is relevant to compare the growth rates of the iceball with respect to its major and minor axis. From Figures 5.4 and 5.5, it is evident that the growth rate of the minor axis is much greater than that of the major axis. Over the time interval from 30 to 595 seconds, the minor axis increases by a factor of approximately 4, while the corresponding increases of the major axis is approximately 25%.

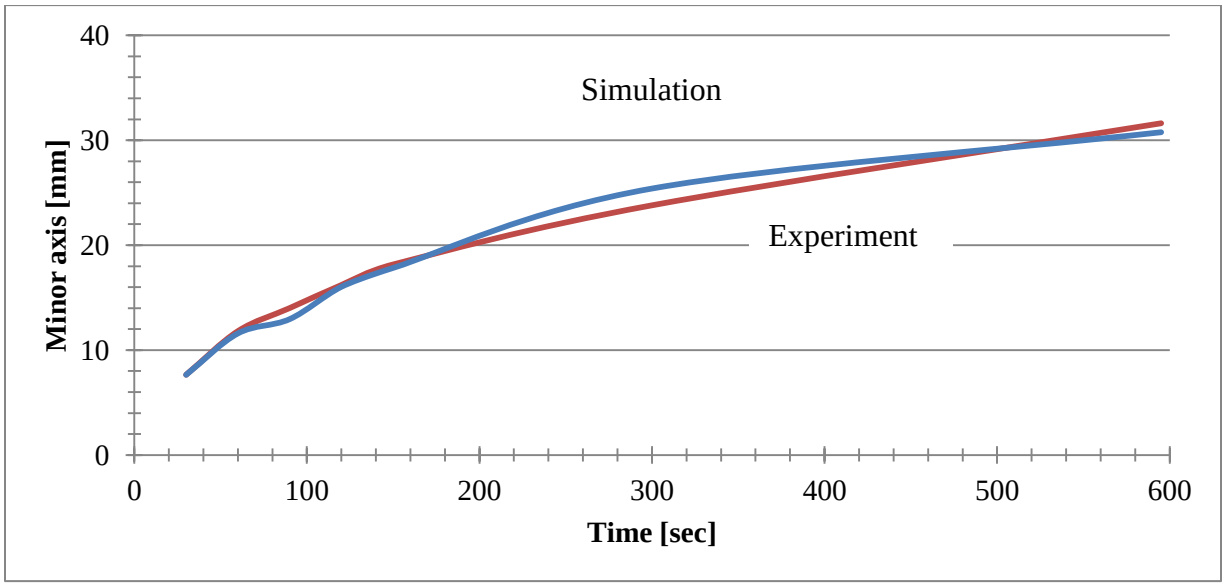

Figure 5.4 Variation of the dimension of the minor axis with time

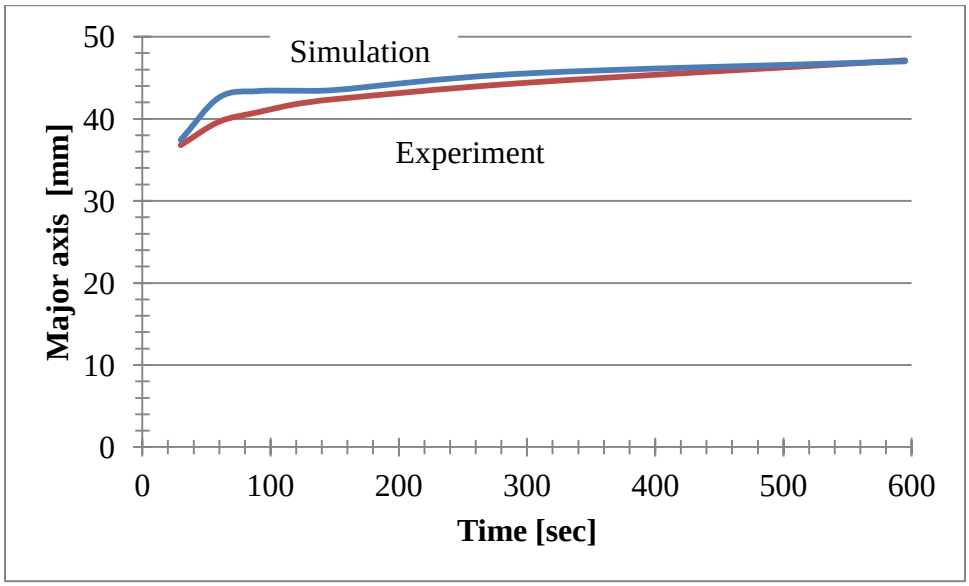

Figure 5.5 Variation of the dimension of the major axis with time

Chapter 6 Concluding Remarks

Cryosurgery has served as an alternative to scalpel-based surgery for at least fifty years. During this time, significant research efforts have been made to facilitate predictions of the efficacy of the methodology. For instance, in cases where large malfunctioning tissue must be necrosed, the means by which multiple cryosurgical probes are deployed has been perfected. The first manifestation of a cryosurgical device was operated with liquid nitrogen as the cryogenic medium. Over the years, it was found more effective to use a gaseous medium which, thanks to the Joule-Thomson effect, enabled such media to achieve temperatures sufficiently low to cause tissue necrosis. The original geometric manifestation of a cryosurgical device was in the form of a slim cylinder, another manifestation was later invented as a means to deal with more extensive nonfunctional tissue without the need for multiple probes. That newer device is the cryoballoon. In that case, a non-inflated balloon is strategically positioned with the aid of a catheter/guide wire device and is subsequently inflated by means of a cryogenic medium. The achievement of the required low-temperature levels is due to a phase-change process rather than a total reliance on the Joule-Thomson effect.

Between the two cryosurgical devices mentioned in the foregoing, research has heavily been focused toward the probe form. Notwithstanding the considerable amount of research, it appears that the literature is void of any reported investigation that is a *complete* model of the entirety of all the participating physical processes. A case in point is the cryoprobe, whose function involves both in-probe and ex-probe phenomena which necessarily interact. There have been numerous ex-probe studies of the cell necrosis process which occurs when the malfunctioning tissue is subjected to sufficiently low temperatures. In a few instances, attempts are reported to link in-probe fluid flow and heat transfer behavior and ex-probe heat conduction and phase change. While these attempts represent a forward step, the in-probe phenomena were profoundly simplified to

the point of not being valid. With regard to the cryoballoon, it appears that the internal fluid flow and heat transfer processes have never been subject to simulation.
The investigated performed in this thesis was aimed at being all encompassing. In the case of the cryoprobe, a rigorous assumption-free simulation was made of the in-probe fluid flow and heat transfer processes and an equally rigorous simulation was made for the ex-probe processes. The in-probe and ex-probe investigation actually were intimately and simultaneously carried out. A key outcome of this rigorous treatment was the total avoidance of any empiricism and simplifying assumptions.

A case in point is the issue of the values of the heat transfer coefficients for the spent cryofluid passing through an annular space in the cryoprobe. The heat transfer coefficient is an unnecessary crutch that has been utilized since time immemorial. Such a crutch may have had merit in an epoch of minimal research resources. However, in the present era, heat transfer rates can be determined directly without the need for the heat-transfer-coefficient crutch. In earlier work which attempted to somehow model the in-probe heat transfer processes, unsupported and perhaps erroneous assumptions were made for values of the heat transfer coefficient. Here, heat transfer coefficients were determined as an *a posteriori* action, although there was no need for these values. The calculated heat transfer coefficients based on the assumption-free model differed substantially from those that were adopted in earlier in-probe models. This outcome is a major contribution and should serve as a guide for any future work involving simplified models.

With regard to the cryoballoon methodology, the theory developed and implemented here was also without assumptions and empirical inputs. That theory necessarily involved change of phase as liquid jets morphed into vapor. Although there are no previous models available for comparison with the results found here, incremental experimental data were available and were used for comparison. The outcomes of the comparisons were extremely positive.

With respect to the cryoprobe, a full-dressed experimental investigation was performed. The experiments involved two different manifestations. In one manifestation, the external surface of the cryoprobe was insulated, and surface temperatures were measured. This manifestation was regarded as a baseline case. The experimental setup was numerically simulated precisely with a view to enabling definitive comparisons. The comparisons of the measured and predicted surface temperatures was very positive and provided definitive support of the fluid flow and heat transfer model of the processes taking place within the cryoprobe without any linkage to the external processes. This approach was felt to be mandatory because it served to separate the internal and external processes so that the internal processes could be evaluated in their own right.

A second experimental manifestation included both the cryoprobe and the heat transfer/phase change processes occurring external to the probe. Again, only first principles were used in developing the model. During the course of the experimentation, the temporal growth of the iceball was recorded. In a post-processing activity, the instantaneous coordinates of the iceball volume were extracted. The extraction process employed both a grid-based visual observation and an open-source software program. Use of two independent means was deemed to be mandatory to ensure the accuracy of the results. The iceball coordinates were rigorously compared with those predicted by the numerical simulations. The outcome of the comparison was extremely positive, thereby lending support to both the simulation and the experimental technique.

It is believed that the models developed in this thesis have been sufficiently supported to enable them to be regarded as standard approaches to be used when other cryosurgical devices are to be evaluated and quantified.

Bibliography

[1] T. E. Cooper and W. K. Petrovic, "An experimental investigation of the temperature field producednby a cryosurgical cannula," *J. of Heat Transfer,* pp. 415-420, 1974.

[2] A. Sguazzi and D. Bracco, "A historical account of the technical means used in cryotherapy," *Minerva Medica,* vol. 65, pp. 3718-3722, 1974.

[3] E. G. Kuflik and A. A. Gage, "Cryosurgical treatment for skin cancer," *IGAKU-SHOIN Medical Publishers, NY,* 1990.

[4] D. J. Larrey, "Memoires de chirugie militaire et companies," pp. 1812-7, 1832.

[5] J. Arnott, "Practical illustrations of the remedial efficacy of a very low anaesthetic temperature," *I. In cancer*, pp. 257-259, 1850.

[6] H. Bird and J. Arnott, "A pioneer a refrigeration," *Anaesthesia,* vol. 4, pp. 10-17, 1949.

[7] F. Anatoli and B. Nathaniel, "History of cryotherapy," *Dermatology online journal,* vol. 11, no. 2, p. 9, 2005.

[8] L. Cailletet, "Recherches sur la liquefaction des gas," *Ann Chemie Physique,* vol. 15, pp. 132-144, 1878.

[9] R. Pictet, "Memoire sur la lequifaction de leoxygen," *Ann Chemie Physique,* vol. 15, pp. 145-147, 1878.

[10] B. Rubinsky, "Cryosurgery," *Ann. Rev. of Biomedical Engineering,* pp. Vol. 2, pp.157-187, 2000.

[11] R. D. S. M. Cooper, "The history of cryosurgery," *J. of the Royal Society of Medicine,* vol. 94, p. 196–201, 2001.

[12] C. A. White, "Liquid air: its applications in medicine and surgery," *Med rec,* vol. 56, pp. 109-112, 1899.

[13] F. Sun, "An integrated model of heat transfer and tissue freezing for cryosurgery using cryospray or sryoprobe," *Dissertation,* 2007.

[14] H. Irvine and D. Turnacliff, "Liquid oxygen in dermatology," *Arch. dermatology syphilol.,* vol. 19, pp. 270-280, 1929.

[15] I. Cooper and A. Lee, "Cryostatic congelation:a system for producing a limited controlled region of cooling or freezing of biological tissue," *J. of nervous and mental disorders,* vol. 133, pp. 259-263, 1961.

[16] W.-K. Yiu, M. Basco and B. Sumpio, "Cryosurgery: a review," *The international journal of aniology: offical publication of the international college of angiology, Inc.,* vol. 16, no. 1, pp. 1-6, 2007.

[17] R. W. Rand, "Sterotactic cryo-hypophysectomy," *The journal of the american medical association,* vol. 189, pp. 255-259, 1964.

[18] M. Gonder, W. Soanes and W. Smith, "Experimental prostate cryosurgery," *Invest. Urology,* vol. 1, pp. 610-619, 1964.

[19] R. Marcover and T. Miller, "The treatment of primary and metastatic bone tumors by cryosurgery," *The surgical clinics of North America,* vol. 49, pp. 421-430, 1969.

[20] S. Zacarian and M. Adham, "Cryotherapy of cutaneous malignancy," *Cryobiology,* vol. 2, pp. 212-218, 1966.

[21] D. Torre, "Cutaneous cryosurgery," *New York state journal of medicine,* vol. 70, pp. 2551-2554, 1970.

[22] W. Cahan, "Cryosuregry of the uterus: description of techniques and potential applciations," *Americal journal of obstetrics and gynecology,* vol. 88, pp. 410-414, 1964.

[23] R. B. Pappenfmort, "Semicircular thermocouple needle depth gauge for cryoprocedure," *Cutis,* vol. 27, pp. 605-608, 1981.

[24] S. Zacarian, "How accurate is temperature monitoring in cryosurgery and is

there an alternative," *J. of dermatologic surgery and oncology,* vol. 6, pp. 627-632, 1980.

[25] "http://www.cancer.gov/cancertopics/factsheet/Therapy/cryosurgery," [Online].

[26] http://stanfordhospital.org/clinicsmedServices/medicalServices/interventionalRadiology/cancer_treatments/ablative.html. [Online].

[27] B. Rubinsky, "Cryosurgery," *Ann.Rev. Biomed, Eng,* vol. 2, pp. 157-187, 2000.

[28] Z. Hua , "Cryogenic thermophysical studies for clinical medicine," *Tsinghua Science and Technology,* vol. 7, pp. 165-170, 2002.

[29] K. Diller, "Engineering-based contributions in cryobiology," *Cryobiology,* vol. 34, p. 304–314, 1997.

[30] P. Mazur, "Freezing of living cells: mechanisms and implications," *American Journal of Physiology-Cell Physiology,* vol. 247, pp. C125-C142, 1984.

[31] I. R. Tao, J. Zhang and T. C. Hua, "An enthalpy method for solving freezing thawing process around a cryoprobe," *Cryobiology,* vol. 41, pp. 378-379, 2000.

[32] J. Zhang, T. C. Hua and E. T. Chen, "Experimental measurement and theoretical analyses of the freezing-thawing processes around a probe," *Cryo Letters,* vol. 21, pp. 245-254, 2000.

[33] A. Fortin and Y. Belhamadia, "Numerical prediction of freezing fronts in cryosurgery: comparison with experimental results," *Computer Methods in Biomechanics and Biomedical Engineering,* vol. 8, p. 241–249, 2005.

[34] T. Rybolt and R. Pierotti, "Investigation of the gas-solid Joule-Thomson effect for argon, nitrogen, and carbon dioxide-carbon powder aerosol systems," *The Journal of Physical Chemistry,* vol. 88, p. 2398–2404, 1984.

[35] P. C. Sprenkle, G. Mirabile, E. Durak , A. Edelstein and M. Gupta, "The effect of argon gas pressure on ice ball size and rate of formation," *J. of Endourology,* vol. 24, pp. 1503-1507, 2010.

[36] J. R. Roebuck and H. Osterberg, "The Joule-Thomson effect in helium,"

Am.Phy.Soc., vol. 43, p. 60–69, 1933.

[37] Y. Rabin, S. P. Steif, J. Taylor, T. B. Julian and N. Wolmark, "An experimental study of the mechanical response of frozen biological tissues at cryogenic temperatures," *Cryobiology,* vol. 33, pp. 472-482, 1996.

[38] D. Whittaker, "Electron microscopy of the ice crystals formed during cryosurgery:relationship to duration of freeze," *Cryobiology,* vol. 15, pp. 603-607, 1978.

[39] H. T. Merryman, Cryobiology, New York, NewYork: Academic Press, 1966.

[40] B. Rubinsky, "Cryosurgery," *Annual Review of Biomedical Engineering,* pp. Vol. 2, pp.157-187, 2000.

[41] J. Baust, A. Gage, H. Ma and C. Zhang, "Minimally invasive cryosurgery-technological advances," *Cryobiology,* vol. 34, pp. 373-384, 1997.

[42] A. Gage and J. Baust, "Mechanisms of tissue injury in cryosurgery," *Cyobiology,* vol. 37, no. 3, pp. 171-186, 1998.

[43] K. Chua, S. Chou and J. Ho, "An analytical study on the thermal effects of cryosurgery on selecive cell destruction," *J. of Biomechanics,* vol. 40, pp. 100-116, 2007.

[44] M. Resnick and I. M. Thompson, Advanced therapy of prostate disease, Vol. 1, Lewiston, New York: B. C. Decker Inc, 2000.

[45] http://radiology.rsna.org/content/258/2/351/F5.expansion.html. [Online].

[46] N. N. Korpan, "A history of cryosurgery: Its development and future," *Journal of American College of Surgeons,* vol. 204, p. 314–324, 2007.

[47] N. Korpan, Basics of cryosurgery, Springer, 2001.

[48] W. Butler , "Cryotherapy," in *American Association of Physicists in Medicine,* 2005.

[49] Saragusty, J., Gacitua, H., Rozenboim, I., Arav, A, "Do physical forces contribute to cryodamage?," *Biotech Bioeng.,* Vols. 104 pages 719-728, 2009.

[50] Z. Hua, "Cryogenic thermophysical studies for clinical medicine," *Tsinghua Science and Technology,* vol. 7, pp. 165-170, 2002.

[51] Yang,G. Zhang,A. Xu, L., "Intracellular ice formation and growth in MCF-7 cancer cells," *Cryobiology,* Vols. 63 pages 38-45, 2011.

[52] A. Gage, "Cryosurgery in the treatment of cancer," *Surgery, Gynecology and Obstetrics,* vol. 174, pp. 73-92, 1992.

[53] c. ablation, "http://krames.sjmctx.com/HealthSheets/3,S,89106?PrinterFriendly=true," [Online].

[54] V. Fuster, L. Ryden and D. Cannom, "2006 guidelines for the management of patients with atrial fibrillation: a report of the american college of cardiology/american heart association task force on practice guidelines and the european society of cardiology committee for practice guidelines," *European Heart Rhythm Association and the Heart Rhythm Society,* vol. 114, no. 7, pp. 257-354, 2006.

[55] C. Ozcan, J. Ruskin and M. Mansour, "Cryoballoon catheter abalation in atrail fibrillation," *SAGE- Hindawi access to research cardiology research and practice,* vol. 2011, p. 6, 2011.

[56] J. Gallagher, R. Svenson, J. Kasell, L. German, G. Bardy and A. Broughton, "Catheter technique for closed-chest abalation of the atriobentricular conduction system," *The new england journal of science,* pp. 194-200, 1982.

[57] R. Cappato, H. Calkins and S. Chen, "Worldwide survery on the methids, efficacy, and safety of catheter ablation for human atrial fibrillation," *Circulation,* vol. 111, no. 6, pp. 1100-1105, 2005.

[58] physicians, "http://www.cc.nih.gov/drd/rfa/pdf/physicians.pdf," [Online].

[59] A. C. Skanes, R. Yee, A. Krahn and G. Klien, "Cryoablation of atrial arrhythmias," *Cardiac electrophysiology review,* pp. 383-388, 2002.

[60] Lafontaine, "Cryo balloon for atrial abalation". USA Patent 666858, 23 Dec 2003.

[61] M. Tang, C. Kriatselis, S. Nedois, M. Roser, E. Fleck and GergsLi, "A novel cryoballoon techniqu for mapping and isolating pulmonary veins: a feasibility and efficacy study," *J. of cardiovascular electrophysiology,* 2009.

[62] G. Chierchia, A. Sorgente, A. Sarkozy, C. Asmundis and P. Brugada, "The use od cryoballoon abaltion in atrial fibrillation: simplifying pulmonray vein isolation?," *J. of atrial fibrillation,* vol. 3, no. 4, pp. 33-43, 2010.

[63] M. gadget, "http://www.medgadget.com/2010/12/medtronic_brings_first_cryoballoon_ablation_system_to_us.html," [Online].

[64] J. Andrade, M. Dubuc, P. Guerra, L. Macle and et.al, "The Biophysics and Biomechanics of cryoballoon ablation," *PACE,* vol. 35, pp. 1162-1169, 2012.

[65] Y. Belle, P. Janse, M. Rivero-Ayerza, A. Thornton, E. Jessurun, D. Theuns and L. Jordaens, "Plumlonary vein isolation using an occluding cryoballoon for circumferential ablation:feasibility, complications, and short-term outcome," *European heart journal,* vol. 28, pp. 2231-2237, 2007.

[66] o. heart, "http://www.oklahomaheart.com/content/cryoablation-cryoballon-ablation," [Online].

[67] V. Reddy and P. Neuzil, "Balloon catheter abalation to treat paroxymal atrail fibrilalation: what is the level of pulmonary venous isloation?," *Heart Rhythm,* vol. 5, no. 3, pp. 353-360, 2008.

[68] A. Sarabanda, T. Bunch and S. Johnson, "Efficacy and safety of circumferential pulmonary vein isolation using a novel cryothermal balloon alation system," *Journal of the american collge of cardiology,* vol. 46, no. 10, pp. 1902-1912, 2005.

[69] FDA, *Summary of safety and effectiveness data.*

[70] "http://www.dana-farber.org/Adult-Care/Treatment-and-Support/Skin-Cancer.aspx#Cancer_Summary," [Online].

[71] G. Onik, "Cryosurgery," *Critical reviews in oncology/hematology,* vol. 19, pp. 219-222, 1996.

[72] A. Gage and J. Baust, "Mechanisms of tissue injury," *Cryobiology,* vol. 37, pp. 171-186.

[73] N. E. Hoffman and J. C. Bischof, "The cryobiology of cryosurgical injury," *Urology,* vol. 60, pp. 40-49, 2002.

[74] Y. Rabin, D. Lung and T. Stahovich, "Computerized planning of cryosurgery using cryoprobes and cryoheaters," *Tech. Cancer Res. Treat.,* vol. 3, no. 3, 2004.

[75] H. Talbot, M. Lekkal, R. Bessard-Duparc and S. Cotin, "Interactive planning of cryotherapy using physics-based simulation," *Studies in health technology and informatics*, vol. 21 , no. 1, 2014.

[76] "http://www.surgeryencyclopedia.com/Ce-Fi/Cryotherapy.html," [Online].

[77] C. Bernard, "Lecons sur la chaleur animale," Bailliere, Paris, 1876.

[78] A. Gagge, C. Winslow and L. Herrington, "The influence of clothing on the physiological reactions of the human body to varying enviornmental temperatures," *American journal of physiology,* vol. 124, p. 30, 1938.

[79] J. Hardy and E. Dubois, "Basal metabolism,radiation,convection, and vaporization at temperatures of 22 to 35C," *The journal of nutrition,* vol. 15, p. 477, 1938.

[80] H. Bazett and B. McGlone, "Temperature gradients in the tissues in man," *American journal of physiology,* vol. 82, p. 415, 1927.

[81] E. Mendelson, "Measurement of superficial temeprature gradient in man," *American journal of physiology,* vol. 114, pp. 642-647, 1936.

[82] H. Pennes, "Analysis of tissue and arterial blood temepratures in the resting

human forearm," *J. of applied physiology,* vol. 1, pp. 93-122, 1948.

[83] C. Charny, "Mathematical models of bioheat transfer," *Advances in heat transfer series, Elsevier Inc,* vol. 22, 1992.

[84] P. Mazur, "Physical-chemical factors underlying cell injury in cryosurgical freexing," *Cryosurgery,* vol. 2, pp. 32-51, 1968.

[85] P. Mazur, "Physical factors implicated in the death of micro-organisms," *Annals New York Academy of Sciences,* vol. 85, pp. 610-628, 1960.

[86] P. Mazur, "Manifestations of injury in yeast cells exposed to subzero temperatures," *J. of Bacteriology,* vol. 82, pp. 662-672, 1961.

[87] P. Mazur, "Kinetics of water loss from cells at subzero temperatures and the likelihood of intracellular freezing," *The Journal of General Physiology,* vol. 47, pp. 347-369, 1963.

[88] P. Mazur , "Cryobiology: the freezing of biological systems," *Science,* vol. 168, pp. 939-949, 1970.

[89] P. Mazur, "Equilibrium, quasi-equilibrium and nonequilibrium freezing of mammalian embryos," *Cell Biophysics,* vol. 17, pp. 53-92, 1990.

[90] P. Mazur, "The role of intracellular freezing in the death of cells cooled at supraoptimal rates," *Cryobiology,* vol. 14, pp. 215-272, 1977.

[91] P. Mazur, S. Leibo and E. Chu, "A two-factor hypothesis of freezing injury," *Experimental Cell Research,* vol. 71, pp. 345-355, 1972.

[92] P. Mazur, ""Principles of Cryobiology"," in *Life in the Frozen State,* New York, CRC Press, 2004, pp. 3-65.

[93] A. Skanes, R. Yee, A. Krahn and G. Klein, "Cryoablation for atrial arrhythmias," *CArdiac Electrophysiology Review,* vol. 2, pp. 383-388, 2002.

[94] I. S. Cooper, "Cryobiology as viewed by the surgeon," *Cryobiology,* vol. 1, pp. 44-54, 1964.

[95] J. J. Smith and J. Fraser, "An estimation of tissue damage and thermal history in

the cryolesion," *Cryobiology*, vol. 11, pp. 139-147, 1974.

[96] J. Smith, J. Fraser and A. G. MacIver, "Ultrastructure after cryosurgery of rat liver," *Cryobiology*, vol. 15, pp. 426-432, 1978.

[97] B. Schreuder, "Cryosurgery of bone tumors," *Basics of Cryosurgery*, pp. 231-251, 2001.

[98] K. J. Chua and S. K. Chou, "On the study of the freeze-thaw thermal process of a biological system," *Applied thermal engineering*, vol. 29, pp. 3696-3709, 2009.

[99] V. R. Chikanjuri, "Heat transfer model for cryosurgery," 2011.

[100] Cooper, T. E., and Trezek, G. J.,, "Mathematical prediction of cryogenic lesion," *Cryogenics in surgery*, Vols. pages 128-150, 1971.

[101] Cooper, T. E., Trezek, G. J.,, "On the freezing of tissue,"*J. of heat transfer* Vols. 94 pages 251-253, 1972.

[102] Warren, R. P . , Bingham, P. E., and Carpinter, J. D.,, "Heat flow in living tissue during cryosurgery," vol. 37, 1974.

[103] Rewcastle J., Sandison G., "A model for the time dependent three-dimensional thermal distribution within iceballs surrounding multiple cryoprobes," *Med Phys*, Vols. 28 pages 1125-1138, 2001.

[104] R. Wan, Z. Liu, K. Muldrew, J. Rewcastle, "A finite element model for ice ball evolution in a multi-probe cryosurgery," *Computer Methods in Biomechanics and Biomedical Engineering*, vol. 6, p. 197–208, 2003.

[105] S. Deljou, S. Haghipour and A. Bayat, "Intelligent planning for cryoprobe placement dyrung cryosurgery," *Life Sci Journal* Vols. 10 pp. 552-557, no. 3, 2013.

[106] S. Singh and S. Kumar, "A study on the effect of metabolc heat generation on biological tissue freezing," *The scientific world journal*, vol. 2013 pp 7, no. 3, 2013.

[107] Z. Liu, K. Muldrew, R. Wan, J. Elliott, "Retardation of ice growth in glass capillaries: measurement of the critical capillary radius," *Computer Methods in Biomechanics and Biomedical Engineering,* vol. 69, p. 197–208, 2004.

[108] S. Leibo, P. Mazur, "The role of cooling rates in low temperature preservation," *Cryobiology*, Vols. 8 pages 447-452, 1971.

[109] S. Lin, D. Y. Gao, X. C. Yu, "Thermal stresses induced by water solidification in a cylindrical tube," *J. of Heat Transfer,* vol. 112, pp. 1079-1082, 1990.

[110] Y. Rabin, S. P. Steif, "Analysis of thermal stresses around cryosurgical probe," *Cryobiology,* vol. 33, pp. 276-290, 1996.

[111] N. Zabaras, Y. Ruan, O. Richmond, "On the calculation of deformations and stresses during axially symmetric solidification," *J. of Applied Mechanics,* vol. 58, pp. 865-871, 1991.

[112] L. Xiao-Zhou, Q. Sun Chang, L. Tao, "The testing methods on fracture toughness of the reservoir ice layer in different temperature and loading rate," *Multimedia Technology conference (ICMT),* 2011.

[113] X. He, J. Bischof, "Analysis of thermal stress in cryosurgery of kidneys," *J.of Biomechanical Engineering,* vol. 127, pp. 656-662, 2005.

[114] Y. Rabin, S. P. Steif, M. J. Taylor, T. B. Julian, N. Wolmark, "An experimental study of the mechanical response of frozen biological tissues at cryogenic temperatures," *Cryobiology,* vol. 33, pp. 472-482, 1996.

[115] F. Popken, J.K. Seifert, R. Engelmann, P. Dutkowski, F. Nassir, T. Junginger, "Comparison of iceball diameter and temperature distribution achieved with 3-mm accuprobe cryoprobes in porcine and human liver tissue and human colorectal liver metastases in vitro," Vols. 40 pages 302-310, 2000.

[116] Deng Z.,n Liu J., "Modeling of multidimensional freezing problem during cryosurgery by the dual reciprocity of boundary element method," Vols. 28 pages 97-108, 2004.

[117] A. Fortin, Y. Belhamadia, "Numerical prediction of freezing fronts in cryosurgery: comparison with experimental results," *Computer Methods in Biomechanics and Biomedical Engineering*, vol. 8, p. 241–249, 2005.

[118] Shitzer, A., "Cryosurgery: analysis and experimentation of cryoprobes in phase changing media," *J. of heat transfer*, vol. 133, 2011.

[119] Widyaparaga, A, Kuwamoto, M.1, Sakoda, N., Kohno, M, Takata, Y, "Theoretical and experimental study of a flexible wiretype joule-thomsonmicrorefrigerator for use in cryosurgery," in *ASME 2010 8th International Conference on Nanochannels, Microchannels, and Minichannels: Parts A and B*, Montreal, Quebec, Canada, 2012.

[120] H. Budman, A. Shitzer, "Investigation of temperature fields around embedded cryoprobes,"*J. of biomed. engg.*, Vols. 108 pages 42-49, 1986.

[121] Kumar, N., Soni, S.,Pankaj, D, "Development of cryo probe for medical application," in *Proceedings - 1st International Conference on Emerging Trends in Engineering and Technology*, Washington, DC, USA, 2008.

[122] V. V. Sychev, The differential equations of thermodynamics, Washington D.C.: Taylor and Francis, 1981.

[123] J. R. Roenbuck and H. Osterberg, "The Joule-Thomson effect in argon," *American Physical Society*, Vols. 46 pages 785-790, 1934.

[124] A. Charnley, G. L. Isles and J. R. Townley, "The direct measurement of the isothermal Joule-Thomson coefficient for gases," *Proceedings of the Royal Society of London*, vol. 128, pp. 133-143, 1953.

[125] J. R. Roebuck and H. Osterberg, "The Joule-Thomson effect in nitrogen," *American Physical Society*, vol. 48, p. 450–457, 1935.

[126] D. Mage, "Joule-Thomson effect on gaseous helium," *American Physical Society*, vol. 42, pp. 60-69, 1933.

[127] E. S. Burnett, "Experimental study of the Joule-Thomson effect in carbon

dioxide," *American Physical Society*, vol. 22, p. 590–616, 1923.

[128] H. Saygin and A. Sisman, "Joule–Thomson coefficients of quantum ideal-gases," *Applied Energy*, vol. 70, p. 49–57, 2001.

[129] O. Gustafsson, "On the joule-thomson effect for gas mixtures," *Physica Scripta*, vol. 2, 1970.

[130] Cooper, T. E., and Trezek, G. J, "Rate of lesion growth around spherical and cylindrical cryoprobe,"*Cryobiology*, Vols. 7 pages 183-190, 1971.

[131] G. Turrel, Gas dynamics: theory and applications, New York, NY: John Wiley & Sons, 1997.

[132] A. S. Dorfman, Conjugate problems in convective heat transfer, Boca Raton, Fl: CRC Press, 2010.

[133] Shamsundar N., Sparrow E., "Analysis of multidimensional conduction phase change via the enthalpy model," *J. of heat transfer*, Vols. pages- 333-340, 1975.

[134] Voller V.,Cross M, "Accurate solutions of moving boundary problems using the enthalpy method," *Int. journal of heat transfer*, Vols. 24 pages 545-556, 1980.

[135] K. Kuehne, S. Osswald and C. Sticherling, "Quantitative assessment of a new generation cryoballoon ablation catheter with new cooling technology," in *European society of cardiologist*, Greece, 2013.

[136] D. W. Davies, "http://www.heartrhythmcongress.com/files/file/HRC2012%20Presentations/120925-1145-Cyro%20Balloon%20at%20St%20Mary's,%20D%20W%20Davies.pdf," [Online].

[137] "http://krames.sjmctx.com/HealthSheets/3,S,89106?PrinterFriendly=true,"

[138] F. Menter, "Two equation eddy viscosity turbulence models for engineerign applciations," *AIAA*, vol. J 30, pp. 1598-1605, 1994.

[139] E. Sparrow, J. Gorman and J. Abraham, "Quantitative assessment of the overall

heat transfer coefficient," *J. of heat transfer,* vol. 135, pp. 61102-1-7, 2013.

[140] J. Abraham, E. Sparrow and J. Tong, "Heat transfer in all pipe flow regimes: laminar, transitional/intermittent, and turbulent flows," *Int. journal of heat and mass transfer,* vol. 52, pp. 557-563, 2009.

[141] J. Stark, J. Gorman, M. Hennessey, F. Reseghetti, J. Willis, J. Lyman, J. Abraham and M. Borghini, "A computational method for determining XBT depths," *Ocean science,* vol. 7, pp. 733-743, 2011.

[142] J. Abraham, J. Gorman, F. Reseghetti, E. Sparrow and W. Minkowycz, "Drag coefficients for rotating expendable bathythermographs and the impact of launch parameters on depth predictions," *Numerical heat transfer Part A,* vol. 62, pp. 25-43, 2012.

[143] F. Menter, B. Langtry, S. Likki, Y. Suzen, P. Huang and S. Volker, "A correlation-based transition model using local variables – part 1: model formulation," *J. of turbomachinery,* vol. 128, pp. 413-422, 2006.

[144] R. Langtry, F. Menter, S. Likki, Y. Suzen, P. Huang and S. Volker, "A correlation-based transition model using local variables – part 2: test cases and industrial applications," *J.of turbomachinery,* vol. 128, pp. 423-434, 2006.

[145] NIST, "http://www.nist.gov/," [Online].

[146] B. Rubinsky, "Cryosurgery," *Annual Review of Biomedical Engineering,* pp. Vol. 2, pp.157-187, 2000.

[147] J. Andrade, M. Dubuc, P. Guerra and et.al, "The Biophysics and biomechanics of cryoballoon," *Pacing and Clinical Electrophysiology,* vol. 35, no. 9, pp. 1162-1169, 2012.

[148] G. B. Chierchia, A. Sorgente, A. Sarkoz, Asmundis and P. Brugada, "The Use of Cryoballoon Ablation in Atrial Fibrillation: Simplifying Pulmonary Vein Isolation?," *J. of Atrial Fibrillation,* vol. 3, no. 4, pp. 33-44, 2011.

[149] J. Zhang, G. Sandison, J. Murthy and L. Xu, "Numerical simulation for heat

transfer in prostate cancer cryosurgery," *J. of Biomedical Engineering,* vol. 127, pp. 279-294, 2005.

[150] M. Etheridge, J. Choi, S. Ramadhyani and J. Bischof, "Methods for characterizing convective cryoprobe heat trasnfer in ultrasound gel pahntoms,"*J. of biomed. engg.,* vol. 135, no. 021002-1, 2013.

Appendix A

Thermophysical properties of nitrous oxide on the saturation line for temperature in °C

t °C	p kPa	ρ(l) kg/m^3	ρ(g) kg/m^3	h(l) kJ/kg	h(g) kJ/kg	$\Delta_{vap}h$ kJ/kg
-90.82	(87.73)	1222.8	(2.613)	(-474.)	(-96.8)	(377.)
-90	(92.29)	1220.6	(2.738)	(-473.)	(-96.3)	(377.)
-88.46	101.325	1216.3	(2.987)	(-470.)	(-95.4)	375.
-85	124.2	(1206.7)	(3.609)	(-464.)	(-93.3)	371.
-80	164.2	(1192.7)	(4.680)	(-455.)	(-90.4)	365.
-75	213.6	(1178.3)	(5.982)	(-446.)	(-87.6)	359.
-70	273.6	(1163.7)	(7.546)	(-438.)	(-85.0)	353.
-65	345.7	(1148.8)	(9.406)	(-429.)	(-82.5)	346.
-60	431.5	(1133.6)	(11.60)	(-420.)	(-80.2)	340.
-55	532.3	(1118.0)	(14.16)	(-411.)	(-78.1)	333.
-50	649.9	(1102.0)	(17.14)	(-402.)	(-76.1)	326.
-45	785.8	(1085.6)	(20.58)	(-392.)	(-74.4)	318.
-40	941.7	(1068.8)	(24.53)	(-383.)	(-72.9)	310.
-35	1119.	(1051.4)	(29.05)	(-374.)	(-71.6)	302.
-30	1321.	1033.4	34.22	(-364.)	(-70.5)	294.
-25	1547.	1014.8	40.11	(-355.)	(-69.8)	285.
-20	1801.	995.4	46.82	(-345.)	(-69.3)	276.
-15	2083.	975.2	54.47	(-335.)	(-69.2)	266.
-10	2397.	953.9	63.21	(-325.)	(-69.5)	255.
-5	2744.	931.4	73.26	(-315.)	(-70.3)	244.
0	3127.	907.4	84.86	(-304.)	(-71.7)	232.
5	3547.	881.6	98.41	(-293.)	(-73.7)	219.
10	4007.	853.5	114.5	(-281.)	(-76.6)	204.
15	4510.	822.2	133.9	(-269.)	(-80.6)	188.
20	5060.	786.6	158.1	(-255.)	(-86.2)	169.
25	5660.	743.9	190.0	(-241.)	(-94.4)	147.
30	6315.	688.0	236.7	(-224.)	(-108.)	117.
35	7033.	589.4	330.4	(-203.)	(-138.)	64.9
36.42	7251.	452.	452.	(-200.)	(-200.)	0

Thermophysical properties of nitrous oxide on the saturation line for temperature in °C (contd)

t °C	c_p(l) kJ/kg K	c_p(g) kJ/kg K	η(l) mN s/m^2	η(g) μN s/m^2	λ(l) mW/m K	λ(g) mW/m K	σ mN/m
-90.82	1.747	(0.7999)	(0.4619)	(9.4)	(146.9)	(8.2)	24.0
-90	1.750	(0.7997)	(0.4507)	(9.5)	(146.4)	(8.3)	23.8
-88.46	1.756	(0.7996)	(0.4306)	(9.6)	(145.6)	(8.4)	(23.5)
-85	1.768	(0.8009)	(0.3900)	(9.7)	(143.8)	(8.7)	(22.7)
-80	(1.781)	(0.8063)	(0.3404)	(10.0)	(141.2)	(9.1)	(21.6)
-75	(1.791)	(0.8160)	(0.2995)	(10.2)	(138.6)	(9.6)	(20.5)
-70	(1.798)	(0.8300)	(0.2654)	(10.5)	(136.0)	(10.0)	(19.4)
-65	(1.803)	(0.8485)	(0.2367)	(10.8)	(133.5)	(10.5)	(18.3)
-60	(1.807)	(0.8716)	(0.2123)	(11.0)	(131.0)	(11.0)	(17.2)
-55	(1.812)	(0.8995)	(0.1915)	(11.3)	(128.5)	(11.5)	(16.2)
-50	(1.818)	(0.9322)	(0.1736)	(11.6)	(126.0)	(12.0)	15.1
-45	(1.827)	(0.9700)	(0.1580)	(11.9)	(123.6)	(12.6)	14.1
-40	(1.840)	(1.013)	(0.1444)	(12.2)	(121.2)	(13.2)	13.1
-35	(1.858)	(1.061)	(0.1325)	(12.5)	(118.8)	(13.8)	12.0
-30	(1.883)	(1.115)	(0.1219)	(12.8)	(116.4)	(14.4)	11.0
-25	(1.915)	(1.176)	(0.1125)	(13.2)	(114.1)	(15.1)	10.1
-20	(1.957)	(1.243)	(0.1041)	(13.5)	(111.8)	(15.8)	9.1
-15	(2.011)	(1.318)	(0.0965)	(13.9)	(109.6)	(16.5)	8.1
-10	(2.079)	(1.402)	(0.0896)	(14.3)	(107.4)	(17.3)	7.2
-5	(2.166)	(1.500)	(0.0833)	(14.7)	(105.2)	(18.2)	6.3
0	(2.274)	(1.618)	(0.0774)	(15.2)	103.0	(19.1)	5.4
5	(2.412)	(1.769)	(0.0720)	(15.7)	100.9	(20.2)	4.5
10	(2.592)	(1.982)	(0.0668)	(16.3)	98.8	(21.4)	3.7
15	(2.834)	(2.322)	(0.0619)	(16.9)			2.9
20	(3.188)	(2.967)	(0.0570)	(17.7)			2.1
25	(3.781)	(4.493)	(0.0520)	(18.7)			1.4
30	(5.143)	(9.718)	(0.0465)	(20.1)			0.7
35							0.1
36.42	∞	∞	∞	∞	∞	∞	0

Thermophysical properties of nitrous oxide on the saturation line for temperature in Kelvin

T	p	ρ(l)	ρ(g)	h(l)	h(g)	$\Delta_{vap}h$
K	kPa	kg/m^3	kg/m^3	kJ/kg	kJ/kg	kJ/kg
182.33	(87.73)	1222.8	(2.613)	(-474.)	(-96.8)	(377.)
184.69	101.325	1216.3	(2.987)	(-470.)	(-95.4)	375.
185	103.2	(1215.5)	(3.039)	(-470.)	(-95.2)	374.
190	138.0	(1201.6)	(3.980)	(-461.)	(-92.2)	369.
195	181.3	(1187.4)	(5.133)	(-452.)	(-89.3)	363.
200	234.5	(1172.9)	(6.528)	(-443.)	(-86.6)	357.
205	298.8	(1158.2)	(8.198)	(-434.)	(-84.0)	350.
210	375.8	(1143.2)	(10.18)	(-425.)	(-81.6)	344.
215	466.9	(1127.8)	(12.50)	(-416.)	(-79.4)	337.
220	573.8	(1112.1)	(15.21)	(-407.)	(-77.3)	330.
225	698.0	(1096.0)	(18.36)	(-398.)	(-75.5)	323.
230	841.1	(1079.5)	(21.98)	(-389.)	(-73.8)	315.
235	1005.	(1062.4)	(26.13)	(-380.)	(-72.3)	307.
240	1191.	(1044.8)	(30.89)	(-370.)	(-71.1)	299.
245	1401.	1026.6	36.31	(-361.)	(-70.2)	291.
250	1638.	1007.7	42.49	(-351.)	(-69.6)	282.
255	1902.	988.0	49.53	(-341.)	(-69.2)	272.
260	2196.	967.4	57.57	(-331.)	(-69.3)	262.
265	2522.	945.7	66.77	(-321.)	(-69.8)	251.
270	2881.	922.7	77.35	(-311.)	(-70.7)	240.
275	3278.	898.1	89.62	(-300.)	(-72.3)	227.
280	3712.	871.5	104.0	(-288.)	(-74.6)	214.
285	4188.	842.3	121.2	(-277.)	(-77.9)	199.
290	4708.	809.7	142.1	(-264.)	(-82.4)	182.
295	5276.	771.8	168.8	(-250.)	(-88.9)	161.
300	5896.	725.3	204.9	(-235.)	(-98.5)	137.
305	6573.	660.5	261.5	(-217.)	(-115.)	102.
309.57	7251.	452.	452.	(-200.)	(-200.)	0

Thermophysical properties of nitrous oxide on the saturation line for temperature in Kelvin(contd)

T K	c_p(l) kJ/kg K	c_p(g) kJ/kg K	η(l) mN s/m^2	η(g) μN s/m^2	λ(l) mW/m K	λ(g) mW/m K	σ mN/m
182.33	1.747	(0.7999)	(0.4619)	(9.4)	(146.9)	(8.2)	24.0
184.69	1.756	(0.7996)	(0.4306)	(9.6)	(145.6)	(8.4)	(23.5)
185	1.757	(0.7997)	(0.4267)	(9.6)	(145.5)	(8.4)	(23.4)
190	(1.773)	(0.8024)	(0.3705)	(9.8)	(142.8)	(8.9)	(22.3)
195	(1.785)	(0.8094)	(0.3244)	(10.1)	(140.2)	(9.3)	(21.2)
200	(1.794)	(0.8206)	(0.2861)	(10.3)	(137.6)	(9.7)	(20.1)
205	(1.800)	(0.8363)	(0.2542)	(10.6)	(135.1)	(10.2)	(19.0)
210	(1.804)	(0.8565)	(0.2272)	(10.9)	(132.6)	(10.7)	(17.9)
215	(1.809)	(0.8813)	(0.2042)	(11.1)	(130.0)	(11.2)	(16.8)
220	(1.814)	(0.9110)	(0.1846)	(11.4)	(127.6)	(11.7)	(15.8)
225	(1.821)	(0.9456)	(0.1676)	(11.7)	(125.1)	(12.2)	14.7
230	(1.832)	(0.9853)	(0.1528)	(12.0)	(122.7)	(12.8)	13.7
235	(1.846)	(1.030)	(0.1399)	(12.3)	(120.3)	(13.4)	12.7
240	(1.866)	(1.081)	(0.1284)	(12.6)	(117.9)	(14.0)	11.7
245	(1.894)	(1.137)	(0.1183)	(12.9)	(115.6)	(14.7)	10.7
250	(1.929)	(1.200)	(0.1093)	(13.3)	(113.3)	(15.3)	9.7
255	(1.976)	(1.269)	(0.1012)	(13.7)	(111.0)	(16.1)	8.7
260	(2.035)	(1.348)	(0.0939)	(14.0)	(108.7)	(16.8)	7.8
265	(2.109)	(1.437)	(0.0872)	(14.4)	(106.5)	(17.6)	6.9
270	(2.203)	(1.541)	(0.0810)	(14.9)	(104.4)	(18.5)	6.0
275	(2.321)	(1.669)	(0.0754)	(15.4)	102.2	(19.5)	5.1
280	(2.473)	(1.838)	(0.0700)	(15.9)	100.1	(20.6)	4.2
285	(2.672)	(2.087)	(0.0650)	(16.5)			3.4
290	(2.948)	(2.509)	(0.0601)	(17.2)			2.6
295	(3.367)	(3.369)	(0.0552)	(18.1)			1.8
300	(4.133)	(5.642)	(0.0501)	(19.2)			1.1
305							0.5
309.57	∞	∞	∞	∞	∞	∞	0